The Ohakuri pyroclastic deposits and the evolution of the Rotorua-Ohakuri volcanotectonic depression

A thesis submitted in fulfilment
of the requirements for the Degree
of
Doctor of Philosophy in Geology
at the
University of Canterbury
by

Darren McClurg Gravley

University of Canterbury
2004

Abstract

The caldera-forming Ohakuri pyroclastic deposits (~ 100 km^3 magma) were erupted at ~ 240 ka from the newly defined Ohakuri caldera, which is located within the central Taupo Volcanic Zone (TVZ) of New Zealand. The Ohakuri pyroclastic deposits are remarkable for their widespread lateral and vertical lithofacies variation that is attributed to phreatomagmatic eruption dynamics and a variable depositional environment. The Ohakuri pyroclastic deposits overlie 3 precursor airfall units erupted from a source within what was to become the Ohakuri caldera. The third of these fall units, which directly underlies the Ohakuri deposits, is a plinian-style deposit (unit 3) that is interbedded with distal Mamaku ignimbrite (> 145 km^3 magma) from the Rotorua caldera, ~ 25 km north of the Ohakuri caldera. It is thus inferred that these two major eruptions must have overlapped such that the Ohakuri pyroclastic deposits and Mamaku ignimbrite were erupted at most weeks to months apart.

The complex Ohakuri deposits, previously documented in part as sediments, are here described in terms of pyroclastic lithofacies that are grouped into 5 geographically distinct lithofacies associations. Each Ohakuri lithofacies association thus represents a distinctive style of deposition in an eruption that was highly variable in time and space. One lithofacies association consists of giant-dune-bedforms with wavelengths up to 42 m that are characterised by an anomalously high fraction of fine ash. Two other lithofacies associations are related to the interaction between primary pyroclastic density currents and a wet depositional environment that triggered several episodes of secondary hydroeruptions. These hydroeruptions and their deposits provide evidence for time breaks in the Ohakuri eruption sequence that, otherwise, could (the time breaks) not be discerned from thick accumulations of structureless ignimbrite. Geochemically, the Ohakuri pumice compositions range from silicic type 1 and 2 compositions to a dacitic type 3 composition. The distribution of the 3 pumice types, matched with the distribution of Ohakuri lithofacies associations, reveals an eruption sequence that can be divided into two main events.

The Ohakuri and Mamaku eruptions, together with the syn-volcanic subsidence of the central Kapenga area (> 100 km^2), formed what is defined here as the Rotorua-Ohakuri volcanotectonic depression. With respect to the central Kapenga area, paleogeographic reconstruction from fieldwork and age data shows that > 250 m of vertical displacement occurred on its western margin (the Horohoro Fault scarp) in one large 'superfault' event. The subsidence of this region was induced by lateral withdrawal of magma, via a NE-SW trending conduit system, which was then erupted from the Ohakuri caldera.

Acknowledgments

This thesis would not have been completed without the help and guidance of so many people. I may forget some of you in writing this so I will apologise up front for my sometimes careless memory. The two most important people associated with the final thesis product are my supervisors Jim Cole and Colin Wilson, without either of you I would have been doomed. Jim, I am truly grateful to you for imparting your years of knowledge and experience in the field of volcanology and the Taupo Volcanic Zone on me. Your moral and always positive support and ability to keep the goal in sight was unrivaled. Colin, without your support and confidence in me as a scientist it would have been impossible to forge my way through a project that, at times, seemed too ominous to complete. In the world of physical volcanology, there are few people as accomplished as you are, and for this I feel extremely lucky to have been under your supervision.

I would like to thank the Foundation for Research, Science, and Technology. Without your financial support this project would not have been possible. I would also like to thank Brian Mason and the Mason Trust for providing me with financial support in the field.

At the University of Canterbury I would like to thank Steve Weaver for always being a relaxing influence on me, and I thank Rob Spiers, Stephen Brown, Jane Guise, Cathy Knight and Kerry Swanson for going out of their way for me so many times. And John Southward, wow, I would have been up the creek without you, thanks. To my Ph.D. comrades Graham Leonard, Karl Spinks, and Dave Milner, thank you for all your help in the field and the great times. Graham, your technical support was a lifesaver. At the Institute of Geological and Nuclear Sciences I would like to thank Mike Rosenberg and Geoff Kilgour for their help in the sieve lab and with the laser sizer, and Dick Beetham, Stuart Read, Joy Hoverd, and Craig Elms for providing me with a computer and office space for my final write-up. Others that I would like to thank for their suggestions in the field are Jocelyn McPhie, Ray Cas, Steve Beresford, and to Tetsuo Kobayashi for sharing his time and knowledge on the field excursion around southern Kyushu, Japan.

Lastly I would like to thank the people who have been most influential in my life. To Peter Borella, if it wasn't for you I would never have been exposed to the wonderful world of geology. To my parents and sister, words cannot offer the kind of gratitude and love you deserve for always being there for me. And to my Marie, I know you feel like you have completed your own Ph.D. vicariously through me. Your help on the production of the thesis and the moral support through the hard times cannot be appreciated enough, thank you.

Contents

Figures

Tables

1 Introduction

The ~ 240 ka Ohakuri pyroclastic deposits, which are the topic of this thesis, are located in the central Taupo Volcanic Zone (TVZ) in the North Island of New Zealand. They are part of the products of an intense period of silicic volcanism characterised by several caldera-forming eruptions and associated large-scale tectonic adjustment events. As a consequence, there are many challenges in unravelling the complex volcanotectonic history as well as in documenting the temporal and spatial relationships within and between the different caldera-forming deposits.

1.1 Geologic setting

1.1.1 Taupo Volcanic Zone

Volcanism associated with the Taupo Volcanic Zone (TVZ), in the North Island of New Zealand, is related to the subduction of oceanic crust of the Pacific plate beneath continental crust of the Australian plate (Figure 1.1) (Cole et al., 1995 and references therein). The TVZ is a NE-SW trending zone that is ~ 300 km long, extending from Mt. Ruapehu in the southwest to White Island in the northeast and beyond to the continental/oceanic crust boundary (Wright, 1992; Gamble et al., 1993; Wilson et al., 1995). The TVZ, which is defined by a boundary drawn around vent positions (i.e. Mt. Ruapehu and Tongariro) and the structural margins of calderas, can be divided into 3 segments based on different styles of volcanism (Figure 1.2) (Wilson et al., 1995). The southwest and northeast sections are dominated by andesitic composite cone volcanism, and the central section (central TVZ), which is the subject of this thesis, is characterised by silicic caldera eruptions.

1.1.2 Central Taupo Volcanic Zone

The central TVZ is the most productive and active silicic volcanic system on Earth in the last 340 ka, erupting rhyolite at 0.28 m^3s^{-1} (Wilson et al., 1995). Its extraordinary magma output rate as well as its longevity and size have drawn comparisons to the Yellowstone system in North America (see Wilson et al., 1984; Houghton et al., 1995). Yellowstone and the central TVZ have both been active for ~ 2 Myr and both resemble one large composite caldera composed of several collapse structures (Wilson et al., 1984). The envelope encompassing the Yellowstone and central TVZ collapse areas is very similar: ~125 x 60 km and ~115 x 60 km, respectively (Figure 1.3) (Wilson et al., 1984). However, despite their similarities, Yellowstone and the central TVZ are polar end-members with respect to frequency and size of eruptions. Yellowstone is characterised by 3 long and voluminous magma cycles with associated climactic caldera collapse events, whereas the central TVZ collapse events are generally smaller and much more frequent (Figure 1.3) (Wilson et al., 1984; Houghton et al., 1995).

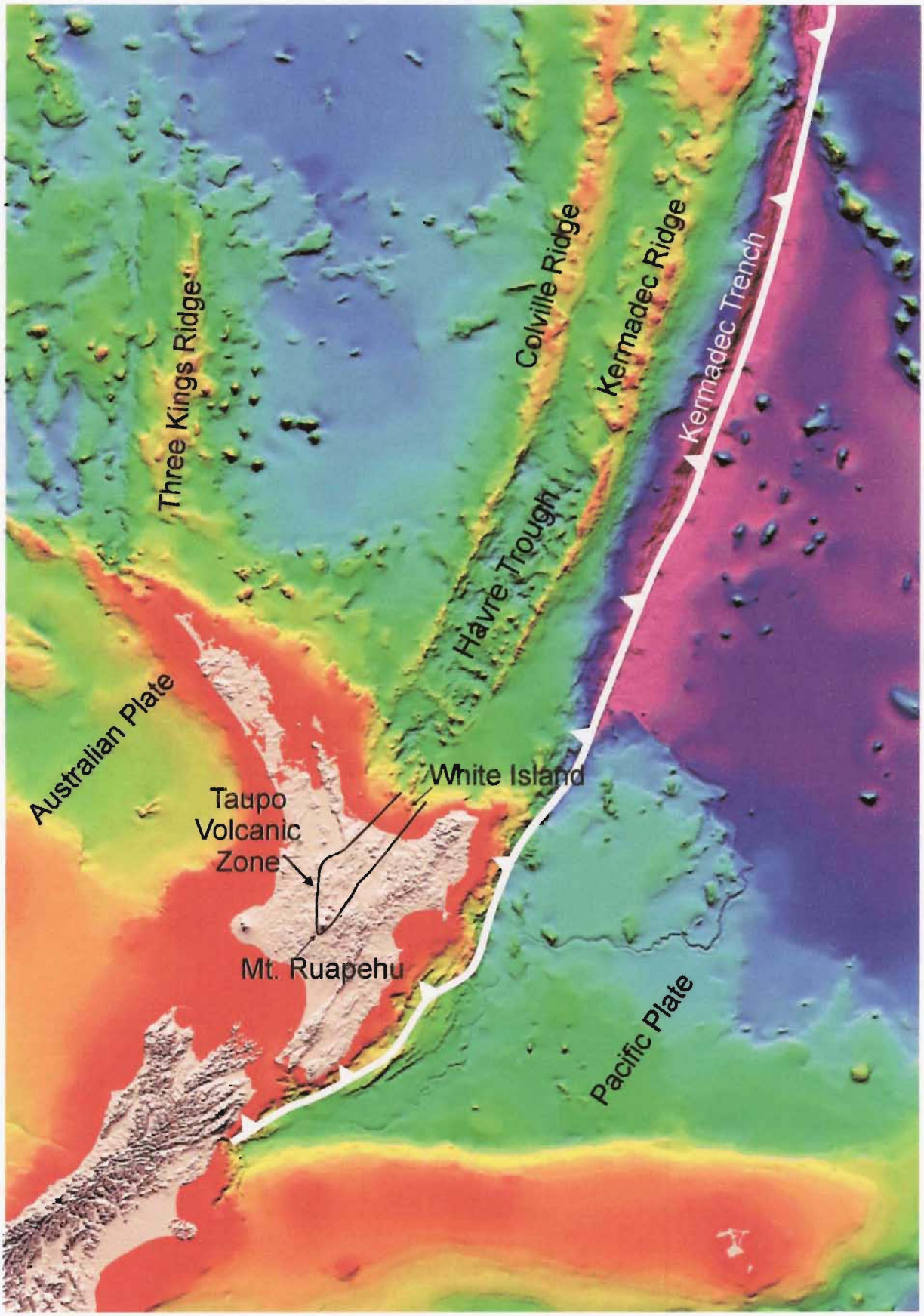

Figure 1.1 Digital bathymetry image of the seafloor surrounding the North island and a portion of the South Island of New Zealand, courtesy of NIWA (CANZ, 1996). Image clearly depicts the Pacific and Australian plate boundary, as well as the Taupo Volcanic Zone which extends beyond the continental/oceanic crust boundary.

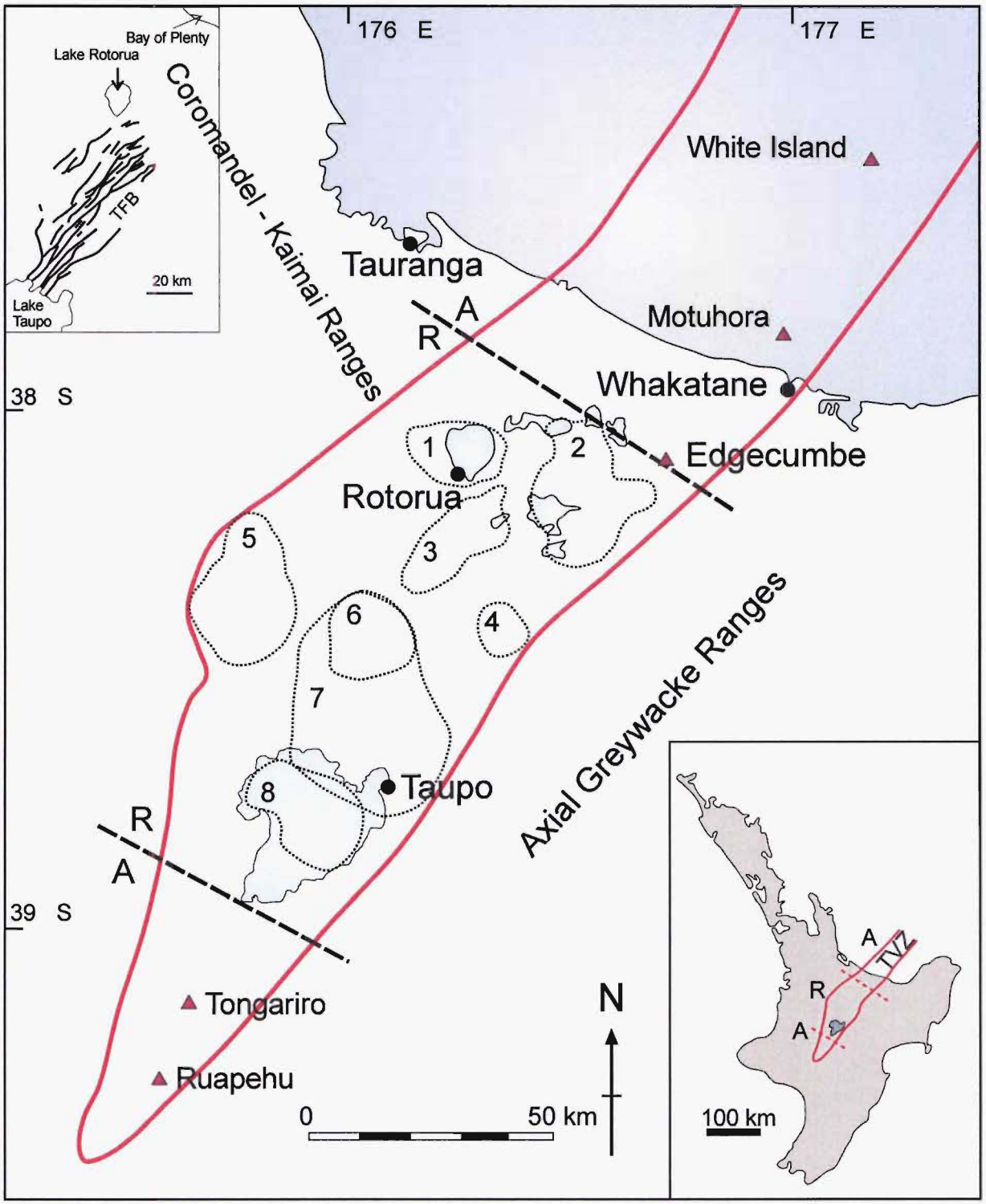

Figure 1.2 Taupo Volcanic Zone (TVZ) and boundaries of calderas. (1) Rotorua; (2) Okataina; (3) Kapenga; (4) Reporoa; (5) Mangakino; (6) Maroa; (7) Whakamaru; (8) Taupo. Thick dashed boundaries show division of TVZ segments with (A) andesite-dacite and (R) rhyolite volcanism. Modified after Houghton et al. (1995) and Wilson et al. (1995). Top inset shows the Taupo Fault Belt (TFB) between Lake Taupo and Lake Rotorua, from Villamor and Berryman (2001).

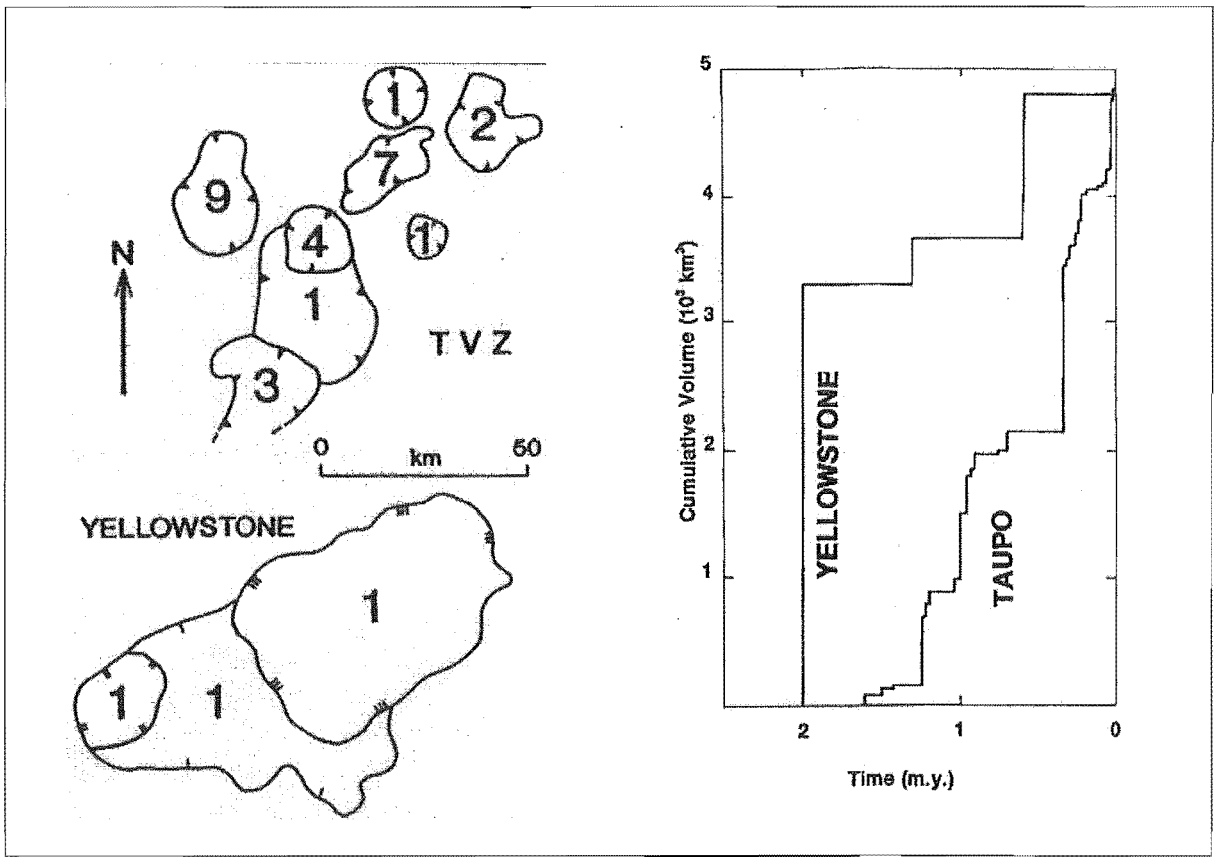

Figure 1.3 Comparison between size and caldera eruption history of the central TVZ and Yellowstone, from Houghton et al. (1995).

Houghton et al. (1995) suggest that the high frequency of caldera eruptions in the central TVZ is related to a young, thinning crust undergoing rapid extension. The combination of caldera subsidence and regional extension has led other authors (e.g. Martin, 1961; Healy, 1962; Wilson et al., 1984) to refer to the central TVZ as a volcanotectonic depression, and has also spurred an ongoing debate as to whether the central TVZ should be designated a true 'backarc basin' or described as a 'rifted arc' (see Wilson et al., 1995 for a review of the debate). Regardless of the interpretation, the central TVZ has been rifting for at least the past 0.9 M.y. (Wilson et al., 1995) and is currently spreading at a rate of 8 ± 2 mm/yr (Darby et al., 2000). The thin crust beneath the central TVZ, estimated from seismic refraction surveys to be ~ 15 km deep (Stern and Davey, 1987), is not only accommodating the rifting but also magma intrusion. Magma being emplaced into the crust is considered to be responsible for an average heat flow of 700 mW/m^2, which is one of the highest documented on earth (Bibby et al., 1995).

1.2 Local setting

From the comparison with Yellowstone in Figure 1.3, it is clear that long time breaks in the central TVZ (straight horizontal lines) persist between episodes of intense caldera activity (stepped lines). As such, Houghton et al. (1995) have divided the eruptive history of the central

TVZ into three periods (Figure 1.4). The IIIB period (280 ka to 150 ka), represents a particularly intense period of activity (8 ignimbrites from 6 different caldera sources) that includes the eruption of the Mamaku ignimbrite from the Rotorua caldera and the Ohakuri pyroclastic deposits from a newly recognised, southerly caldera source (the Ohakuri caldera; Chapter 2). New stratigraphic data presented in this thesis suggest that these two eruptions occurred in unusually close

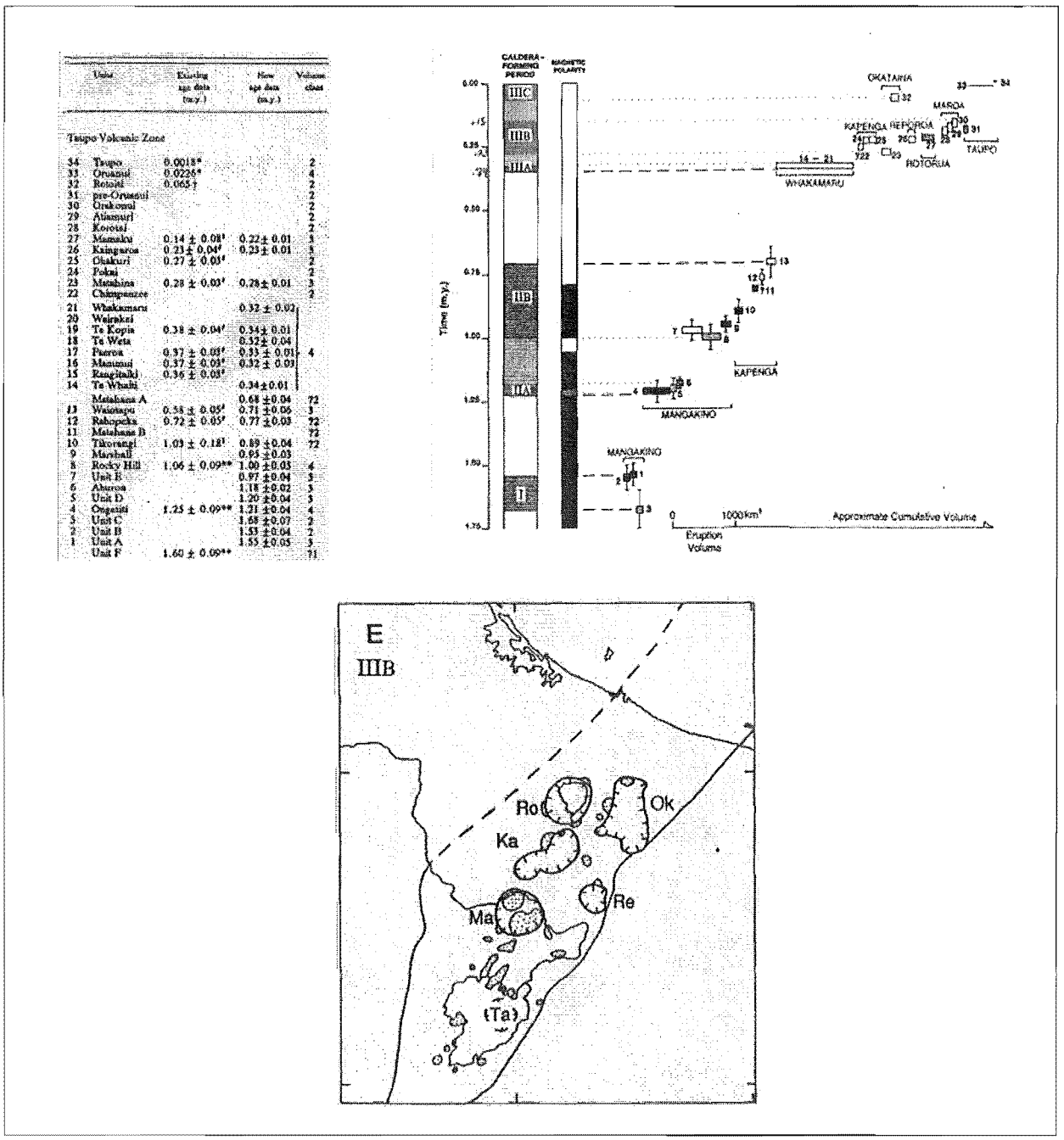

Figure 1.4 Stratigraphy and episodicity associated with the central TVZ caldera eruptives, and a map showing the calderas active during the IIIB period from Houghton et al. (1995).

succession, at approximately 240 ka (see Leonard, 2003 for new age data). As will be seen, the temporal and spatial relationships of the Mamaku and Ohakuri eruptives are fundamental to

unravelling the volcanotectonic history of the area referred to in this thesis as the Rotorua-Ohakuri volcanotectonic depression. The Rotorua-Ohakuri volcanotectonic depression encompasses the Rotorua and Maroa volcanic centres and the area in between, referred to by Martin (1961) as the Paeroa Graben (see Figure 1.5).

The Paeroa Graben is bounded on the east and west by the Paeroa and Horohoro faults, respectively, and is an amalgamation of the smaller Guthrie and Ngakuru grabens of Grindley (1959). The Paeroa Graben is coincident with the Kapenga composite caldera, which is defined by an envelope drawn around the margins of 3 geophysically inferred subsidence structures (see Rogan, 1982; Wilson et al., 1984). Although no pyroclastic deposits have been positively correlated with any of the Kapenga subsidence structures, several pyroclastic units have been suggested to have erupted from the area. The eruptives include the Waiotapu ignimbrite (Wilson et al., 1984), the Paeroa Range group ignimbrites which are Whakamaru group ignimbrite correlatives (Martin, 1961; Wilson et al., 1986; Keall, 1988) and younger eruptives including the Pokai ignimbrite (Karhunen, 1993) and the Ohakuri pyroclastic deposits (Langridge, 1990).

The names 'Paeroa Graben' and 'Kapenga composite caldera' suggest mutually exclusive tectonic and volcanic origins, respectively; however, it is likely that the relationship between tectonic and volcanic activity is much more complex (cf. Manville and Wilson, 2003). The Taupo Fault Belt (TFB), a generalised zone that incorporates the young faults of the TVZ, is dominated by NE-SW trending normal faults (see inset in Figure 1.2), that are inferred by Villamor and Berryman (2001) and Rowland and Sibson (2001) to be associated with rifting. However, at Taupo volcano, Manville and Wilson (2003) provide evidence for rifting without long-term accumulation and net subsidence on TFB normal faults. The implication is that rifting and normal fault offset are also related to silicic magmatism and caldera volcanism (Manville and Wilson, 2003). With respect to the area enclosed by the Kapenga composite caldera and the Paeroa Graben, research has focused on normal faulting active in the last ~ 20 kyr (e.g. the modern TFB of Villamor and Berryman, 2001) (see Figure 1.5); however, very little emphasis has been placed on unravelling the broader volcanotectonic history of the area.

1.3 The Ohakuri pyroclastic deposits

The 'Ohakuri pyroclastic deposits' is an informal genetic name used in this thesis to represent a large volcaniclastic deposit (> 100 km^3), located approximately halfway between Lake Rotorua and Lake Taupo (Figure 1.2), that shows remarkable lithofacies variations and ranges of transport mechanisms and modes of emplacement. In the past, 'Ohakuri' has been used as a sack term for deposits in the central Taupo Volcanic Zone (TVZ) that share a similar range of

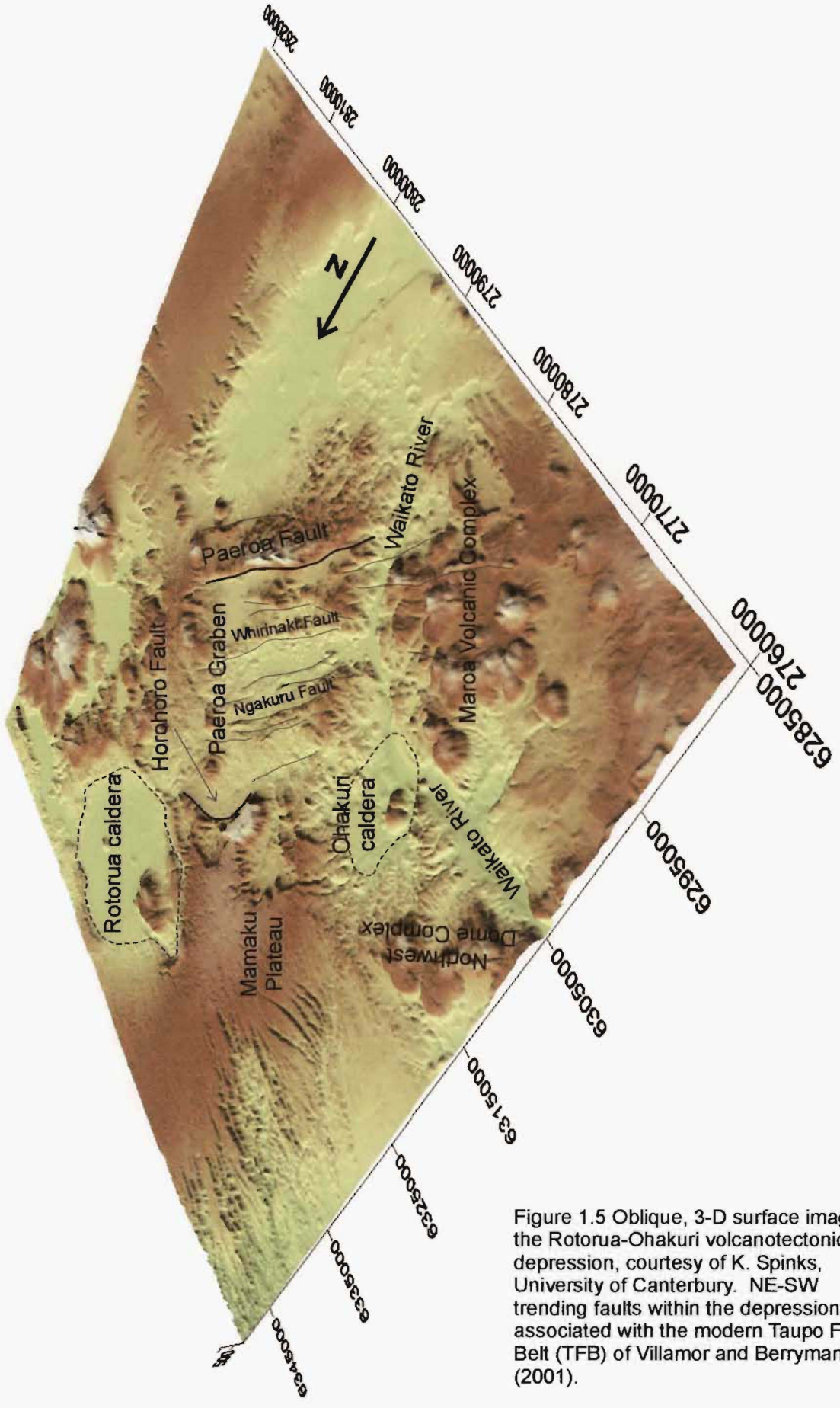

Figure 1.5 Oblique, 3-D surface image of the Rotorua-Ohakuri volcanotectonic depression, courtesy of K. Spinks, University of Canterbury. NE-SW trending faults within the depression are associated with the modern Taupo Fault Belt (TFB) of Villamor and Berryman (2001).

structural and lithological appearances. As a result, the Ohakuri deposits have been misinterpreted on several occasions with respect to their age, distribution and origin (including caldera source and mode of emplacement). Grindley (1965) and Healy et al. (1964) suggested that the type locality for the Ohakuri deposits was the Ohakuri dam site on the Waikato River (see Map 1); an area that is within the distribution of the Ohakuri deposits described in this thesis. Grindley (1960) interpreted these deposits to be a thick sequence of interbedded primary pyroclastics and resedimented volcaniclastics and, therefore, proposed the name 'Ohakuri Group' which he changed from his earlier nomenclature of 'Ohakuri Formation' (see Grindley, 1959). The Ohakuri Group deposits were correlated with thick accumulations of primary pyroclastics and sediments recorded deep in geothermal drillholes as far south as Wairakei (see Grindley, 1965). Grindley (1960; 1965) and Healy et al. (1964) suggested that the widespread distribution and thickness of the Ohakuri Group was related to reworking of several early TVZ eruptives. In fact, Grindley (1959) referred to the Ohakuri Group as "the oldest known pumiceous volcanics in the central volcanic district," and adopted a late Pliocene to early Pleistocene age.

At approximately the same time, Martin (1961) used lithologic, structural and stratigraphic evidence to correlate the type locality Ohakuri deposits with the Waiora Formation in the Wairakei geothermal drillholes. Specifically, Martin (1961) recognised a new stratigraphic unit, the Atiamuri Ignimbrite, overlying the Ohakuri deposits near the type locality, and correlated it with what he recognised as Atiamuri Ignimbrite in the Wairakei drillholes, interbedded with the Waiora Formation. The Waiora Formation is present at a much higher stratigraphic level in the Wairakei drillholes than the deposits that Grindley (1959) originally correlated with the Ohakuri Group and, therefore, Martin's (1961) work suggested a much younger age for the Ohakuri deposits (see Figure 1.6).

Martin's (1961) younger relative age for the Ohakuri deposits was adopted by the next generation of workers, including Henneberger (1983) and Langridge (1990). However, neither Henneberger (1983) nor Langridge (1990) adopted the correlations between the Ohakuri type locality deposits (including the Atiamuri Ignimbrite) and the Wairakei drillhole deposits. Part of the reason for this may have been the fact that E.F. Lloyd (pers. comm., 2001), from his mapping in the 1970's and early 1980's (unpublished maps held at the Institute of Geological and Nuclear Sciences), suggested that the Ohakuri deposits were not as widespread as originally thought and may not have been reworked by sedimentary processes. A primary pyroclastic origin was adopted by Henneberger (1983), who recognized a thick sequence of deposits in the Ohakuri dam area, which he described as mostly "massive nonwelded ignimbrite with lesser thicknesses of bedded airfall and cross-stratified surge deposits." Henneberger (1983) found no evidence for resedimentation associated with the sequence and therefore

proposed the name 'Ohakuri Ignimbrite'. (Note that the word 'Ignimbrite' (capitalised) was used by Henneberger (1983) as a formal stratigraphic term that does not discriminate among the pyroclastic origins (i.e. airfall or pyroclastic density current deposit) of the unit (cf. Mamaku Ignimbrite from Milner et al., 2003). In this thesis, I use the term 'ignimbrite' (not capitalised) as a physical volcanological label for a deposit from a concentrated pyroclastic density current, and the term 'Ignimbrite' to refer to a concentrated pyroclastic density current deposit that has been stratigraphically formalised.

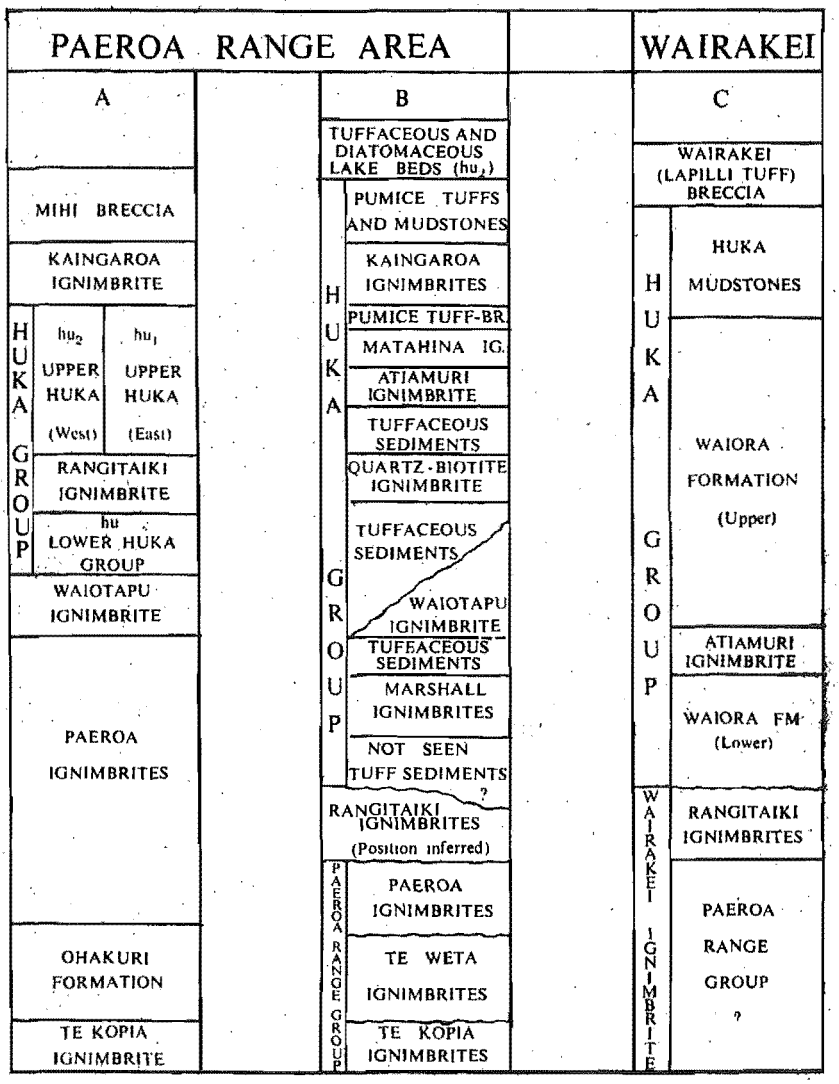

Figure 1.6 Stratigraphy of the Paeroa Range area (incorporates the Ohakuri type locality) and Wairakei drillholes, from Martin (1961). Column A is the succession from Grindley (1959), column B is Martin's stratigraphy, and column C is the re-interpretation of the Wairakei drillhole deposits (Martin, 1961). In column B, the Ohakuri deposits are inferred to be at a similar stratigraphic level as the Atiamuri Ignimbrite (see text above).

Langridge (1990) adopted Henneberger's (1983) primary pyroclastic hypothesis, suggesting that features present in the Ohakuri deposits (such as cross-stratification and bedding) had led Grindley (1959; 1960; 1965) and Healy et al. (1964) to originally infer a resedimented origin. Langridge (1990), using a more modern physical volcanological approach (e.g. Sparks et al., 1973; Wilson and Walker, 1982; Walker, 1983; McPhie, 1986), investigated the bedding and

stratification features and concluded that they represented primary pyroclastic processes (i.e. airfall, surge, and flow). Correlating the 'type' deposits in the Ohakuri dam area with other deposits nearby, Langridge (1990) constructed a preliminary volcanic facies model and divided the Ohakuri into three different eruptive phases, although noting that the complexity of the Ohakuri deposits does not lend itself to correlating individual pyroclastic units, and that detailed future investigations within and outside his study area (see Langridge, 1990) would be necessary "to build up an eruptive history of the Ohakuri pyroclastics."

In this thesis, I characterise and determine the origin(s) of the complex lithofacies variation associated with the Ohakuri deposits (Chapters 3, 4, and 5) and then put together the eruptive history of the Ohakuri deposits (Chapter 3). However, it is clear from the miscellany of interpretations from previous workers, that to properly characterise the Ohakuri deposits they need to firstly be placed within the context of the paleogeographic and volcanic history of the Ohakuri area (Chapter 2).

1.4 Thesis layout and objectives

The objectives for this thesis are divided between chapters. In Chapter 2, the paleogeographic evolution of the Rotorua-Ohakuri volcanotectonic depression (from ~ 340 ka to recent times) is presented. Most of the paleogeographic information has been compiled from work done by other authors; however, this compilation centres on new stratigraphic evidence for the Mamaku-Ohakuri relationship, based on fieldwork associated with this thesis. The new stratigraphy demonstrates that very little time elapsed between the emplacement of these two deposits (i.e. no evidence for substantial reworking below the contact or the development of a soil) and, in addition, evidence is provided that suggests that the Mamaku and Ohakuri are unambiguously different from another (i.e. they are not simply distinct lithofacies associated with a single eruption). As such, the temporal linkage between two large eruptions from geographically distinct caldera sources (the Rotorua and Ohakuri calderas) raises several questions that are not only relevant to the central TVZ and the Rotorua-Ohakuri volcanotectonic depression but have a more widespread significance that may further our understanding of complex caldera systems worldwide. The themes associated with these questions include:

- tectonically-linked caldera collapse events
- lateral migration of magma and passive (non-eruptive) subsidence structures
- statistical averages for the frequency of caldera eruptions vs. simultaneous, clustered caldera eruptions
- tectonic controls on the shape, size, and location of silicic magma reservoirs in extensional environments
- magma residence times

The paleogeographic information presented in Chapter 2 provides a context for the characterisation of the complex lithofacies variation associated with the Ohakuri pyroclastic deposits. In Chapter 3, more background information for the Ohakuri pyroclastic deposits is provided, including results of petrographic and geochemical analyses (major and trace element and isotopic) that are compared with geochemical data from other central TVZ pyroclastic deposits (particularly the Mamaku ignimbrite) and lavas. The Ohakuri pyroclastic deposits are then described with respect to a range of lithofacies and lithofacies associations (cf. Reading, 1986) in order to set up a discussion of their origins. The Ohakuri lithofacies are, first, evaluated with respect to transport and emplacement by normal sedimentary processes (i.e. I explore the possibility of the resedimented origin, originally inferred by Grindley, 1960). Then the deposits are evaluated with respect to several different pyroclastic origins, which includes a discussion of primary vs. secondary processes, vertical vs. horizontal transport components, and concentrated pyroclastic density currents (pyroclastic flows, s.s.) vs. dilute pyroclastic density currents (pyroclastic surges, s.s.). As will be seen, the lateral and vertical variations of the Ohakuri lithofacies are related to a wide range of pyroclastic processes that are not solely related to variable pyroclastic transport processes (cf. the Taupo ignimbrite of Wilson and Walker, 1982; Walker, 1983; Wilson, 1985). In the final part of Chapter 3, the lithofacies, lithofacies associations, and geochemical data are synthesised and compared with paleogeographic information from Chapter 2 in a discussion of the eruptive history of the Ohakuri caldera. In the discussion, episodic eruptions and depositional time breaks, phreatomagmatism, and variable depositional environments are all highlighted.

Chapters 4 and 5 focus on 3 unusual Ohakuri lithofacies: the giant-dune bed lithofacies C, and the secondary hydroeruption deposits (lithofacies F and G), respectively. In Chapter 4, the morphology of the giant-dune beds is revealed from a ground penetrating radar (GPR) survey, and compared with results from grainsize analyses of the deposits. The dune beds are unusual because they exhibit characteristics of both pyroclastic surges and flows (s.s.). There are only a few documented deposits (worldwide) with similar characteristics. By comparing the giant-dune beds with these similar deposits, hypotheses for transport processes and eruption dynamics are developed. In Chapter 5, a review of secondary hydroeruptions is presented first, including background information on magnitude and periodicity of documented prehistoric and historic hydroeruption events. The Ohakuri secondary hydroeruption deposits (lithofacies F and G) are compared with documented secondary hydroeruption deposits from Mount St. Helens (U.S.A), Taupo (New Zealand), Aira and Ikeda (Japan). Then, the Ohakuri secondary hydroeruptions are discussed with respect to episodic magmatic eruption sequences, wet depositional environments, and the potential misinterpretation of hydroeruption deposits in general.

1.5 Terminology

The following is a brief list of terms that are used in this thesis. The definition given for each term is not meant to be comprehensive, and is only applied to usage in this thesis.

caldera: a subsidence or collapse feature formed after large volumes of magma are removed from the upper crust during explosive volcanism and the production of voluminous pyroclastic flows and associated plumes of ash

flow unit: a deposit left by the passage of a single pyroclastic density current.

ignimbrite: the deposit of a concentrated pyroclastic density current (pyroclastic flow, s.s.), with a predominantly pumiceous juvenile component

non-eruptive subsidence structure: a subsidence or collapse feature formed following lateral removal of magma in the upper crust

package: a term used to describe deposits with similar components and lithological characteristics erupted during a defined portion of an eruption (cf. Wilson and Hildreth, 1997)

pyroclastics: a primary volcaniclastic deposit generated by explosive volcanism and emplaced by primary volcanic processes

pyroclastic density current (PDC): a gravity-driven current comprising hot primary volcanic particles, generated by explosive volcanism

pyroclastic flow: a concentrated pyroclastic density current

pyroclastic surge: a dilute pyroclastic density current

reworked (resedimented) deposit: a volcaniclastic deposit transported and emplaced by aeolian or fluvial processes at ambient temperatures

secondary hydroeruption: steam explosions induced by the vaporisation of surface water that comes into contact with hot pyroclasts

secondary pyroclastic deposit: a volcaniclastic deposit generated and emplaced by secondary volcanic processes (i.e. avalanches of primary pyroclastic density current deposits, or surge deposits from secondary hydroeruptions)

volcaniclastics: a descriptive term that refers to a clastic deposit composed of volcanic fragments (i.e. pumice lapilli, lithics, ash, crystals) transported and emplaced by primary volcanic processes (i.e. pyroclastic density current, fallout) or normal sedimentary processes

2 Eruptive history and paleogeography of the Rotorua-Ohakuri volcanotectonic depression with specific relevance to Mamaku-Ohakuri relationships

2.1 Introduction

The relationship between caldera volcanism and tectonics in the central TVZ is poorly understood; however, new geomorphic and stratigraphic evidence presented here and elsewhere sheds some light with respect to cause and effect. From their observations of modern and paleo-lake levels at Taupo caldera, Manville and Wilson (2003) suggest that "rifting is apparently occurring without the accumulation of long-term vertical offsets and net subsidence on adjacent normal faults," and provide evidence for vertical deformation associated with large-scale volcanic eruptions. For instance, Wilson (2001) suggests that the formation of a graben and > 400 m of vertical displacement along a regional fault structure occurred synchronously with the 26.5 ka Oruanui caldera collapse. More geomorphic and stratigraphic evidence for vertical tectonic deformation associated with caldera volcanism is presented in this chapter, as well as for the role tectonics may be playing in the remarkable frequency of caldera collapse events in the central TVZ.

Of particular interest to this thesis is Houghton et al.'s (1995) central TVZ eruptive period IIIB (280 ka to 150 ka) that includes 8 ignimbrites from 6 different caldera sources (see Figure 1.4). In Figure 2.1 new age data (Leonard, 2003) and observations from fieldwork (this thesis) are summarised. These modify Houghton et al.'s (1995) ignimbrite stratigraphy for period IIIB, the calderas active during this period and, most importantly, introduce the intimate temporal relationship between the Mamaku and Ohakuri eruptions. Stratigraphic evidence is presented in this chapter that reveals the essentially synchronous (within days to weeks) eruptions and caldera collapse events of the Rotorua caldera (Mamaku ignimbrite) and the newly recognised Ohakuri caldera (Ohakuri pyroclastic deposits). Documenting the temporal linkages between the collapse of these two calderas is important for three reasons: 1) it further elucidates the remarkable frequency of the central TVZ caldera eruptions; 2) it may indicate that statistical averages for the frequency of caldera collapse may be, in some cases, obscuring the clustering of such events; and 3) it may provide a greater understanding of the relationship between caldera volcanism and tectonics in extensional environments.

The new age data and fieldwork findings also provide novel insights into the paleogeographic evolution of a substantial portion of the central TVZ stretching between, and including, Rotorua

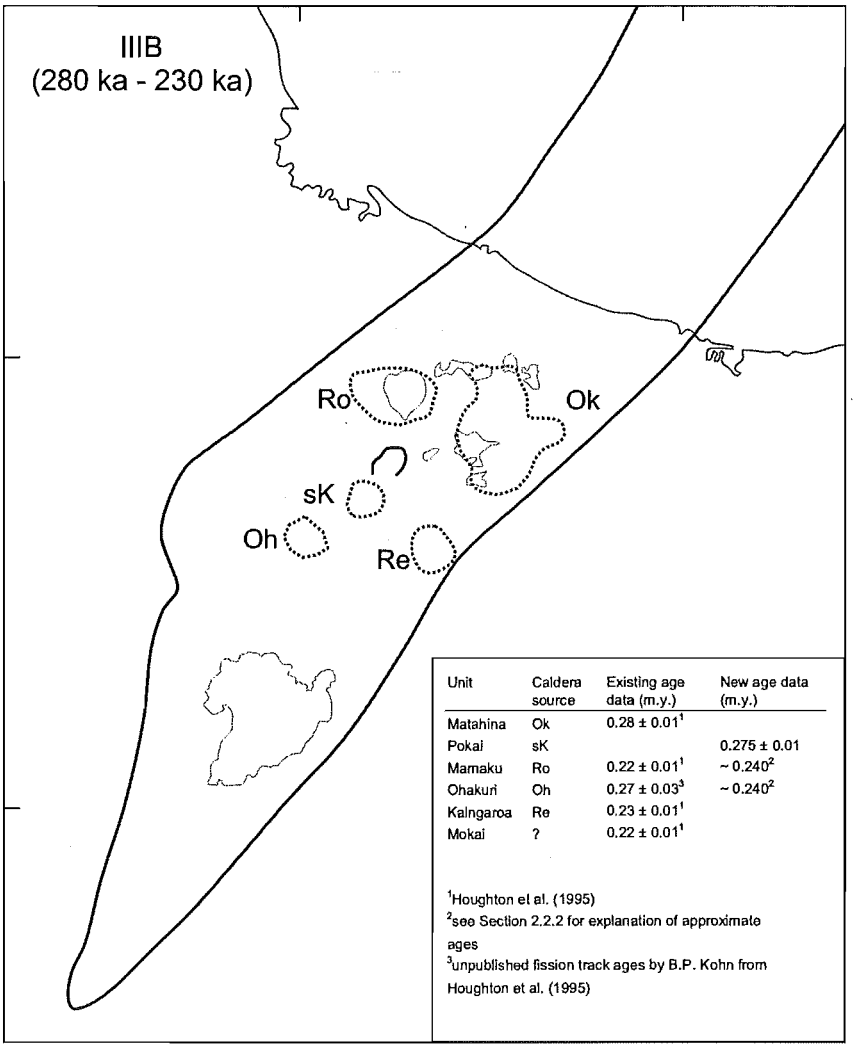

Unit	Caldera source	Existing age data (m.y.)	New age data (m.y.)
Matahina	Ok	0.28 ± 0.01[1]	
Pokai	sK		0.275 ± 0.01
Mamaku	Ro	0.22 ± 0.01[1]	~ 0.240[2]
Ohakuri	Oh	0.27 ± 0.03[3]	~ 0.240[2]
Kaingaroa	Re	0.23 ± 0.01[1]	
Mokai	?	0.22 ± 0.01[1]	

[1]Houghton et al. (1995)
[2]see Section 2.2.2 for explanation of approximate ages
[3]unpublished fission track ages by B.P. Kohn from Houghton et al. (1995)

Figure 2.1 Summary of IIIB stratigraphy and caldera activity presented in this chapter. Modified from Houghton et al. (1995).

caldera in the north and the Maroa Volcanic Centre (MVC) in the south. As previously mentioned in Chapter 1, this area is referred to in this thesis as the Rotorua-Ohakuri volcanotectonic depression, and the evolution of its paleogeography is presented in this chapter with accompanying cartoon maps. These are divided into 3 time periods between ~ 340 ka and the present-day: 1) pre Rotorua and Ohakuri caldera collapse events (Section 2.2.1); 2) the Rotorua and Ohakuri caldera collapse events (Section 2.2.2); and 3) post Rotorua and Ohakuri caldera collapse events (Section 2.2.3). A summary of the paleogeographic evolution is presented in Table 2.1. In Section 2.3, the Rotorua and Ohakuri eruption sequence is discussed with respect to tectonically-linked caldera collapse events (Section 2.3.1), and evidence for the Ohakuri caldera is presented in Section 2.3.2.

Section	Sub-section	Period	Highlighted Events
2.2.1 Pre-Rotorua and Ohakuri caldera collapse events	Whakamaru caldera collapse	340 to 320 ka	• Whakamaru caldera collapse • Syn-volcanic displacement on the Paeroa Fault?
	Whakamaru caldera collapse to the Pokai ignimbrite	< 340 - 320 ka to ~ 275 ka	• Dome-building activity associated with the Western and Northwestern Dome Complexes, and Tumunui and Haparangi domes • Eruptions of the caldera-forming Matahina and Pokai ignimbrites from Okataina and southern Kapenga, respectively
	Post-Pokai to the Rotorua and Ohakuri caldera collapse events	< ~ 275 ka to ~ 240 ka	• The evolution of two large parallel dome complexes within the MVC, and dome-building eruptions from the Western and Northwestern Dome Complexes, and Horohoro dome • Small-scale pyroclastic eruptions from the MVC • The formation of paleo-Lake Ohakuri
2.2.2 Rotorua and Ohakuri caldera collapse events		~ 240 ka	• Rotorua-Ohakuri eruption sequence including the caldera-forming eruptions of the Mamaku ignimbrite and the Ohakuri pyroclastic deposits • Syn-volcanic formation of the Horohoro Fault scarp
2.2.3 Post-Rotorua and Ohakuri caldera collapse events	Immediately post-collapse events	< ~ 240 ka	• Lake formation within the Rotorua and Ohakuri calderas • Breach of Lake Rotorua via the Hemo Gorge
	The Rotorua-Ohakuri volcanotectonic depression lakes	< ~ 240 ka to ~ 200 ka	• Caldera-forming eruption of the Kaingaroa ignimbrite from Reporoa. • Eruption of the Mokai ignimbrite from an unknown source? • MVC dome-building and pyroclastic eruptions • Formation of one large lake within the Rotorua-Ohakuri volcanotectonic depression • Formation of Lake Huka • Faulting associated with the Taupo Fault Belt (TFB)
	~ 200 ka to eruption of Rotoiti and Earthquake Flat pyroclastics	~ 200 ka to ~ 62 ka	• TFB faulting and the formation of smaller lakes within isolated grabens • Eruption of the Rotoiti and Earthquake Flat pyroclastics from Okataina and a vent within northern Kapenga, respectively
	Post-Rotoiti and Earthquake Flat pyroclastics to the present-day	~ 62 ka to present-day	• Caldera-forming eruptions of the Oruanui and Taupo ignimbrites from Taupo caldera • Lake formation within the Ngakuru-Whirinaki graben and the Whangapoa Basin associated with the damming of the Waikato River by the Taupo ignimbrite

Table 2.1 Summary of the paleogeographic evolution of the Rotorua-Ohakuri volcanotectonic depression.

2.2 Paleogeography and volcanotectonic history

2.2.1 Pre- Rotorua and Ohakuri caldera collapse events

Whakamaru caldera collapse (340 – 320 ka)

Following a c. 340 kyr period with no caldera forming eruptions (Houghton et al., 1995), the widespread Whakamaru group ignimbrites were erupted (340 - 320 ka), resulting in the collapse of the Whakamaru caldera (Wilson et al., 1986; Brown et al., 1998). The Whakamaru group ignimbrites (including units variously mapped as Whakamaru, Mananui, Rangitaiki, Te Whaiti, Wairakei, and the Paeroa Range Group ignimbrites) formed a sheet across the central TVZ, covering an area > 13,000 km^2 with a volume of > 1000 km^3 DRE (Wilson et al., 1986; Brown et al., 1998). The presence of Whakamaru ignimbrite lithics within the Mamaku ignimbrite (Milner, 2001) suggests the Whakamaru sheet originally extended as far north as, and possibly beyond, the Rotorua caldera.

There has been some debate as to whether all the Whakamaru group ignimbrites were sourced from the Whakamaru caldera. In particular, the Paeroa Range group ignimbrites (Te Kopia, Te Weta, and Paeroa ignimbrites) are only exposed in the Paeroa Fault scarp (see Figure 1.5) and may have been erupted from a source further north than the Whakamaru caldera (Martin, 1961; Wilson et al., 1984; Keall, 1988). Keall (1988) describes lithic breccias within the Te Weta and Te Kopia ignimbrites, respectively, and infers a proximal source, close to the present-day Paeroa Fault scarp. The Paeroa Fault scarp is interpreted by Villamor and Berryman (2001) to be a regional tectonic feature younger than the Paeroa Range group ignimbrites which are displaced by > 500 m (Keall, 1988; Villamor and Berryman, 2001). Villamor and Berryman (2001) provide evidence for vertical displacement on the fault since 64 ka ± 4 ka (1.56 ± 0.15 mm/yr) with recent movement in the last 11.8 to 13.5 ka (1.37 ± 0.2 mm/yr). However, evidence is lacking as to whether the Paeroa Fault accumulated slip at a steady rate back to the age of the Paeroa Range group ignimbrites (340 - 320 ka). Keall's (1988) inference that the Paeroa Range group ignimbrites are proximal to volcanic source suggests the initial vertical displacement along the Paeroa Fault may have been tectonically linked to a large volcanic eruption associated with the displaced ignimbrites. It is clear that more research is needed to constrain the volcanotectonic history in this area.

Whakamaru caldera collapse (< 340 - 320 ka) to the Pokai ignimbrite (~ 275 ka)

Following the collapse of the Whakamaru caldera it is probable that a large lake formed within its boundaries. The extent and longevity of such a lake is unknown; however, there is some indication of sediment and primary volcanic infilling of the caldera. From drill hole data, new Ar/Ar age data and volume calculations for primary volcanics, Leonard et al. (2003) have determined that the Whakamaru caldera was 85% filled within 35 kyr of the collapse. A portion

of this fill was associated with lavas from the Western and Northwestern Dome Complexes that began to evolve along the western and northwestern margins of the Whakamaru caldera, respectively (Houghton et al., 1991) (see Figure 2.2). Rhyolite lava domes also evolved further to the north, and west of the Paeroa Fault scarp (including Tumunui and Haparangi domes; Nairn, 2002).

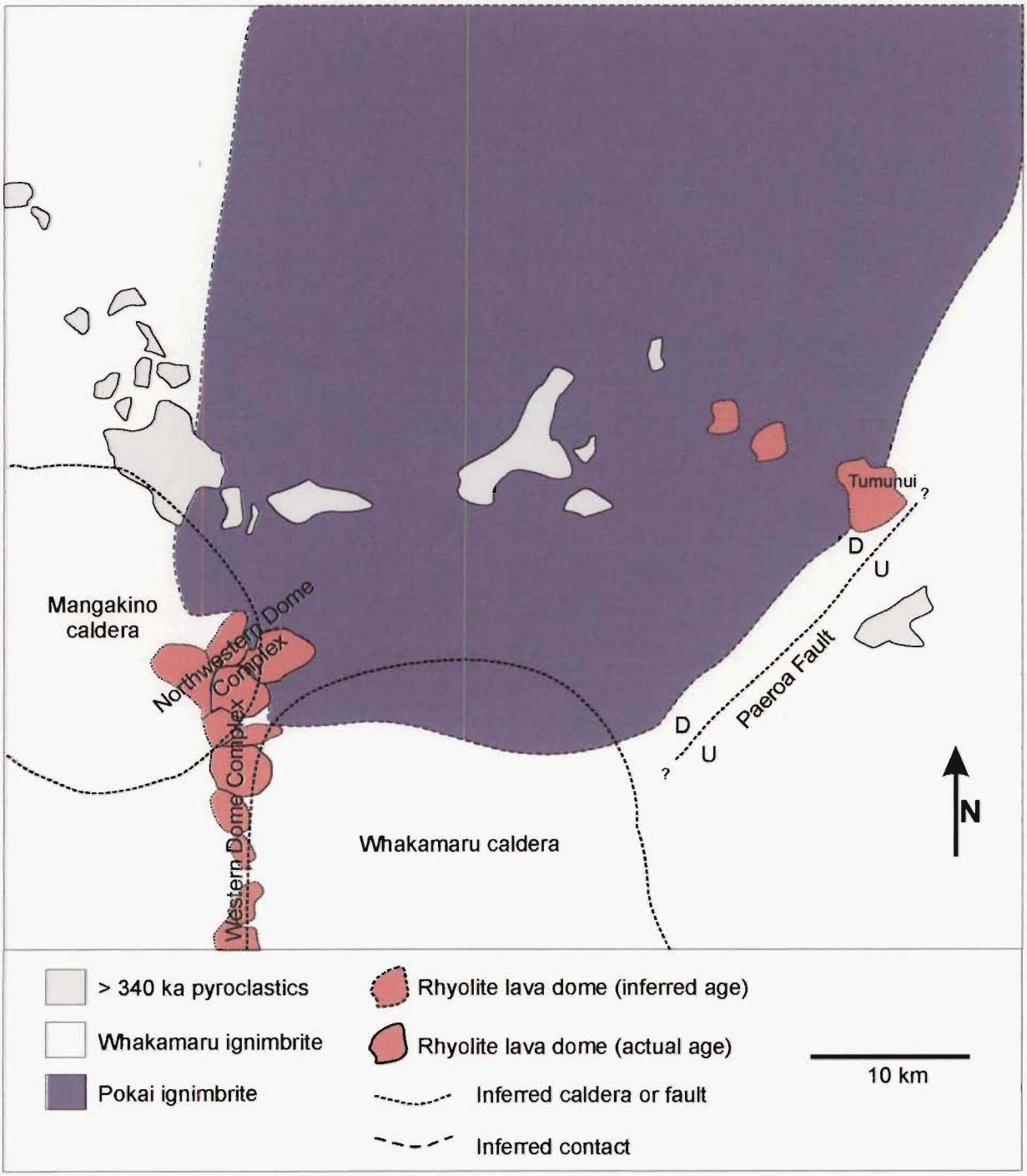

Figure 2.2 Cartoon map of paleogeography at ~ 275 ka. Calderas are superimposed on the geology in order to show their inferred boundaries.

Pyroclastic activity during this period includes the eruptions of the caldera-forming Matahina and Pokai ignimbrites. The 280 ka Matahina ignimbrite was erupted from what became the Haroharo caldera in the Okataina Volcanic Centre (Bailey and Carr, 1994). The Matahina ignimbrite has an outflow volume equivalent to ~ 75 km^3 of magma, and was asymmetrically distributed to the east and northeast (Bailey and Carr, 1994). It has not been identified within the Rotorua-Ohakuri volcanotectonic depression. The 275 ± 10 ka Pokai ignimbrite (new Ar/Ar age from Leonard, 2003) was erupted from a source within the Rotorua-Ohakuri volcanotectonic depression (see below). It is another extensive ignimbrite sheet with a present-day exposure of ~ 360 km^2 and volume of 33 km^3 DRE (Karhunen, 1993). Fragments of Pokai ignimbrite occur as accessory lithics in both the Mamaku ignimbrite from Rotorua caldera (Milner, 2001) and the Ohakuri pyroclastic deposits from the Ohakuri caldera, confirming that the Pokai ignimbrite was much more extensive than its present-day distribution would suggest. To the east, there have been no observed exposures beyond the Paeroa Fault scarp, suggesting either that the Pokai ignimbrite has been eroded from this area or was never deposited there. It is possible that the non-energetic Pokai pyroclastic density currents (PDC's) that deposited the ignimbrite, described by Karhunen (1993) as valley-ponded, were not capable of surmounting the Paeroa Fault scarp.

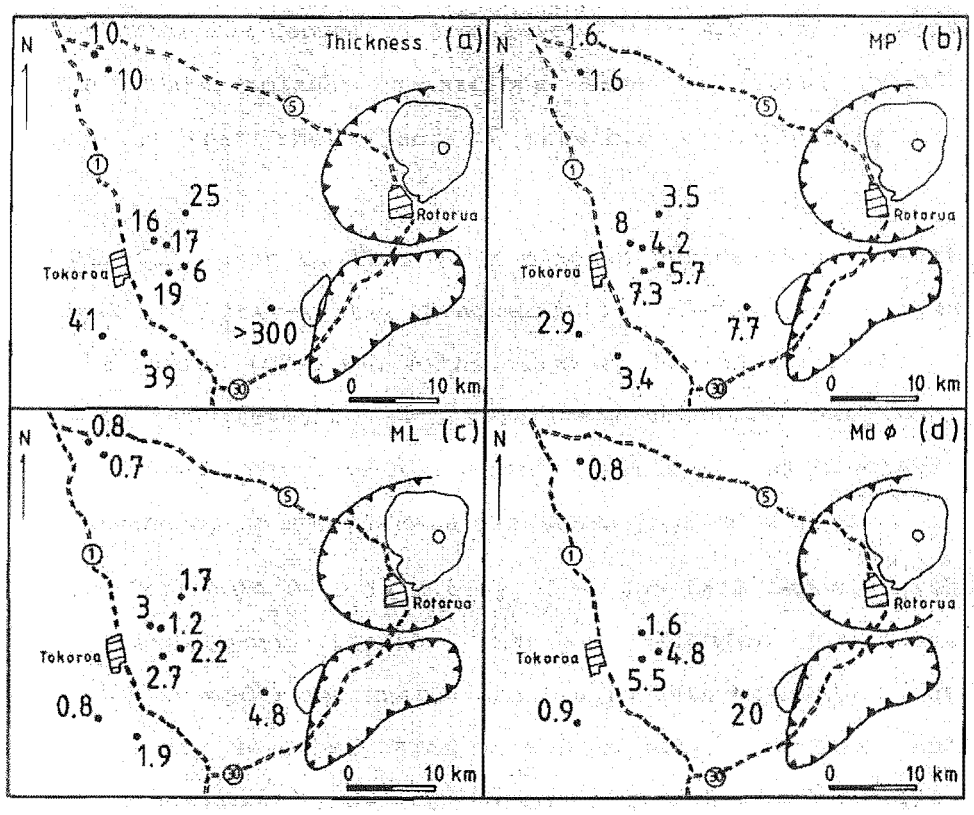

Figure 2.3 Grain size data for the Pokai plinian airfall from Karhunen (1993). Values for thickness, MP and ML (averages of 5 largest clasts) are in cm, Md values in mm. Boundaries for the Rotorua caldera and the Kapenga composite caldera are depicted by thick lines with inward pointing arrows.

Several possible caldera sources for the Pokai ignimbrite have been suggested including: Rotorua caldera, Kapenga composite caldera, and the Maroa Volcanic Centre (MVC) (see Karhunen, 1993). From maximum lithic and pumice clast size data in the Pokai plinian airfall, Karhunen (1993) concludes that the Kapenga composite caldera is the most likely source. In addition, Milner et al. (2002) confirm that the Rotorua caldera is a single event collapse structure associated with the Mamaku ignimbrite, and Leonard's (2003) lack of evidence for a caldera structure within the MVC eliminates the possibility of either Rotorua or MVC being the Pokai source. Re-evaluating the isopleth and isopach data from Karhunen (1993) (Figure 2.3), it is likely that the Pokai ignimbrite was erupted from a source near the southwestern end of the Kapenga composite caldera.

Post-Pokai (< ~ 275 ka) to the Rotorua and Ohakuri caldera collapse events (~ 240 ka)

Soon after the caldera-forming eruption of the Pokai ignimbrite, the volumetrically minor Korotai ignimbrite was erupted from a source adjacent to the buried northern margin of the Whakamaru caldera (Figure 2.4). The Korotai ignimbrite has an Ar/Ar age of 283 ± 7 ka that is older than, but within 1 s.d. overlap of, the age for the Pokai ignimbrite (Leonard, 2003). However, field relationships show that the Pokai ignimbrite lies stratigraphically beneath the Korotai ignimbrite. The Korotai ignimbrite has a very high concentration of obsidian lithics suggesting that it is a deposit associated with the explosive destruction of a rhyolite dome.

Other volcanic activity during this period was associated with rhyolite dome growth and relatively small volume, dome-related, pyroclastic eruptions. The 222 ± 10 ka Horohoro dome (see Figure 2.4) has a similar Ar/Ar age as the Mamaku ignimbrite (Houghton et al., in prep); however, stratigraphic field relations suggest the dome is older, as the Mamaku ignimbrite was emplaced around the dome (Milner, 2001). Further south, dome building occurred in both the Northwestern and Western Dome Complexes, and two large parallel dome complexes evolved within the MVC (Leonard, 2003). Also within the MVC, the 272 ± 10 ka Putauaki and 256 ± 12 ka Orakonui ignimbrites (Leonard, 2003) were erupted.

Evidence presented below suggests there was a lake (referred to herein as 'paleo-Lake Ohakuri', not to be confused with the modern day Lake Ohakuri which is associated with the dammed Waikato River) in the area of the Ohakuri caldera immediately prior to and during the eruption of the Ohakuri pyroclastic deposits. The sloping surface of the Mamaku ignimbrite on the southeastern margin of the Mamaku Plateau suggests that it was emplaced on a paleoslope that descended into a low depression or lake. In addition, the phreatomagmatic nature of the Ohakuri pyroclastic deposits (see Section 2.2.2 and Chapter 3, respectively) supports the presence of paleo-Lake Ohakuri. It is probable that paleo-Lake Ohakuri evolved from the depression left by the caldera-forming eruption of the Pokai ignimbrite. The likely boundary of

the lake can be inferred from high ground associated with the Mamaku Plateau to the northwest, rhyolite domes to the north, the Paeroa Fault scarp to the east, the MVC to the south, and Northwest Dome Complex to the west (see Figure 2.4).

2.2.2 *Rotorua and Ohakuri caldera collapse events (~ 240 ka)*

New fieldwork reveals a rapid succession of eruptions from the Rotorua and Ohakuri calderas. In this section the eruptive stratigraphy is presented as well as background information on both the Rotorua and Ohakuri calderas. The products of the Rotorua and Ohakuri caldera collapse

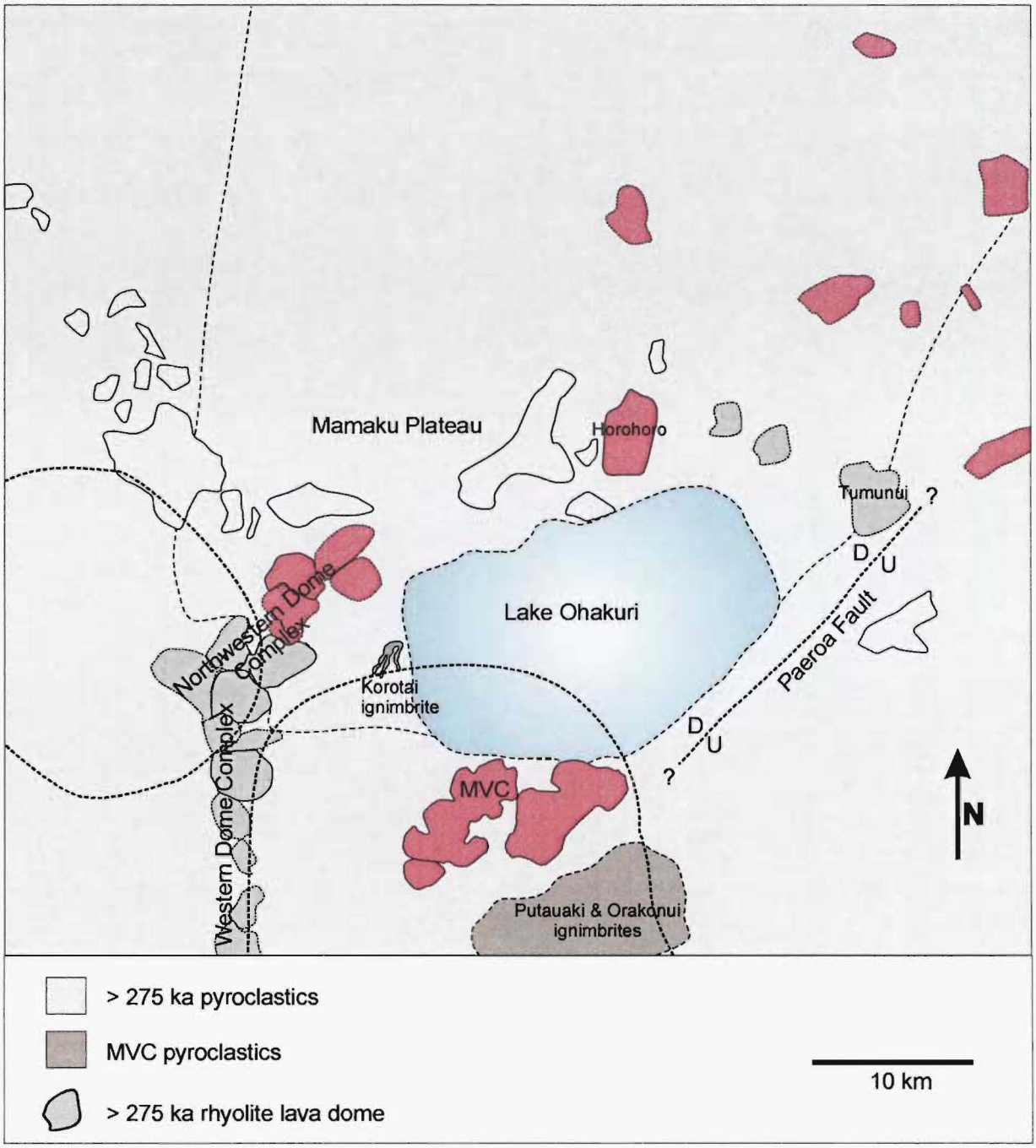

Figure 2.4 Cartoon map of paleogeography at ~ 240 ka (prior to the Rotorua and Ohakuri eruptions). Coloured fills depict eruptives associated with this period. See text for explanation. Unlabled features are from Figure 2.2.

events are the Mamaku ignimbrite and Ohakuri pyroclastic deposits, respectively. The relationship between the Mamaku ignimbrite and Ohakuri pyroclastic deposits has been the subject of debate and there has previously been confusion as to whether; a) the Ohakuri pyroclastic deposits are older or younger than the Mamaku ignimbrite, or b) whether the Ohakuri pyroclastic deposits are, in fact, simply an unusual lithofacies of the Mamaku ignimbrite. Evidence for the Ohakuri pyroclastic deposits being a separate eruptive deposit from an independent caldera source is presented in this section. Finally, the Mokai ignimbrite is introduced and discussed with respect to its relationship with both the Mamaku ignimbrite and Ohakuri pyroclastic deposits. The timing of the Mokai ignimbrite emplacement has previously been considered to be similar to the Mamaku and Ohakuri caldera-forming eruptions, yet its precise stratigraphic relationships and source are unknown.

Rotorua caldera

The Rotorua caldera is located adjacent to the northwestern margin of the central TVZ (see Figure 1.2) and was recently studied with respect to structural geometry and caldera collapse models (see Milner, 2002). Milner (2002) describes the Rotorua caldera as a "single event, asymmetric, multiple-block, single locus collapse structure" attributed to downsag, plate, trapdoor, and piecemeal mechanisms. The caldera collapse followed the eruption of the Mamaku ignimbrite which has an in-situ bulk volume of > 96 km^3 DRE (> 145 km^3 probable volume) and it covers > 3200 km^2 (Milner et al., 2003), making it one of the more widespread ignimbrites from the central TVZ.

Ohakuri caldera

The Ohakuri caldera is a newly recognized caldera within the central TVZ, approximately 25 km south-southwest of Rotorua. It overlaps the northern margin of the older Whakamaru caldera and lies adjacent to the axis of the modern Taupo Fault Belt (TFB) (see Figure 1.5). Accumulation of volcaniclastic sediment within the central TVZ has largely buried the topographic caldera margin. The presence of the caldera is inferred from the distribution of the Ohakuri pyroclastic deposits, pyroclastic density current transport directions, isopleth maps for airfall deposits, drill core data, and geophysical data (discussed in Section 2.3.2).

Ohakuri pyroclastic deposits, separate eruptive deposit from a distinct caldera source

In the central TVZ literature there has been some discussion about the origin of the Ohakuri pyroclastic deposits (e.g. Grindley, 1959; Martin 1961; Healy, 1964; Henneberger, 1983; Langridge 1990) and its relationship to the Mamaku ignimbrite. The following is a list of observations that, together, distinguish the Ohakuri pyroclastic deposits from the Mamaku ignimbrite and confirm the existence of a separate caldera source.

1) The field character of Ohakuri pyroclastic deposits and the Mamaku ignimbrite are different; Ohakuri is an episodically emplaced, non-welded, low-grade, landscape-filling deposit with remarkable lithofacies variation (discussed in detail in Chapter 3), whereas the Mamaku ignimbrite is partially welded, landscape-forming, and exhibits little facies variation (Milner et al., 2003).
2) Where the Mamaku ignimbrite and Ohakuri pyroclastic deposits are found in contact (see Map 1), the Mamaku was emplaced relatively sluggishly and can be observed wedging out against modest slopes (discussed below in the 'Distribution of the Mamaku ignimbrite and the Ohakuri pyroclastic deposits' section), whereas the Ohakuri pyroclastic deposits have a radially-distributed, landscape-mantling character.
3) Non-welded Ohakuri pyroclastic deposits are greater than 600 m thick in an area (the inferred Ohakuri caldera) ~ 25 km southwest of Rotorua caldera (see drill core data; Section 2.3.2). This is important for two reasons: 1) in the present-day central TVZ, there are no valleys or lake basins that are 600 m deep; 2) in the same area (~ 25 km southwest of Rotorua caldera) the Mamaku ignimbrite is < 20 metres thick and still shows some degree of welding.
4) Transport directions measured for proximal to medial Ohakuri pyroclastic density current (PDC) deposits radiate from the inferred Ohakuri caldera (discussed in more detail in Section 2.3.2, and depicted in Figure 2.34).
5) The Ohakuri pyroclastic deposits contain a third, less evolved pumice type not found in the Mamaku ignimbrite (see Section 3.3 for geochemical distinctions between the Mamaku and Ohakuri).

Unit	Sample	Grid Ref.	Ar/Ar age	Laboratory	Source
Mamaku	MP27		216 ± 8	Stanford	Tanaka et al. (1996)
Mamaku	MP27		230 ± 10	Menlo Park	Houghton et al. (in prep)
Mamaku	MP27		237 ± 8	Stanford	McWilliams (2001)
Mamaku	MP25		224 ± 6	Stanford	Tanaka et al. (1996)
Mamaku	MK	U16/740340	240 ± 11	Menlo Park	Leonard (2003)
Ohakuri	MP25		230 ± 10	Menlo Park	Houghton et al. (in prep)
Ohakuri	D40	U16/807157	272 ± 16	Menlo Park	Leonard (2003)
Ohakuri	D64	U16/851130	244 ± 10	Menlo Park	Leonard (2003)
Ohakuri	D139	T16/694182	259 ± 9	Menlo Park	Leonard (2003)
Mokai	263		210 ± 20	Menlo Park	Houghton et al. (in prep)
Mokai	263		212 ± 6	Stanford	Tanaka et al. (1996)
Mokai	429		224 ± 14	Stanford	Tanaka et al. (1996)

Table 2.2 Ar/Ar age determinations for Mamaku, Ohakuri, and Mokai pyroclastic deposits.

Age of the Ohakuri pyroclastic deposits and the Mamaku ignimbrite

New stratigraphic evidence presented in the next sub-section demonstrates that the Mamaku ignimbrite and the Ohakuri pyroclastic deposits were erupted in rapid succession from the Rotorua and Ohakuri caldera, respectively. The question is: what are the ages of the Rotorua and Ohakuri deposits? The answer to this question is mostly predicated on the age of the Mamaku ignimbrite which has a transitional paleomagnetic direction and has therefore been a popular deposit to date. A list of Ar/Ar age dates is presented in Table 2.2, including the most recent dates provided by Leonard (2003). Leonard (2003) questions earlier age dates provided for the Mamaku ignimbrite, particularly those dates for sample MP27 (originally collected by B.F. Houghton et al. in 1989). MP27 has been dated by 3 separate researchers from 2 different laboratories with results ranging from 216 ± 8 ka to 237 ± 8 ka. As a result, none of the MP27 dates can be considered accurate. Leonard (2003) also suggests the reported 1 s.d. error values for the Stanford laboratory samples are problematically low. For these reasons, Leonard (2003) prefers his date of 240 ± 11 ka for the Mamaku ignimbrite. With respect to the variation in the Ar/Ar ages for the Ohakuri pyroclastic deposits (Table 2.2), Leonard (2003) suggests that xenocrystic plagioclase contamination (despite care to avoid obvious xenocrysts) may be a contributing factor, as well as incomplete Ar degassing in some or all of the Ohakuri magma.

In this thesis, an age of ~ 240 ka is assigned to the closely-spaced (temporally) eruptions of the Mamaku and Ohakuri pyroclastic deposits. This age reflects the youngest Ohakuri age (244 ± 10 ka) which falls within 1 s.d. of the Mamaku ignimbrite age (Leonard, 2003).

Eruptive Stratigraphy

The eruptive sequence is observed at seven localities between the Rotorua and Ohakuri calderas. There are seven eruptive units that overlie a dark brown to black paleosol that in turn is developed on top of the ~ 275 ka Pokai ignimbrite (see Figure 2.5 for the stratigraphy at each of the seven localities). The units are subdivided on the basis of lithology and field character and can be attributed to phases in the eruptive sequence (see Table 2.3 for a detailed description of each unit). There are four eruptive phases that, in total, occurred over a period of years. The eruptive phases are summarised in a series of oblique block diagram cartoons.

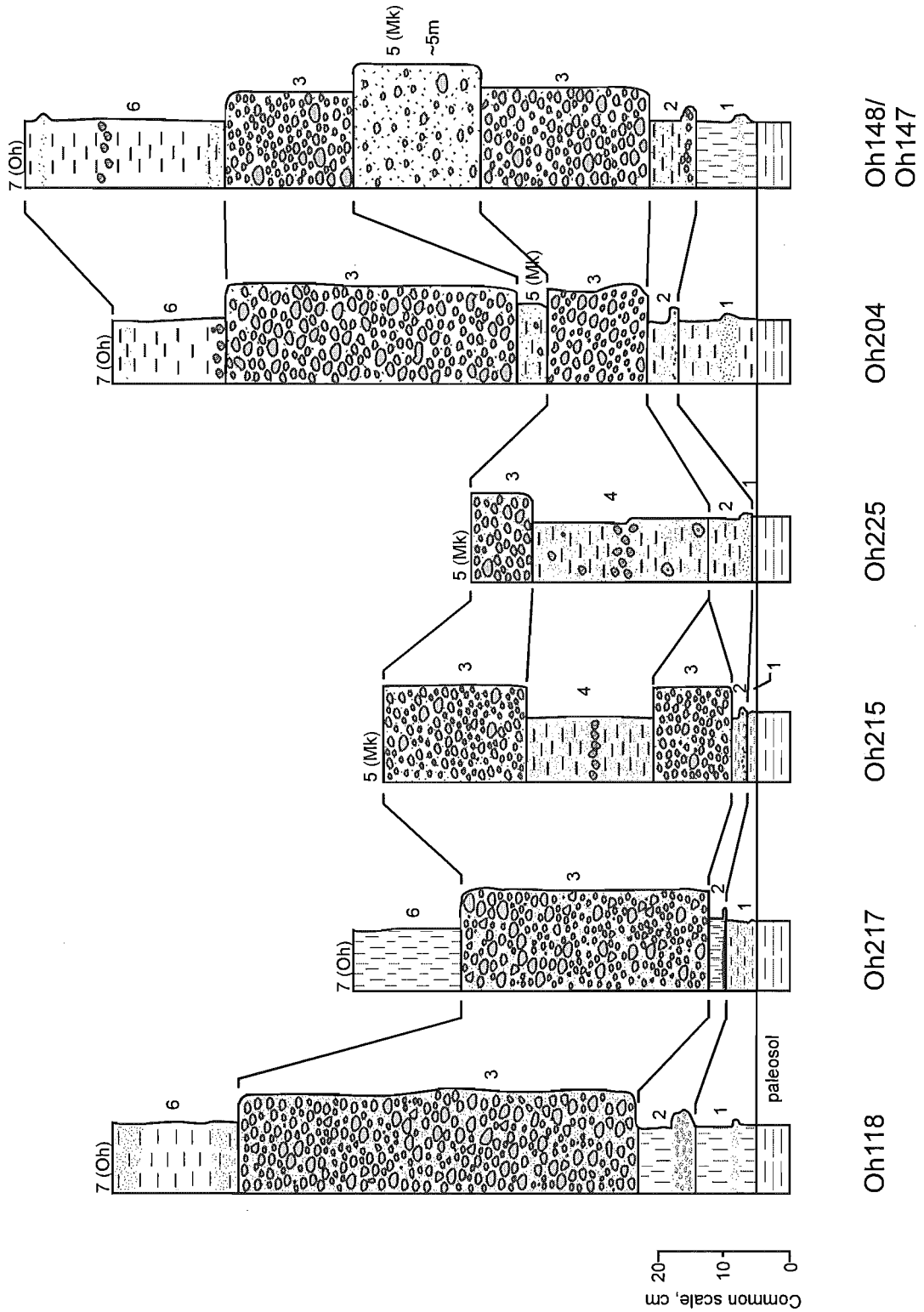

Figure 2.5 Fence diagram showing the stratigraphy of the ~ 240 ka Rotorua and Ohakuri eruptives. The stratigraphic column on the right end combines deposits from Oh148 (on top) and Oh147 (on bottom). Refer to text and photo figures for explanation of units.

Unit	Description
1	Fall deposit: gray, poorly sorted, tripartite layering with ultra fine ash basal layer (sometimes missing), overlain by gritty layer (fine to medium ash with fine lapilli), overlain by normally graded (vaguely laminated) fine to medium ash with ultra fine, cohesive ash top; penecontemporaneous reworking; juvenile obsidian lithics; capped by a carbonised thin soil.
2	Fall deposit: basal contact is yellow, very poorly sorted, ultra fine ash to fine lapilli, lapilli rich; normally grades into gray ultra fine to medium ash; top of unit is silver-gray, ultra fine ash that sometimes exhibits a sharp basal boundary defined by contemporaneous water reworking (low-angle ripples). Unit is vesicular with occasional leaf impressions (wet)
3	Fall deposit: plinian-style; massive to vaguely stratified, cream to buff, medium ash to medium lapilli, contains occasional charcoal fragments, devitrified rhyolite lithics
4	Thin PDC units: mostly massive fine-ash with some diffusely stratified pumice lapilli bands and scattered accretionary lapilli.
5	Mamaku ignimbrite: massive, welded with a cream coloured, non-welded base; pink, vapour-phase altered, non-welded top.
6	Fall deposit: pink and gray cross-laminations (low-energy water reworking) of ultra fine, cohesive ash with occasional accretionary lapilli and fine pumice lapilli layers, very lithic poor
7	Ohakuri pyroclastic deposits: giant dune-bedded, non-welded, buff colour, fine to coarse ash matrix, pumice-lapilli rich, higher lithic content (juvenile obsidian and devitrified rhyolite) near basal contact

Table 2.3 Detailed description of the Rotorua-Ohakuri eruptive units.

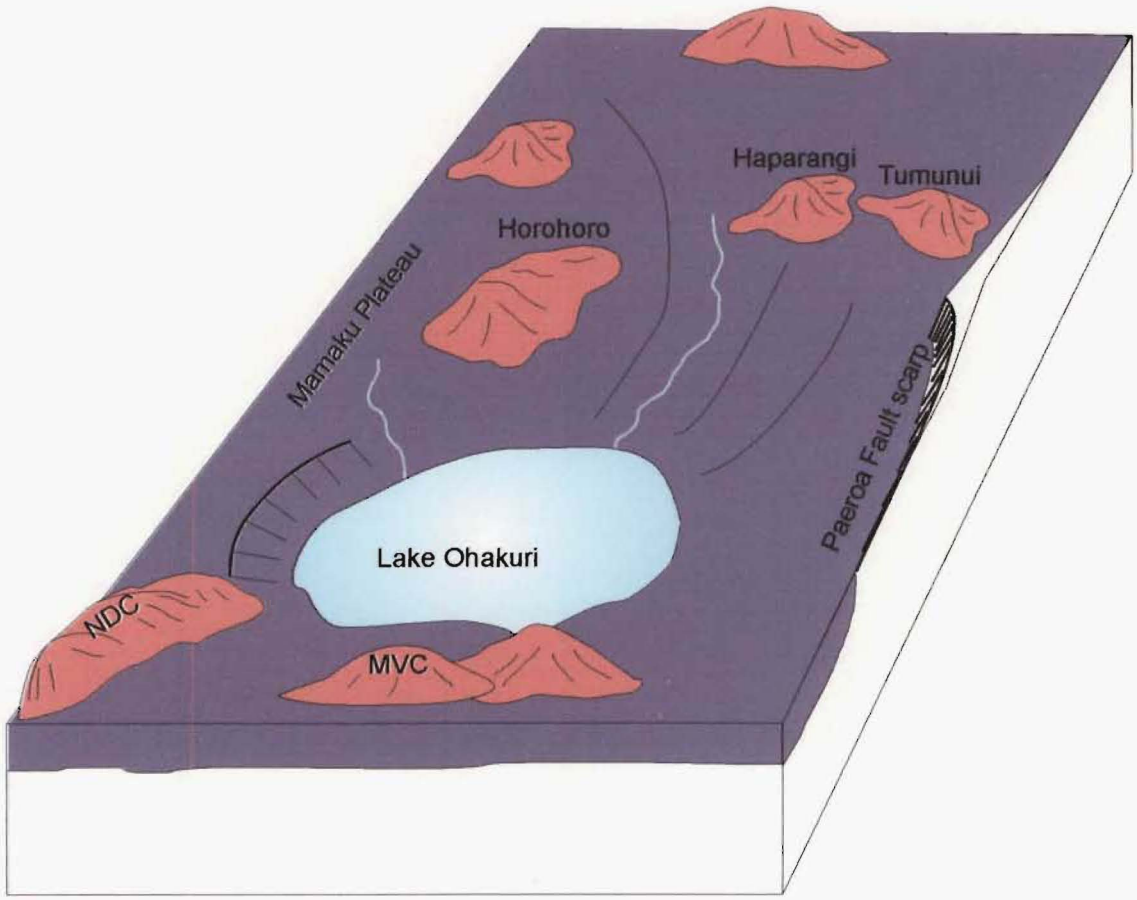

Figure 2.6 Schematic, oblique block diagram of the paleogeographic setting just prior to eruptive phase 1. Coloured fills are consistent with the fills used for the paleogeography cartoon maps.

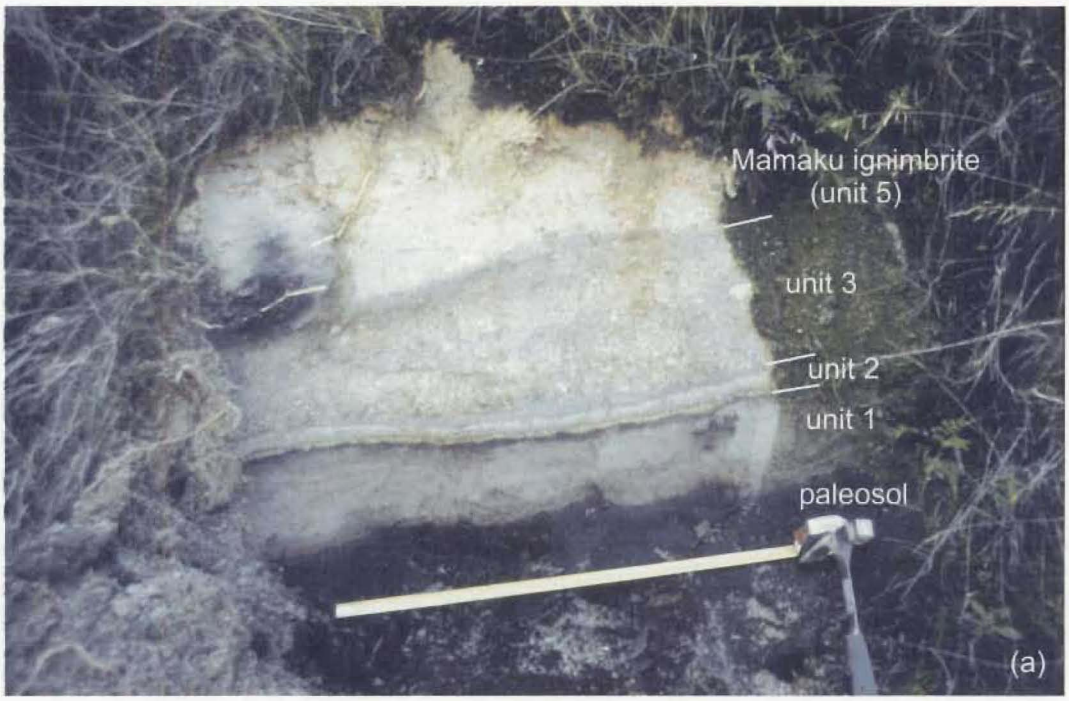

Figure 2.7 Locality Oh147, U16/71391557. (a) Phase 1, 2, and 3 eruptives overlying a dark, organic paleosol. (b) Close-up showing thin soil layer on top of unit 1, and evidence for subtle water reworking at the top of unit 2.

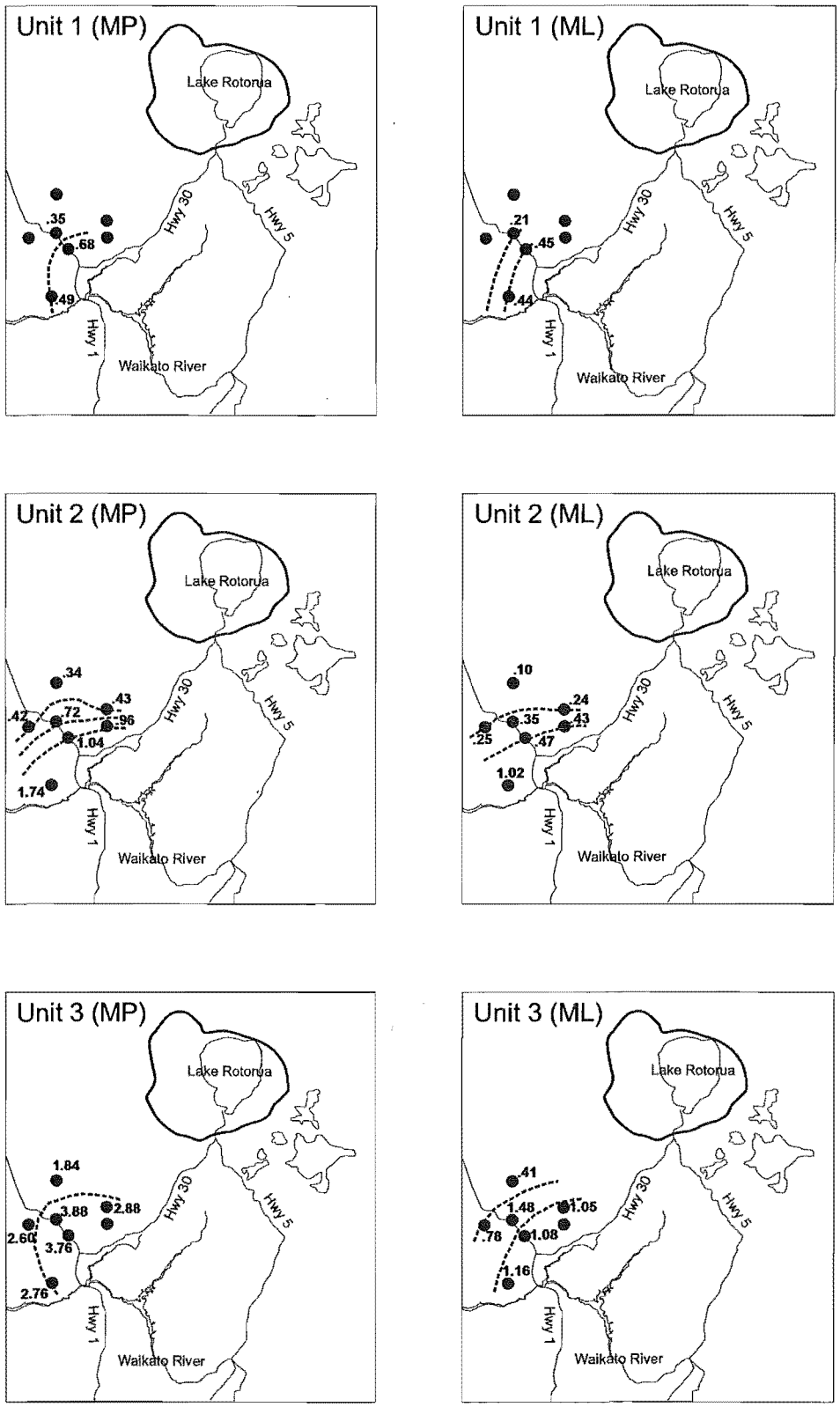

Figure 2.9 Maximum pumice (MP) and lithic (ML) isopleth maps for units 1, 2, and 3. Values (averages of 5 largest clasts) are in cm.

A period of quiescence followed the deposition of unit 1 and a soil began to form (see Figure 2.7b). The presence of carbonised vegetation within the soil layer suggests there was an extensive forest fire. From the thickness of the soil and the preservation of charcoal, I estimate a quiescent period of decades (C.J.N. Wilson, pers. comm., 2003).

Phase 2

Phase 2 is also associated with a phreatomagmatic eruption (Figure 2.10) of a single airfall unit (unit 2). I infer from the very fine-grained and cohesive nature of the unit 2 ash and the presence of leaf impressions, that the forest fire was an isolated event prior to phase 2 and could not have been triggered by wet pyroclastic fallout. Unit 2 is characterised by a conspicuous, yellow, lapilli-rich basal layer that grades into an ultra-fine ash top. Maximum pumice and lithic size data for the basal layer suggest a source within the Ohakuri caldera (Figure 2.9). Bed thicknesses for unit 2, like unit 1, cannot be used to determine the source direction. Post-depositional reworking has disrupted the original thickness of the bed at most localities, particularly the ultra-fine ash layer on top (Figure 2.7b).

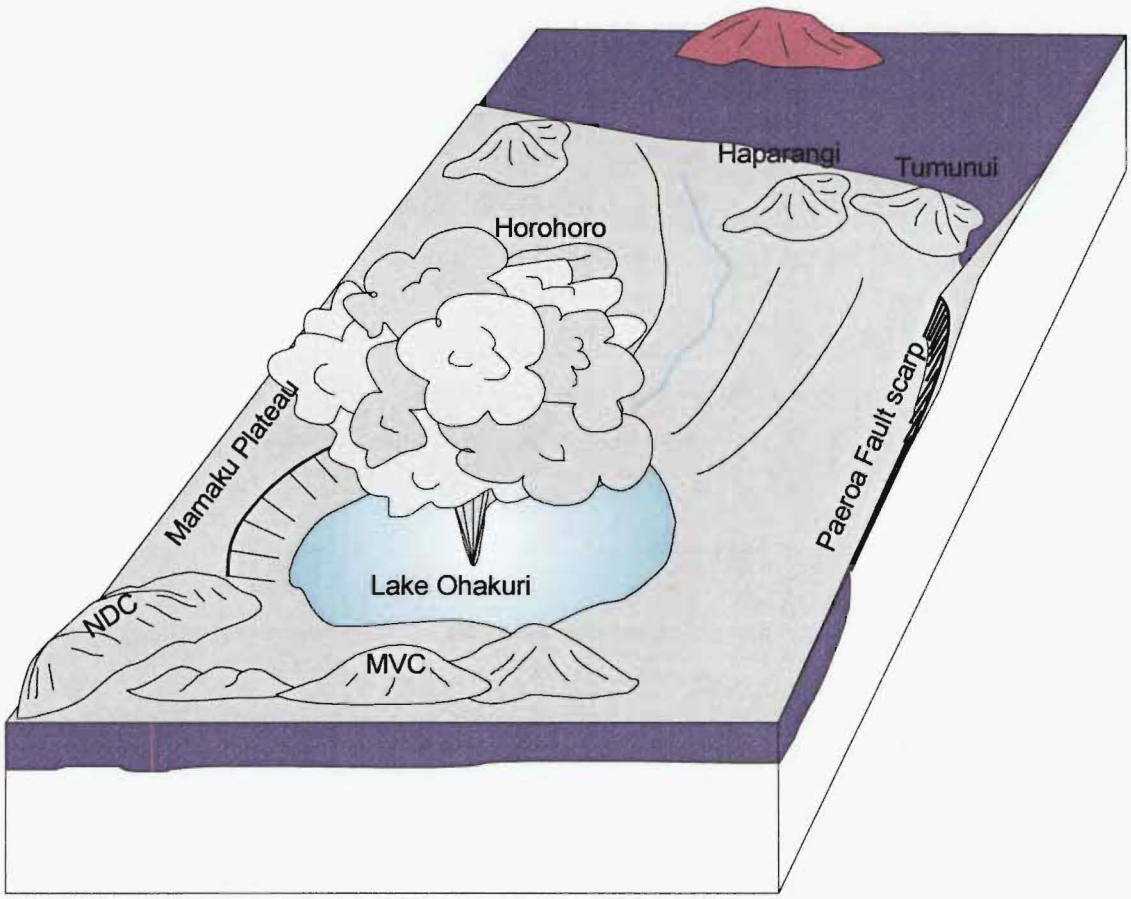

Figure 2.10 Schematic, oblique block diagram of eruptive phase 2.

Phase 3

Minor post-depositional reworking at the top of unit 2 suggests there was a time break of only hours to days before Phase 3 commenced (Figure 2.11). Phase 3 produced 4 eruptive units: a coarse-grained airfall (unit 3); thin, fine-ash PDC packages with diffusely stratified pumice lapilli bands and scattered accretionary lapilli (unit 4); the Mamaku ignimbrite (unit 5),

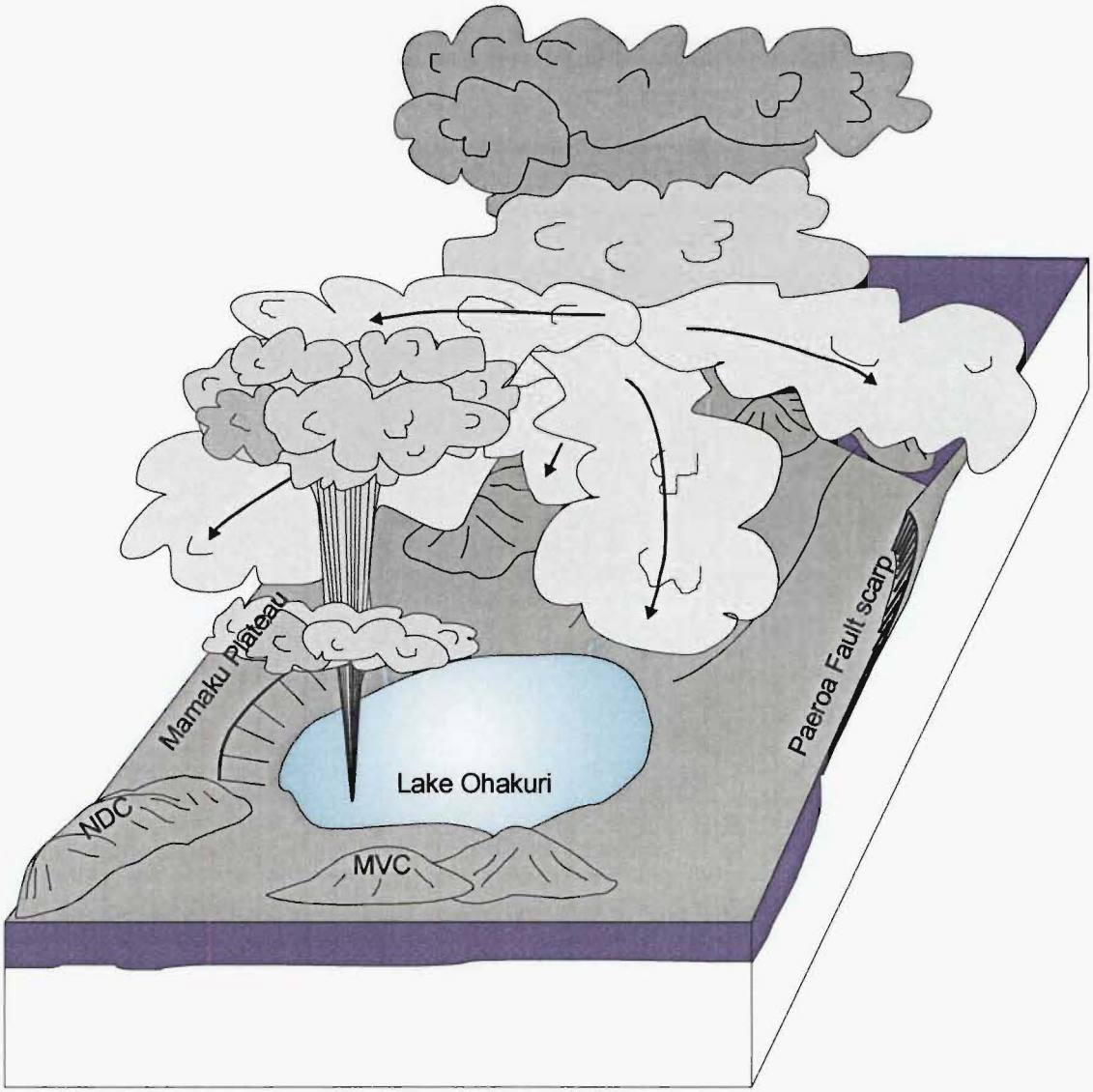

Figure 2.11 Schematic, oblique block diagram of eruptive phase 3.

and an ultra-fine ash (unit 6). Unit 3 (Figure 2.7a) is a plinian-style fall deposit (following Walker, 1973) that has previously been assumed by Milner et al. (2003) to be the early phase of the Mamaku event from Rotorua caldera. However, isopleth maps for maximum pumice and lithic clast sizes from 6 different localities (see Figure 2.9) reveal that unit 3 was erupted from a source within the area that became the Ohakuri caldera. At Oh215 and Oh225 (closest localities to the Rotorua caldera) unit 3 is interbedded with diffusely stratified fine-ash PDC deposits (unit 4; Figure 2.12 and Figure 2.13). Unit 4 is not observed in the localities closest to the Ohakuri caldera; hence, the PDC deposits are likely to be associated with early Mamaku flows from Rotorua. Unit 5, the Mamaku ignimbrite, is also sandwiched between the unit 3 fall

deposit (see Oh148/Oh147 and Oh204 stratigraphic representation in Figure 2.5 fence diagram) and, together with unit 4, suggest that simultaneous eruptions were occurring from Rotorua and Ohakuri. At Oh148 the Mamaku ignimbrite is approximately 5 metres thick and welded (Figure 2.14a), and at Oh204 (only 3 km away and up a gentle gradient) it forms a < 5 cm thick bed (Figure 2.15). The implication is that ~ 25 km south of Rotorua caldera, the Mamaku PDC's were relatively sluggish and incapable of surmounting gentle hill-slopes.

Phase 3 ended with the emplacement of an extremely fine-grained, wet, cohesive ash with conspicuous accretionary lapilli (unit 6) that lies conformably on top of unit 3 (see Figure 2.15). It is difficult to determine the precise origin of unit 6 and I suggest three possibilities: 1) fine-grained airfall associated with unit 3; 2) co-ignimbrite ash associated with the Mamaku ignimbrite (unit 5); or 3) a secondary pyroclastic deposit of an explosive hydroeruption associated with Mamaku PDC's coming into contact with paleo-Lake Ohakuri, which most likely occupied the area of what was to become the Ohakuri caldera (see Figure 2.11).

Phase 4

Some layers within unit 6 have faint cross-laminations and low-angle ripple structures suggesting contemporaneous reworking by water, but the absence of deep gullying or weathering suggests very little, if any, time elapsed before the eruption and emplacement of the caldera-forming Ohakuri pyroclastic deposits (unit 7; Figure 2.16 and Figure 2.17). The base of

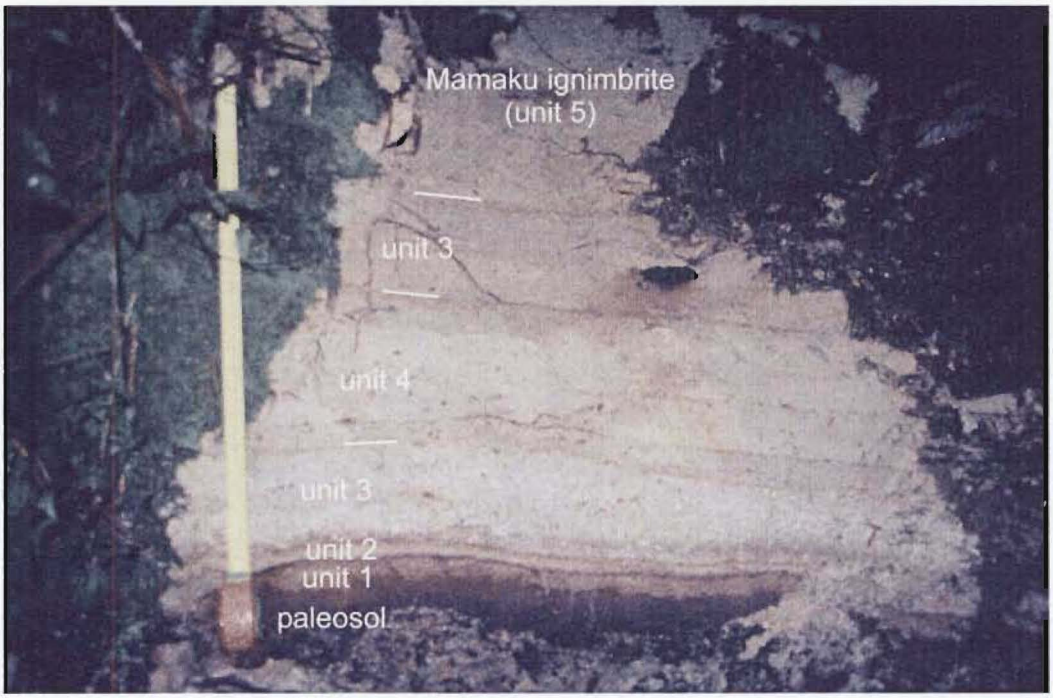

Figure 2.12 Locality Oh215, T16/695243. Early Mamaku PDC deposits (unit 4) interbedded with unit 3.

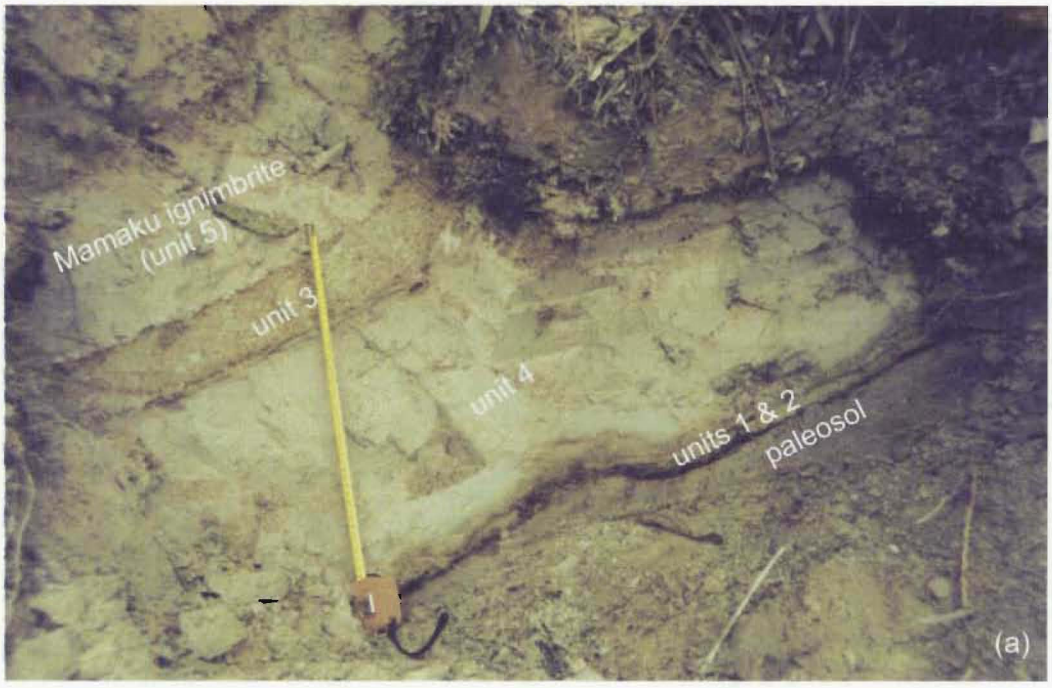

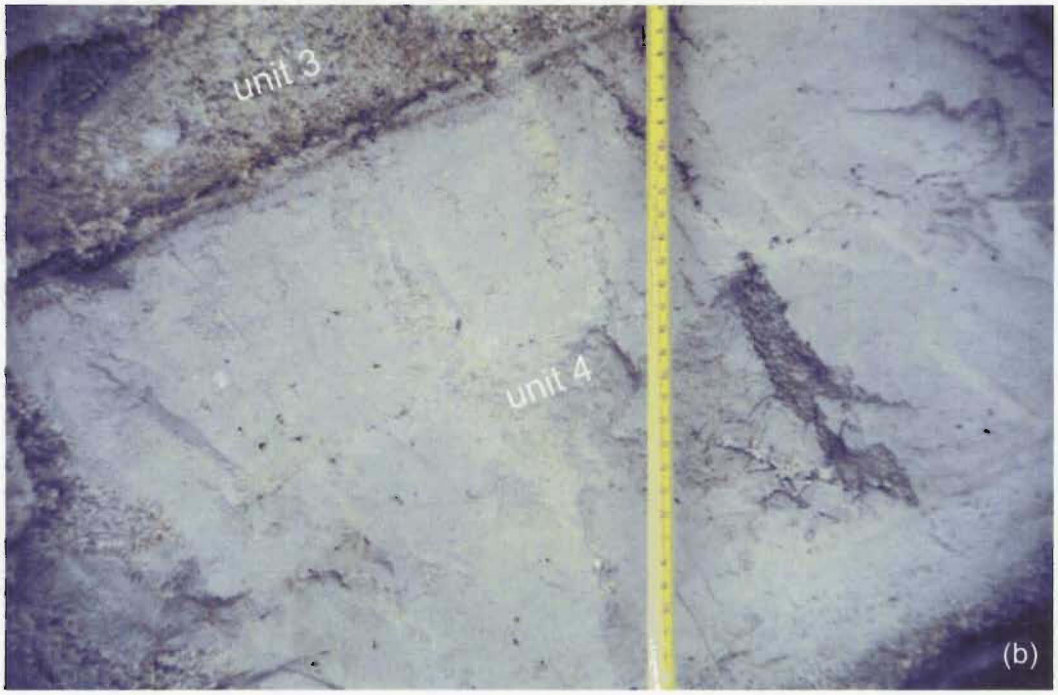

Figure 2.13 Locality Oh225, U16/77122015. (a) Early Mamaku PDC deposits (unit 4) between units 2 and 3. (b) Close-up of unit 4; notice accretionary lapilli concentration layer directly above 'unit 4' label.

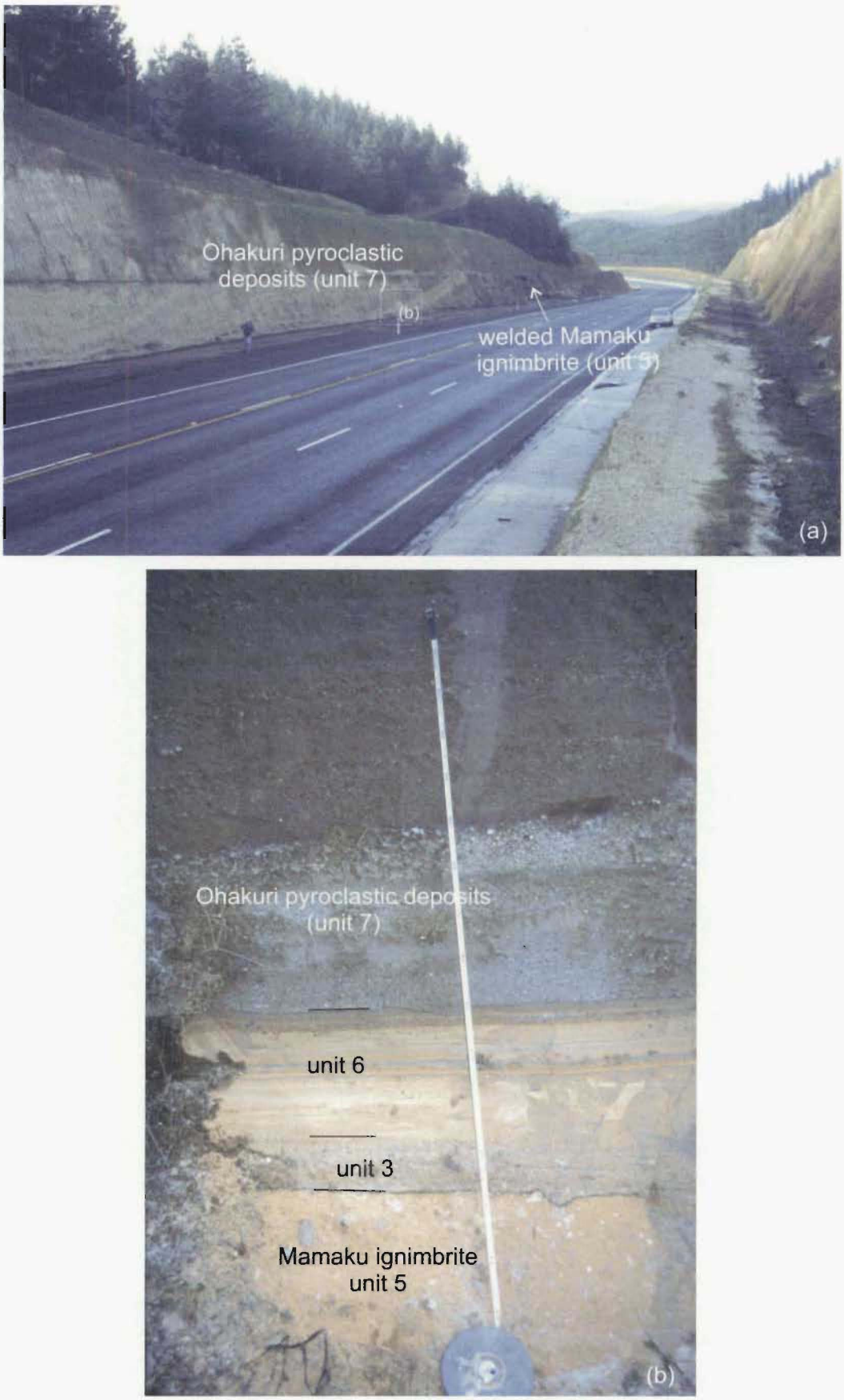

Figure 2.14 Locality Oh148, U16/71301572. (a) Welded Mamaku ignimbrite (~ 5 m thick) overlain by giant dune bedded Ohakuri pyroclastic deposits in HWY1 roadcut. (b) Close-up of phase 3 and 4 deposits. Together, this photo and Figure 2.7a (Oh147) depict the Rotorua-Ohakuri eruption sequence from top to bottom.

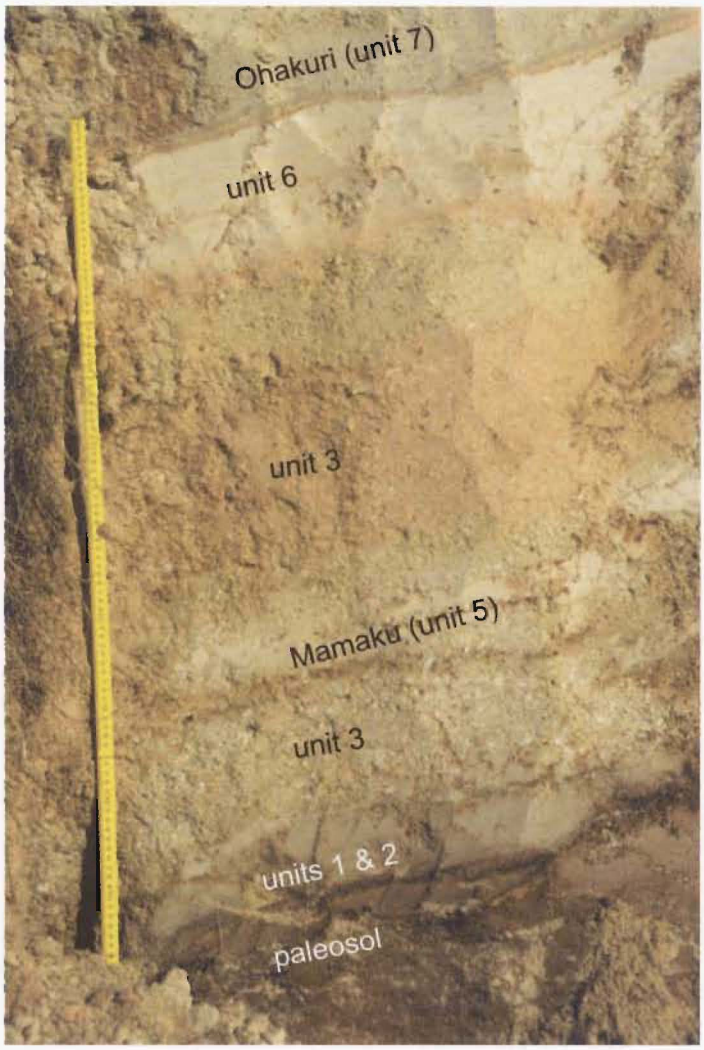

Figure 2.15 Locality Oh204, T16/694182. Rotorua-Ohakuri eruption sequence from bottom to top. Mamaku ignimbrite is < 5 cm thick.

the Ohakuri pyroclastic deposits is characterised by pyroclastic density currents with giant-dunes up to 35 m in wavelength. The giant-dunes indicate a transport direction back to the Ohakuri caldera, providing further evidence that the Ohakuri is not simply a distal facies of the Mamaku ignimbrite. See Chapters 3 and 4 for more detail on the giant-dunes and transport directions.

During phase 4 there is evidence that the Horohoro Fault scarp formed in one large tectonic event associated with the Ohakuri caldera-forming eruption (Figure 2.16 and Figure 2.17). A detailed description of the synvolcanic formation of the Horohoro Fault scarp is discussed in Section 2.3.1.

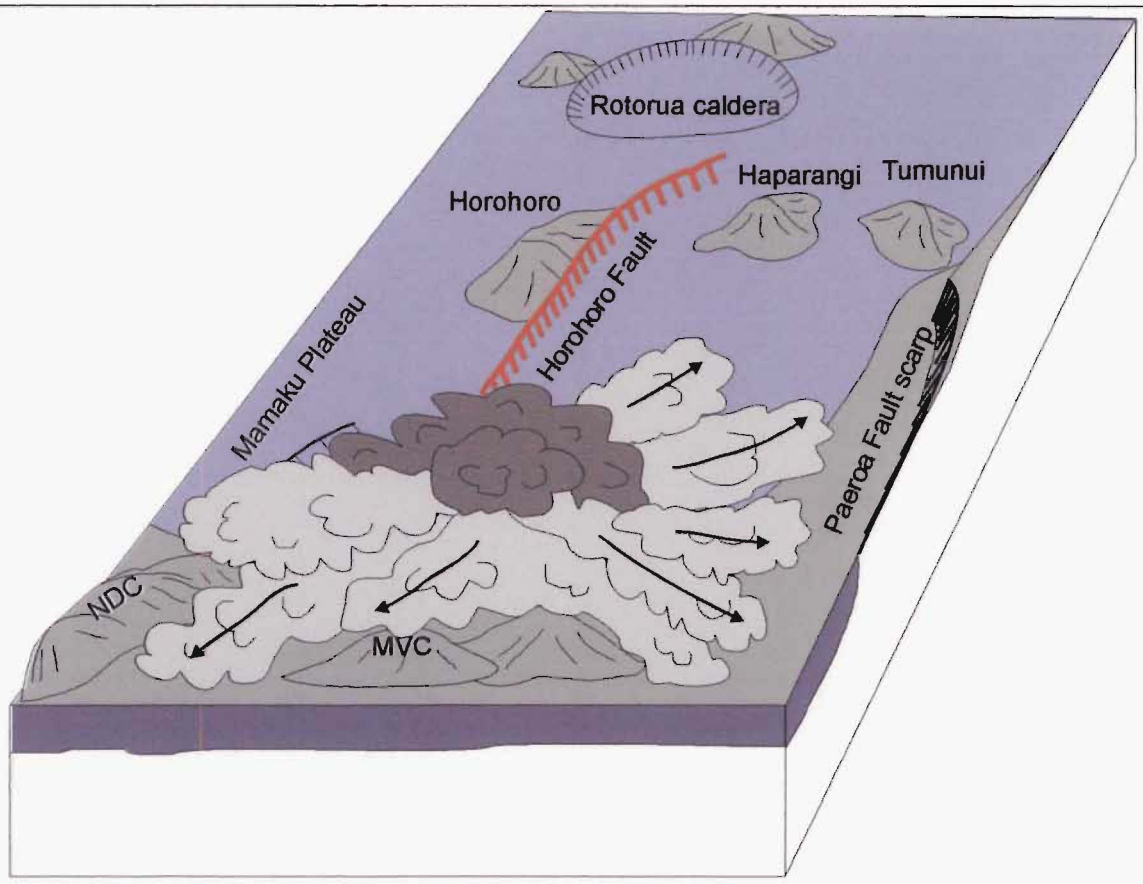

Figure 2.16 Schematic, oblique block diagram of eruptive phase 4. The Horohoro Fault scarp formed during this phase.

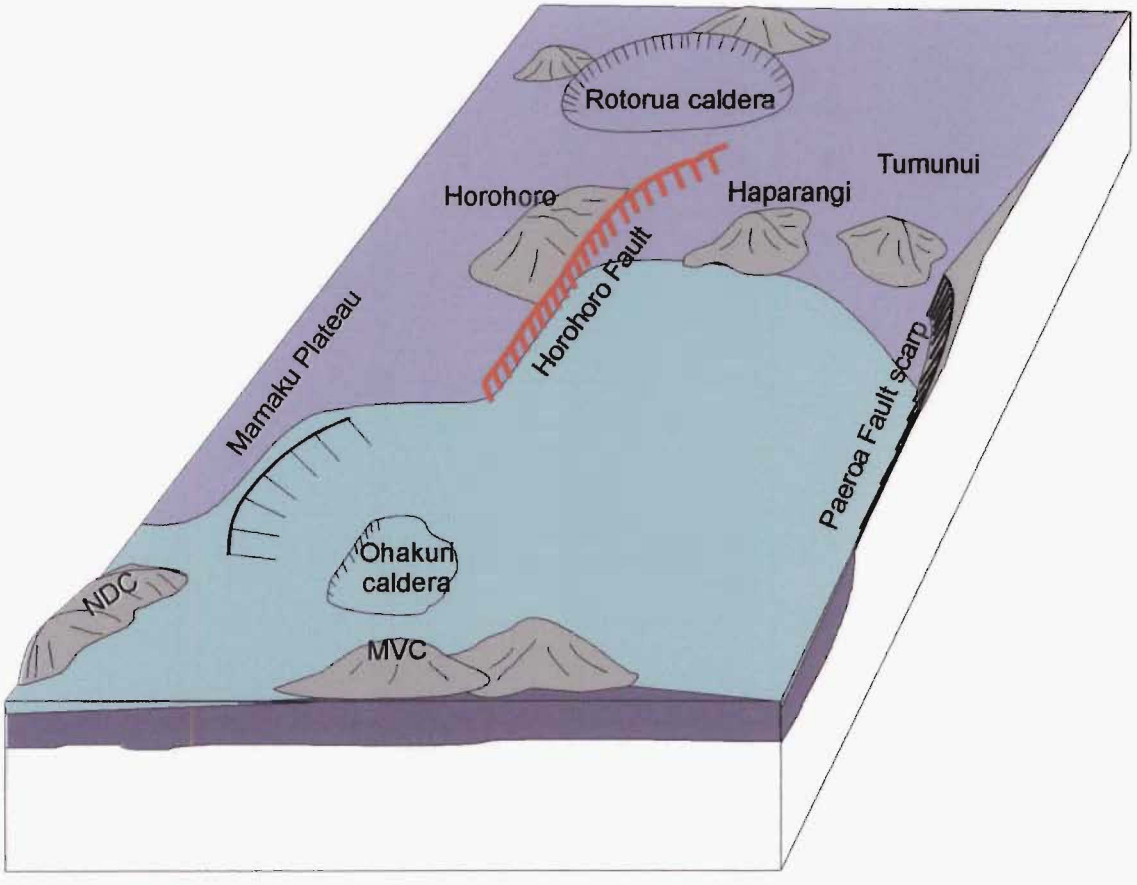

Figure 2.17 Schematic, oblique block diagram of the paleogeography after eruptive phase 4.

Distribution of the Mamaku ignimbrite and the Ohakuri pyroclastic deposits

Refer to Figure 2.18 for the following descriptions.

Mamaku ignimbrite

The Mamaku ignimbrite is one of the more widespread ignimbrites in the central TVZ with a present day exposure of > 3200 km^2 and an original distribution up to 3900 km^2 (Milner, 2001). Today, the ignimbrite is primarily exposed as a fan covering areas to the north, northwest, west, and southwest of Rotorua caldera, with patchy exposure to the south and outcrops as far east as Lake Tarawera (Milner et al., 2003). To the southwest, > 100 m of Mamaku ignimbrite is exposed on either side of the Horohoro fault scarp, suggesting the fault scarp is younger than the Mamaku pyroclastic density currents that travelled around the Horohoro rhyolite dome (see Figure 2.11 and Figure 2.16) (Milner et al., 2003). Milner (2001) infers a displacement of > 250 m between Mamaku ignimbrite west of the Horohoro Fault scarp and east of the scarp (within the Dillon drill hole, U16/876230). From the > 250 m displacement it is clear that the topography east of the Horohoro Fault scarp was as high as the Mamaku Plateau prior to the Rotorua collapse event. An isolated high stand of Mamaku ignimbrite adjacent to Tumunui Hill, 557 m above sea level (ASL) and only ~ 100 m below the Mamaku Plateau exposure, suggests this area may have been even higher than the plateau. At the southern extent of its exposure, the Mamaku ignimbrite is < 20 m thick and field evidence suggests it was incapable of surmounting moderate hill-slopes (see 'Phase 3', Section 2.2.2). The sluggishly-emplaced nature of the distal Mamaku ignimbrite is particularly important with respect to its association with the Mokai ignimbrite and is explained in further detail below.

Ohakuri pyroclastic deposits

The Ohakuri pyroclastic deposits are exposed within an area encompassing ~ 500 km^2 (see Map 1). The pyroclastics were primarily distributed to the east and northeast, infilling a large portion of the Rotorua-Ohakuri volcanotectonic depression between the Mamaku Plateau and the Paeroa Fault scarp. Within the volcanotectonic depression, the Ohakuri pyroclastic deposits are exposed in NE-SW trending horst structures, with maximum thicknesses of ~ 200 m. The surface exposure in this area veils the great thickness of Ohakuri pyroclastic deposits in the subsurface, as the deposit has been identified in several drillholes to a depth of > 450 m (see Section 2.3.2). There are no Ohakuri pyroclastic deposits exposed east of the Te Weta fault block or north of the present-day Haparangi and Tumunui rhyolite domes where it is assumed that high ground in this area formed a backstop for the northeast travelling Ohakuri PDC's.

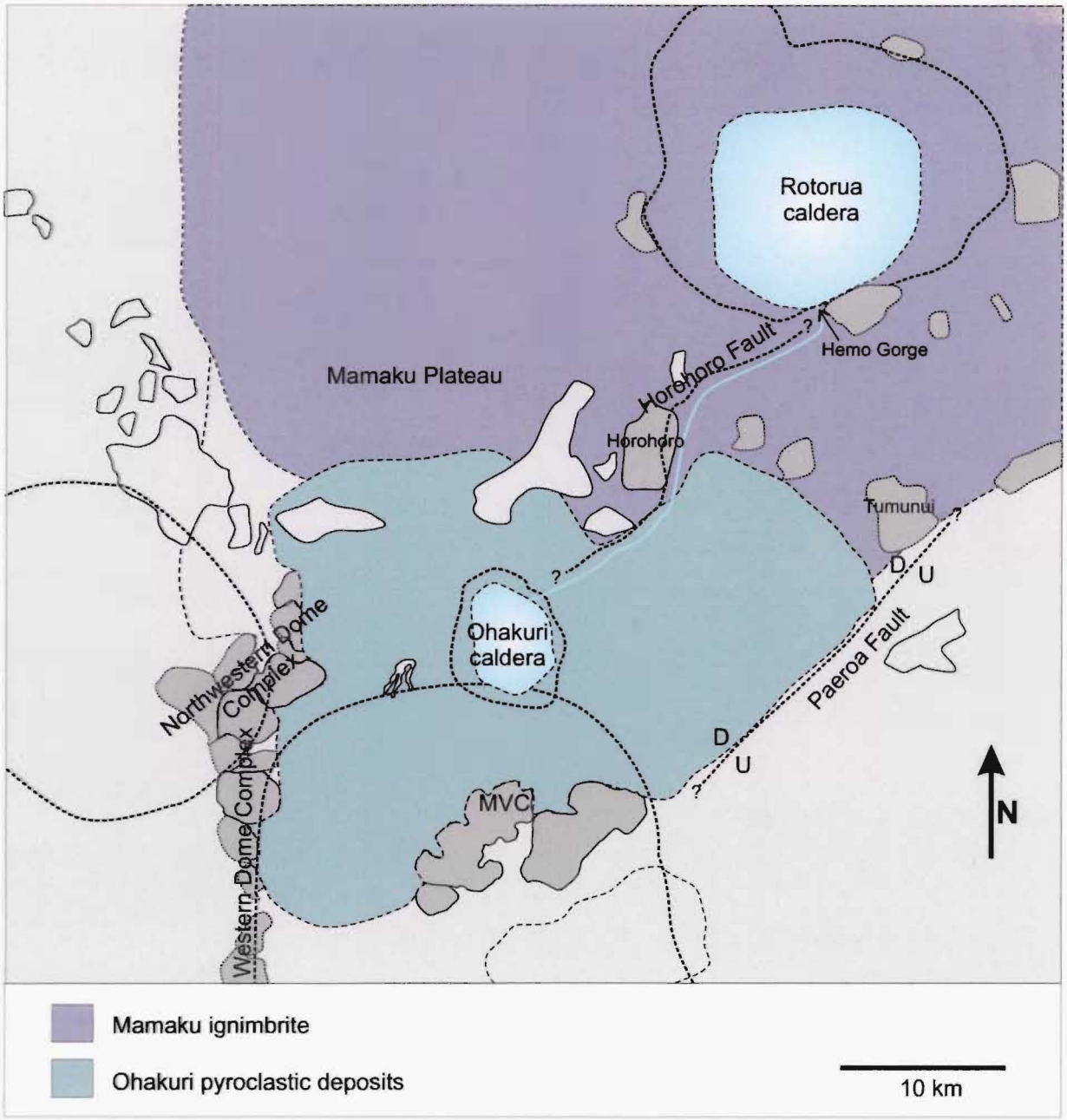

Figure 2.18 Cartoon map of paleogeography soon after the Rotorua and Ohakuri caldera-forming eruptions. The inferred distribution of the Mamaku ignimbrite and Ohakuri pyroclastic deposits are shown.

The base of the Ohakuri pyroclastic deposits can only be observed in the north and northwest sectors of the Ohakuri distribution. Here, the Ohakuri pyroclastic deposits form a thin veneer on top of the Mamaku ignimbrite slope which descends from the Mamaku Plateau down to the Whangapoa Basin (see Map 1). On top of the Mamaku Plateau, the exposure of the Ohakuri pyroclastic deposits thins rapidly. Southwest of the Mamaku ignimbrite slope and the Mamaku Plateau, a significant volume of Ohakuri pyroclastic deposits are exposed between the Whangapoa Basin and the Northwest Dome Complex. In this area they form conspicuous 50 to 100 m high conical hills (Figure 2.19) that are juxtaposed against the slopes of the Northwest Dome Complex. Presumably, at the time of the Ohakuri eruption, this area formed a gentle

Figure 2.19 Conical-shaped hills of Ohakuri pyroclastic deposits (foreground) up against the eastern slopes of the Northwest Dome Complex (right side of panorama). Flat, grassy area in the background (left side of panorama) is the inferred Ohakuri caldera.

slope off the existing Northwest Dome Complex, underlain by fan material, lavas and possibly Pokai ignimbrite. West of the Northwest Dome Complex (i.e. Oh118, T16/68890834), only a thin veneer of Ohakuri pyroclastic deposits overlie the Pokai ignimbrite.To the south, the Ohakuri pyroclastic deposits are not exposed beyond the present-day MVC. Age data from Leonard (2003) indicates that the two linear dome complexes in the central MVC were constructed prior to the Ohakuri eruption. The northern sides of these two dome lineaments appear to have formed an insurmountable obstacle for the southward travelling Ohakuri PDC's.

Mokai ignimbrite: description and stratigraphic relationship

The Mokai ignimbrite is exposed over an ~ 132 km^2 area south of the Waikato River and abuts against the older Western Dome Complex (Milner, 2001) (see Map 1). The extent of the present-day outcrop and the estimated average thickness of 181 m, provide a minimum volume of ~ 24 km^3 (11 km^3 DRE) for the Mokai ignimbrite (Milner, 2001). It is predominantly welded and composed of 3 units separated by time breaks (Milner, 2001). It has been suggested by several workers, including Martin (1961), that the Mokai and Mamaku ignimbrites are the same. The Mokai ignimbrite has the same transitional paleomagnetic direction as the Mamaku ignimbrite and a similar radiometric age date of 220 ± 10 ka (Tanaka et al., 1996). In addition, the major element, trace element, and plagioclase chemistry for the Mokai ignimbrite pumice is the same as that for the Mamaku type 2 pumice (Milner, 2001). However, despite such similarities, Milner (2001) concluded that the Mokai ignimbrite is too thick to be the distal equivalent of the Mamaku ignimbrite. Field observations for this thesis support Milner's (2001) conclusion. The southernmost exposure of the Mamaku ignimbrite, ~ 25 km southwest of Rotorua caldera (OH148, U16/71301572), is < 20 m while the Mokai ignimbrite is thickest (> 200 m) near the southern end of its distribution, > 40 km from Rotorua caldera (Milner, 2001). It is hardly conceivable that the sluggish Mamaku PDC's, which were incapable of topping moderate slopes ~ 20 km southwest of Rotorua caldera, could have climbed a gradient to an

area where > 200 m of pyroclastic material has ponded > 40 km from Rotorua caldera. As a separate ignimbrite deposit, the Mokai ignimbrite has not been linked to a source.

Where does the Mokai ignimbrite fit in with the Mamaku ignimbrite and Ohakuri pyroclastic stratigraphy? Paleomagnetic data suggest the Mokai is of closely similar age to the Mamaku and Ohakuri deposits, but was it emplaced during a simultaneous collapse of the Rotorua and Ohakuri calderas? It is conceivable that the eruption of the Mokai ignimbrite could have been triggered by the Rotorua and Ohakuri caldera collapse events; however, there is no stratigraphic evidence for this. The northernmost exposure of the Mokai ignimbrite (just south of the Waikato River) is at the same approximate topographic elevation as the Ohakuri pyroclastic deposits on the north side of the river; neither deposit has been recognised across its respective opposite side of the river. This modern topographic relationship suggests 3 possibilities: 1) the Mokai ignimbrite is older and was erupted from a southerly source, forming a backstop for the Ohakuri PDC's; 2) the older Ohakuri pyroclastic deposits formed a backstop for the Mokai ignimbrite which was erupted from a southerly source; or 3) an east-west trending fault structure (which has not been recognised by existing detailed mapping by E.F. Lloyd, unpublished data) separates the two deposits, in which case there is no implication for the Mokai ignimbrite source direction. Based on limited field data, any of these scenarios could be possible; the Ohakuri pyroclastic deposits and the Mokai ignimbrite need to be found in direct contact before their relative ages can be distinguished. At present, associating the Mokai ignimbrite with the Rotorua and Ohakuri caldera collapse events is speculative, despite the paleomagnetic evidence for their contemporeneity (Tanaka et al., 1996; McWilliams, 2001).

2.2.3 Post- Rotorua and Ohakuri caldera collapse events

Immediately post-collapse events

Following the caldera-forming eruptions of the Mamaku ignimbrite and the Ohakuri pyroclastic deposits, there is evidence to suggest that both Rotorua and Ohakuri calderas filled with water, forming two large lakes. The formation of lakes following caldera-forming ignimbrite eruptions is common, as is the inevitable catastrophic breach of their pyroclastic dams (cf. Manville et al., 1999) (Figure 2.20). The formation of the post-1.8 ka Taupo caldera lake and the catastrophic breach of its pyroclastic dam have been recently reconstructed from physical sedimentological studies of perched lake sediments (e.g. Riggs et al., 2001), and flood deposits and geomorphic features (Manville et al., 1999), respectively. Data from these studies suggest that Lake Taupo rapidly refilled to its maximum level (700 km^2 surface area and 34 m above its present-day level) within 20 years (Riggs et al., 2001). The catastrophic breach of the pyroclastic dam occurred 20 to 25 years after the eruption (Manville, 2002).

Figure 2.20 Oblique view of Aniakchak caldera, Alaska from Waythomas et al. (1996). 'The Gates' is the trapezoidal shaped breach structure associated with the catastrophic breakout flood.

Figure 2.21 View of the trapezoidal shaped Hemo Gorge from across Lake Rotorua. Photo is courtesy of R. Marx (University of Otago).

Assuming lake formation within Rotorua and Ohakuri calderas occurred at a similar rate to their modern Taupo caldera analogue, the breach and formation of an outlet for these lakes may have occurred within decades. With respect to Lake Rotorua, Marx et al. (2003) suggest that the present day Hemo Gorge (Figure 2.21) may represent the original outlet for Lake Rotorua at

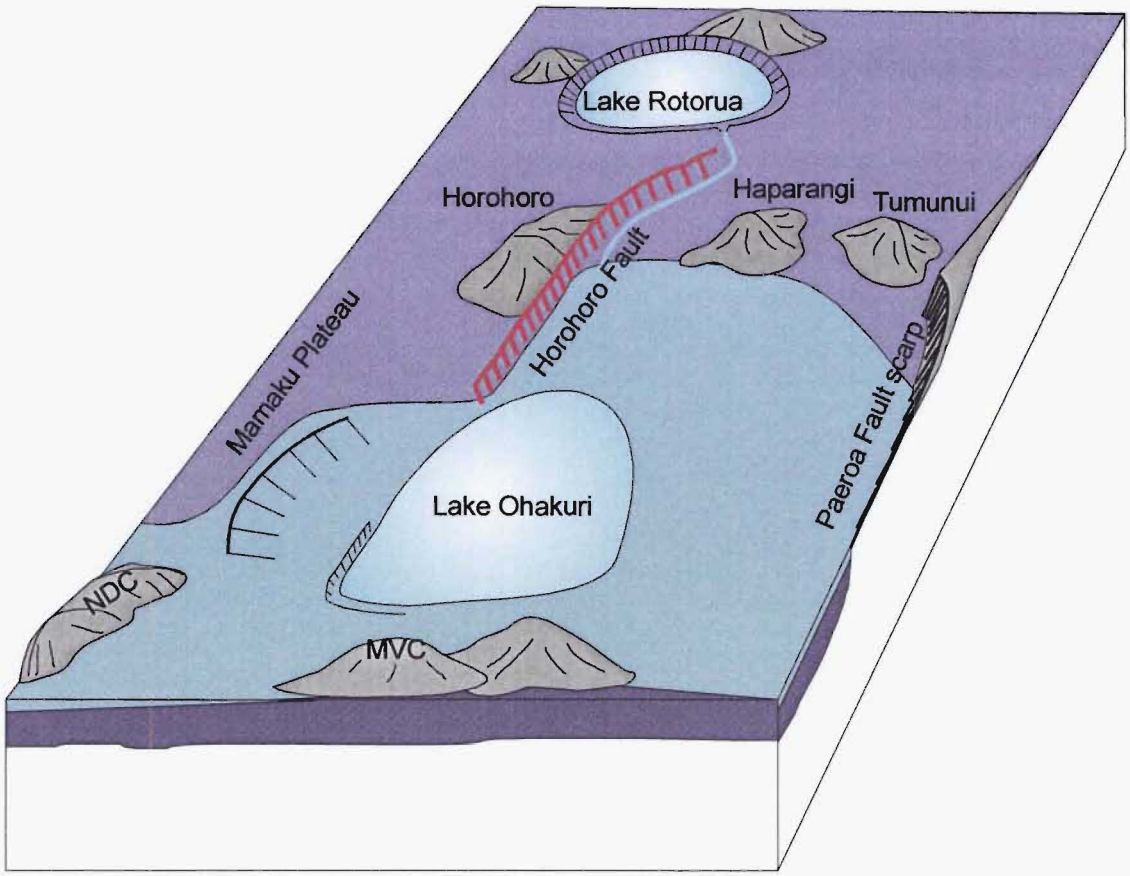

Figure 2.22 Schematic, oblique block diagram depicting the formation of Lake Rotorua and Ohakuri, and the probable breach point of the Rotorua caldera at its southern end.

its southern end (depicted in Figure 2.18 and Figure 2.22). Morphologically, the trapezoidal shape of the Hemo Gorge (observed in early aerial photos by Marx et al., 2003) is consistent with typical caldera lake breach structures (cf. Figure 2.20) (V. Manville, pers. comm., 2003). In addition, perched fluvial sediments exposed in the Hemo Gorge are consistent with the high stand lake level after the Mamaku ignimbrite eruption (R. Marx, pers. comm., 2003). With respect to the Ohakuri caldera lake (Lake Ohakuri) and its original outlet, there is little in the way of preserved geomorphic evidence. However, based on the paleogeography and the surrounding high ground described above and depicted in Figure 2.18, a gap through the Northwestern Dome Complex (the present day 'Ongaroto Gorge', where the Waikato River currently flows through and has done since at least before the 26.5 ka Oruanui eruption) was the most likely outlet. Alternatively, there may have been an outlet to the northeast where drainage could have conceivably paralleled the base of the Paeroa Fault scarp and flowed out to the Bay of Plenty.

The Rotorua-Ohakuri volcanotectonic depression (~ 240 ka to ~ 200 ka)

Volcanism during this period occurred both outside and within the Rotorua-Ohakuri volcanotectonic depression. Immediately east of the volcanotectonic depression, the 230 ± 10 ka Kaingaroa ignimbrite (Houghton et al., 1995) was erupted during the collapse of the Reporoa caldera (Nairn et al., 1994; Beresford and Cole, 2000). The Kaingaroa ignimbrite is ~ 100 km^3 DRE (Nairn et al., 1994; Beresford and Cole, 2000) with an inferred outflow area ranging from 800 to 1870 km^2 (Beresford and Cole, 2000). It is predominantly distributed to the east; however, the Kaingaroa ignimbrite has been mapped west of the Paeroa Fault scarp, within the Rotorua-Ohakuri volcanotectonic depression. The Kaingaroa ignimbrite has not been observed in contact with the Mamaku ignimbrite or the Ohakuri pyroclastic deposits (see Bailey and Carr, 1994; Houghton et al., 1995) and therefore it is not certain whether it is older or younger. No new evidence was found during my work to resolve the relative stratigraphic relationship. I have, somewhat arbitrarily, placed the Kaingaroa ignimbrite in this period based on its Ar/Ar age which is younger (although within 1 s.d.) of the ~ 240 ka age for the Mamaku and Ohakuri pyroclastic deposits.

Volcanism within the Rotorua-Ohakuri volcanotectonic depression occurred primarily in the MVC, including ignimbrite-forming explosive eruptions and the extrusion of rhyolite lavas associated with dome building. Pukeahua dome (northern MVC) evolved over a long period (~ 229 to 196 ka) from several extrusive episodes and at least two explosive episodes (Leonard, 2003). Vestiges of the Pukeahua explosive episodes are preserved as pyroclastic fans that form a ring around the dome. During the early stages of the Pukeahua evolution, an explosive eruption occurred nearby that produced the Atiamuri ignimbrite (229 ± 12 ka; Leonard, 2003), which covers an area of 10 km^2 and has a volume > 1 km^3 DRE (Leonard, 2003). Leonard (2003) suggests the Atiamuri ignimbrite is associated with an explosive eruption from a rhyolite dome in the northeastern sector of the MVC. At the northern end of its distribution, the Atiamuri ignimbrite overlies the Ohakuri pyroclastic deposits.

With respect to Lake Rotorua and Lake Ohakuri, the present day distribution of lake sediments suggests that they may have coalesced and formed one large lake that occupied much of the Rotorua-Ohakuri volcanotectonic depression (see Figure 2.23). Grindley (1965) formally named the lake sediments in this area the Ngakuru Formation which is considered to be younger than the Mamaku ignimbrite (~ 240 ka) and older than the Hinuera Formation (~ 26 ka) (Briggs, 1973; Dunham, 1981; Langridge, 1990). Villamor and Berryman (2001) propose a relationship between lake sedimentation and faulting. They divide the Ngakuru Formation into two informal groups; older Ls1 (post Mamaku ignimbrite, pre Earthquake Flat pyroclastics) and younger Ls2 (post Earthquake Flat pyroclastics to syn-Oruanui eruption). From the juxtaposition of older lake sediments and the Ohakuri pyroclastic deposits, in the Ngakuru and Whirinaki horst

structures (see Villamor and Berryman, 2001), it is probable that faulting associated with the TFB commenced coevally or soon after the inception of lake sedimentation. The Ngakuru, Whirinaki, and Paeroa Faults are believed to have been active during this time period (Villamor and Berryman, 2001) and are included in Figure 2.23.

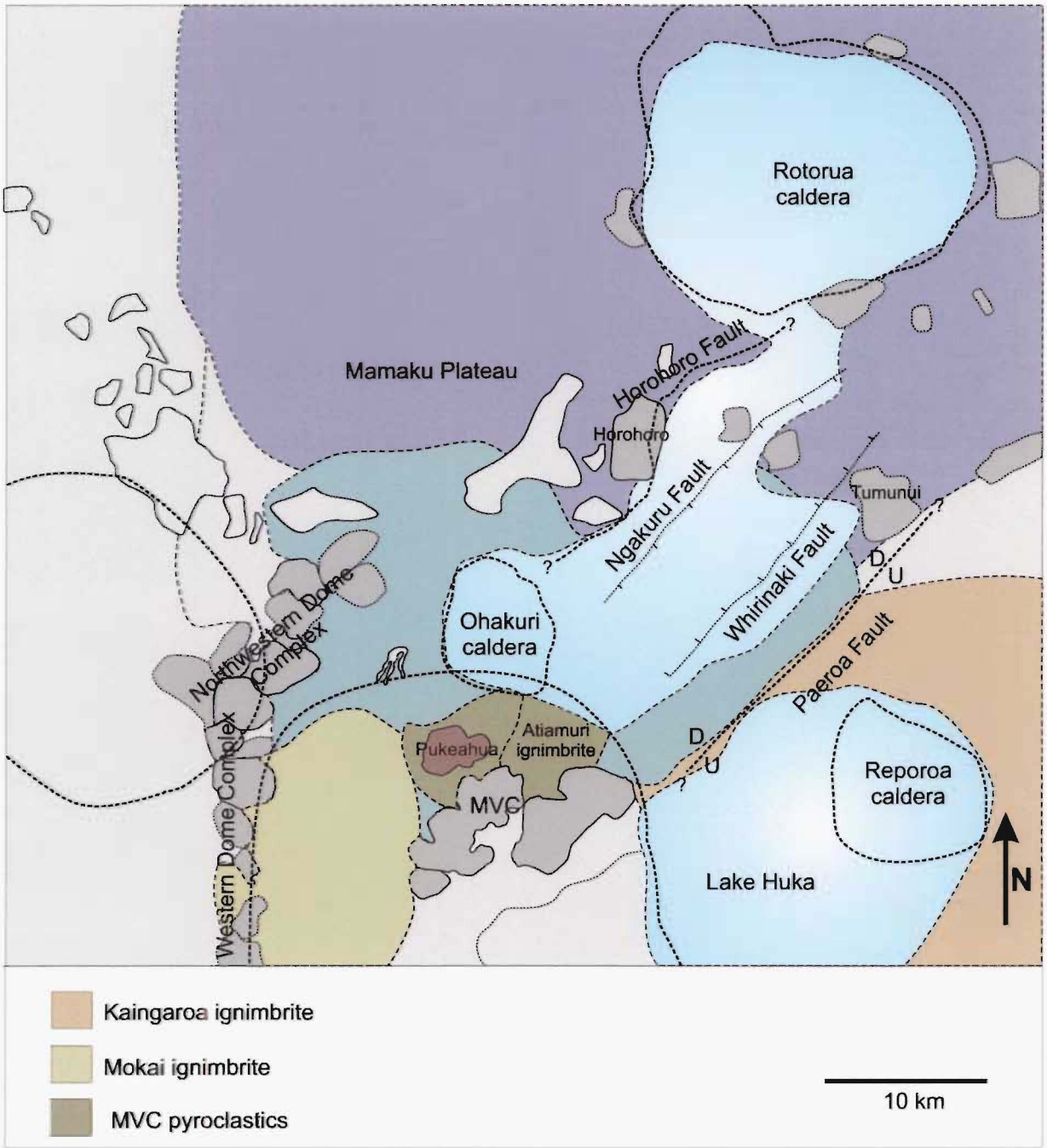

Figure 2.23 Cartoon map of paleogeography at ~ 200 ka. Refer to text for explanation.

Lake formation and sedimentation during this period was not confined to the Rotorua-Ohakuri volcanotectonic depression, but also took place in the Taupo-Reporoa basin. Following the collapse of the Reporoa caldera it is likely that a lake quickly formed. This lake is informally referred to as Lake Huka and its sediments are formally known as the Huka Group (Grindley, 1959). The Huka Group lake sediments in the Taupo-Reporoa basin are > 300 m thick and

overlie pyroclastics, volcaniclastics and lavas that in turn, overlie the intra-caldera Kaingaroa ignimbrite (Nairn et al., 1994; Manville, 2001). Martin (1961) correlated the Huka Group lake sediments with the Ngakuru Formation lake sediments in the Rotorua-Ohakuri volcanotectonic depression.

~ 200 ka to eruption of Rotoiti and Earthquake Flat pyroclastics (~62 ka)

Volcanically, the period between ~ 200 ka and ~ 62 ka was relatively quiet with only isolated dome building events. Lava dome-building activity occurred from Rotorua caldera to the southern end of the MVC (Figure 2.24). Explosive pyroclastic activity did not resume until ~ 62 ka. Both the Rotoiti and Earthquake Flat pyroclastics, 62 ± 2 ka (Charlier et al., 2003) were

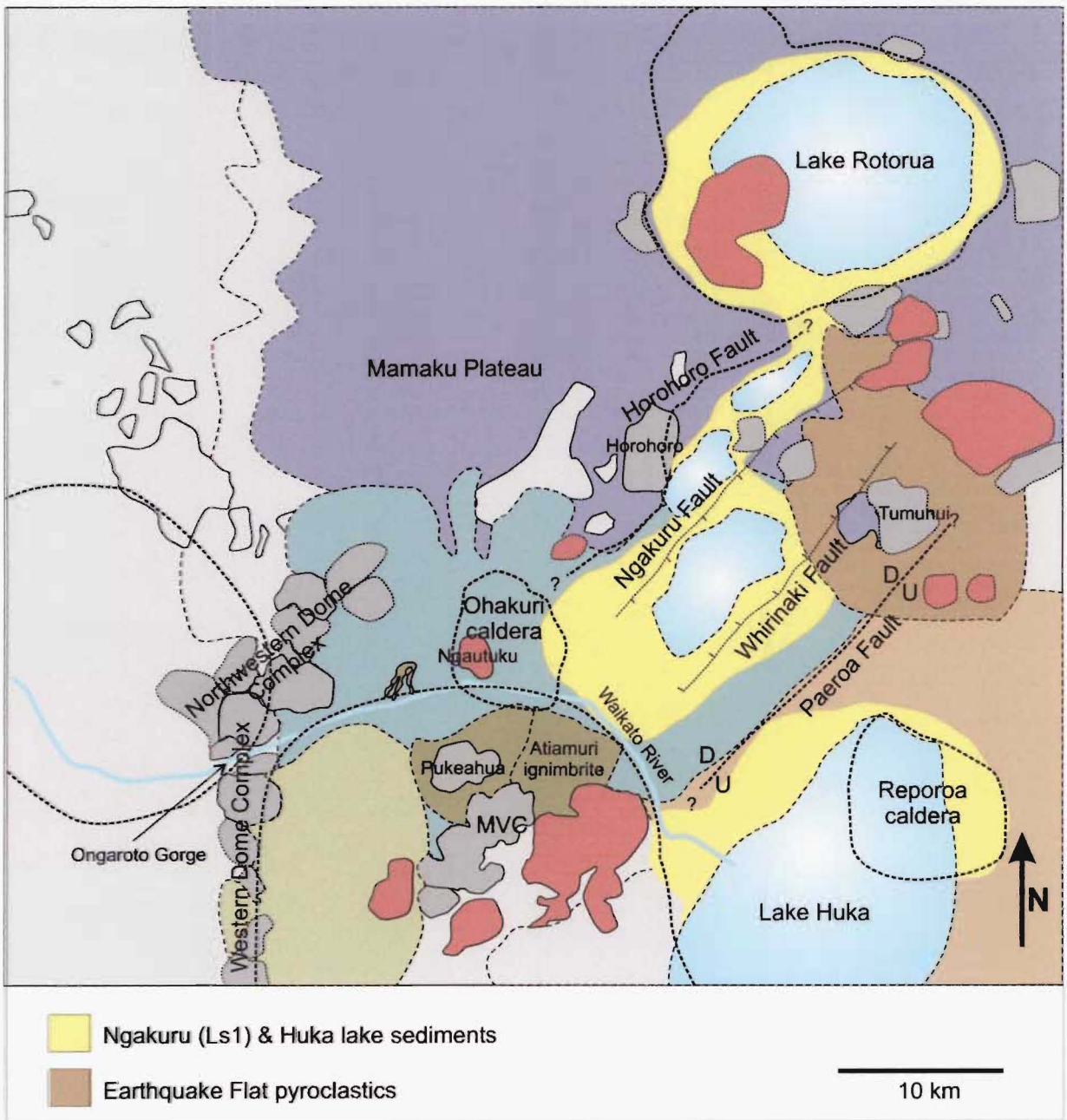

Figure 2.24 Cartoon map of paleogeography at ~ 62 ka.

erupted in close succession (see Section 2.3.1) from a vent within the Okataina caldera and a source further south (Earthquake Flat), respectively (Nairn and Kohn, 1973). The Rotoiti pyroclastics were distributed to the north, beyond the limits of the cartoon map (Figure 2.24), while the Earthquake Flat pyroclastics were distributed in a 110 km^2 area to the southwest of the present-day Lake Tarawera. Villamor and Berryman (2001) suggest that the eruption and emplacement of the Earthquake Flat pyroclastics was coincident with the termination of sedimentation of the older lake sediments (Ls1). In particular, "on the upthrown side of the Ngakuru Fault, the low-angle constructional fan of Earthquake Flat pyroclastics is graded to the upper surface of the older lacustrine sediments (Ls1)," and dissection of these two deposits in the area is similar (Villamor and Berryman, 2001).

There is very little known about the precise location and timing of lake formation within the Rotorua-Ohakuri volcanotectonic depression between ~ 200 ka and ~ 62 ka; however, Dunham (1981) suggests there were several cycles of lake formation and accompanying fluvial activity during this period. Both the timing and location of lakes were tectonically controlled by contemporaneous faulting within the basin (Dunham, 1981; Villamor and Berryman, 2001). The contemporaneous faulting may have caused the break-up of the large lake between Rotorua and Ohakuri confining smaller lakes to isolated grabens (see Figure 2.24). It is probable Lake Ohakuri disappeared during this period as no lake terraces or perched sediments have been found on Ngautuku dome (dated at 160 ± 8 ka by Houghton et al., in prep) located within the Ohakuri caldera. Although there is no evidence for the drainage outlet of Lake Ohakuri, the most feasible outlet was through the present day Ongaroto Gorge area, possibly associated with an ancestral, pre-Oruanui, Waikato River course through the Hauraki Basin. More research needs to be conducted in this area before further speculation can be made with respect to the drainage of Lake Ohakuri.

Post-Rotoiti and Earthquake Flat pyroclastics (< 62 ka) to the present day

The paleogeographic evolution of the Rotorua-Ohakuri volcanotectonic depression, between ~ 62 ka and the present day, can be discerned mostly by comparing Figure 2.24 with the present day geologic map (Figure 2.25). Volcanism during this period has been almost entirely associated with the Okataina and Taupo calderas. As such, contributions to the volcaniclastic geology of the Rotorua-Ohakuri volcanotectonic depression are predominantly associated with the 26.5 ka and 1.8 ka Taupo caldera eruptions, and their sedimentary aftermaths. Figure 2.25 shows that the Oruanui ignimbrite (26.5 ka) and the Taupo ignimbrite (1.8 ka) were deposited within topographic lows related to drained lake basins, fluvial channels, and graben structures. Both the Oruanui and Taupo ignimbrites (as well as pre-Oruanui tephra sequences from Taupo and Okataina) are useful stratigraphic markers employed to measure slip rates for fault movement within the modern TFB. The modern TFB includes faults that have been active since

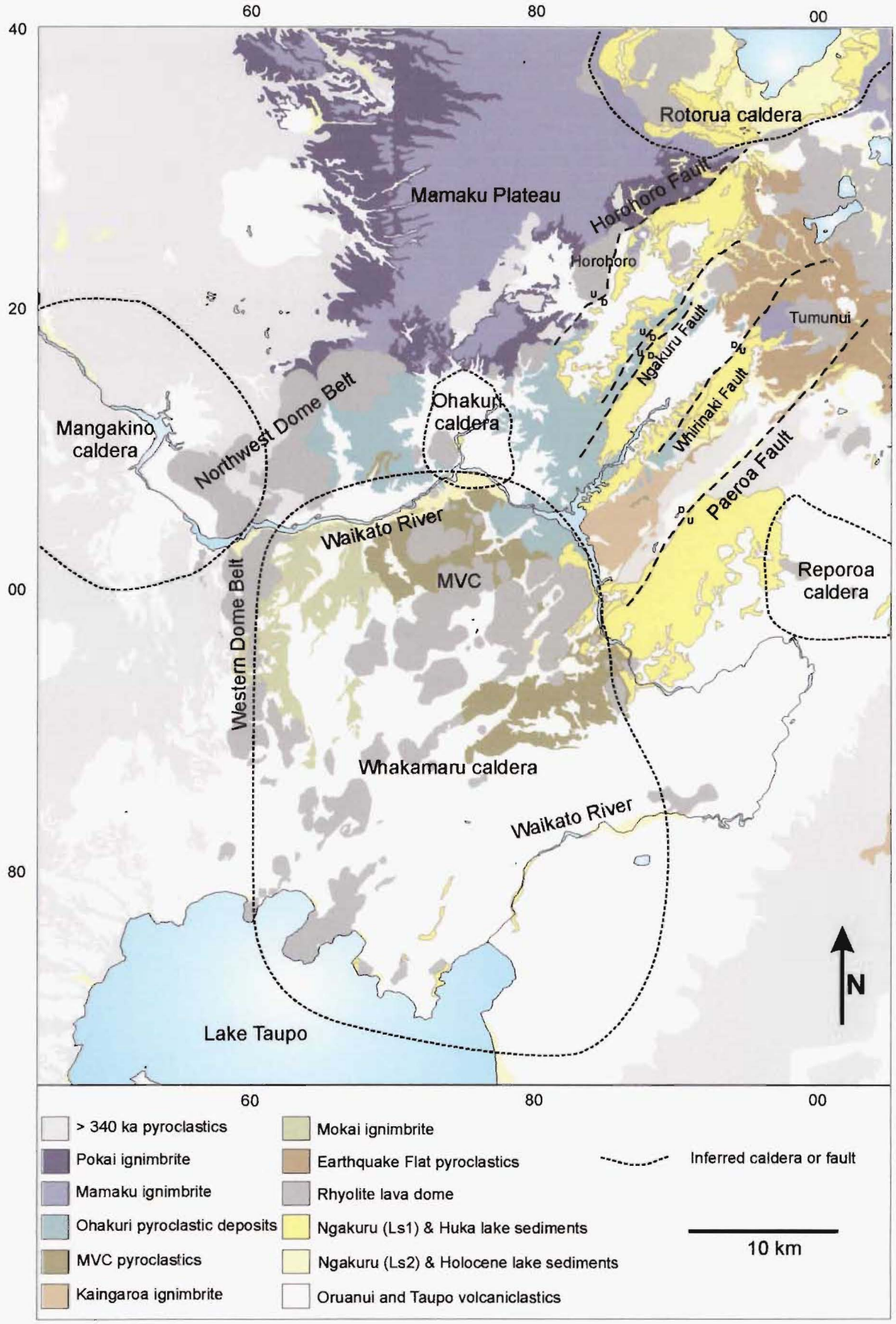

Figure 2.25 Present-day geologic map. Compiled by G.S. Leonard from mapping by E.F. Lloyd, C.P. Wood, I.A. Nairn, B.F. Houghton and others, courtesy of IGNS.

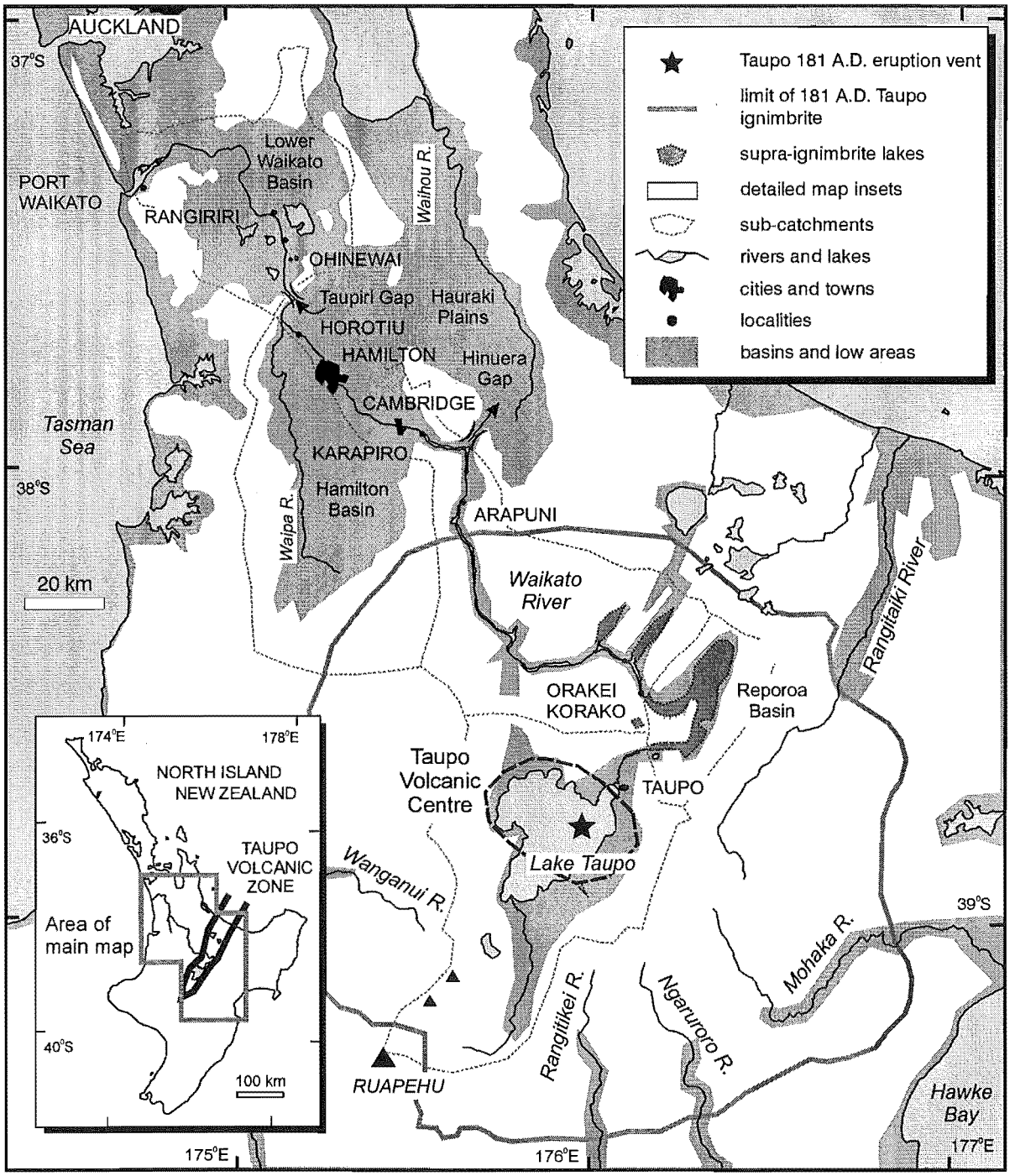

Figure 2.26 Map of supra-ignimbrite lakes after the 1.8 ka Taupo ignimbrite eruption, modified from Manville (2002). Two lakes formed within the Rotorua-Ohakuri volcanotectonic depression (above the 'Orakei Korako' label) due to damming of the Waikato River.

the 26.5 ka Oruanui eruption and, with respect to the Rotorua-Ohakuri volcanotectonic depression, is associated with the narrow zone between the Ngakuru Fault and the Ngapouri Fault (~ 2 km southeast of the Paeroa Fault; see Figure 1.5) (Villamor and Berryman, 2001).

In the last 62 k.y., lakes and drainage within and adjacent to the Rotorua-Ohakuri volcanotectonic depression have been controlled by contemporaneous TFB faulting as well as large-scale eruptions from Taupo caldera.. The 26.5 ka Oruanui eruption and its deposits

destroyed Lake Huka and choked associated drainage (i.e. the Waikato River) with debris. Between the 26.5 ka eruption and the 1.8 ka Taupo ignimbrite eruption the Waikato River course between the present day Reporoa Basin and the Ongaroto Gorge was re-established (Manville, 2003). Following the 1.8 ka Taupo eruption and emplacement of the Taupo ignimbrite, the Waikato River was dammed at several locations along its course impounding many supra-ignimbrite lakes (Manville, 2001; 2002). The supra-ignimbrite lakes included Lake Reporoa, a lake in the Ngakuru-Whirinaki graben (covering an area including and extending beyond the boundaries of the present day Lake Ohakuri), and a lake within the inferred Ohakuri caldera (coincident with the present day Whangapoa Basin) (see Figure 2.26). A few years at most after the establishment of these lakes, the pyroclastic dams failed, flooding occurred and the Waikato River was re-established.

2.3 Discussion

2.3.1 Tectonically-linked caldera collapse events

The relationship between tectonics and volcanism in the extensional setting of the central TVZ is a complex one, which involves the ascent and production of magma in the crust. Does magmatism provoke rifting and the propagation of vertical fault structures in the crust; or does extension, accommodated by vertical deformation, provide pathways and space for the ascent and storage of magma in the crust? The answer to this question of cause and effect is beyond the scope of this thesis; however, the shape and location of crustal magma reservoirs with respect to tectonic setting is discussed in this section as a by-product of the role tectonics may be playing in caldera volcanism in the central TVZ, and conversely, the role caldera volcanism may be playing in tectonics.

In section 2.2.2, I presented evidence for a rapid succession of eruptions from Rotorua and Ohakuri calderas, and in particular, minimal time breaks in the eruption sequence of phase 3 and 4 (including the collapse of both calderas) has provoked the following questions: 1) what triggers the eruptions associated with the collapse of a caldera? and 2) how are eruptions from geographically distinct calderas linked? In the central TVZ and at many other caldera systems worldwide (see Newhall and Dzurisin, 1988) regional tectonics and silicic volcanism are intimately linked (see Wilson et al., 1984; Cole, 1990; Wilson et al., 1995; Rowland and Sibson, 2001; Manville and Wilson, 2003). I suggest, from the rifted setting of the central TVZ (presently widening at a rate of 8mm/yr; Darby et al., 2000), the closely-spaced (temporally) caldera-forming eruptions from the Rotorua and Ohakuri calderas may have been triggered by a regional tectonic event or, alternatively, the Rotorua caldera collapse may have induced a tectonic event that triggered the Ohakuri eruption. Although I am not aware of a similar rapidity of events involving the collapse of two geographically distinct calderas; multiple temporally- and possibly tectonically- linked eruptions have been documented.

Tectonic controls on temporally-linked eruptions

In the TVZ there have been two documented instances where the existing tectonic fabric has been implicated in the successive eruptions of two or more geographically distinct volcanoes: 1) the ~ 62 ka Rotoiti and Earthquake Flat eruptions (Nairn and Kohn, 1973; Charlier et al., 2003), and 2) the ~ 10 ka eruptions from the Tongariro Volcanic Centre and the Taupo Volcanic Centre (Kohn and Topping, 1978; Nairn et al., 1998). The sources and distribution of the Rotoiti and Earthquake Flat eruptions are presented in Section 2.2.3. Within months of the eruption and emplacement of the caldera-forming Rotoiti pyroclastics, the Earthquake Flat pyroclastics were erupted. Charlier et al. (2003) presents U-Th disequilibrium age data that demonstrates the two pyroclastic deposits were erupted from "independent and unconnected magma bodies." As such, there is no evidence for the movement of subsurface magma between the two systems; instead, the eruptions are considered to be linked by a network of regional northeast-southwest tectonic faults. Specifically, the localised collapse of the Rotoiti caldera possibly perturbed the existing stress field and triggered an eruption, ~ 20 km away, by regional tectonic readjustment. Regional tectonic readjustment associated with caldera collapse has been documented in southern Kyushu, Japan. The 6.5 ka eruption from Kikai caldera, 30 km offshore of Kagoshima Bay (Fig. 2.29), activated regional fault structures and triggered large-scale earthquakes (Naruo and Kobayashi, 2002). Conspicuous and numerous clastic dykes have been described in southern Kyushu, penetrating the ignimbrite and co-ignimbrite ash from the Kikai caldera eruption, immediately following their emplacement (Naruo and Kobayashi, 2002). These clastic dykes provide evidence for ground-shaking and the liquefaction of underlying sediments as a consequence to large-scale earthquakes (Naruo and Kobayashi, 2002).

The other TVZ example of temporally linked volcanic activity is the ~ 10 ka eruptions from the Tongariro and Taupo Volcanic Centres (Figure 1.2). The Tongariro and Taupo eruptions occurred on a longer time scale, possibly over centuries (Kohn and Topping, 1978), than the Rotoiti-Earthquake flat example; nonetheless, these eruptions suggest that there was an intrinsic link with regional tectonics (see Nairn et al., 1998). Kohn and Topping (1978) present stratigraphic evidence for a succession of pyroclastic eruptions, alternating between these two volcanic centres which are ~ 50 km apart. Eruptions at both centres were associated with multiple linear vents consistent with the NNE-SSW regional fault pattern. In particular, the Tongariro eruptions tapped multiple magma bodies along a 20 km long, en-echelon, linear vent zone (Nairn et al., 1998; Nakagawa et al., 1998). The eruptions from Tongariro and Taupo are believed to be associated with a period of "accelerated regional extension" at the southern end of the TVZ (Nairn et al., 1998). It is probable the eruption sequence and displacement on regional graben faults (Nairn et al., 1998) were triggered by tectonic readjustment associated with an episode of accelerated rifting.

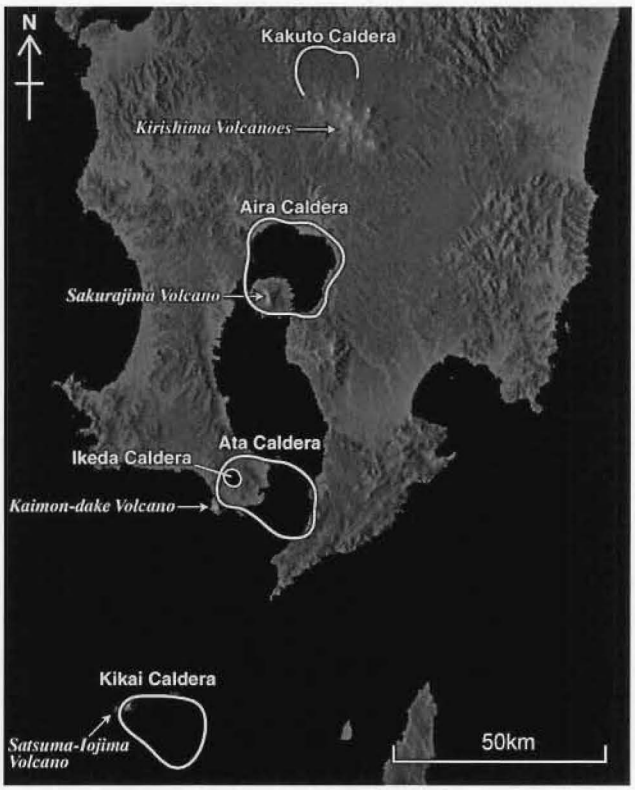

Figure 2.27 NE-SW alignment of calderas within the Kagoshima graben in southern Kyushu, Japan, from Kobayashi et al. (2003).

Tectonically linked eruptions have also been documented in Japan (southern Kyushu and Hokkaido) and the western United States. The tectonic setting of southern Kyushu is very similar to the Taupo Volcanic Zone, with contemporaneous subduction- and extensional-related volcanism. In the Quaternary, volcanism has been concentrated in the Kagoshima graben (a NNE-SSW regional structure) which defines the eastern margin of the Okinawa trough, a large volcanotectonic depression (Kobayashi et al., 1988; 2003). Like the TVZ, the Kagoshima graben encompasses several caldera volcanoes including Kakuto, Aira, and Ata calderas and the offshore Kikai caldera (Figure 2.27). The intimate volcanotectonic relationship within the Kagoshima graben has translated into a high frequency of eruptions, with 8 pyroclastic eruptions in the last 100 ka from Aira caldera alone (Kobayashi et al., 1988), including simultaneous eruptions from multiple vents. New data for the 24.5 ka eruption within the Aira caldera, suggests the Ito ignimbrite was deposited in the final phase of an eruption sequence that migrated from an initial southwest vent to a northeast vent location (Fukushima and Kobayashi, 2003). The eruption sequence commenced with the plinian eruption of the Osumi pumice (98 km^3) and the intra-plinian Lower-Tsumaya ignimbrite (Phase 1) from a source vent coincident with the present day Sakurajima volcano, followed by the emplacement of the Upper-Tsumaya ignimbrite (Phase 2) erupted from the same vent, and after a short time break culminated in the eruption and emplacement of the Ito ignimbrite (Phase 3) from the initial vent site and a vent in the northeast of the caldera (Fukushima and Kobayashi, 2003; Kobayashi et

al., 2003). Fukushima and Kobayashi (2003) suggest both vents were erupting simultaneously. A tectonic linkage of multiple caldera vents has not been suggested in the most recent Aira literature; however, it is possible that such a tectonic relationship exists considering that the northeast-southwest trend of the proposed vents is sub-parallel to the regional tectonic grain of the Kagoshima graben.

Further south, but still within the Kagoshima graben, a 5.7 ka eruption sequence from the Ibusuki volcanic area, within the Ata caldera, is also characterised by eruptions from multiple vent sources (Figure 2.28). The deposits from this sequence indicate a complex sequence of events beginning with phreatic activity that evolved into magmatic activity and culminated in the collapse and formation of the ~ 4 km wide Ikeda caldera (Kobayashi et al., 2003). Following the caldera collapse, five aligned maar structures were formed, including a particularly explosive eruption from the Yamakawa maar in which thick base surge deposits were emplaced (T. Kobayashi, pers. comm., 2003). Activity then returned to the initial Ikeda caldera source as the Ikedako phreatomagmatic ash was erupted (T. Kobayashi, pers. comm., 2003). In similar fashion to the Rotoiti caldera collapse and Earthquake Flat eruption in the central TVZ, the collapse of the Ikeda caldera may have altered the local or regional stress field, causing tectonic readjustment and triggering eruptions from the five maar vents.

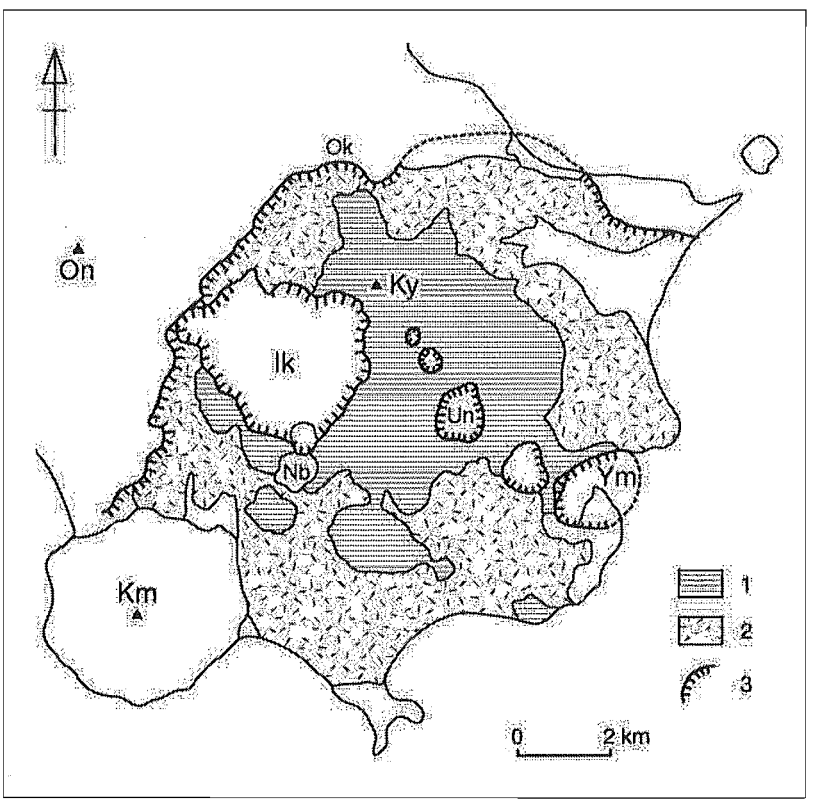

Figure 2.28 Ibuski volcanic area and the structural boundaries of the Ikeda caldera (Ik) and associated maar volcanoes including Yamakawa (Ym), from Kobayashi et al. (2003).

At Shikotsu caldera, southwestern Hokkaido, Japan, Nakagawa et al. (2003) provide petrological evidence suggesting that the 40 ka caldera-forming event (> 200 km^3) was associated with multiple, simultaneously erupting vents. As opposed to tapping a single large magma chamber underlying the caldera, "compositional distribution of phenocrystic minerals, trace element chemistry of plagioclase and orthopyroxene, and whole rock chemistry" suggest each vent tapped a distinct magma chamber in a fissure-like eruption (Nakagawa et al., 2003; M. Nakagawa, pers. comm., 2003). At Long Valley caldera in the western United States, Wilson and Hildreth (1997) provide physical stratigraphic evidence for coeval eruptions from more than one vent site during the 0.76 Ma eruption of the Bishop Tuff. The 0.76 Ma eruption began in the south-southeastern part of the caldera (Hildreth and Mahood, 1986) and was followed by a short break before eruptive activity resumed at the initial source area and from vent(s) in the northwestern part of the caldera (Wilson and Hildreth, 1997). Stratigraphic evidence confirms the northwest and southeast source areas consisted of multiple vents that were erupting simultaneously and that compositionally distinct pumice types characterise their respective pyroclastic products, i.e. airfall and ignimbrite packages. Wilson and Hildreth (1997) suggest that the stratigraphy, combined with the variation in pumice compositions, may not support a simple model for withdrawal from a vertically zoned magma reservoir (Hildreth, 1979), and that further examination may reveal a lateral juxtaposition of chemically distinct magma bodies, i.e. lateral variation in a large magma reservoir, or possibly multiple reservoirs (similar to Shikotsu caldera). In addition, Wilson and Hildreth (1997) imply that the coeval eruptions in the southeast and northwest portions of the caldera and the initiation of collapse may have been somewhat controlled by regional tectonics. Today, these two source areas are connected by several active strands of the NW-SE trending Hilton Creek fault which is a major extensional fault associated with the front of the Sierra Nevada mountain range (Bailey et al., 1976).

From the above examples it is clear that, particularly in extensional settings, tectonics play a vital role in caldera volcanism and volcanism in general. The role tectonics play may manifest itself as a complex network of regional fault structures with adjustable stress fields or more simply as a linear structure or fissure providing a conduit for the ascent of magma. I infer that the multi-phase eruption sequence between Rotorua and Ohakuri calderas was tectonically linked and that the sequence is comparable to other documented eruptions in the TVZ, Japan, and the USA. The question is how were the eruptions from these two calderas linked, specifically phase 3 and 4 (see Section 2.2.2) of the eruption sequence? Although the alignment of the Rotorua and Ohakuri calderas is sub-parallel to the regional northeast-southwest structural trend within the central TVZ, it is unlikely that phase 3 and 4 were associated with a large-scale fissure event similar to the caldera-forming Shikotsu eruption in Hokkaido, Japan. The distance between the Rotorua and Ohakuri calderas (~ 25 km) is similar to the distance between the southsoutheast and northwest source vent areas associated with

the 0.76 Ma Long Valley eruption. In addition, there is no evidence for contemporaneous source vents between the Rotorua and Ohakuri calderas, nor between the vent areas at Long Valley. As a result, I suggest that phase 3 and 4 of the eruption sequence are similar to the ~ 62 ka Rotoiti and Earthquake Flat eruption sequence, and the linkage between the two caldera-forming events were most likely associated with regional tectonic readjustment.

Volcanotectonic faults: tectonic response to caldera-volcanism

It has been established above that tectonics play an integral role in caldera volcanism in extensional settings; however, caldera volcanism plays an equally important role in tectonics. In particular, caldera volcanism is fundamental in triggering volcanotectonic faulting. Branney and Kokelaar (1994) provide a thorough and useful definition for volcanotectonic faults:

> "... a fault whose displacement was intimately associated with subsurface movement or eruption of magma. This use includes faults due to gravitational instability created by magma movement and excludes faults solely due to regional stress, which are also common in most volcanic fields. We recognise that many volcanotectonic faults originate as purely tectonic structures, and also that regional stresses are likely to be at least partly accommodated by faulting initiated by magma movement. Volcanotectonic fault movements accompany all moderate to large-scale volcanic eruptions and shallow magmatic intrusions. In contrast to regional tectonic faults, volcanotectonic faults characteristically are local in scale, are short-lived, and can involve very large and rapid vertical displacements (several hundreds of metres in the case of large-magnitude eruptions)."

At Scafell caldera in the English Lake District, Branney and Kokelaar (1994) discuss the rapid succession of eruption events, the activation of volcanotectonic faults, and piecemeal caldera collapse. The block-faulted floor of the Scafell caldera, as well as abrupt thickness and facies variations of the intra-caldera ignimbrites, provides evidence for multiple eruptive episodes and piecemeal collapse. Piecemeal collapse is considered to be rare and differs from the more conventional piston-style collapse which is characterised by the growth of ring faults and subsidence of a coherent caldera floor (Lipman, 1997). At Scafell, piecemeal collapse is controlled, partly, by regional northwest trending faults associated with an "immature continental crust" and rifting (Branney and Kokelaar, 1994). As such, some of the volcanotectonic faults active during the eruption sequence are parallel to the regional tectonic grain (Branney and Kokelaar, 1994).

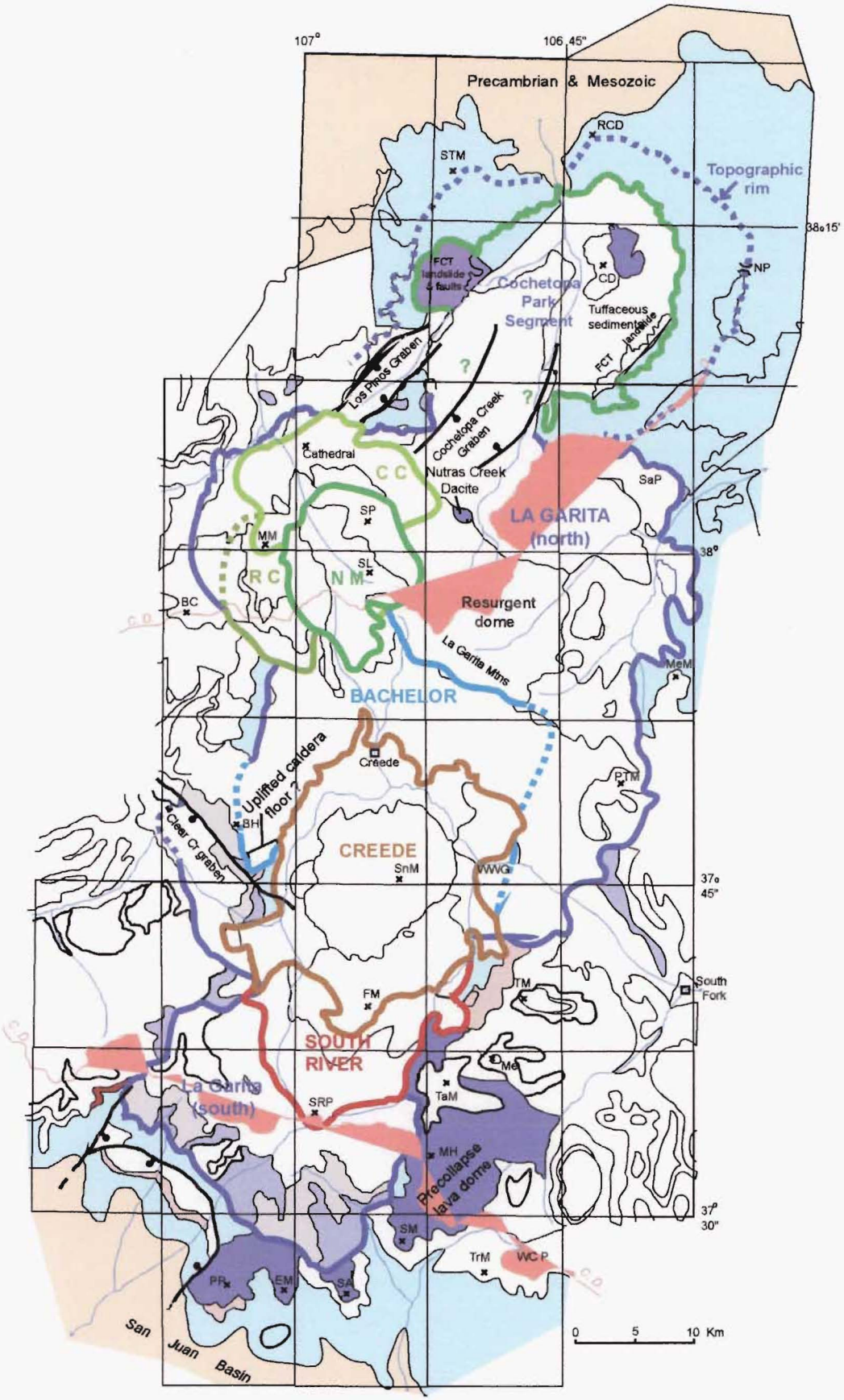

Figure 2.29 Geometry of the La Garita caldera and associated rocks (Lipman 2003). Cochetopa Park and the San Luis caldera complex (thick green boundaries) are at the north end of the La Garita caldera, and are connected by Cochetopa Creek graben.

Volcanotectonic faulting is not exclusively related to piecemeal collapse of a caldera and has been recently documented in the TVZ, New Zealand and in the San Juan volcanic field, western United States. Volcanotectonic faulting has been recognised outside the structural boundary of the collapsing caldera and is intimately linked to lateral migration or movement of magma. Lateral migration of magma and subsidence of an area distant from the eruptive vent source was first documented at Katmai volcano. The 1912 eruption from Novarupta volcano resulted in the collapse of the Katmai caldera ~ 10 km away (Hildreth, 1983). Magma beneath Katmai volcano is believed to have migrated laterally along a system of dykes connected to the Novarupta vent, and created space for non-eruptive subsidence (see Hildreth, 1983; Eichelberger and Izbekov, 2000). The total erupted volume of magma from the Novarupta vent was ~ 15 km^3 (Hildreth, 1983); however, much larger caldera eruptions involving the lateral migration of magma have been recently documented. In a new study Lipman (2003) suggests the Cochetopa Park caldera in the north-central San Juan volcanic field is actually a "passive (non-eruptive) subsidence" structure that collapsed during the ~ 26.5 Ma eruption of the Nelson Mountain Tuff (~ 500 km^3) from the San Luis caldera complex 30 km to the southwest (Figure 2.29). In this large-scale caldera-forming event, magma moved along a southwest trending dike system, "expressed at the surface by a large graben," from beneath the Cochetopa Park area to the San Luis caldera complex (Lipman, 2003). Similarly, in the TVZ passive subsidence is inferred to have occurred, expressed as a large asymmetric graben, due to lateral withdrawal of magma associated with the 26.5 ka Oruanui eruption (~ 530 km^3 DRE) (Wilson, 2001). Specifically, magma beneath an area southwest of the structural caldera may have migrated laterally to the northeast and been erupted from other vents (C.J.N. Wilson, pers. comm., 2003), triggering synvolcanic displacement (> 400 m) along a pre-existing regional fault, the Waihi Fault (Wilson, 2001; see Figure 2.30).

Like Scafell, the Cochetopa Park and Taupo caldera examples involve the activation of volcanotectonic faults; however, at Cochetopa and Taupo, volcanotectonic faulting is on a much larger scale and is exclusively related to the regional tectonic grain. Thus, I have expanded Branney and Kokelaar's (1994) definition for volcanotectonic faulting to include regional scale faulting associated with the lateral migration of magma. Lateral movement of magma and volcanotectonic faulting in extensional settings raise some interesting questions: 1) does regional tectonic structure control the shape, size, and location of magma bodies? 2) how does regional tectonic structure control the connectivity and path between two distinct geographic areas? Although the answers to these questions are beyond the scope of this thesis, they are peripherally discussed with respect to withdrawal and lateral migration of magma during phase 4 of the Rotorua and Ohakuri caldera eruption sequence.

In summary, phase 3 and 4 of the Rotorua-Ohakuri eruption sequence involved the simultaneous eruptions of unit 3 from the Ohakuri caldera and the caldera-forming Mamaku ignimbrite from Rotorua, followed by the Ohakuri caldera-forming eruption. There is sufficient evidence to suggest that the Ohakuri caldera-forming eruption was associated with volcanotectonic faulting (i.e. movement of magma) that resulted in most of the ~ 400 m vertical

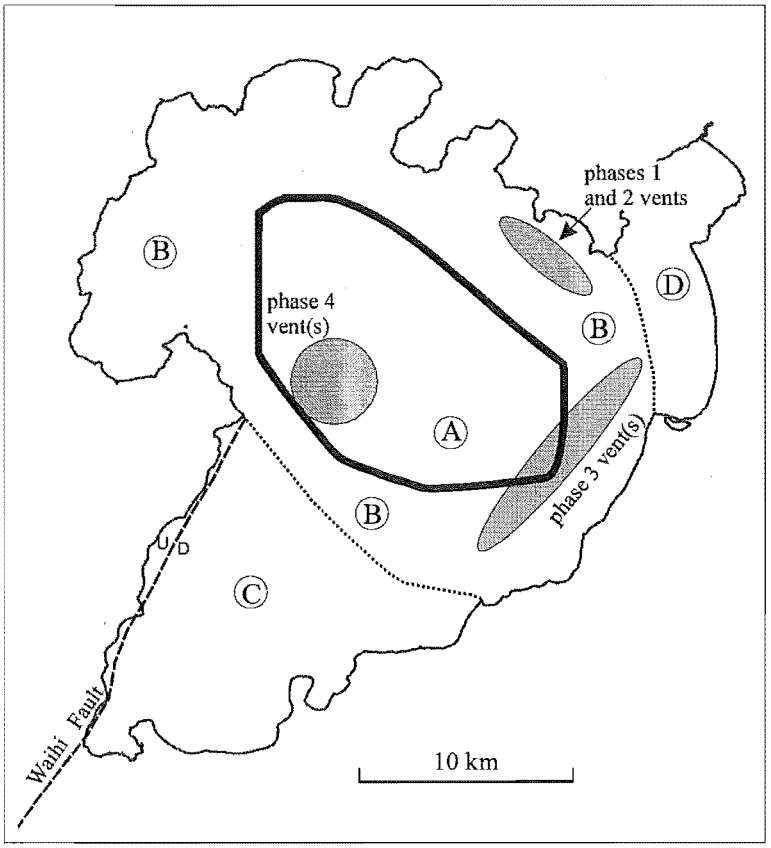

Figure 2.30 26.5 ka Oruanui vent locations and the Taupo caldera, modified from Wilson (2001). Area 'C' is a graben structure associated with syn-volcanic subsidence along the Waihi Fault.

displacement along the Horohoro Fault (as previously mentioned in 'Phase 4' of Section 2.2.2; see Figure 2.16 and Figure 2.31). The origin of the Horohoro Fault scarp is controversial. It has been attributed to the collapse of an older caldera within the Kapenga composite structure, as well as being described as the structural margin of the Taupo Fault Belt (TFB). The fault truncates the Horohoro rhyolite dome which has an age of 222 ± 10 ka (Houghton et al., in prep), roughly the same age as the Mamaku ignimbrite; however, field evidence suggests that the dome predates the Mamaku ignimbrite (see 'Distribution of the Mamaku ignimbrite and the Ohakuri pyroclastic deposits' in Section 2.2.2). The Mamaku ignimbrite has approximately the same thickness (> 100 m) on either side of the fault (Milner, 2001), suggesting that the fault scarp cannot be related to an older caldera structure and has to be younger than the Mamaku ignimbrite. The question is, how much younger than the Mamaku ignimbrite is the Horohoro Fault scarp? There is little paleoseismic data available on the Horohoro Fault; however, Villamor and Berryman (2001) and P. Villamor (pers. comm., 2003) suggest that any

Figure 2.32 Oblique aerial views of the Horohoro Fault scarp

displacement on the Horohoro Fault is older than 20 ka and is not associated with their active, modern TFB (Figure 1.5). New paleogeographic evidence suggests that the majority of the Horohoro Fault displacement is much older than 20 ka and occurred immediately after the emplacement of the Mamaku ignimbrite.

The following discussion is based on the paleogeographic information presented in Section 2.2.2. Prior to the collapse of the Rotorua caldera, the area east of the Horohoro rhyolite dome was just as high or higher than the Mamaku Plateau. Following the collapse of the Rotorua caldera and the formation of an intra-caldera lake, it is probable that overtopping and a breach of the Mamaku ignimbrite dam occurred shortly thereafter (see Section 2.2.3). Marx et al. (2003) suggest that a catastrophic breach of the dam may have occurred at the southern end of the lake, which would indicate that the area to the south was topographically lower than the lake level. This topographic low to the south of the caldera occupies the same area that formed the topographic high prior to the Rotorua caldera collapse, suggesting that a large tectonic event took place within the short period of time between the caldera collapse and the breach of the caldera lake. I infer that the tectonic event was controlled by volcanotectonic faulting triggered by the collapse of the Ohakuri caldera. The magnitude of the vertical displacement (i.e. > 250 m vertical fault offset of the Mamaku ignimbrite) that occurred along the Horohoro Fault during this event is presumably too large to be associated with regional graben faulting (i.e. regional fault readjustment to the Rotorua caldera collapse). In addition, the Horohoro Fault is not a simple NE-SW (regional) linear feature, but instead it exhibits both linear and arcuate components (see Figure 2.31). As a result, I infer that volcanotectonic faulting associated with the Ohakuri caldera collapse may be analogous to the Cochetopa and Taupo examples i.e. lateral magma withdrawal and passive (non-eruptive) subsidence.

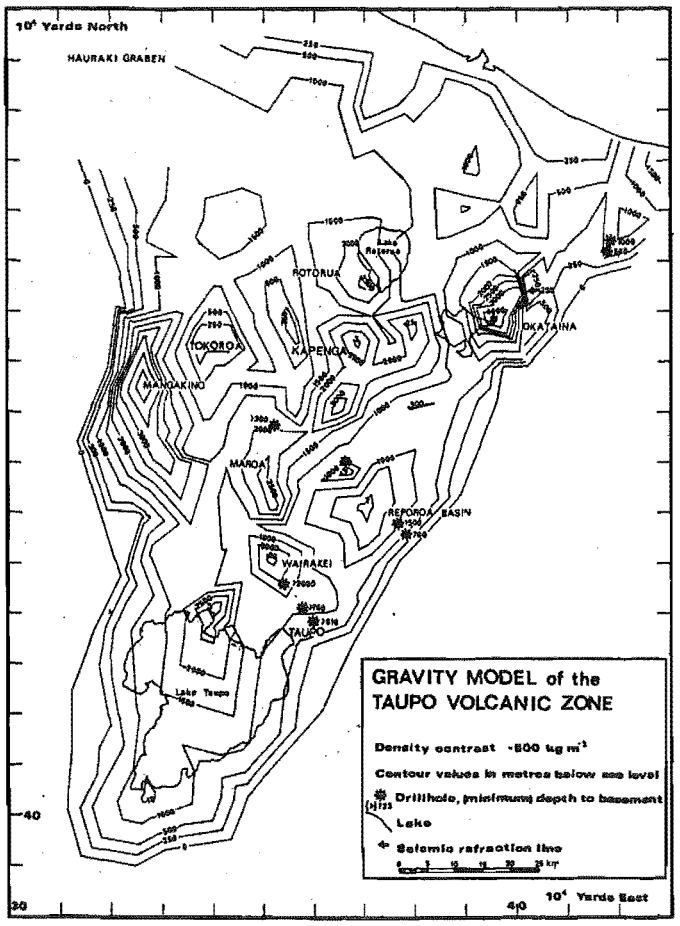

Figure 2.32 Gravity anomaly map of the TVZ, from Rogan (1982). The inferred Kapenga composite caldera combines the 3 negative anomalies in the Kapenga area (refer to text for interpretation).

The Horohoro Fault scarp is inferred by some to be the northwestern structural margin of the Kapenga composite caldera. Kapenga is a geophysically inferred composite caldera (Rogan, 1982) that, based on distinct gravity anomalies, can be divided into multiple collapse structures; a 2.5-km-deep northeast basin, and two 3-km-deep basins in the centre and the south (Wilson et al., 1984) (Figure 2.32). Evidence presented above confirms that the central basin, bounded on the west and northwest by the arcuate Horohoro Fault scarp, is not a caldera collapse feature. No caldera-forming deposits younger than the Mamaku ignimbrite have been erupted from this part of Kapenga and, therefore, I infer it to be analogous to the Cochetopa Park structure formed by passive (non-eruptive) subsidence. The implication is that magma was withdrawn laterally from beneath the central Kapenga area and migrated to the southwest, where it was erupted from the Ohakuri source. In a recently published residual gravity map of the TVZ (Figure 2.33), it is clear that a NE-SW elongate, graben structure exists between the central Kapenga subsidence structure and the Ohakuri caldera. However, it is not clear whether this graben structure represents an elongate southern continuation of the central Kapenga magma body, i.e. sill-like magma body (cf. disk-shaped holding chambers from Charlier et al., sub judice), or whether it formed from collapse over a lateral conduit system (cf. Lipman, 2003) where magma travelled from central Kapenga to the Ohakuri source.

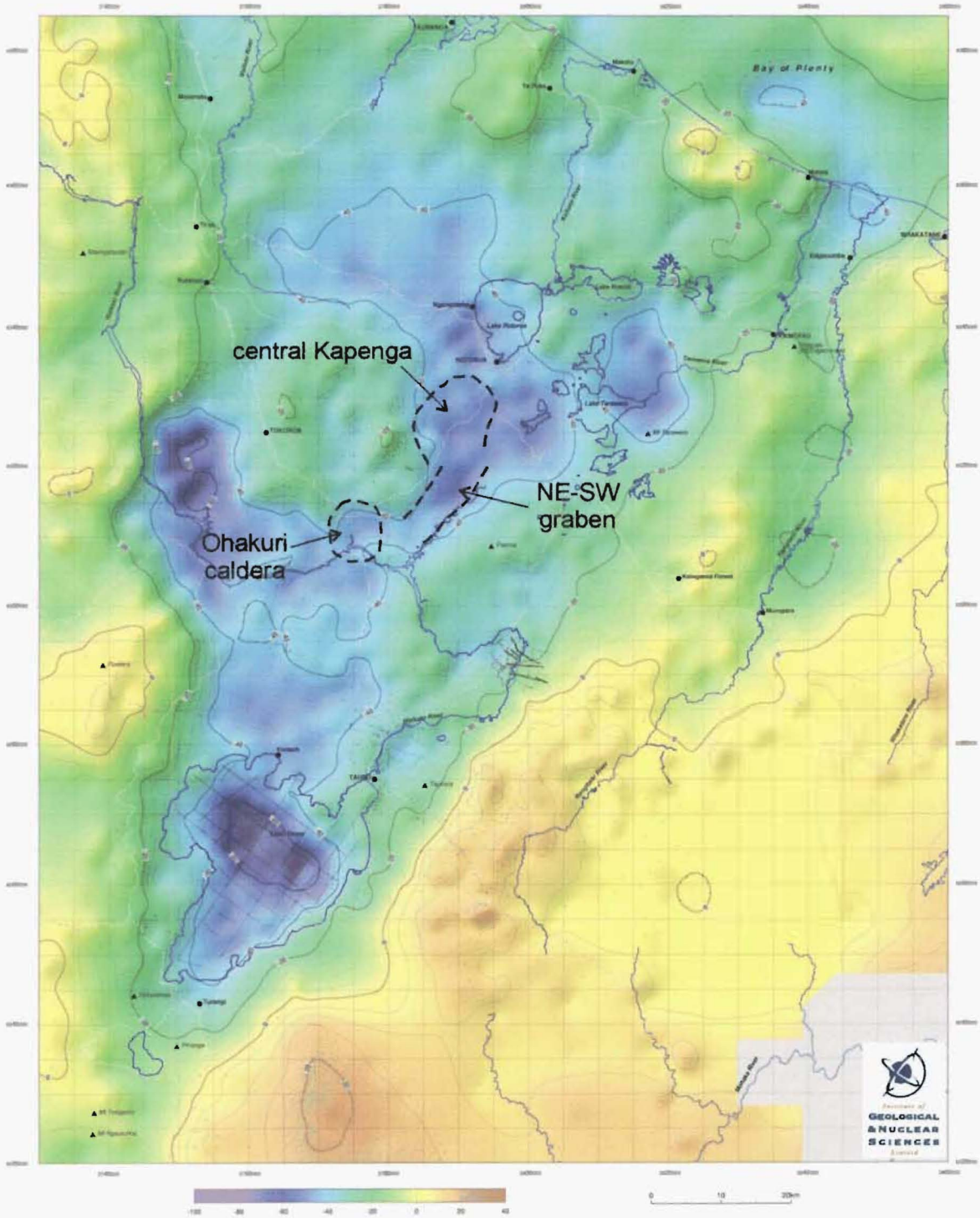

Figure 2.33 Residual gravity anomaly map of the TVZ (Stagpoole and Bibby, 1999). The blue areas represent gravity lows, some of which are coincident with caldera structures. Dashed lines have been drawn to show the inferred boundaries of the central Kapenga subsidence structure, the Ohakuri caldera and the elongate NE-SW structure between them.

Regardless, the NE-SW structure emphasises the inter-relationship between caldera volcanism and the regional tectonic structure. The lateral withdrawal of magma and the passive (non-eruptive) subsidence of the central Kapenga structure is discussed further in Chapter 3 with respect to geochemical and lithofacies data for the Ohakuri pyroclastic deposits.

The Cochetopa Park, Oruanui, and central Kapenga structures, as well as their graben-conduit systems, provide unique insight into the relationship between regional tectonics and magma sources and magma mobility. The elongate shape and inherent relationship with linear regional faults of these passive (non-eruptive) subsidence features suggest that the geometry of the magma bodies beneath them differ from equant magma reservoirs associated with sub-circular caldera structures, and probably reflect the existing tectonic basement structure and/or regional stress field. All 3 of these examples are associated with extensional tectonic settings which, to some extent, probably dictate the shape and size of the upper-crustal magma bodies. It is clear, that at least, the regional graben structures associated with passive subsidence features reflect the subsurface conduit systems responsible for lateral migration of magma. Much more research needs to be performed before we begin to really understand the intimate relationship between regional tectonic structure and magma reservoirs.

2.3.2 The newly recognised Ohakuri caldera

The Kapenga composite caldera and the Maroa Volcanic Centre (MVC) have been suggested by Langridge (1990) and Henneberger (1983), respectively, as the source for the Ohakuri pyroclastic deposits. With respect to Kapenga, Langridge (1990) describes 'surge-like' Ohakuri deposits in the area of the Tahunaatara stream (see Map 1), and inferred these to be proximal deposits erupted from the southwest end of the Kapenga composite caldera (i.e. the southern subsidence structure from Rogan, 1982; see Figure 2.32). However, in Chapter 3 (Section 3.6.4) I provide evidence that suggests an alternative and very localised origin for the 'surge-like' deposits in the Tahunaatara area that does not invoke an eruption from a primary volcanic source.

The MVC has also been inferred as the source for the Ohakuri pyroclastic deposits. However, age data from Leonard (2003) indicate that the two major dome lineaments in the central MVC are of similar or older ages than the adopted age for the Ohakuri pyroclastic deposits. In addition, the age data are supported by field observations of the Ohakuri pyroclastic deposits banking up against the central Maroa domes (Section 2.2.2). Although gravity data were used to suggest that the central MVC represents a caldera structure (e.g. Rogan, 1982; Wilson et al., 1984), the distribution of the Ohakuri pyroclastic deposits to the south and Leonard's (2003) age data preclude any putative caldera from being related to the Ohakuri event.

In this study, evidence presented strongly suggests the Ohakuri pyroclastic deposits come from a newly recognised caldera source, the Ohakuri caldera. It has been suggested by J.W. Cole (pers. comm., 1999), E.F. Lloyd (pers. comm., 2000) and C.P. Wood (pers. comm., 2000) that the present-day Whangapoa Basin (see Map 1) may be a depression associated with the eruption of the Ohakuri pyroclastic deposits. From the paleogeography cartoon maps it is clear that the area encompassed by the present day Whangapoa Basin has been a depocentre for volcaniclastic material as far back, potentially, as the ~ 275 ka caldera-forming Pokai eruption. Although the Whangapoa Basin is indirectly associated with the collapse of the Ohakuri caldera, its present manifestation by no means reflects the structural or topographical margin of the original caldera. The structural margin for the Ohakuri caldera cannot be determined with any accuracy, as ~ 240 k.y. of volcaniclastic deposition has buried any vestige. However, an approximate location for the caldera, between and possibly overlapping with the MVC and the inferred southern collapse structure of the Kapenga composite caldera, is inferred from the combination of: 1) remnants of the surrounding paleogeography immediately prior to the Ohakuri caldera collapse; 2) isopleth data for units 1, 2 and 3 in the Rotorua-Ohakuri eruption sequence; 3) paleo-flow directions for the Ohakuri PDC's; 4) drill core data; and 5) geophysical data. The formation of the Ohakuri caldera is discussed in Chapter 3.

Remnants of the surrounding paleogeography immediately prior to the Ohakuri caldera collapse

Prior to the collapse of the Ohakuri caldera there is evidence for surrounding high ground in the north, west and south, impounding a lake in the approximate area of the caldera. To the north, the current morphology has hardly changed from the paleotopography that existed just prior to the collapse of the Ohakuri caldera. The Mamaku ignimbrite forms a flat top surface covering the majority of the Mamaku plateau up to its southeastern edge; at this point there is an inflection where the Mamaku ignimbrite begins to slope to the southeast. Near Highway 1 (see Map 1, locality Oh147) the Mamaku ignimbrite is only a few 10's of metres above the base level of the Whangapoa Basin. Presumably, prior to the Mamaku eruption an eroded slope on the Pokai ignimbrite surface had formed due to runoff into a lake basin (Section 2.2.1) (Figure 2.4). The Mamaku ignimbrite and unit 3 from the Rotorua-Ohakuri eruption sequence were deposited simultaneously on the paleoslope (Section 2.2.2).

To the west, the backbone of the present day Northwest Dome Complex existed prior to the Ohakuri caldera collapse (see Section 2.2.1) (Figure 2.4). The Ohakuri pyroclastic deposits onlap parts of the Northwest Dome Complex (Figure 2.19) which impeded the Ohakuri PDC's from travelling further west. To the south, MVC rhyolite domes and lavas would have marked the maximum southern extent of a lake and at the same time would have provided a barrier for

the Ohakuri PDC's. Ohakuri PDC deposits are not exposed further south than the northeastern and southeastern ridges of the MVC (Figure 2.25).

Isopleth data for the Ohakuri airfall deposits

Maximum pumice and lithic data for units 1, 2, and 3 in the Rotorua-Ohakuri eruption sequence (Section 2.2.2) confirm a southerly volcanic source in the approximate area of the Ohakuri caldera. In addition, the phreatomagmatic character of units 1 and 2 suggest that magma came into contact with surface water of Lake Ohakuri (Section 2.2.1, Figure 2.4). The high juvenile obsidian content in unit 1 suggests an explosive, closed-vent eruption from a rhyolite dome source that may have been within the lake. Unit 2 does not have the same juvenile obsidian component and may be associated with a different vent source within the lake or a more open vent than the unit 1 source. Unit 3 has a similar distribution to units 1 and 2; however, there is no evidence for magma-water interaction.

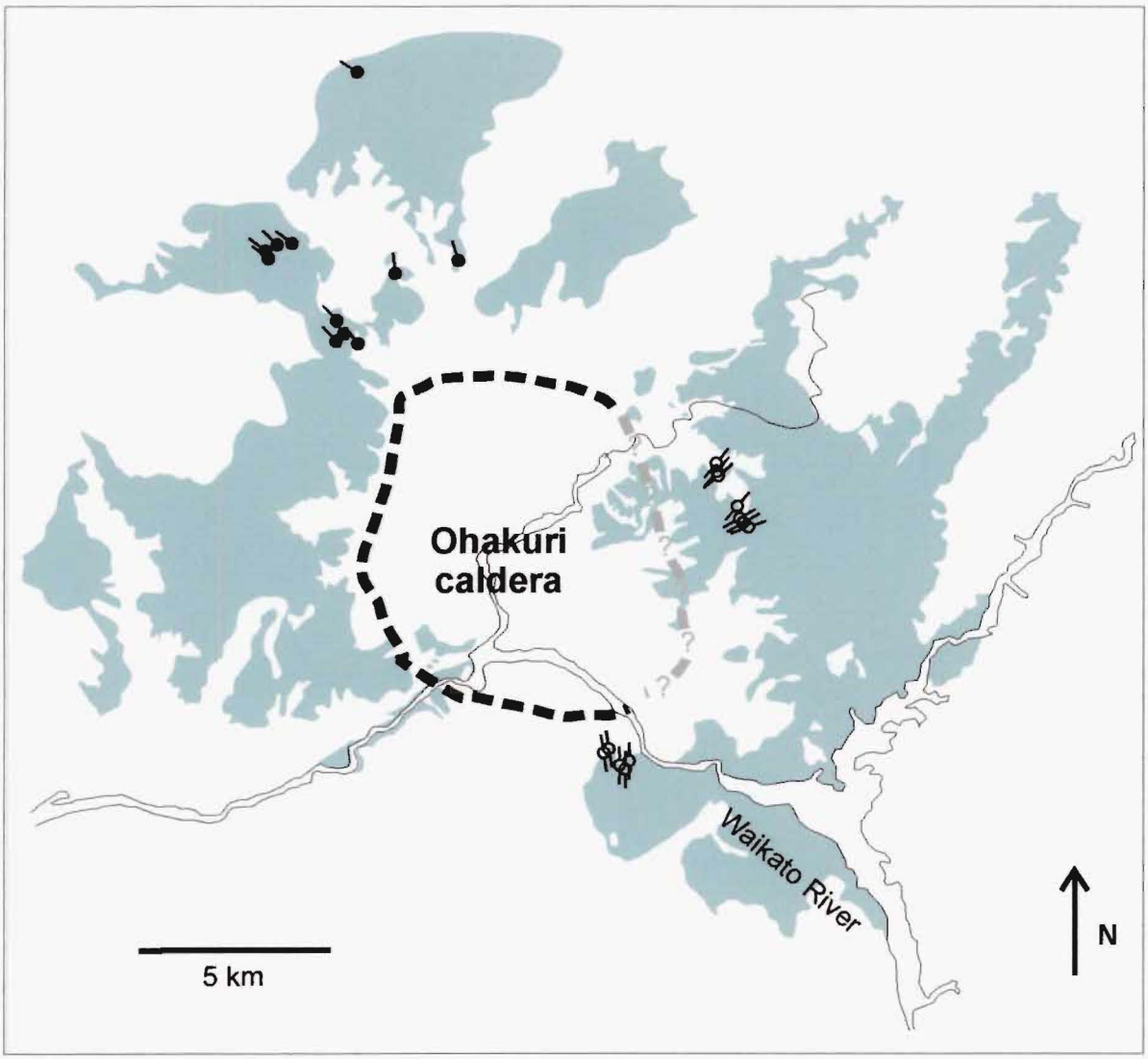

Figure 2.34 Paleoflow direction indicators observed in the Ohakuri pyroclastic deposits. Filled circles with one arm (pointing in the direction of flow) represent uni-directional indicators from dune structures. Open circles with two arms represent bi-directional indicators measured from channel structures.

Paleo-flow directions for the Ohakuri PDC's

Paleo-flow directions have been determined from dune-bedding and channel structures within the bedded lithofacies of proximal Ohakuri pyroclastic deposits (see Chapter 3 for a description of Ohakuri pyroclastic lithofacies). Although there is not much data, Figure 2.34 shows that uni-directional indicators from dune structures, and bi-directional indicators from channel structures reveal flow directions from an Ohakuri source area that are consistent with the isopleth data above.

Drill core data

In recent years the Ohakuri and Atiamuri areas have been explored for geothermal and epithermal prospects. Geothermal investigations included one well (AT1), while almost 50 holes have been drilled by 4 different companies interested in epithermal gold. With respect to the Ohakuri pyroclastic deposits, a summary of the core recovered from geothermal well AT1 and from one Delta Gold drill hole (OHDG-3) is presented below. AT1 (U16/758101) is located within the Whangapoa Basin and the inferred Ohakuri caldera and OHDG-3 (U17/797076) is located at the inferred east-northeast margin of the caldera (see Map 1).

Both E.F. Lloyd and C.P. Wood (of the then Department of Scientific and Industrial Research, DSIR) described the core from AT-1. In an unpublished DSIR report, C.P. Wood suggests that the stratigraphic sequence from 121 m to the total depth of 608 m represents one pyroclastic unit characterised by 'co-magmatic ash and lapilli flow deposits'. C.P. Wood also describes a lithic rich breccia (between 440 and 448 m depth) with cobbles of rhyolite lava in a lapilli tuff matrix identical to the matrix in the pyroclastic deposits above and below. E.F. Lloyd and C.P. Wood (pers. comm., 2000) are confident that the pyroclastic unit correlates best with the Ohakuri pyroclastic deposits. The location of AT1 within the Whangapoa Basin and the significant depth of the Ohakuri pyroclastic deposits correlate well with the isopleth, paleo-flow, and geophysical data. I therefore infer the AT1 Ohakuri pyroclastic deposits to be intra-caldera deposits.

The core from OHDG-3, held at the Crown Mineral core shed in Paeroa, has been re-logged as part of this thesis. The Ohakuri pyroclastic deposits are observed from ~ 79 m to a total depth of 498 m, and are depicted in a schematic log (Appendix 5) that depicts a vertical variation in lithologies, including massive, diffusely stratified, and bedded deposits. The core also reveals hydrothermal brecciation zones and fault zones.

Geophysical data

Geophysical data alone cannot be used to delineate caldera sources. However, combined with geologic evidence (i.e. isopleth data, paleo-flow directions, and drill core), geophysical

information can be very useful. In the central TVZ, one of the more useful techniques for visualising subsurface anomalies in the upper crust is residual gravity. Figure 2.33 is a recently published residual gravity anomaly map compiled and produced by Stagpoole and Bibby (1999). The map shows a clear gravity low in the same area inferred to be the Ohakuri caldera from geologic evidence.

2.4 Conclusions

The central TVZ has erupted ≥ 15,000 km^3 of rhyolitic magma in 1.6 m.y. which equals an eruption rate of ~ 0.30 m^3s^{-1} (Houghton et al., 1995; Wilson et al., 1995). This rate is one of the highest documented on earth for a silicic system; higher than the eruption rates for the Platoro caldera complex, 0.073 m^3s^{-1} (Lipman et al., 1996); San Juan caldera cluster, 0.13 m^3s^{-1} (Lipman et al., 1996); and Yellowstone, 0.1 m^3s^{-1} (Wilson et al., 1984) put together. It is a unique system that is characterised by smaller and more frequent caldera-forming eruptions than its North American counterparts. Houghton et al. (1995) found that caldera-forming eruptions in the central TVZ cluster into short episodic periods, separated by large time gaps (Figure 1.4). These episodic periods are characterised by a remarkably high frequency of caldera collapse events and of particular interest to this thesis is Houghton et al.'s (1995) eruptive period IIIB from 280 ka to 150 ka. By reconstructing the paleogeography, with new age data and fieldwork findings from within the Rotorua-Ohakuri volcanotectonic depression, I have modified the eruptive period IIIB and recognised a sub-period (~ 280 ka to ~ 230 ka) characterised by 6 caldera-forming events (Figure 2.1). The close of this period was particularly vigorous with 4 of the 6 caldera-forming events occurring between ~ 240 and 230 ka. From ~ 240 to 230 ka the Kaingaroa ignimbrite erupted from the Reporoa caldera, the Mokai ignimbrite erupted from an unknown source probably within the Whakamaru caldera, and the Rotorua and Ohakuri calderas erupted in a rapid sequence of events that culminated in the emplacement of the Mamaku and Ohakuri ignimbrites. The stratigraphic relationship between these 4 deposits is problematic with the exception of the Mamaku ignimbrite and the Ohakuri pyroclastic deposits.

The frequency of the Rotorua-Ohakuri events indicates that within the TVZ and possibly other complex caldera systems worldwide, statistical averages for the frequency of caldera collapse may be, in some cases, obscuring the clustering of such events. In addition, statistical averages for caldera collapse frequencies may be disguising the intimate volcanotectonic relationship associated with the clustering of these collapses. Is the frequency of caldera collapses in the central TVZ, and in particular the rapid succession of events at Rotorua and Ohakuri calderas, unique to extensional tectonic settings? Calderas like Scafell caldera in the English Lake District, the Kagoshima graben calderas in southern Kyushu, and the 'central TVZ caldera complex', all overlie thin, rifted continental crust. As such, active rifting may facilitate

injection of magma into crustal reservoirs, regional tectonic response or readjustment associated with caldera eruptions, and lateral migration of magma within the crust causing the growth of regional volcanotectonic faults and passive (non-eruptive) subsidence. The result could be an increase in the frequency of caldera eruptions and subsidence, with the penecontemporaneous collapse of Rotorua and Ohakuri calderas being the extreme example.

The intimacy of caldera volcanism and tectonics raises a few questions that could provoke future research.

1. *Should the central TVZ be considered a large area that encompasses several unassociated caldera centres, or could it be considered one large composite caldera volcano that encompasses several smaller collapse features (Wilson et al., 1995)?*

Wilson et al. (1995) suggested that these two end-member models for the central TVZ could not be distinguished based on available data. The term 'caldera' has been used by many volcanologists to define subsidence structures with multiple genetic origins (Cole et al., in press). As a result, confusion has arisen over what is and what is not a caldera. The most recent definitions for caldera (see Chapter 1) imply subsidence or collapse into the top of a magma chamber; however, none of these definitions include constraints on the geometry of the underlying magma body or the possibility of multiple magma bodies. The definition also does not distinguish between single collapse caldera structures, compound caldera structures (multiple, temporally-linked, overlapping depressions), and composite calderas or caldera complexes (confocal or overlapping depressions that are not temporally-linked). From recent caldera studies, researchers are beginning to recognise that not all large ignimbrite calderas are associated with "equant upper-crustal magma reservoirs" (Lipman, 2003), and many calderas may be associated with irregularly shaped magma bodies or multiple magma bodies (Branney and Kokelaar, 1994; Lipman, 1997; Lipman, 2000a; Lipman, 2003; Nakagawa et al., 2003; Cole et al., in press). In the case of Scafell caldera, multiple magma bodies and the rapid succession of eruptions led to several localised subsidence structures that are encompassed by what Branney and Kokelaar (1994) refer to as a single, piecemeal caldera. Shikotsu caldera in Hokkaido, Japan is also a collapse feature that resulted from simultaneous eruptions associated with several distinct magma bodies. Branney and Kokelaar (1994) suggest that it is the rapid nature of the successive eruptions that qualifies these examples as a single caldera. This poses the question: how much time needs to elapse between collapse events to distinguish between a single caldera and a compound caldera? The central TVZ, as previously discussed, is characterised by episodicity with respect to caldera collapse eruptions. Within the recognised episodes of activity there are clusters of caldera collapse events, the ~ 240 ka example being a significant clustering event. Within approximately ten thousand years, 4 calderas collapsed in

an area encompassing approximately half of the central TVZ. Although each of these caldera structures are geographically distinct, do they qualify as localised depressions within a large caldera envelope similar to the Scafell example? If thousands of years between caldera collapse events are not rapid enough to qualify these localised collapses as a single caldera, what about the almost simultaneous collapse of the Rotorua caldera, Ohakuri caldera, and the central Kapenga region? The rapid succession of subsidence events associated with the Rotorua-Ohakuri eruptive sequence may provide useful data for Wilson et al.'s (1995) original argument of whether the central TVZ is a large composite caldera or not. The answer to this question may be a semantic issue but it is clear that the term caldera needs further refining with respect to magma body or bodies, and time elapsed between collapse events.

2. *In extensional environments, how does regional tectonic structure control the shape, size and location of magma reservoirs associated with caldera volcanism?*

A brief discussion related to this question has been presented above at the end of Section 2.3.1. In summary, passive (non-eruptive) subsidence structures could provide valuable insight into the relationship between magma reservoir geometry and regional tectonics. Consistent with most caldera research, the recognition and study of deeply eroded calderas and passive subsidence structures may provide the most useful information and answers. In addition, single crystal geochemistry is becoming a useful tool for constraining the physical properties of magma reservoirs (see discussion below for question 3).

3. *How do magma residence times beneath calderas differ in active rifting environments compared to continental environments with older and considerably thicker crusts?*

With respect to large silicic magma chambers associated with catastrophic caldera-forming eruptions, Jellinek and DePaolo (2003) suggest that magma must accumulate over periods of 10^5 to 10^6 years. Their model for the origin of these large-scale magma chambers correlates well with some of the large North American caldera systems, such as the San Juan Mountains in Colorado where caldera eruption periodicities are 10's to 100's of thousands of years (see Lipman, 1997). However, their model may not be so applicable to the Taupo Volcanic Zone (TVZ) where the frequency of caldera eruptions is much higher. New U-Pb and U-Th zircon age data from Taupo volcano in New Zealand suggest that large quantities of magma (~ 530 km^3) erupted in the 26.5 ka Oruanui caldera-forming event accumulated in a holding chamber within ~ 17 kyr prior to eruption (Charlier et al., sub judice). The inference is not only that magma must have been generated rapidly from a source zone, but that magma chambers are relatively negligible during periods of volcanic quiescence and may not become important until just prior (on a geologic time-scale) to the eruption event (Charlier et al., sub judice). Could the tectonic

structure of the extensional TVZ environment be facilitating such rapid accumulation rates; and, are rapid accumulation rates associated with more frequent caldera eruptions or, possibly, temporally-linked events (i.e. the Rotorua and Ohakuri caldera-forming eruptions)?

Does the idea of applying slip rates to regional faults in an extensional, volcanotectonic setting need to be reviewed?

Spray (1997) provides evidence for what he terms a 'superfault' which is a fault characterised by a displacement of ≥ 100 m during a single slip event. Types of superfaults include faults associated with slope instabilities, hypervelocity impacts, and caldera collapse (Spray, 1997). I suggest, here, that the growth of volcanotectonic faults such as the Horohoro Fault (> 250 m of vertical displacement that occurred during a single slip event associated with the lateral withdrawal of magma from beneath central Kapenga) should be considered a type of superfault. Because of the close relationship between volcanism and tectonics in the central TVZ, it is possible that more volcanotectonic superfaults may exist (e.g. the Waihi Fault) and some of these may be regional fault structures that have been assigned a slip rate (i.e. the Paeroa Fault). It is clear that the application of slip rates in the active volcanotectonic setting of the central TVZ may be obscuring large single slip events associated with the movement of magma.

3 Ohakuri pyroclastic deposits

3.1 Introduction

The study of Quaternary calderas in active volcanotectonic regions, such as central TVZ and the Kagoshima graben, can be difficult due to poor preservation of the caldera and its eruption products. In active volcanotectonic regions the surface expression of calderas is often obscured (Lipman, 1997) and the original geometry and distribution of pyroclastic deposits may be modified by faulting (e.g. Bailey and Carr, 1994), erosion, and/or high sedimentation rates (e.g. Smith, 1991a; Smith, 1991b). Additional problems arise in reconstructing eruptive histories of calderas in ancient volcanic successions (e.g. McPhie, 1986; Branney, 1991; Riggs and Busby-Spera, 1991) which, in some cases, have been subjected to one or more episodes of tectonic deformation, hydrothermal alteration, and metamorphism (e.g. McPhie, 1987). In ancient volcanic successions the full set of indicators (lithology, depositional structures, context, geometry, and distribution), or 'facies descriptors' as Cas and Wright (1987) refer to them, is incomplete and therefore determining volcanic vent locations and investigating the genetic origin of pyroclastic deposits may be problematic (McPhie, 1984; Cas and Wright, 1987).

The Ohakuri pyroclastic deposits are unusual because they are a deposit of Quaternary age but resemble an ancient one in several respects. In the ~ 240 kyr since their emplacement, the Ohakuri pyroclastic deposits have been faulted, eroded, silicified, and hydrothermally altered. Consequently, their present-day geometry and distribution provide few obvious clues into their mode of emplacement and the location of vent sites. In order to glean as much information with respect to the origin of the Ohakuri pyroclastic deposits, I describe the deposits within a sedimentological lithofacies framework (cf. Reading, 1986; Cas and Wright, 1987). Based on variations in structural and lithological properties, the Ohakuri pyroclastic deposits can be divided into 7 lithofacies (4 massive and 3 bedded). Furthermore, by evaluating the geometry and the context of these 7 lithofacies, they can be grouped into 5 lithofacies associations.

With respect to the Ohakuri pyroclastic deposits, some background information has already been presented including the previous work (see Chapter 1), and the caldera source, age, and distribution (see Chapter 2). In this chapter, more background information is given including the general lithology and the volume of the Ohakuri pyroclastic deposits (Section 3.2), then a summary of the Ohakuri geochemistry is presented (Section 3.3), followed by a description of the lithofacies (Section 3.4) and lithofacies associations (Section 3.5). The lithofacies and lithofacies associations, together with geochemical fingerprinting of the Ohakuri pyroclastic deposits, provide enough information to determine: 1) the modes of emplacement for the unique

lithofacies (Section 3.5); 2) the depositional environments associated with some of the lithofacies associations (Section 3.5); and 3) inferences into the Ohakuri eruption sequence and dynamics, and the formation of the Ohakuri caldera (Section 3.6).

3.2 Background

3.2.1 General lithology

The following generalised lithological description is based on primary pyroclastic density current (PDC) deposits which comprise > 90 vol% of the Ohakuri pyroclastic deposits. Fresh, unaltered deposits are nonwelded, buff to light gray coloured and moderately compacted (chunks can be excavated by a hammer and broken apart along grain boundaries by hand), whereas weathered and/or hydrothermally altered deposits are yellowish in colour and have a characteristic silica case-hardened crust. The Ohakuri PDC deposits consist primarily of pumice, lithic, ash, and free crystals, and the clast to matrix ratio used in this thesis is based on the lapilli to ash size boundary (ratio of grains > 2 mm versus grains < 2 mm; e.g. Cas and Wright, 1987). Clast and matrix componentry is determined by comparing a ~ 1 m^2 area of an individual outcrop (in the field) with a grainsize percentage chart. For example, pumice clasts comprise 15 to 30 areal% of the Ohakuri deposits (rarely < 10 areal% or > 40 areal%) based on a 1 m^2 area of an individual outcrop. From the 'areal%', a volume percent is inferred and is quoted as 'vol%' below.

Ohakuri pumice clasts are generally < 20 mm in diameter (but are observed up to 400 mm across), rounded to subrounded, gray to white, and moderately to highly vesicular with elongated fine vesicles that give the pumice a fibrous texture and often a woody or streaky appearance. In thin section, the pumice clasts are generally crystal poor, 1 to 5 vol% phenocrysts; however, some pumices contain 10 to 15 vol% phenocrysts. The phenocryst assemblage, in order of decreasing abundance, is plagioclase feldspar, quartz, orthopyroxene, and opaque minerals (see Section 3.3). The more crystal-rich pumice clasts also contain minor amounts of hornblende.

The PDC deposits are lithic-poor, typically < 1 vol% but occasionally up to 5 vol%. Lithic lithologies include devitrified rhyolite lava (flow-banded and spherulitic varieties), obsidian, ignimbrite, and rare granophyric intrusive clasts. Compared to pumice, lithic clasts are generally smaller, mostly < 10 mm but occasionally as large as 200 mm. The matrix is composed of fine to coarse ash with minor amounts of crystals (mostly plagioclase feldspar and quartz).

3.2.2 Volume

Later erosion, sedimentation, tectonic overprinting, and volcanic events make it impossible to calculate the original volume of the Ohakuri pyroclastic deposits with any precision. However, simple calculations provide approximate minimum and maximum volumes based on the area covered by the pyroclastics and thicknesses observed from surface exposure and drill core data. The Ohakuri pyroclastic deposits cover ~ 500 km^2, range in thickness from > 600 m to < 20 m, and have an average observed thickness of 100 m. This provides a minimum volume estimate of ~ 50 km^3. For the maximum value, I have assumed a uniform linear wedge of material from a proximal depth of > 600 m to a distal depth of 0 m for the area east of the Ohakuri caldera and then added the volumes for the areas where the base of the Ohakuri pyroclastic deposits are observed. This calculation is based on the sequence of eruption events described in Section 3.7.3, and provides a maximum volume estimate of 120 km^3 (~ 100 km^3 Dense Rock Equivalent, DRE). The relatively high DRE value takes into account the deep burial of deposits to the east of the Ohakuri caldera.

3.3 Geochemistry

Geochemical analyses for the Ohakuri pyroclastic deposits include XRF pumice chemistry, and Sr isotope analysis. The geochemical analyses have been performed to: 1) characterise juvenile clast compositions of the Ohakuri pyroclastic deposits, in order to compare with the immediately preceding Mamaku ignimbrite; 2) fingerprint any variability in juvenile compositions with respect to stratigraphic position and/or geographic distribution; and 3) help interpret the Ohakuri eruption sequence and dynamics.

3.3.1 XRF pumice chemistry

Major and trace element chemistries have been determined for 129 Ohakuri pumice clasts, including 29 analyses from S.D. Weaver and B.F. Houghton (unpublished data). All major and trace element data for the Ohakuri pyroclastic deposits are presented in Appendix 2. All quoted and illustrated geochemical analyses are recalculated to 100% volatile-free.

A Total-Alkali vs. Silica (TAS) diagram (Figure 3.1) shows that Ohakuri pumices represent magma that varies in composition from dacite to rhyolite. In addition, 2 juvenile blebs are andesitic. Based on concentrations of Rb and Sr, the dacite to rhyolite pumice analyses cluster into 3 groups (magma types) (Figure 3.2). The 3 magma types are: type 1) Rb (99 to 150 ppm), Sr (32 to 76 ppm); type 2) Rb (68 to 129 ppm), Sr (89 to 181 ppm); and type 3) Rb (65 to 86 ppm), Sr (213 to 325 ppm). Defined by the fields established from Rb and Sr variation, the Ohakuri pumice analyses are plotted on other major and trace element variation diagrams in Figure 3.3 and Figure 3.4. In major element plots there is some overlap between the 3 magma types. In particular, the type 2 magma shows a broad range with respect to SiO_2 (67.75 to

76.48%) and overlaps with the type 1 and 3 fields on the Na_2O, K_2O, Al_2O_3, and Fe_2O_3T plots. The type 1 and 3 magmas exhibit narrower ranges with respect to SiO_2 (73.54 to 77.96% and 65.57 to 70.08%, respectively). With respect to trace elements, only Rb, Sr, Ba, Zn, and Zr show a wide spread in the data (Figure 3.4). The magma types are distinguished best on the Sr vs. Ba plot, whereas the Zr vs. Zn and the Zr vs. Ba plots reveal overlap between the 3 magma fields. Type 1 and 2 magmas have conspicuous outliers with respect to Ba and Zn.

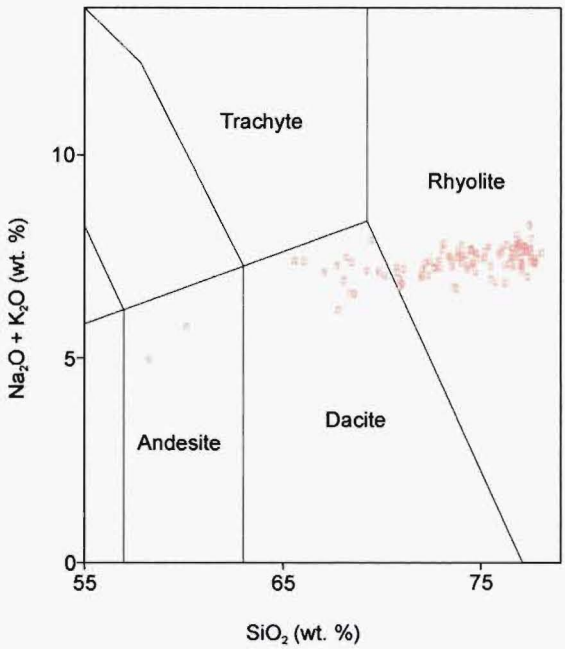

Figure 3.1 Total Alkali-Silica plot after Le Maitre et al. (1989), of all the Ohakuri XRF samples, including analyses provided by S.D. Weaver and B.F. Houghton (unpublished data).

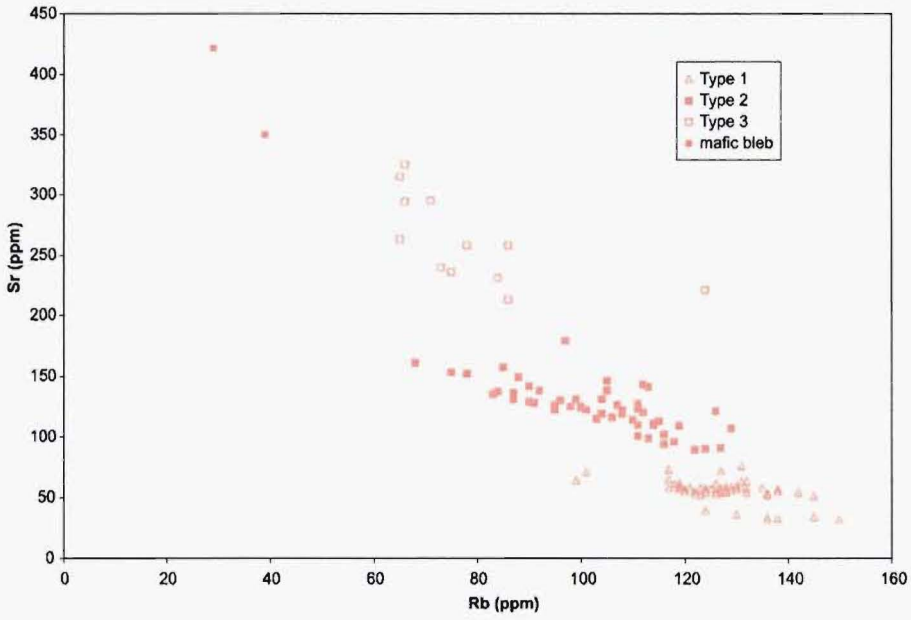

Figure 3.2 Ohakuri magma types defined by Sr-Rb variation. Also includes two juvenile (mafic) bleb analyses.

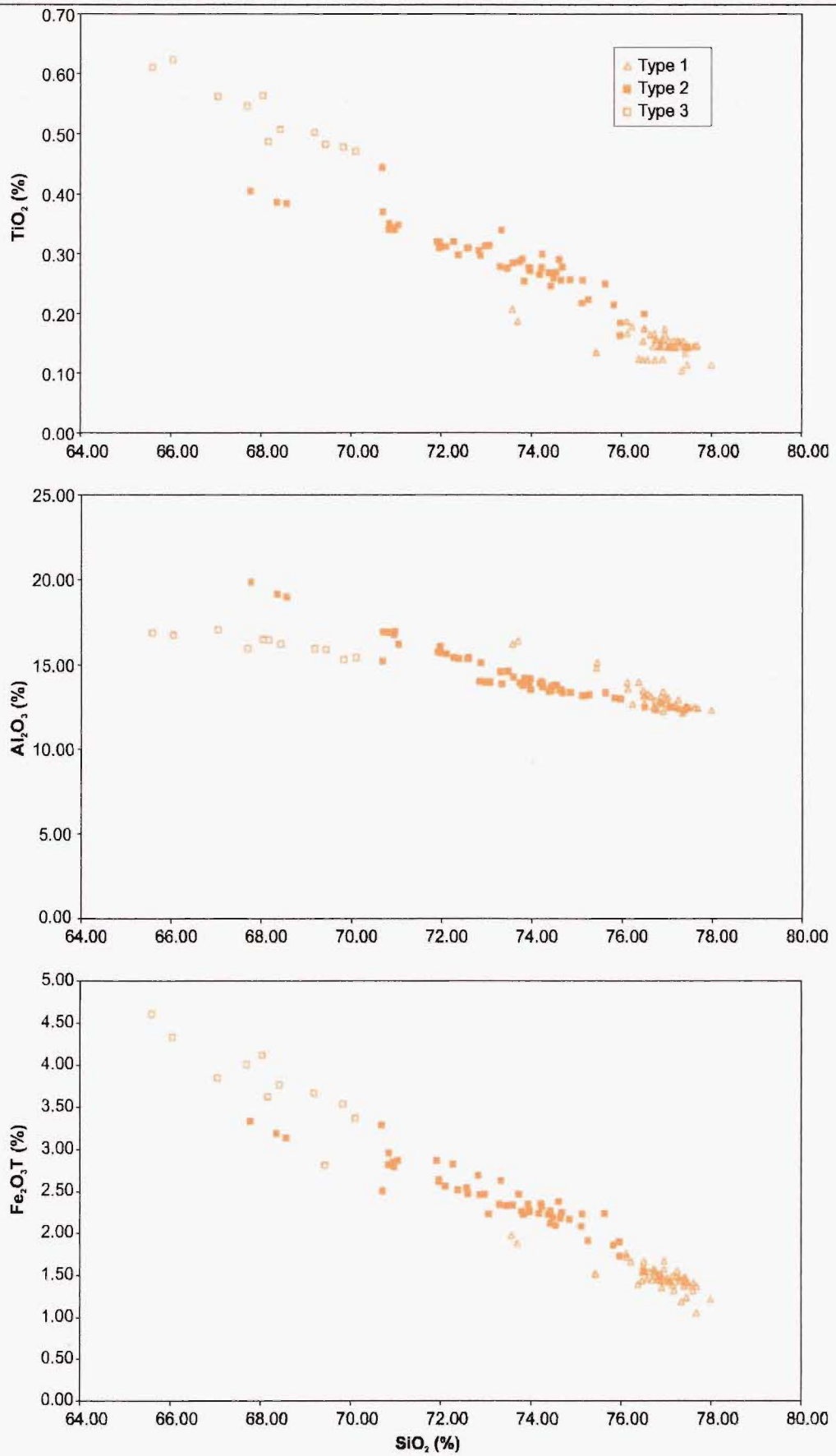

Figure 3.3 Major element variation diagrams including TiO_2, Al_2O_3, Fe_2O_3T, CaO, Na_2O, and K_2O plotted against SiO_2. Ohakuri magma types are based on Sr-Rb variation from Fig. 3.2.

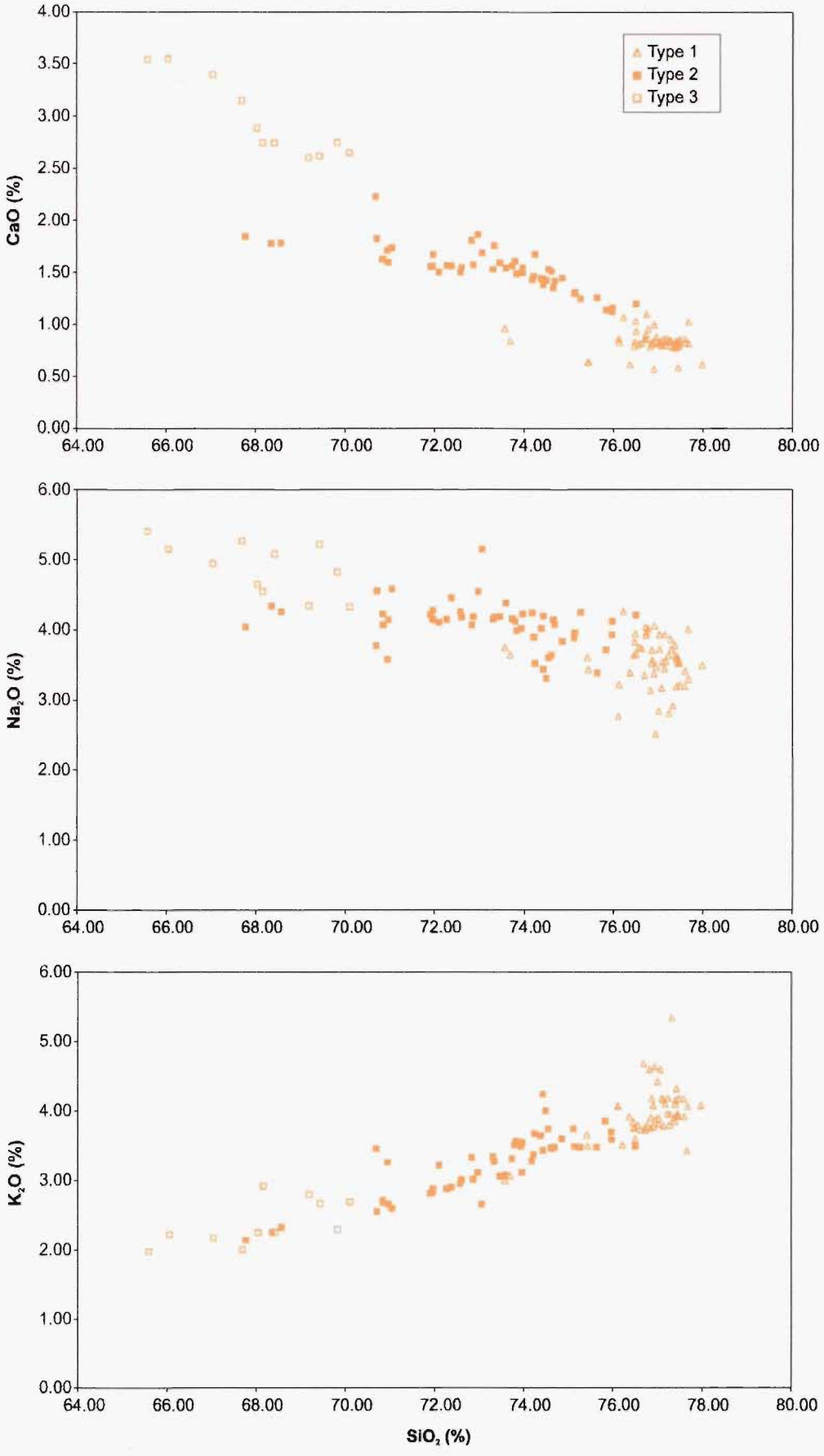

Figure 3.3 (con't)

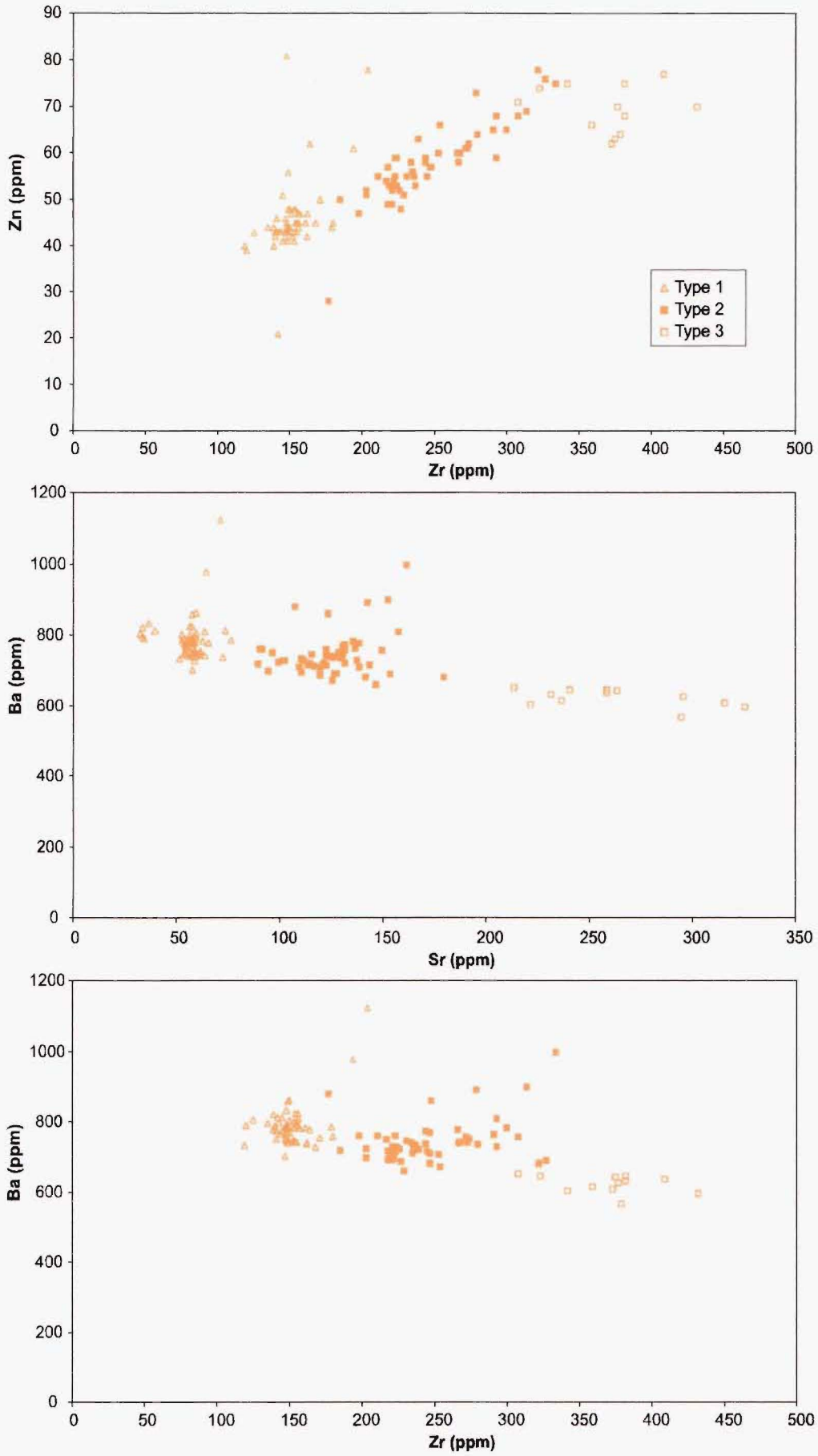

Figure 3.4 Trace element variation diagrams for Ohakuri analyses, including Zn-Zr, Ba-Sr, and Ba-Zr. Magma types are based on Sr-Rb variation from Fig. 3.2.

Table 3.1 Representative samples for the 3 different Ohakuri magma types.

Sample	D3	D3a	D40	D59	D60	D64	D87	D95	D97	D139	D153a	D154b
Pum. Type	type 3	type 2	type 1	type 3	type 2	type 1	type 3	type 2	type 2	type 1	type 2	type 1
Locality	Oh256	Oh256	Oh162	Oh137	Oh137	Oh137	Oh254	Oh204	Oh204	Oh204	Oh130	Oh130
Grid Ref.	U16/798146	U16/798146	U16/807157	U16/851130	U16/851130	U16/851130	U16/806117	T16/694182	T16/694182	T16/694182	U16/803117	U16/803117
SiO2	68.02	75.61	77.27	69.17	74.47	76.93	69.80	73.31	74.83	77.21	74.59	77.46
TiO2	0.56	0.25	0.15	0.50	0.26	0.17	0.48	0.34	0.26	0.15	0.29	0.15
Al2O3	16.53	13.42	12.43	16.02	13.87	13.11	15.35	13.92	13.44	12.49	13.57	12.53
Fe2O3T	4.12	2.24	1.44	3.68	2.20	1.58	3.55	2.64	2.17	1.50	2.39	1.38
MnO	0.13	0.07	0.05	0.12	0.08	0.06	0.12	0.09	0.08	0.05	0.08	0.06
MgO	0.80	0.24	0.11	0.67	0.30	0.14	0.69	0.40	0.29	0.13	0.38	0.13
CaO	2.89	1.26	0.84	2.61	1.43	0.84	2.75	1.76	1.45	0.84	1.51	0.86
Na2O	4.66	3.39	3.73	4.35	3.31	2.52	4.83	4.18	3.84	3.64	3.64	3.21
K2O	2.26	3.49	3.96	2.80	4.01	4.64	2.30	3.28	3.60	3.97	3.48	4.19
P2O5	0.02	0.02	0.02	0.08	0.07	0.01	0.12	0.06	0.04	0.02	0.06	0.03
LOI	2.54	4.51	3.41	3.06	3.76	3.95	2.17	3.24	3.13	2.84	3.90	3.95
V	21	10	8	17	10	9	19	12	10	13	13	11
Cr	3	3	3	3	3	3	3	3	3	3	3	3
Ni	3	4	3	3	3	3	3	3	3	3	3	3
Zn	77	54	42	75	54	46	66	57	52	44	59	46
Zr	408	216	146	381	221	146	358	246	220	155	223	140
Nb	10	9	8	11	9	9	10	10	9	9	9	8
Ba	639	751	704	634	697	752	617	711	731	791	722	777
La	9	22	23	14	17	24	14	18	24	37	33	37
Ce	49	65	61	62	60	61	52	59	57	63	70	68
Nd	15	25	41	16	33	21	30	25	39	38	45	32
Ga	18	14	13	16	14	14	16	15	14	14	15	13
Pb	12	17	18	12	17	20	13	15	19	20	16	19
Rb	78	118	130	84	114	138	75	105	114	131	110	120
Sr	258	96	57	231	110	57	236	138	111	57	114	57
Th	8	12	12	6	8	12	5	11	10	13	11	13
Y	25	35	36	26	33	34	29	34	35	38	36	37
$^{87}Sr/^{86}Sr$				0.705287				0.705239		0.705296	0.705291	0.705329

A summary of magma types (representative samples) is presented in Table 3.1, and the areal distribution of magma types is given in Figure 3.5. Figure 3.5 shows that the type 3 pumice only occurs in the east and northeastern sectors of the Ohakuri pyroclastic distribution. The andesitic blebs have only been observed in the west and northwestern sectors.

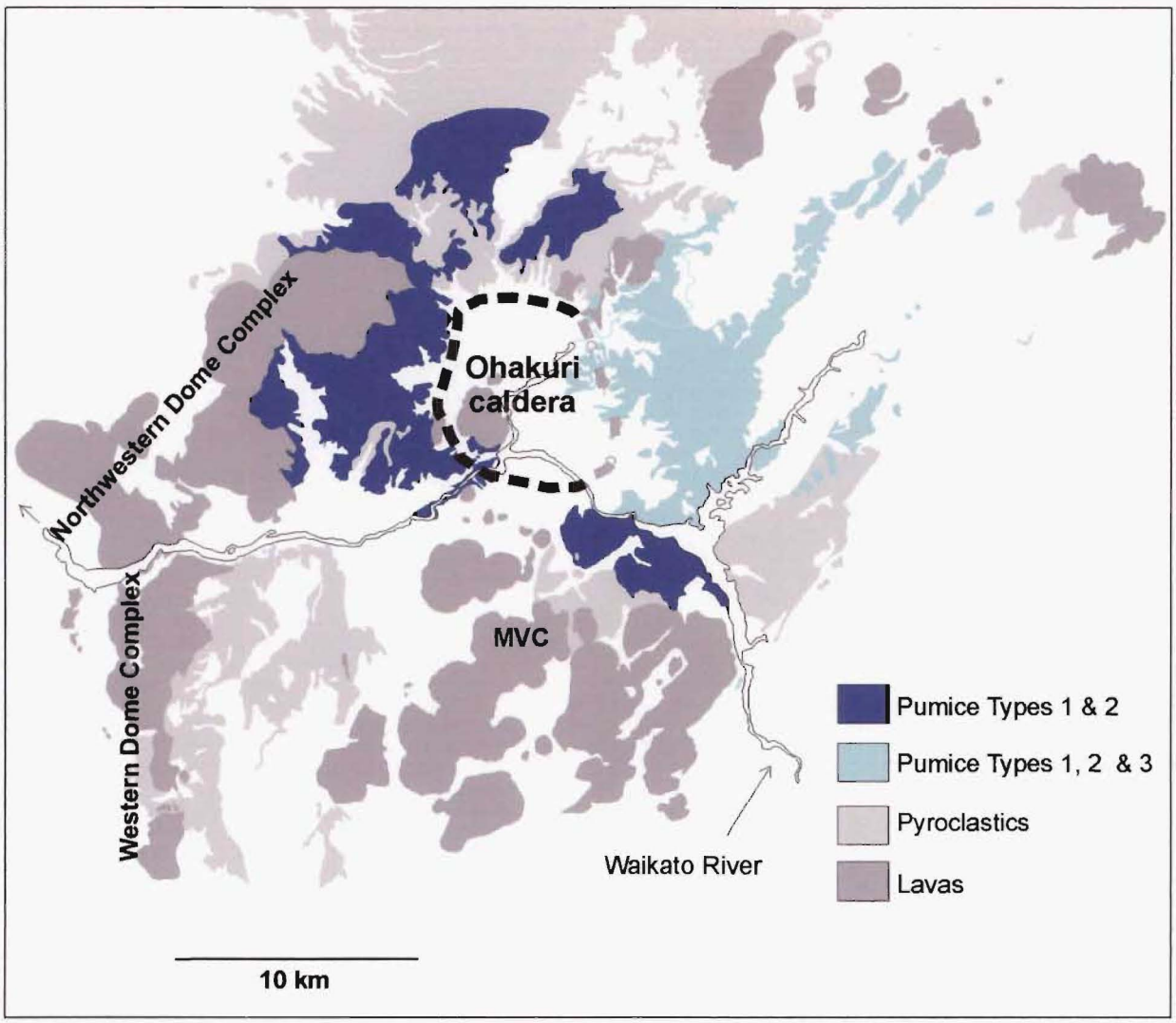

Figure 3.5 Distribution of Ohakuri pumice types 1, 2, and 3. Nearby lavas and pyroclastic deposits are included for context. Significantly older (> Whakamaru age, ~ 340 to 320 ka) and younger (< Rotoiti age, ~ 62 ka) volcaniclastics are excluded from the map.

Petrography of the pumice types

Petrographically, the 3 Ohakuri pumice types can be distinguished by variations in crystal content, plagioclase to quartz ratios, and to a lesser extent mineral assemblage. Petrographic data are summarised for selected pumice samples in Table 3.2. All 3 types contain plagioclase feldspar, quartz, orthopyroxene, and opaques (in order of decreasing abundance), but the type 3 pumice also contains minor amounts of hornblende. Type 3 pumice is relatively crystal-rich (10 to 15 vol%) and is characterised by a very high plagioclase to quartz ratio and large abundant phenocrysts of orthopyroxene. The high plagioclase to quartz ratio correlates well with the less-evolved nature of this particular magma (i.e. the lower SiO_2 content and higher Sr

content). Type 2 pumice is characterised by a crystal abundance of < 3 to 5 vol%; however, there are rare examples of higher crystal abundances (5 to 10 vol%). Type 2 pumice contains more plagioclase than quartz but the ratio is considerably less than for the type 3 pumice. Type 1 pumice are very crystal poor (< 1 vol%), have a plagioclase to quartz ratio of approximately 1:1, and a paucity of orthopyroxene phenocrysts (none in some samples). The greater abundance of quartz relative to plagioclase correlates well with the higher SiO_2 content for the type 1 pumice.

Parameter	Ohakuri type 1	Ohakuri type 2	Ohakuri type 3	Mamaku type 1	Mamaku type 2
Crystal content	< 1 vol%	< 3 to 5 vol%	10 to 15 vol%	6 to 7 vol%	4 to 7 vol%
Plagioclase : Quartz ratio	~ 1	~ 2	~ 4	~ 2	~ 2

Table 3.2 Summary of petrographic data for the Ohakuri and Mamaku pumice types

Comparison with other central TVZ pyroclastic deposits and lavas

In Figure 3.6, representative pumice chemistries for the Mamaku, Pokai, Mokai, and Korotai ignimbrites are superimposed on the Ohakuri fields. The Korotai chemistry overlaps with the Ohakuri type 1 and 2 magmas, the Mokai chemistry plots within the Ohakuri type 2 field and the Pokai chemistry shows a broader range of data that plots within the Ohakuri type 1 and 2 fields. The Mamaku data exhibit an almost-identical chemistry to the Ohakuri type 1 and 2 magmas and are discussed in more detail below. Maroa Volcanic Centre (MVC) and Northwest Dome Complex lavas are plotted on top of the Ohakuri fields in Figure 3.7. In similar fashion to the Korotai ignimbrite, the Northwest Dome Complex chemistry overlaps Ohakuri type 1 and 2 magmas; while MVC chemistry overlaps with the Ohakuri type 1 magma.

The similarities between the Ohakuri pyroclastic deposits and the Mamaku ignimbrite are particularly important because of the temporal linkage between the eruptions of these deposits (see Section 2.2.2). Comparing Rb and Sr concentrations (Figure 3.8), the Ohakuri pyroclastic deposits and the Mamaku ignimbrite share very similar fields for their type 1 and 2 magmas. It is only the less-evolved dacitic magma type (type 3) that chemically distinguishes the Ohakuri pyroclastic deposits from the Mamaku ignimbrite in this diagram. In addition, other trace element plots (Figure 3.8) reveal subtle differences that distinguish the two deposits, including: 1) the Zr concentration of the Mamaku type 2 magma exhibits broad variation, with a greater overlap of the Ohakuri type 3 magma than exhibited by the Ohakuri type 2 magma; 2) with respect to Rb/Sr ratio, the Ohakuri type 1 magma shows considerably more variation than the Mamaku type 1 magma; and 3) andesitic juvenile blebs for both the Ohakuri and Mamaku deposits show different chemistries.

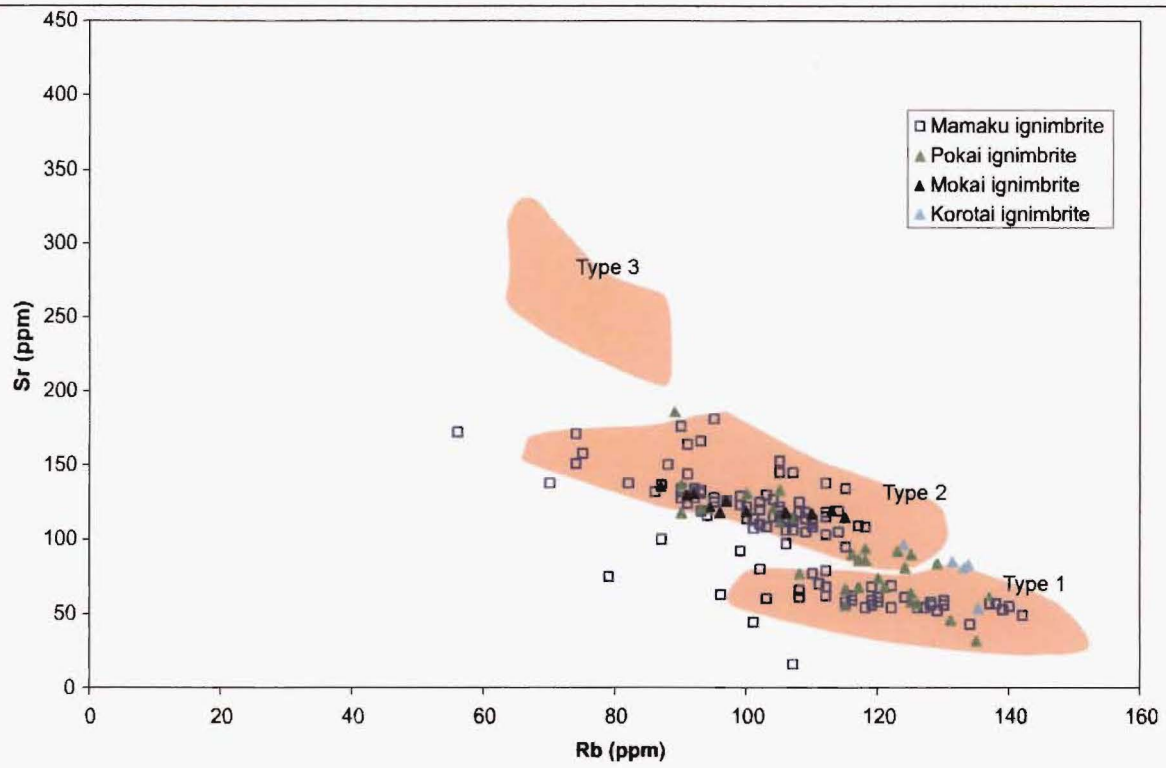

Figure 3.6 Sr-Rb variation diagram comparing the Ohakuri magma types (orange fields) with the Mamaku (data from Milner, 2001, and this thesis), Pokai (data from Karhunen, 1993), Mokai (data from Milner, 2001), and Korotai (data from Leonard, 2003) ignimbrites.

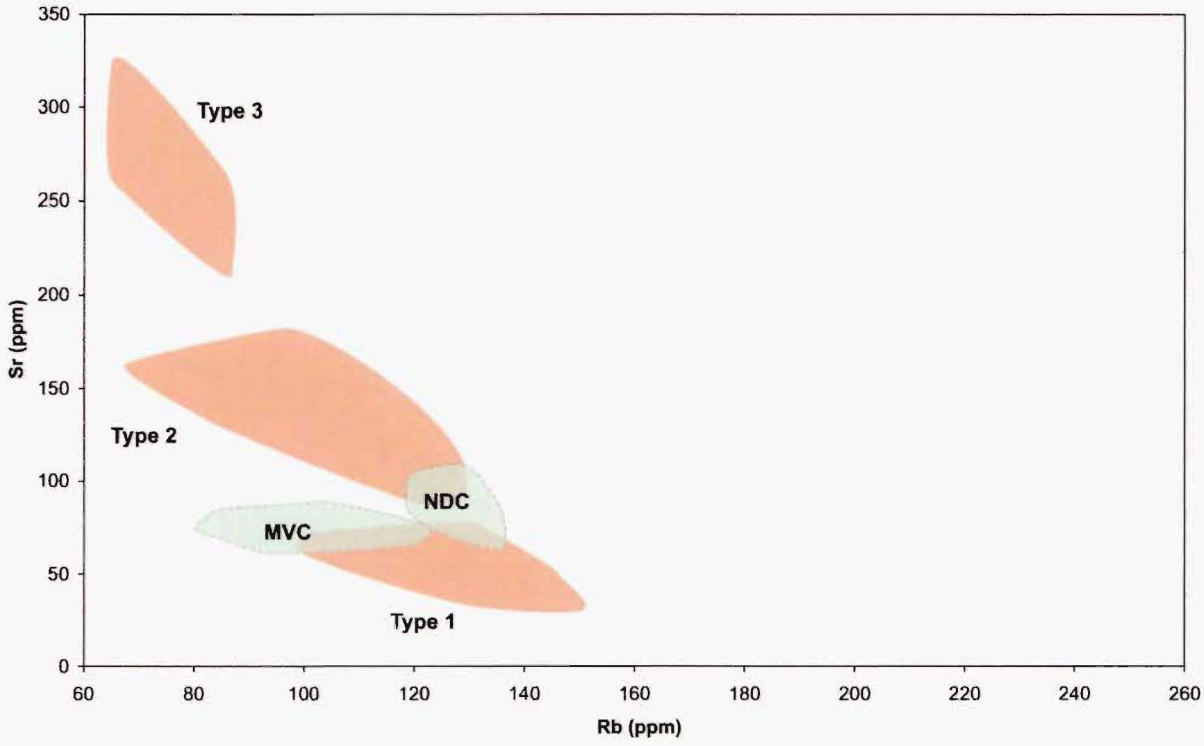

Figure 3.7 Sr-Rb variation diagram comparing Ohakuri magma types (orange fields) with fields for Maroa Volcanic Centre (MVC data from Leonard, 2003) and the Northwest Dome Complex (NDC data from Brown, 1994).

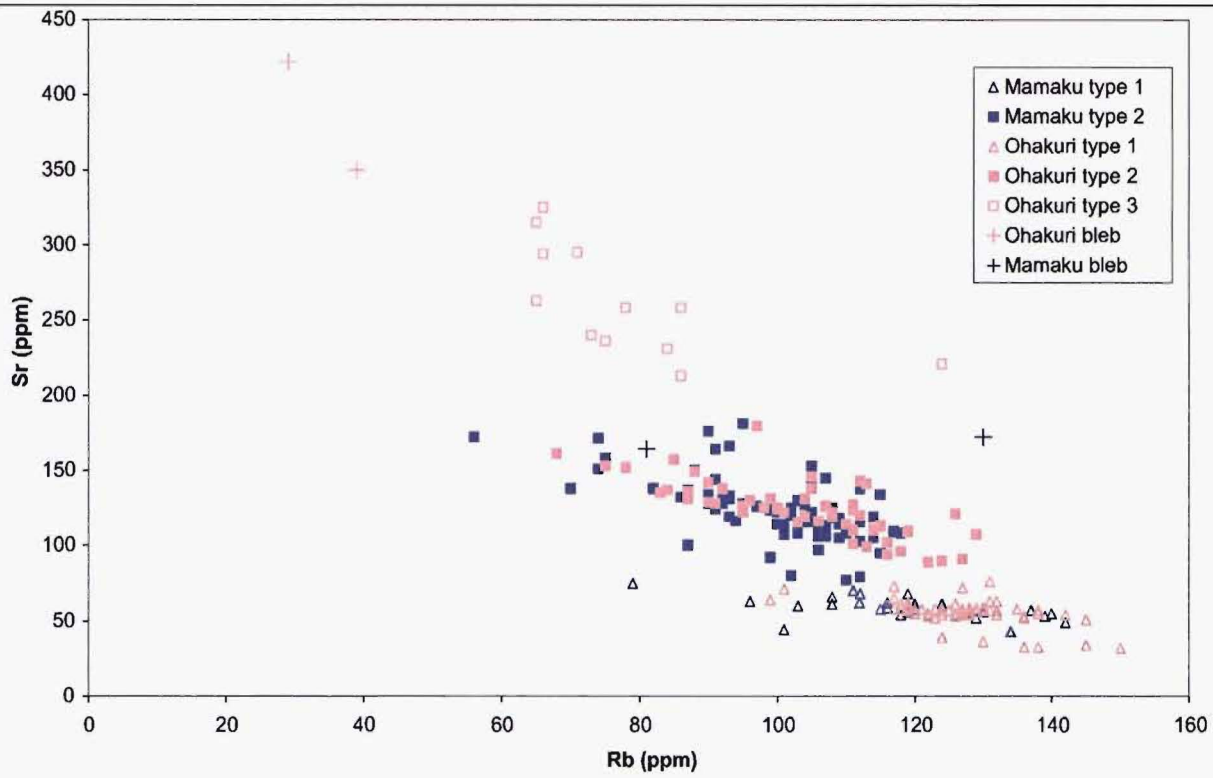

Figure 3.8 Selected variation diagrams comparing Ohakuri and Mamaku magma types. Diagrams include Sr-Rb, Zn-Zr, Zr-Rb/Sr, Ba-Sr. For ease of comparison I refer to Milner et al.'s (2003) Mamaku type 2 and 3 magmas as type 2 because they correlate well with the Ohakuri type 2 magma. See below for the other variation diagrams.

Petrographically, the Mamaku and Ohakuri pumices have a similar phenocryst assemblage but the crystal abundances and their plagioclase to quartz ratios are significantly different (Table 3.2). Compared with the Ohakuri type 1 pumice, the Mamaku type 1 pumice is relatively crystal-rich (6 to 7 vol%) and has a plagioclase to quartz ratio of ~ 2:1. The Mamaku type 2 pumice (cf. type 2 and 3 from Milner et al., 2003) contains 4 to 7 vol% phenocrysts and is also characterised by a plagioclase to quartz ratio of approximately 2:1.

In summary, the Ohakuri type 1 and 2 magmas are similar in major and trace element chemistries to other nearby pyroclastic deposits and lavas; however, the additional type 3 magma distinguishes the Ohakuri chemistry from the rest. The range of Ohakuri magma types is comparable to magma variation associated with the Whakamaru ignimbrite (Brown et al., 1998) (Figure 3.9). Possible reasons for the magma types are discussed in Section 3.7.3.

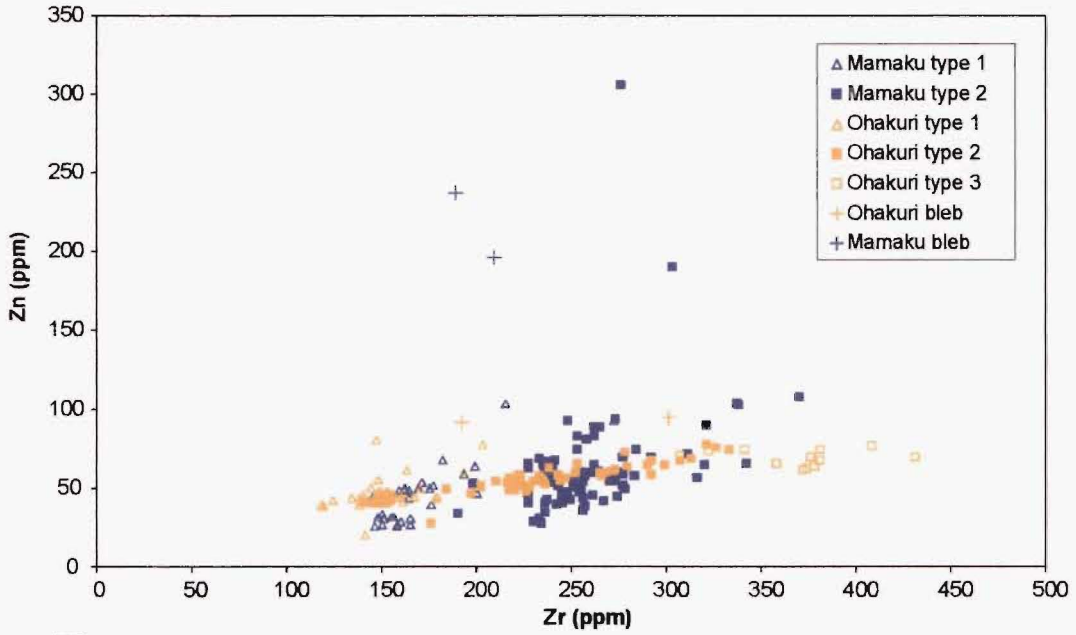

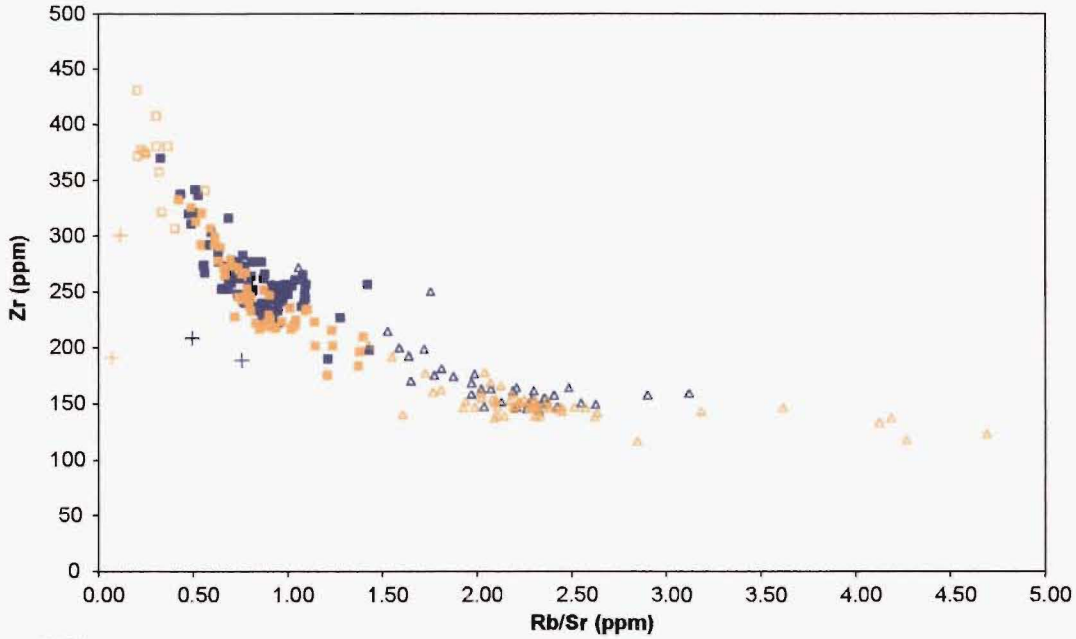

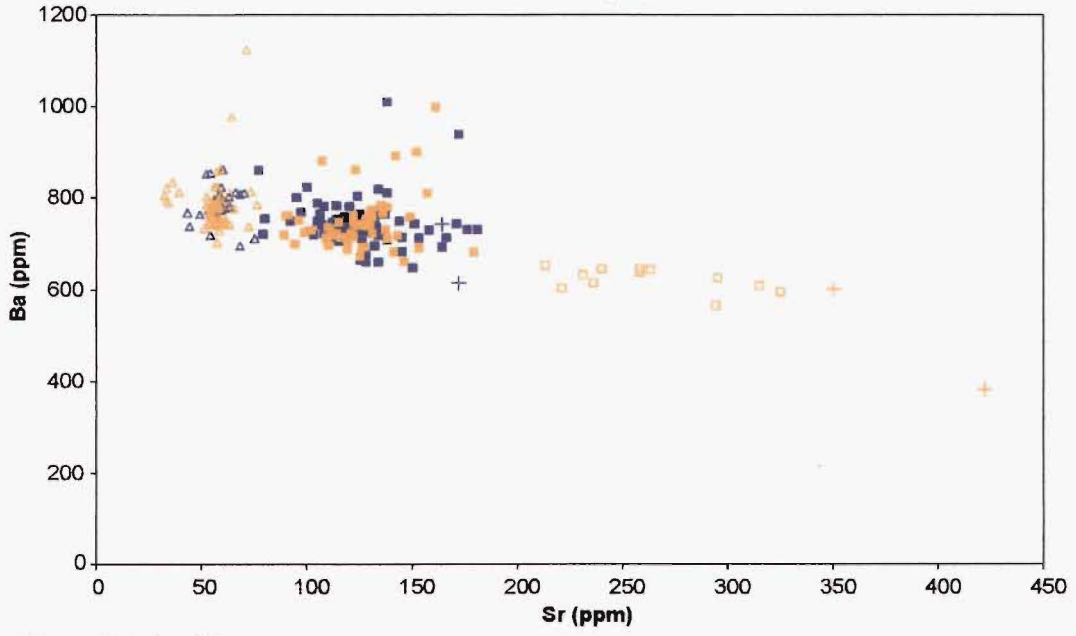

Figure 3.8 (con't)

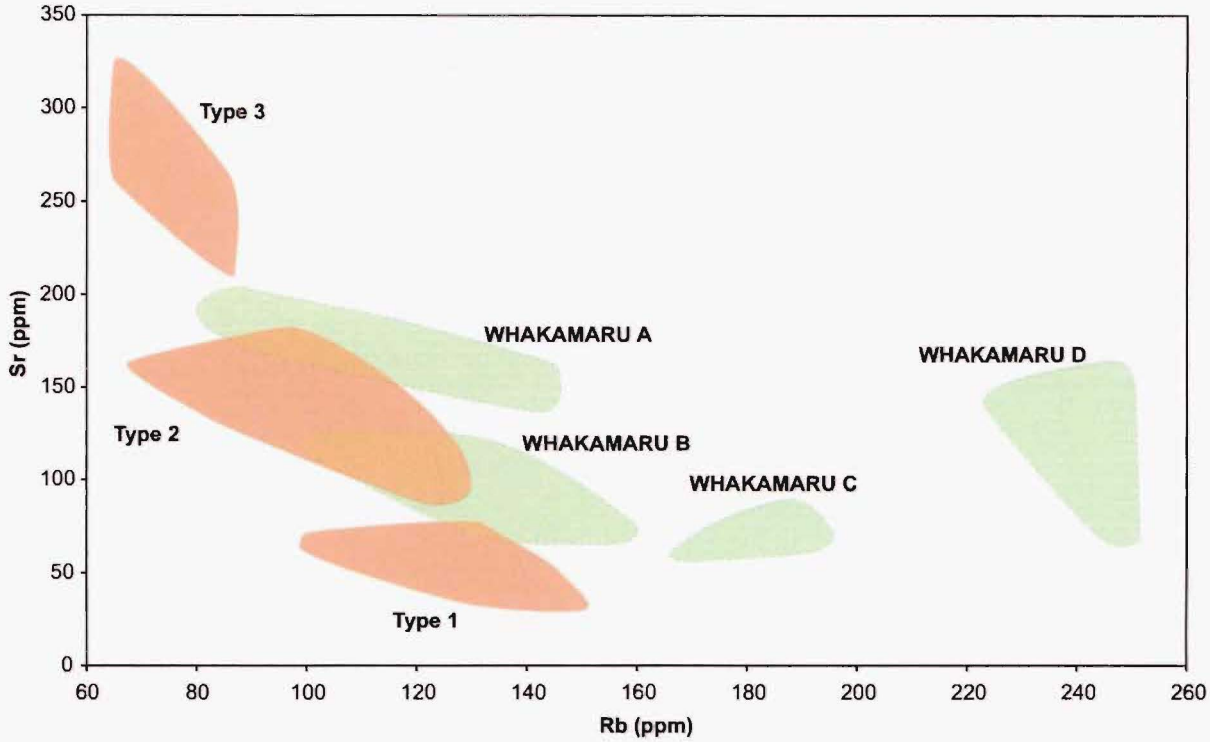

Figure 3.9 Sr-Rb variation diagram comparing Ohakuri (orange fields) and Whakamaru (green fields) magma types. Whakamaru data is from Brown et al. (1998).

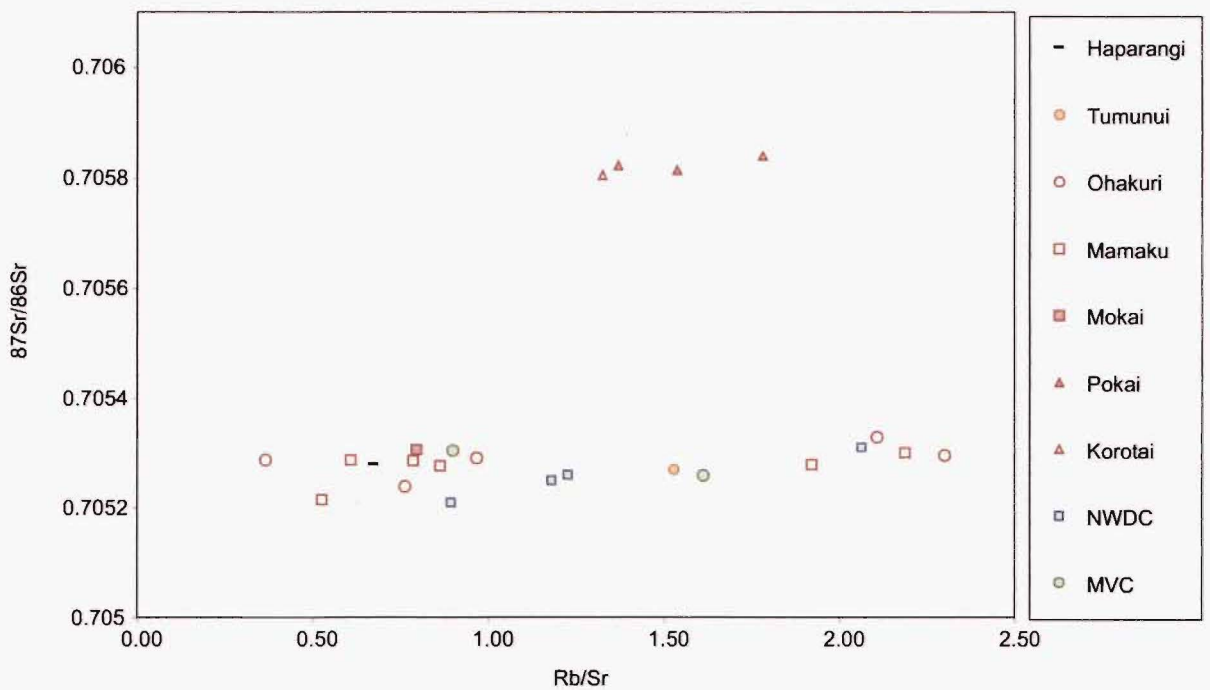

Figure 3.10 87Sr/86Sr vs. Rb/Sr variation diagram for selected pyroclastic deposits and lavas.

3.3.2 Sr isotope chemistry

$^{87}Sr/^{86}Sr$ ratios were determined for 24 samples by TIMS mass spectrometry at Arthur Holmes Isotope Geology Laboratory, University of Durham, UK; data are courtesy of Dr. Bruce Charlier. Nineteen of the 24 samples are applicable to research associated with this thesis and include the Ohakuri pyroclastic deposits, Mamaku ignimbrite, Pokai ignimbrite, Mokai ignimbrite, Korotai ignimbrite and MVC lavas. The raw data are presented in Appendix 3.

$^{87}Sr/^{86}Sr$ data for the Ohakuri pyroclastic deposits are presented in Table 3.1 and compared with data for the Mamaku, Pokai, Mokai, and Korotai ignimbrites, as well as lavas from the Northwest Dome Complex, MVC, and the Haparangi and Tumunui domes on a $^{87}Sr/^{86}Sr$ vs. Rb/Sr variation diagram (Figure 3.10). The plot reveals two conspicuous $^{87}Sr/^{86}Sr$ groups, with the Pokai and Korotai clustering at ~.7058 and the rest of the deposits clustering between ~.7052 and .7053.

Lithofacies	Description	Relationship to other lithofacies
A. Massive deposit (structureless)	Structureless; poorly sorted; matrix-rich; pumice lapilli dominant (10 to > 35%), pumice lapilli range from 2 to 400 mm; lithic poor (< 1%); can be **> 200 m thick**; sometimes fines-poor	Found in contact with lithofacies B, D, E, F, and G
B. Massive deposit (diffusely stratified)	Similar lithology as lithofacies A but has **conspicuous pumice concentration bands**, pumice bands are continuous over 10's of metres; packages < 1 m to > 10 m thick	Found in contact with lithofacies A, E, F, and G
C. Dune bedded deposit	Similar lithology as lithofacies B; characterised by **giant-dune-bedforms with wavelengths > 40 m and amplitudes > 5 m**	Not found in contact with other lithofacies
D. Massive (reverse graded sub-packages)	Poorly sorted, matrix-rich; pumice lapilli concentrations range from 1 to 40%, similar range of pumice sizes as lithofacies A; lithic poor (< 1%); up to 2m thick; **comprised of reverse graded sub-packages**	Only found in contact with lithofacies A
E. Bedded deposit (channel bedded)	**Stacked channel and fill structures with uniform orientations**; cross and plane-parallel infill beds; characterised by a range of bed lithologies (sub-lithofacies, see Table 3.4)	Found in contact with lithofacies A and B
F. Bedded deposit (plane-parallel to cross-bedded)	Plane-parallel packages and cross-bedded channel-fill packages **interdigitated with lithofacies A**; some **broader bowl-shaped structures**; **random channel orientations**; similar range of sub-lithofacies as lithofacies E (refer to Table 3.4); **rare sandwaves**	Found in contact with lithofacies A and B
G. Bedded deposit (plane-parallel bedded)	Characterised by relatively thin packages (< 1 m) of plane-parallel beds; lithologies include coarse-ash (lapilli poor) beds, pumice lapilli-rich beds, and very fine-grained ash (**accretionary lapilli-bearing)** beds; **accretionary lapilli concentrations up to 50%; some packages are laterally continuous for > 200 m**	Found in contact with lithofacies A and B

Table 3.3 Diagnostic characteristics of the different Ohakuri lithofacies

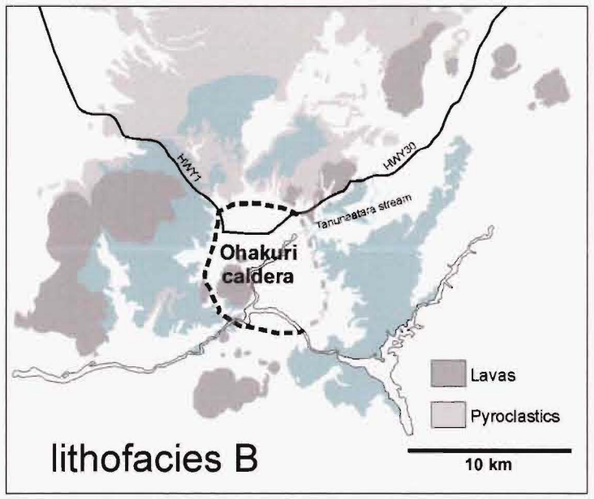

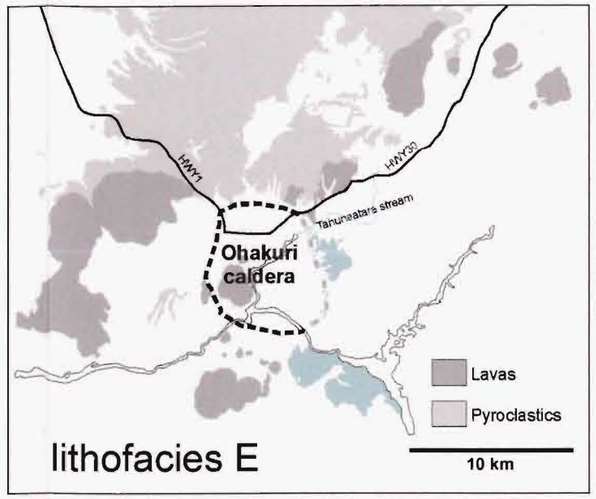

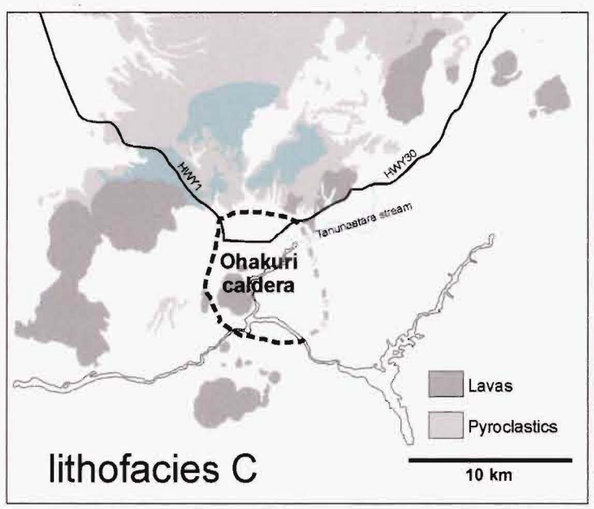

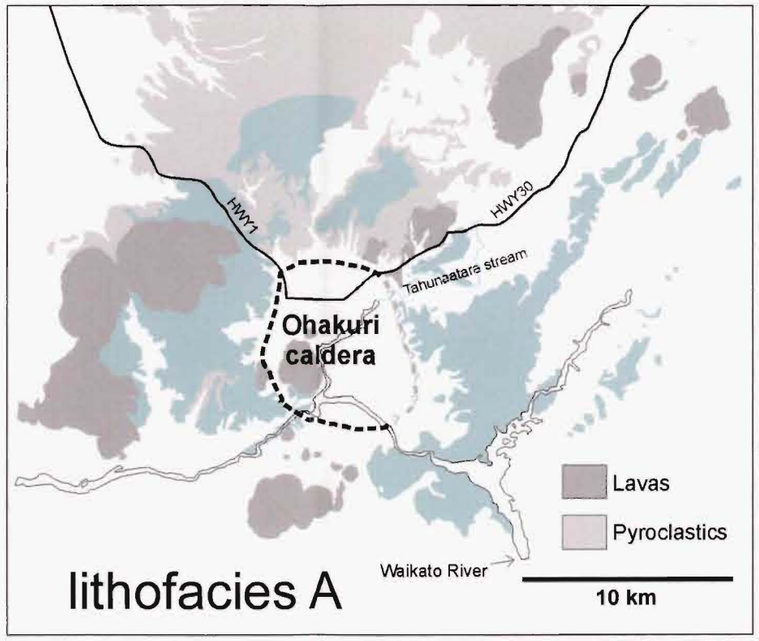

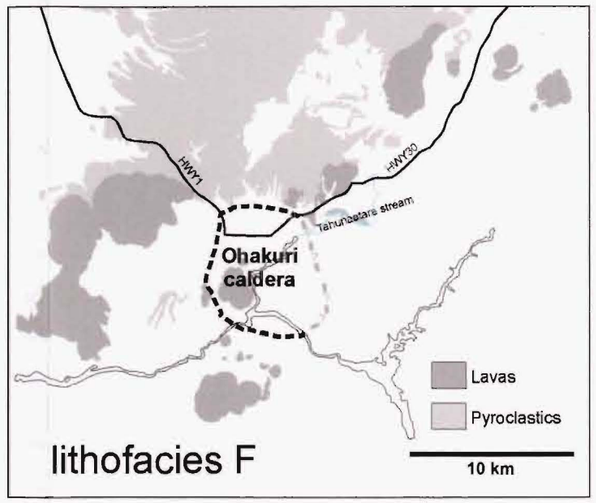

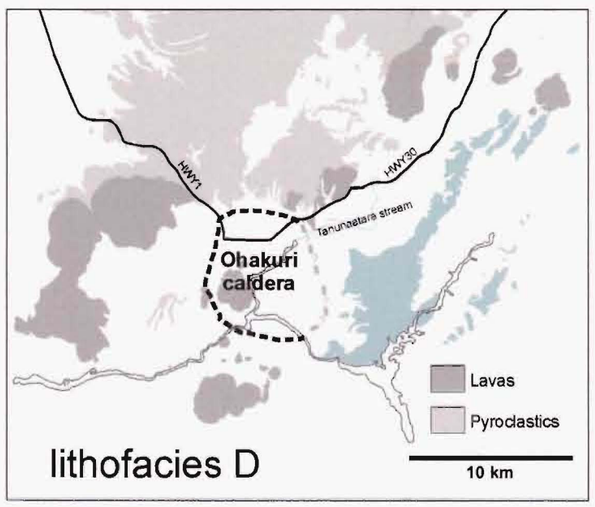

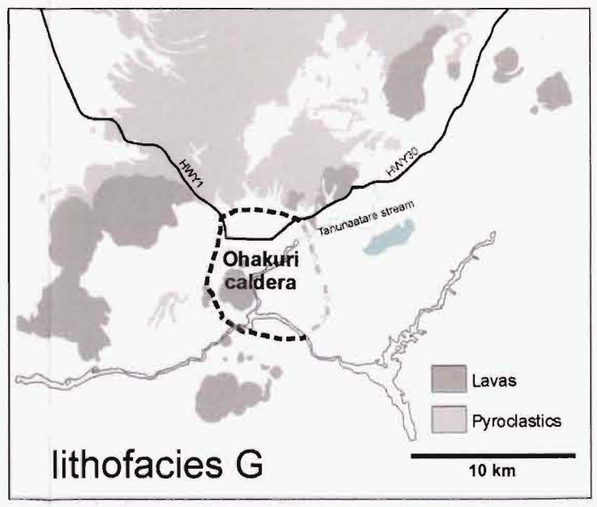

Figure 3.11 Distribution of the Ohakuri lithofacies. Other lavas and pyroclastic deposits are included in the maps to provide a context (significantly older and younger volcaniclastics are excluded, see Fig. 3.5).

3.4 Ohakuri lithofacies

The Ohakuri deposits have, thus far, been referred to as the Ohakuri pyroclastic deposits, where 'pyroclastic' is used in a genetic sense; however, in this section I describe them using non-genetic terms, with the exception of grainsize terminology (i.e. ash and lapilli), in order to set up a discussion of their origin(s) in Section 3.6. The reason for doing this is to develop a lithofacies model (cf. McPhie, 1986; Branney, 1991; Houghton et al., 2004) for the Ohakuri deposits without making any assumptions with respect to their origin(s) (i.e. pyroclastic processes vs. reworked or normal sedimentary processes). A summary of each Ohakuri lithofacies and its diagnostic characteristics is presented in Table 3.3, and Figure 3.11 shows each of their areal distributions.

Figure 3.12 Locality Oh167, U16/80471131. Massive, structureless, poorly sorted lithofacies A. Hammer handle is 13 cm long.

3.4.1 Lithofacies A: Massive deposit (structureless)

Lithofacies A is a massive, structureless, poorly sorted, matrix-rich deposit (Figure 3.12) that can be a few metres to > 200 m thick. The clast to matrix ratio (ratio of grains > 2 mm versus grains < 2 mm) is highly variable (10 to 40 vol%), with clast grainsizes ranging from fine lapilli to blocks. Pumice lapilli are the dominant clast type (10 to > 35 vol%), ranging in size from 2 to 400 mm and generally rounded to sub-rounded in shape. Lithofacies A is lithic-poor (< 1 to 5 vol%), with rare lithic-rich lenses up to 50 vol% in concentration. The matrix is primarily fine to coarse ash with variable crystal content. Some exposures of lithofacies A are characterised by a matrix that is fines-poor. Two outcrops of the fines-poor lithofacies A are located in the western sector of the field area, one of which is underlain by a crystal- and lithic-rich layer that

contains relatively large lithics (including a 220 mm block of Whakamaru ignimbrite) (Figure 3.13). Lithofacies A contains accretionary lapilli clasts up to 62 mm in diameter; however, they are rarely observed.

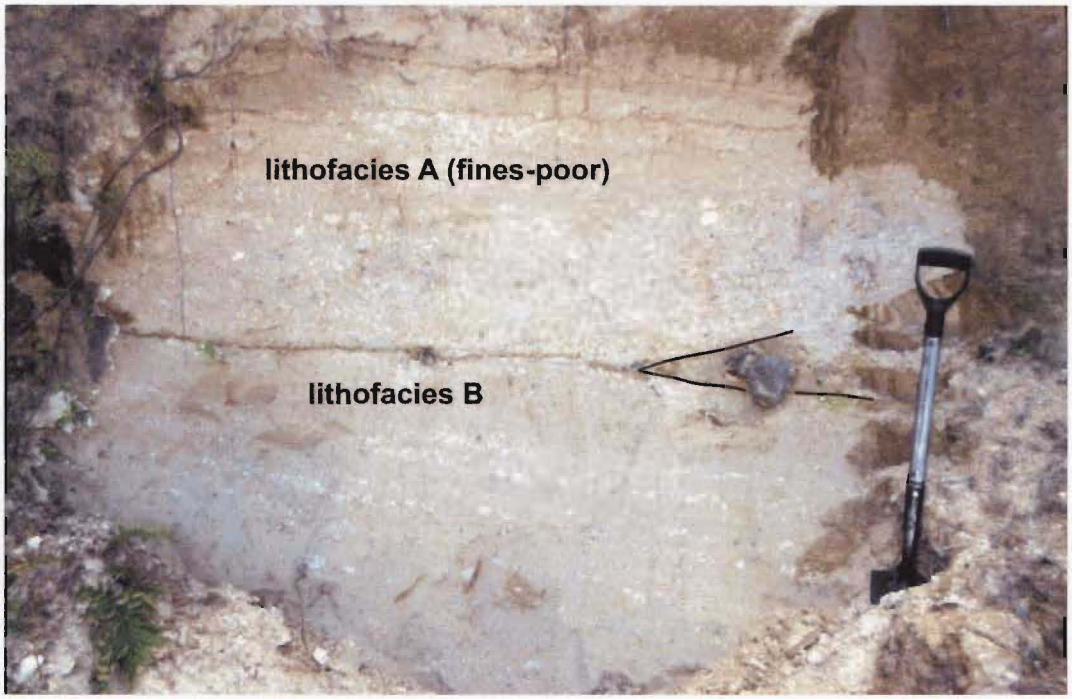

Figure 3.13 Locality Oh110, T17/691087. Sharp depositional boundary between lithofacies A (fines-poor) and lithofacies B package. 220 mm block of Whakamaru ignimbrite is set in a wedge-shaped crystal- and lithic-rich layer. The spade is 1 m long.

Figure 3.14 Locality Oh139, U16/84931300. Greater than 100 metre high vertical cliff section of structureless lithofacies A. Measured from bottom of photo to the top of the cliff.

Lithofacies A dominates the east and northeastern sectors of the distribution area (Figure 3.11), forming > 100 m high continuous and structureless outcrops (Figure 3.14), occasionally interbedded with rare reverse graded packages[1] of material defined here as lithofacies D. To the south, southeast, southwest, and west, lithofacies A is not nearly as thick (a few metres to 10's of metres) and is often found in contact with diffusely stratified deposits (lithofacies B) and bedded deposits (lithofacies E). To the north and northwest, it is observed in contact with lithofacies B, E and F.

3.4.2 Lithofacies B: Massive deposit (diffusely stratified)

The diffusely stratified deposit can be < 1 m to > 10 metres thick and is observed throughout most of the areal distribution of the Ohakuri deposits (Figure 3.11). The lithology of lithofacies B is very similar to the structureless deposit (lithofacies A); however, lithofacies B exhibits internal banding (Figure 3.13 and Figure 3.15). The banding is defined primarily by variations in the concentration of pumice lapilli and, sometimes, by an increase in the maximum pumice size. Bands usually contain similar sized pumice clasts and form continuous sub-parallel laminations that are metres to 10's of metres long. Low-angle cross-stratification is sometimes observed where a pumice band is truncated by overlying deposits. The separation between successive pumice concentration bands is variable from outcrop to outcrop, ranging from a few centimetres to up to a metre. The deposits between bands are identical to poorly sorted massive deposits with a range of pumice and lithic concentrations; the greater the clast concentration between pumice bands the more subtle the bands appear (Figure 3.15b). Some exposures of lithofacies B contain accretionary lapilli and fine-ash coated pumice clasts (Figure 3.16). The accretionary lapilli occur individually or in clusters that exhibit a wide range of sizes from 10 to 60 mm.

Where observed, lithofacies B almost always grades vertically into lithofacies A or vice-versa. The transition between the two lithofacies is very subtle, as the pumice concentrations of the deposits between bands gradually become the same as the pumice concentrations within the bands. Lithofacies B is also observed in contact with lithofacies E.

[1] The term 'package' is defined after Wilson and Hildreth (1997), see Section 1.5 for definition.

Figure 3.15 Diffusely stratified lithofacies B. (a) Locality Oh162, U16/ 80711574. (b) Locality Oh168, U16/80621119. Pumice banding is more subtle with a higher concentration of clasts between bands. Hammer is 28 cm long.

Figure 3.16 Locality Oh159, U16/8091588. Clusters of accretionary lapilli and ash-coated pumice lapilli in diffusely stratified lithofacies B. Pencil is 13 cm long.

3.4.3 Lithofacies C: Dune bedded deposit

Lithofacies C is observed in the north and northwest sectors of the field area (Figure 3.11) and ranges in thickness from a few metres to up to 20 m. It is characterised by giant-dune-bedforms (Figure 3.17) with wavelengths up to 42 m and waveheights[2] > 5 m. Successive dunes exhibit an onlap relationship and show low angles of deposition on lee sides and low angle truncations on stoss sides. Lithologically, lithofacies C is very similar to lithofacies B. Both are characterised by diffuse pumice concentration bands; however, the pumice bands in lithofacies C (Figure 3.18) define the dune structures. In some outcrops it is difficult to distinguish diffusely stratified from reverse graded lithologies, i.e. diffuse pumice concentration bands may be construed as a high concentration of larger pumice clasts at the top of a reverse graded package. The grainsize distribution of lithofacies C is similar to massive lithofacies A and B (see Section 3.5.2).

Figure 3.17 Locality Oh204, T16/694182. Giant-dune-bedforms in HWY1 roadcuts.

[2] The term 'waveheight' (height from bottom to top of a dune) is defined after Schmincke et al. (1973) and is not to be confused with the term 'amplitude' (difference in height between the dune crest and the dune trough).

Figure 3.18 Locality Oh204, T16/69391819. Pumice banding in lithofacies C. Spade is 1 m long.

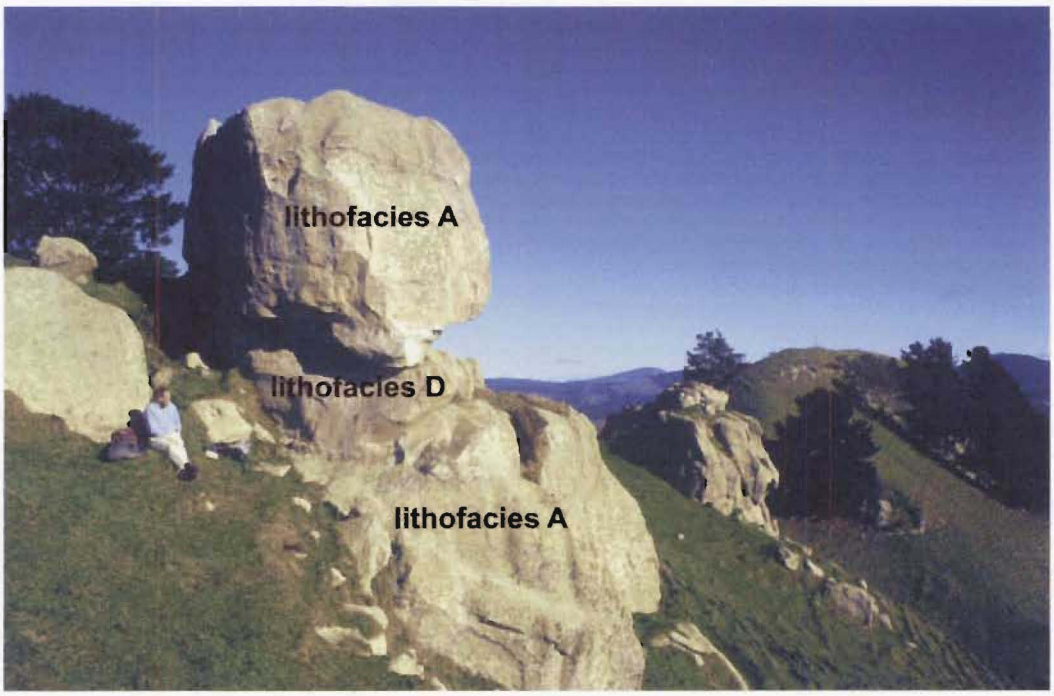

Figure 3.19 Locality Oh192, U16/82111086. Lithofacies D package between massive lithofacies A packages.

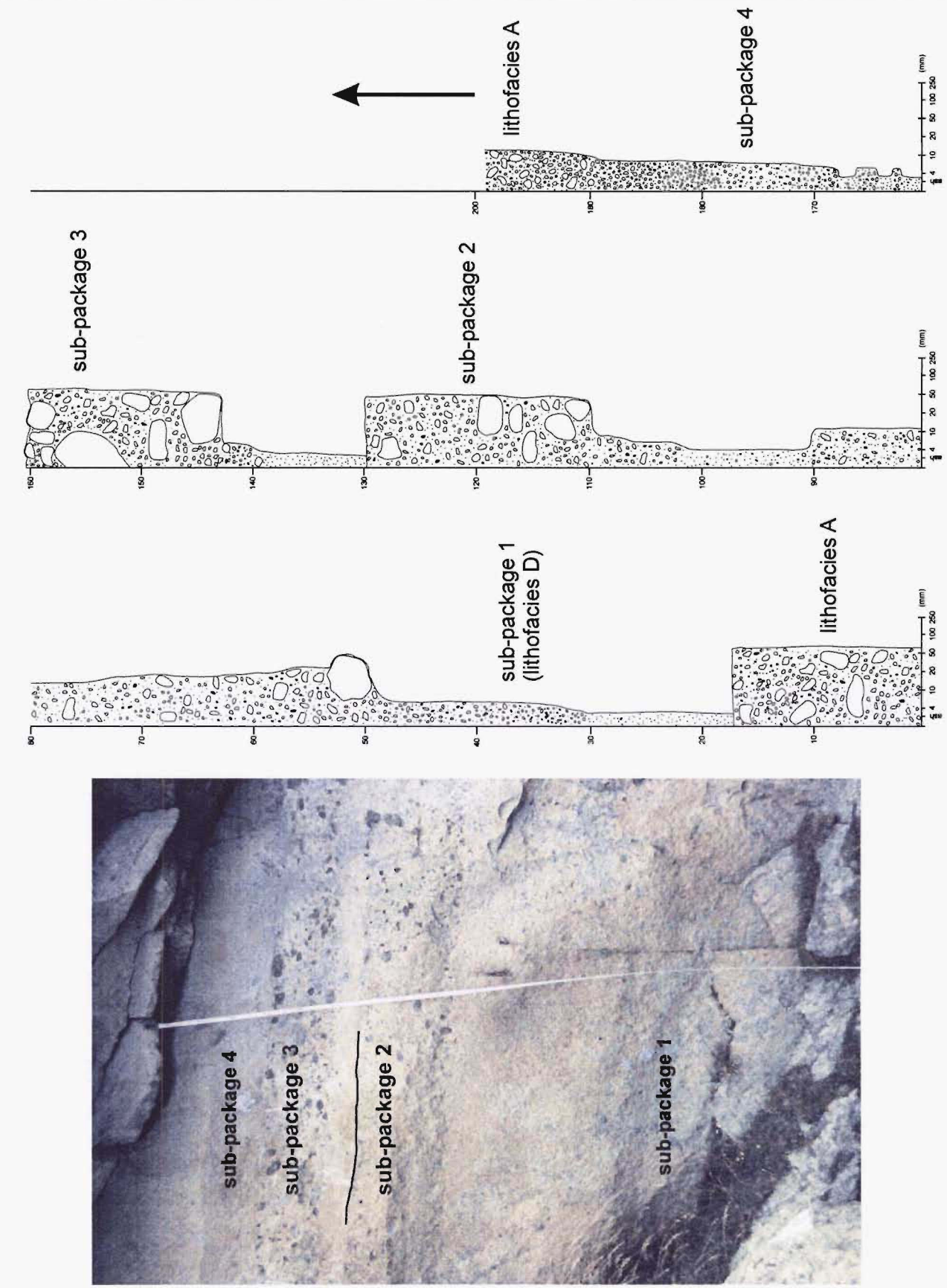

Figure 3.20 Close-up photo and graphic log of lithofacies D package from Fig. 3.19. The graphic log combines exposure on either side of the tape in the photo, and shows a series of reverse graded sub-packages, as well as lithofacies A above and below. The graphic log illustrates the graded relationship between lithofacies D (sub-package 4) and the overlying lithofacies A. The vertical scale of the graphic log is in centimetres, and the horizontal logarithmic scale is in millimetres. Horizontal width represents estimated grainsizes.

3.4.4 Lithofacies D: Massive deposit (reverse graded sub-packages)

Relatively thin packages of lithofacies D are rare and spatially confined to the north and northeast sectors (Figure 3.11), occurring exclusively within lithofacies A (Figure 3.19). Packages are up to 2 m thick, and consist of poorly sorted, reverse graded, tabular shaped sub-packages (Figure 3.20). Lithofacies D is consistently lithic-poor (< 1%) and has a pumice lapilli concentration that varies between 1 and 40%. The size distribution of the pumices is comparable to lithofacies A and, packages of lithofacies D have a similar fine- to coarse-ash matrix with variable crystal content.

The distinguishing feature of lithofacies D is the conspicuous reverse grading of pumices within each sub-package. Sub-packages are defined by a fine-grained pumice lapilli base with a rapid increase in grainsize that continues to the top. The coarse-grained top of one sub-package is usually in sharp contact with the fine-grained bottom of the overlying sub-package (Figure 3.21); the change in grainsize occurring over a few millimetres. The contact is sometimes visible as a sharp line or as a blurred or mingled demarcation where the fine-grained material above appears to have been deposited around the large clasts of the sub-package below. In some examples, individual sub-packages are not so obvious and the reverse grading is not so simple; instead, there appears to be a diffuse internal stratification similar to lithofacies B. The stratification is defined by alternations between lapilli-free zones and lapilli-rich zones (10 to 30 mm thick laminae) with a relatively uniform pumice grainsize. The alternations ultimately cease and blend into a uniform pumice lapilli concentration at the top of the sub-package.

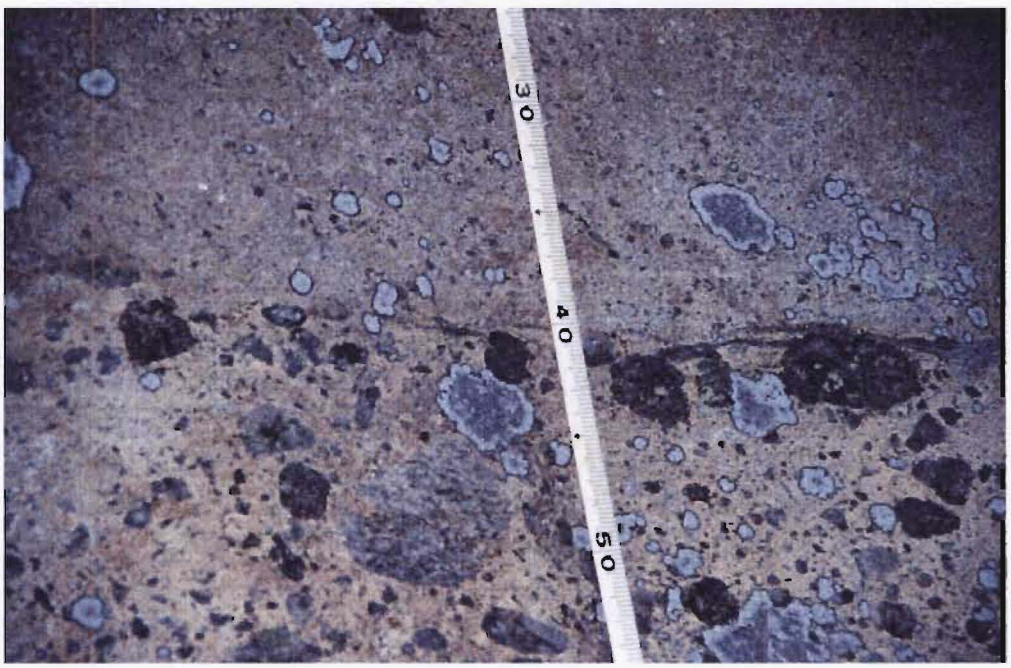

Figure 3.21 Close-up view of the sharp upper contact of sub-package 3 (from Figure 3.20) at the 40 cm mark on the tape.

3.4.5 Lithofacies E: Bedded deposit (channel bedded)

Lithofacies E is exposed to the east, southeast, and south (Figure 3.11), and is usually in contact with or in the vicinity of both structureless and diffusely stratified lithofacies A and B. Packages of lithofacies E are defined by a range of sub-lithofacies (Table 3.4) and conspicuous channel and fill structures (the term 'channel' is used here in a descriptive sense with no genetic connotations). The channel and fill structures are characterised by cross and plane-parallel beds that are continuous up to a few metres before they wedge out against a channel margin or are truncated by an overlying channel and fill package (Figure 3.22 and Figure 3.23). Infill cross beds are actually trough bedded, mimicking the curvature of the channel margin and thickening towards the channel axis. The cross beds grade upwards into plane-parallel beds that are less affected by the shape of the channel. Only a portion of each channel and fill package is preserved due to the erosion associated with overlying channels. From the dimensions of their preserved portions, it can be estimated that full-size channels are 5 to 10 metres wide and 0.5 to 1 metre deep. In cross-section, stacked and interdigitated channels exhibit uniform channel (axes) directions, inferred from their consistent shapes and orientations (see Figure 3.22). Together, the interdigitated channel structures form laterally extensive exposures (> 100 m) that are quasi-conformable with lithofacies A and/or B packages above and below (see Section 3.5.4).

Sub-lithofacies	Diagnostic Characteristics
Massive, structureless beds	Identical lithology to lithofacies A, pumice lapilli concentrations range from 5 to 25%, matrix is relatively fine-ash poor
Diffusely stratified beds	Pumice lapilli concentration bands (10 to 40% pumice); the lower the concentration of pumice lapilli within the bands, the lower the concentration between the bands (the reverse is also true)
Reverse graded beds	Beds with a finer-grained base and a coarse pumice lapilli top, 10 to 30% pumice lapilli
Coarse ash beds	Relatively fines-poor, no pumice lapilli, poorly sorted, resembles the fine to coarse ash matrix of the massive lithology
Pumice-lapilli supported beds	Fines-poor, up to 90% pumice lapilli, very lithic-poor, little to no matrix
Fine ash beds	Pumice-poor, massive, contains conspicuous accretionary lapilli.

Table 3.4 Sub-lithofacies of lithofacies E, and their diagnostic characteristics

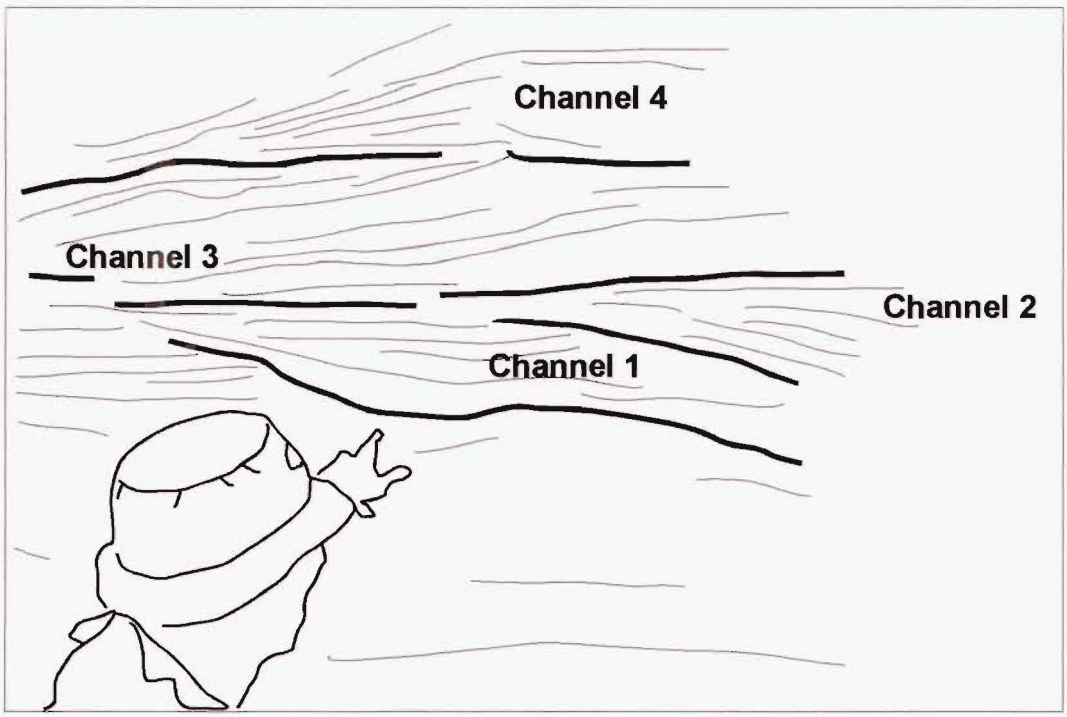

Figure 3.22 Locality Oh228, U17/774063. View of stacked and interdigitated channel and fill packages (lithofacies E). The channels show a uniform morphology and orientation. Curvature of infill beds that thicken towards channel axes are consistent with a transport direction that is roughly parallel to the direction the finger is pointing (transport is either away from, or towards the person).

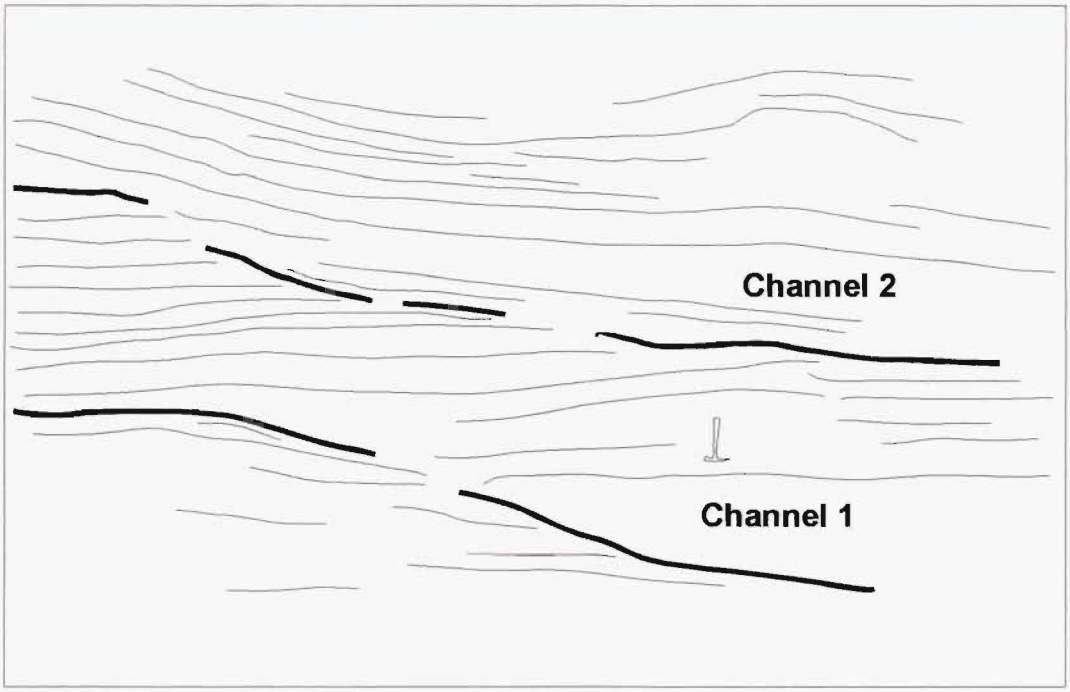

Figure 3.23 Locality Oh130, U16/80301172. Erosive contact between 2 lithofacies E channel and fill packages. The orientation and morphology of both channels are consistent with a transport direction that is parallel with the direction the photo is taken (either into or out of the page).

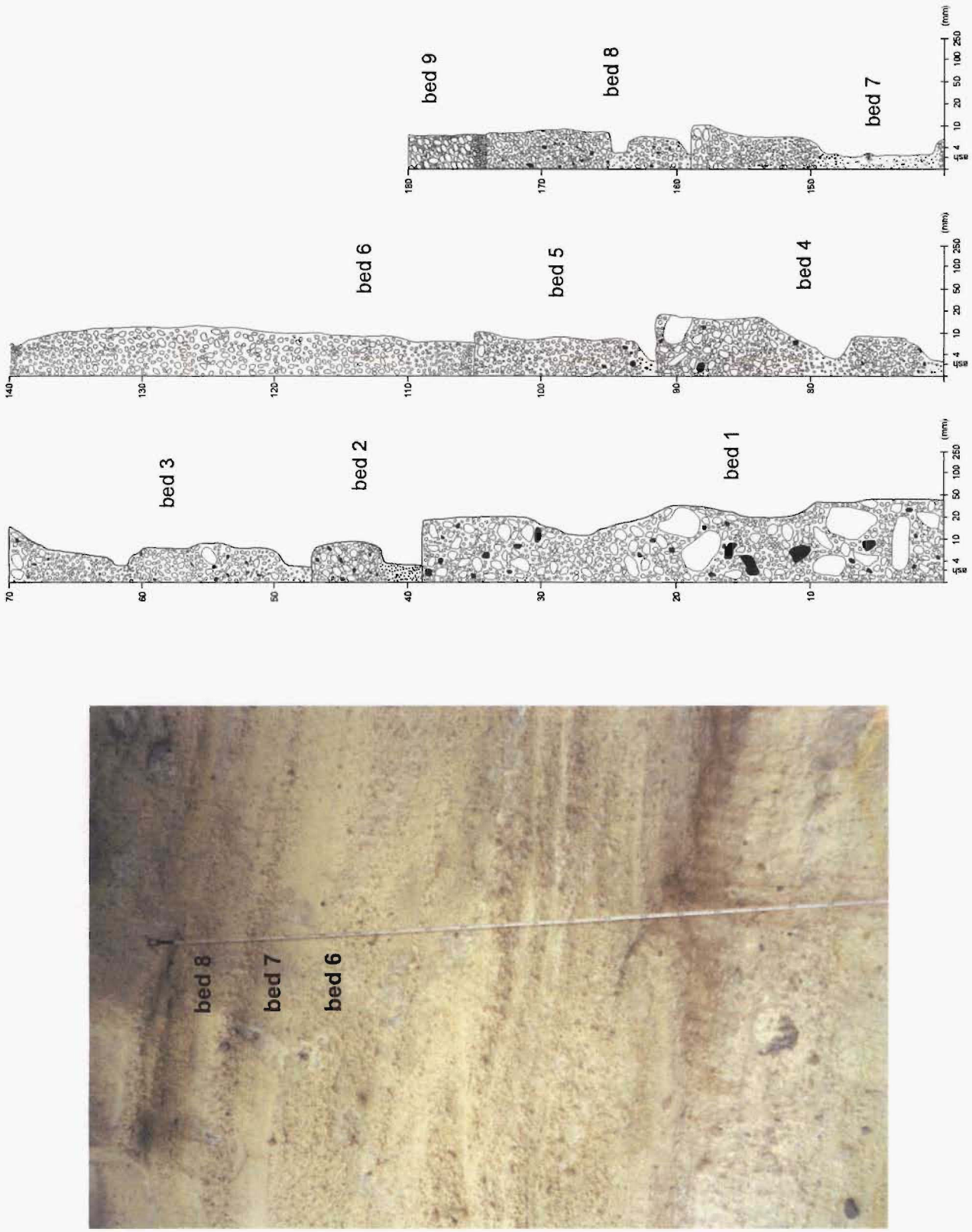

Figure 3.24 Locality Oh130, U16/80301172. Close-up view of Fig. 3.23, and graphic log. Channel fill beds are relatively fines-poor and include massive, reverse graded, and reverse to normal graded lithologies. The graphic log depicts the material behind the tape. The vertical scale is in centimetres and the horizontal logarithmic scale is in millimetres. The width of the horizontal scale represents estimated grainsizes.

The infill beds are centimetres to decimetres thick and are lithologically diverse (Table 3.4). Massive beds predominate and include structureless, diffusely stratified, and reverse graded lithologies (sub-lithofacies; Figure 3.24 and Figure 3.25). As with lithofacies C, it can be difficult to distinguish diffusely stratified from reverse graded sub-lithofacies, i.e. some diffusely stratified beds are not simply comprised of diffuse pumice concentration bands, but borderline on reverse graded beds with a high concentration of larger pumice clasts at the top of each bed. Other sub-lithofacies observed in packages of lithofacies E include fine to coarse ash beds, pumice-lapilli supported (fines-poor) beds, and fine-ash-rich accretionary lapilli-bearing beds. These three sub-lithofacies are much more abundant in the eastern exposures of

Figure 3.25 Locality Oh165, U16/80411160. View of channel fill beds that depict a range of lithofacies E sub-lithofacies. See enlarged photos of (a), (b), and (c) on following page. (a) thin pumice-lapilli supported beds that are reverse to normally graded, and very fine-grained ash beds with conspicuous accretionary lapilli and occasional pumice lapilli. (b) fine- to coarse-grained ash beds (lapilli-poor) overlying and truncating (out of the view of photo) a reverse graded pumice-lapilli supported bed. (c) massive, stuctureless bed at the bottom of the photo, that grades into a very fine-grained ash layer that contains scattered accretionary lapilli.

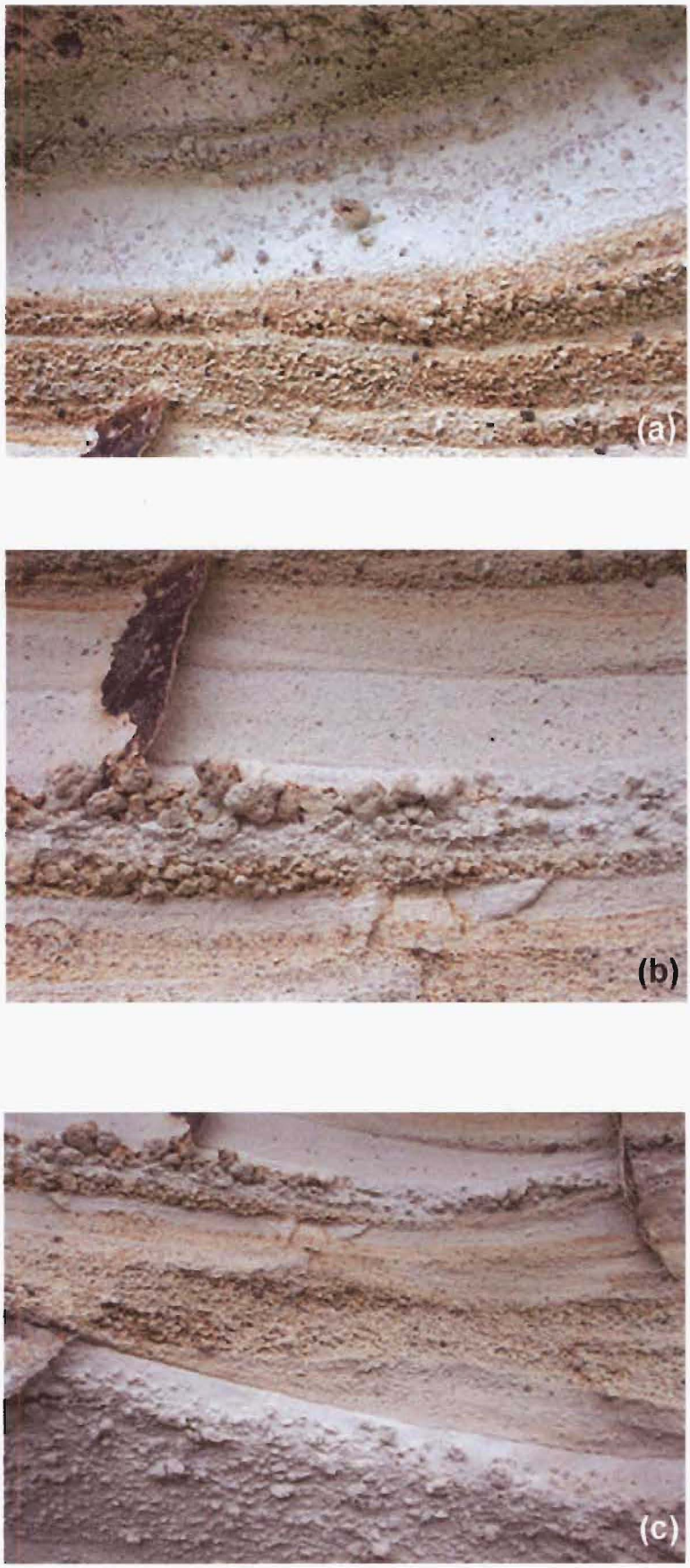

Figure 3.25

lithofacies E (Matapan lithofacies association, Section 3.5.4) and, in some cases, they comprise at least half of the channel fill (Figure 3.25). The fine ash beds are characterised by accretionary lapilli that are generally smaller (up to 30 mm) and much more uniform in size than those found in lithofacies B.

3.4.6 Lithofacies F: Bedded deposit (plane-parallel to cross-bedded)

Lithofacies F is normally observed in sharp or gradational contact with lithofacies A and has a restricted areal distribution on the northeast side of the field area (Figure 3.11). Lithofacies F is characterised by the same range of lithologies (sub-lithofacies, Figure 3.26) as lithofacies E (refer to Table 3.4); however, the lithofacies F sub-lithologies are organised into packages that are characterised by a significantly different architecture. Compared with the consistent interdigitated stacking of channel fill structures observed in lithofacies E (i.e. Figure 3.22), lithofacies F consists of a random arrangement of plane-parallel bedded packages, cross-bedded channel-fill packages, and interdigitated lithofacies A packages (Figure 3.27). Observed individually, plane-parallel packages in Figure 3.28 are laterally more extensive (> 20 m) than the plane-parallel beds associated with the lithofacies E channel structures, and some channels (used here in the descriptive sense) are actually broader bowl-shaped structures (> 30 m wide, Figure 3.29). In lithofacies F, the bowl-shaped structures, as well as smaller channel structures (Figure 3.30), exhibit random channel axis directions (Figure 3.31) that are inferred from variable channel orientations and morphologies.

As mentioned above and shown in Figure 3.27, lithofacies F packages are interdigitated with structureless lithofacies A packages, whereas stacked lithofacies E packages, together, form a quasi-conformable stratigraphic relationship with underlying and overlying lithofacies A or B packages (Section 3.4.5). The result of their distinctive associations with massive lithofacies A and/or B is that lithofacies F is laterally discontinuous over tens of metres, whereas lithofacies E can form exposures that are laterally continuous over hundreds of metres (Section 3.4.5). This is, perhaps, the fundamental distinction between lithofacies F and E and is discussed in further

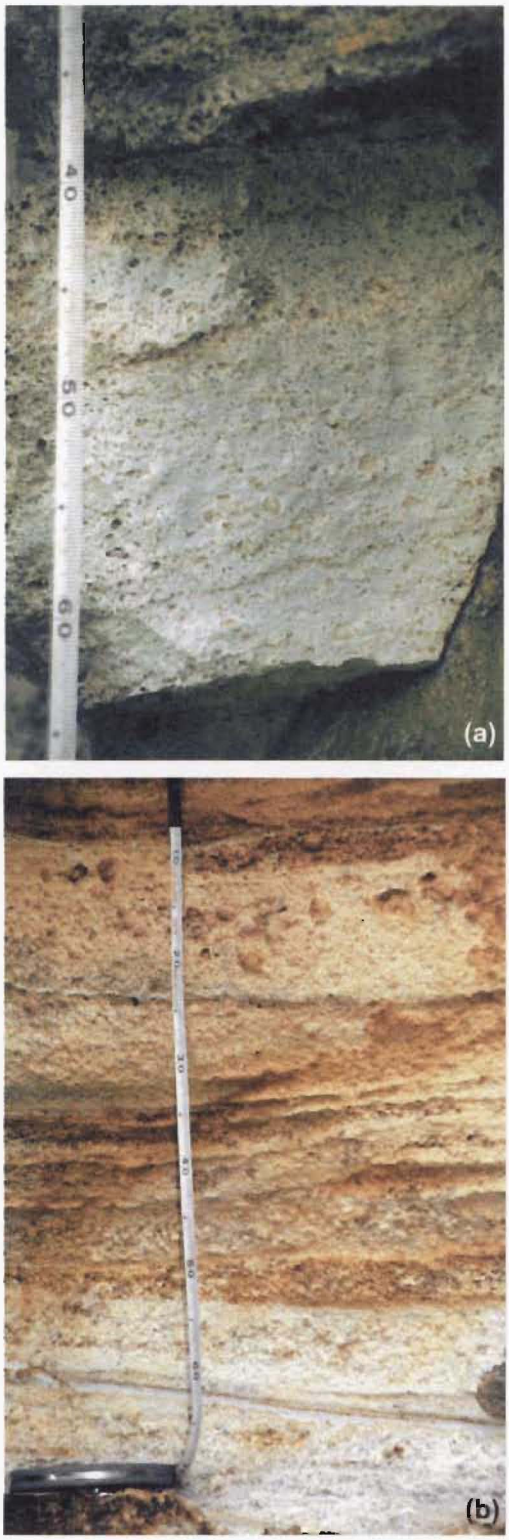

Figure 3.26 Lithofacies F is sometimes difficult to characterise because silica case-hardening can obscure the grain fabric and in places the pumices have been eroded, leaving behind a honeycomb-like texture. (a) Locality Oh120, U16/78991439. Honeycomb-like texture reveals a diffusely stratified lithology. (b) Locality Oh124, U16/79331458. Thin fine- to coarse-grained ash beds (pumice-lapilli poor), massive structureless beds (i.e. bed at the top of the photo), and reverse graded pumice-lapilli supported beds. (c) Locality Oh262, U16/79651465. Fine- to coarse-grained ash bed with scattered accretionary lapilli. (d) Locality Oh267, U16/798146. Alternating fine-grained ash beds with ripple laminations, and reverse graded to structureless beds with conspicuous accretionary lapilli. Lens cap is 7.5 cm in diameter.

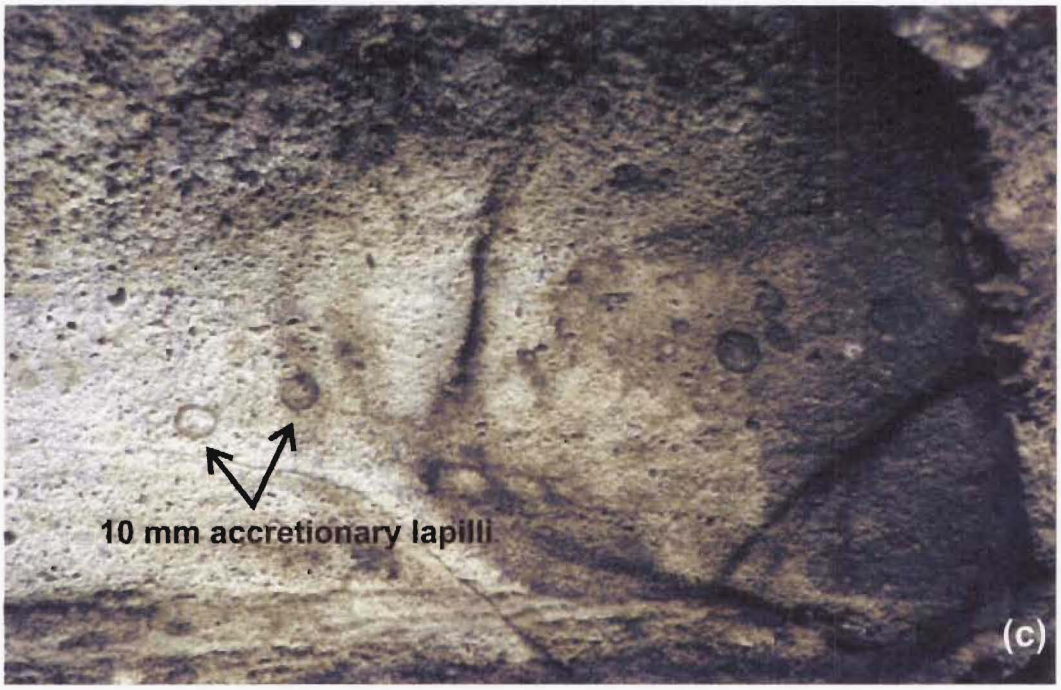

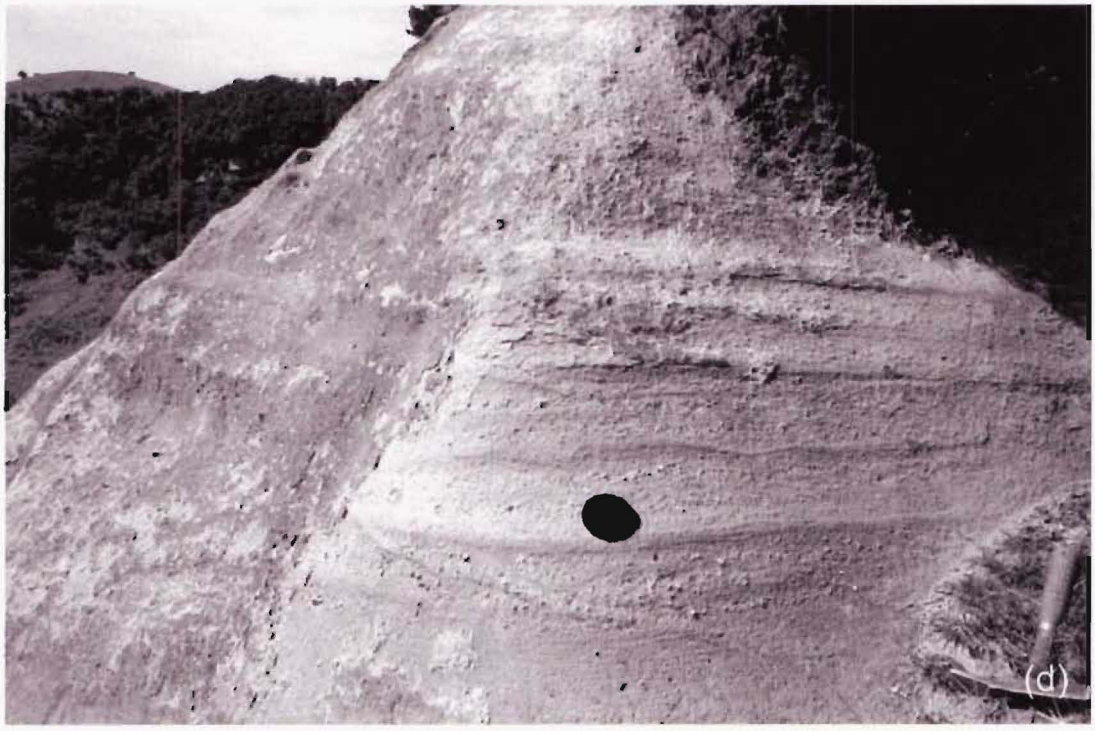

Figure 3.26 (con't)

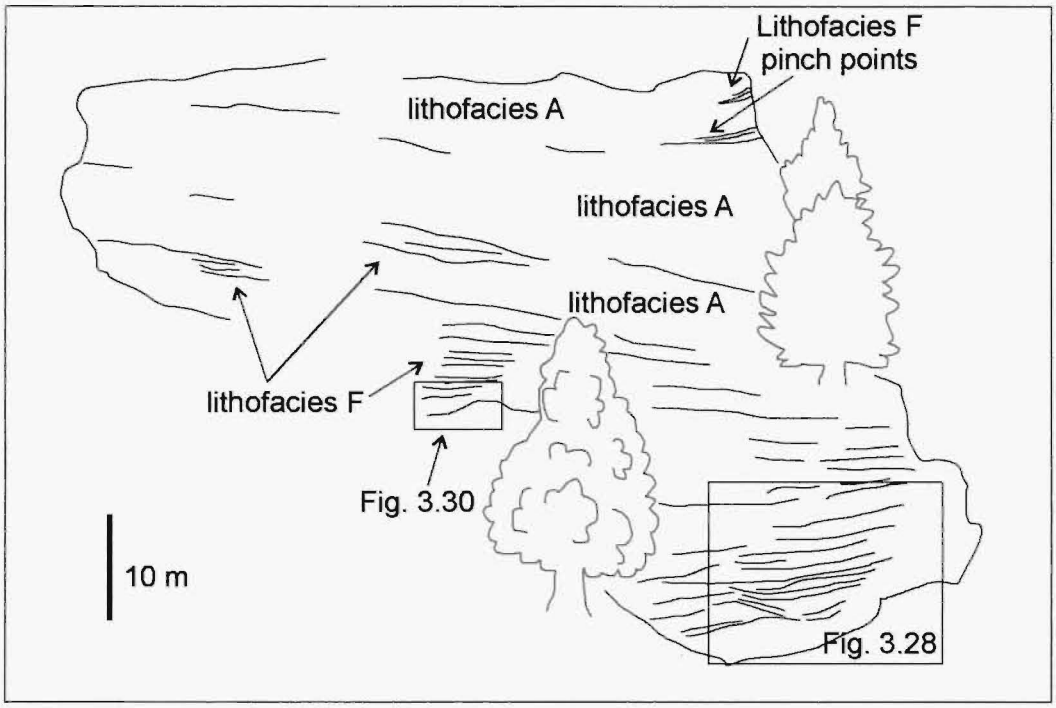

Figure 3.27 Locality Oh124. View of alternating and interdigitated lithofacies A and F deposits. Lithofacies F is often observed wedging or pinching out between overlying and underlying lithofacies A packages. Broad bowl-shaped structures (Fig. 3.28) and channel structures (Fig. 3.30) are observed in the cliff section.

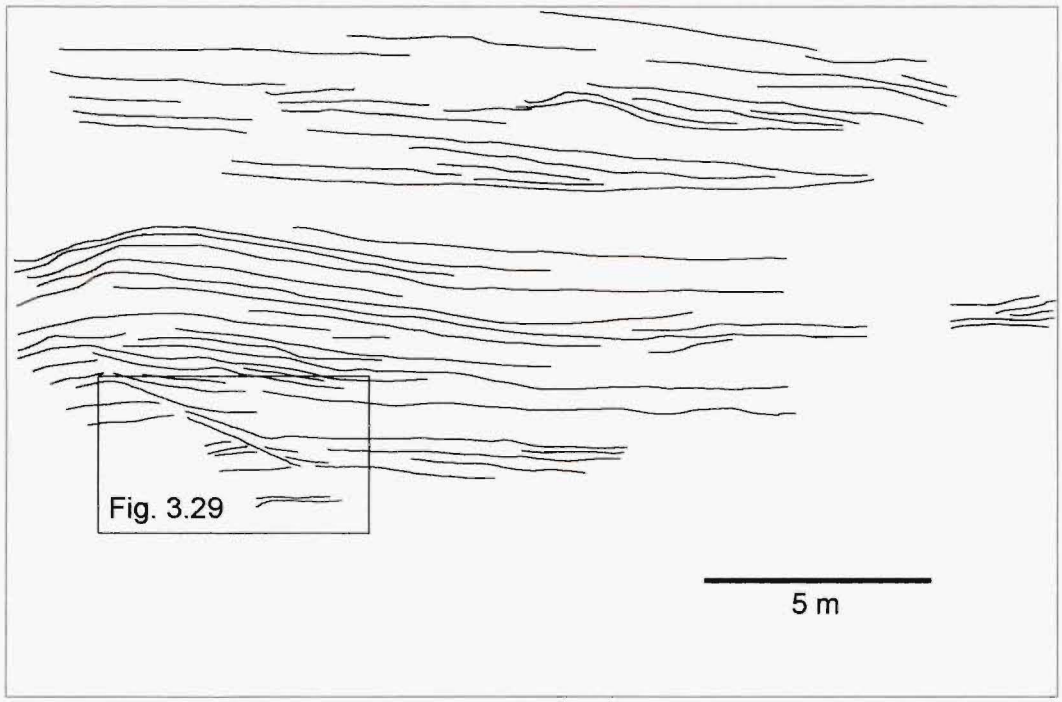

Figure 3.28 Locality Oh124, U16/79331455. Cross- and plane parallel- beds (lithofacies F). Cross-bedding is associated with a broad bowl-shaped structure > 30 metres across (only a portion of the bowl-shaped structure is exposed).

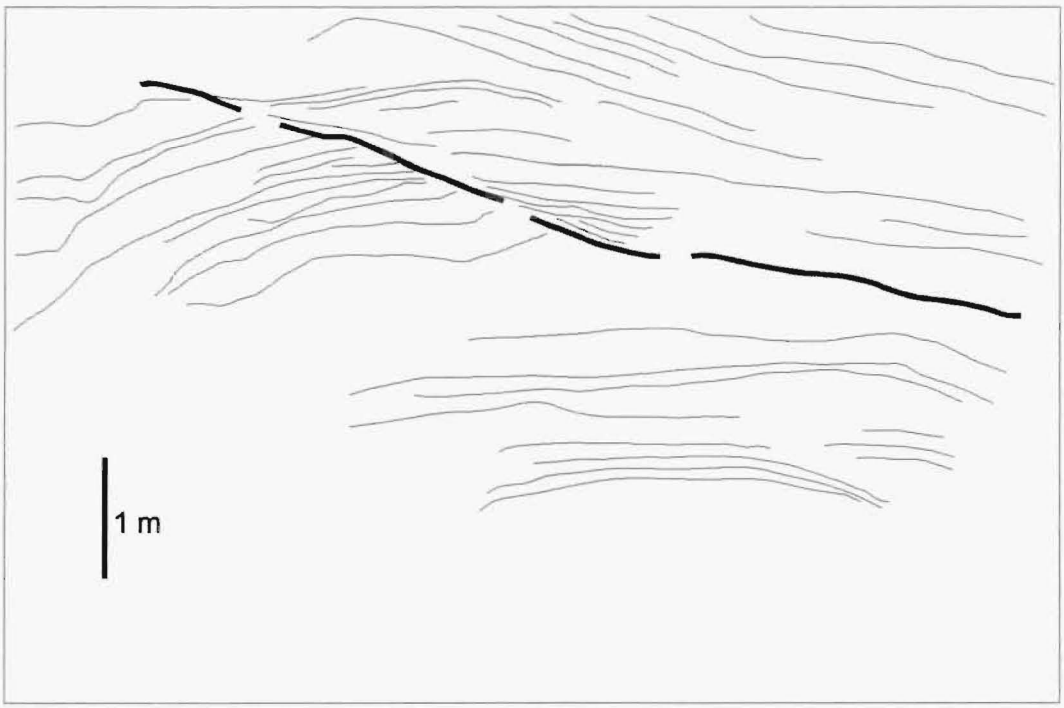

Figure 3.29 Close-up view of the margin of the broad bowl-shaped structure. Infill beds wedge out against the margin and thicken towards the middle of the bowl.

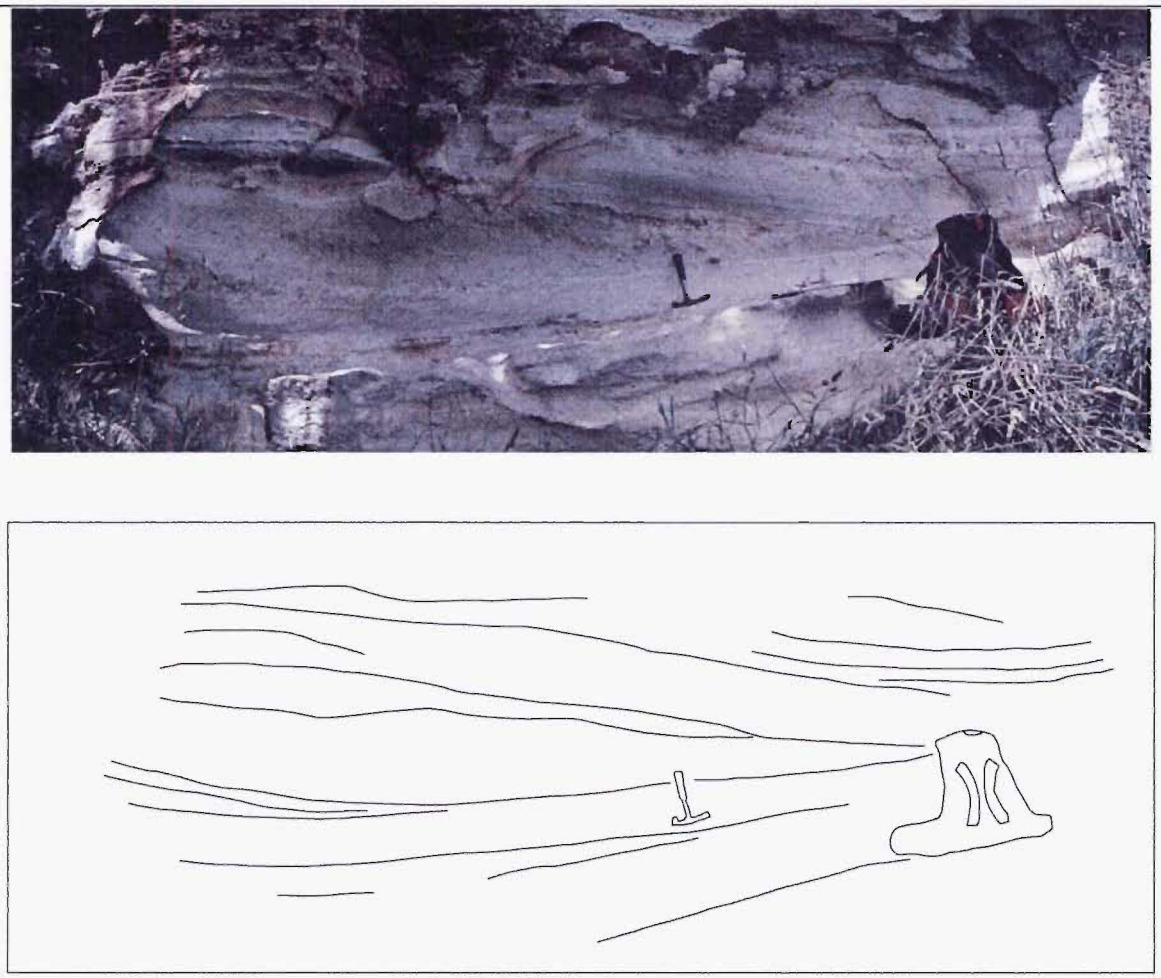

Figure 3.30 Erosive contact (above the hammer) between 2 channel fill structures. The channels have a similar morphology to lithofacies E channels.

detail with respect to the Tahunaatara lithofacies association (*Tla*, Section 3.5.3) and the Matapan lithofacies association (*Mla*, Section 3.5.4), respectively.

One other distinction between lithofacies F and E, is the presence of sandwaves which are sometimes observed in close association with lithofacies F plane-parallel bedding. The sandwaves are rare, and it is not apparent whether this is due to lack of outcrop exposure or to a limited, original distribution. Observed sandwaves are relatively miniature (compared with lithofacies C giant-dunes) with waveheights up to 5 cm and wavelengths up to 750 cm (Figure 3.32).

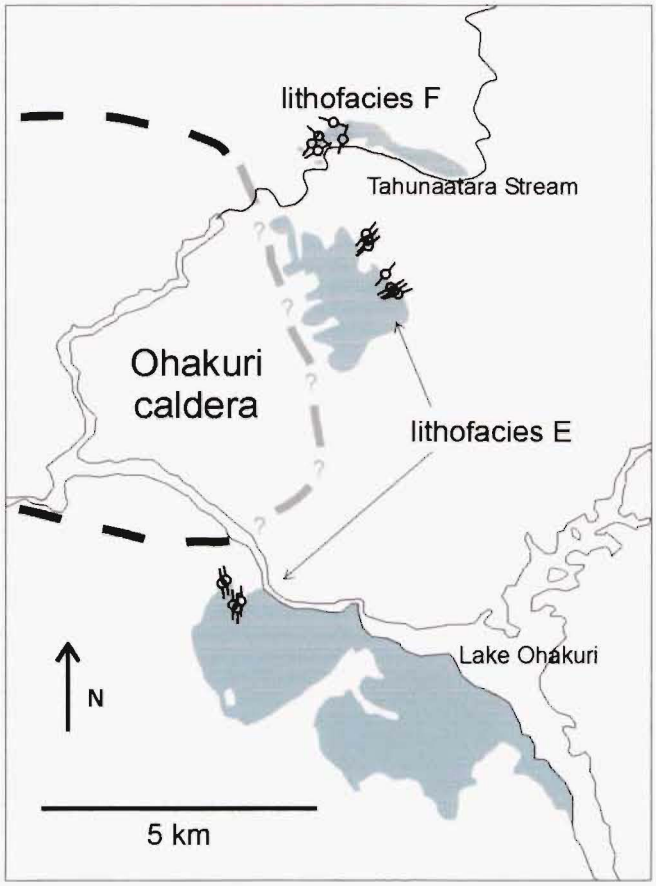

Figure 3.31 Channel axes directions for lithofacies E and F, inferred from channel orientations and morphologies.

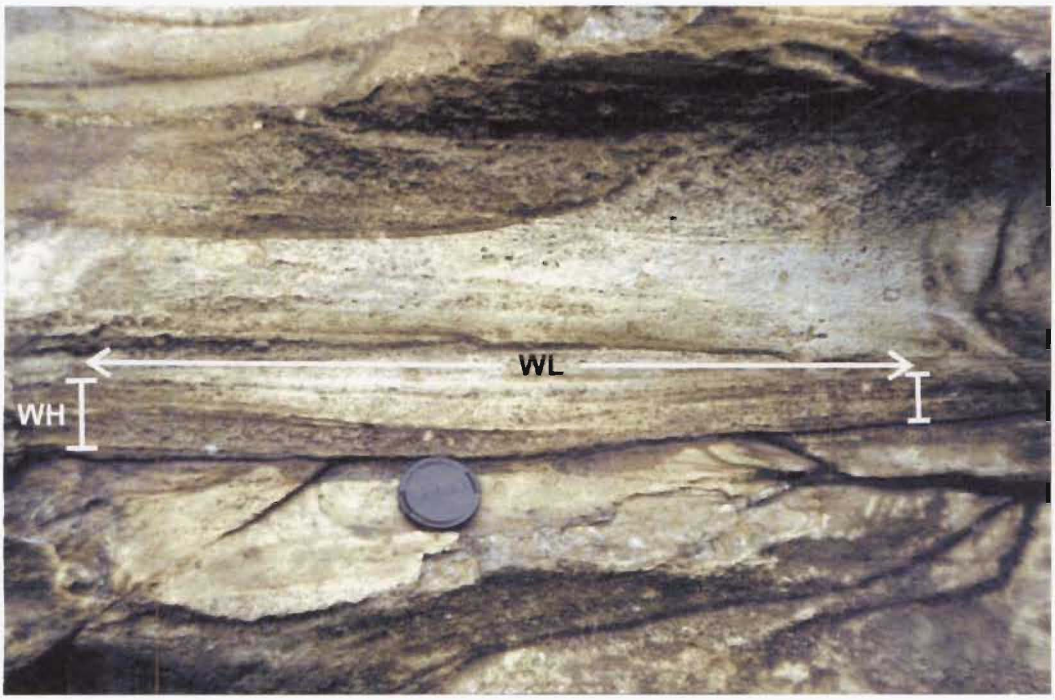

Figure 3.32 Locality Oh262, U16/79651465. Lithofacies F sandwave (waveheight (WH) is ~ 5 cm and wavelength (WL) is ~ 75 cm). Lens cap is 7.5 cm in diameter.

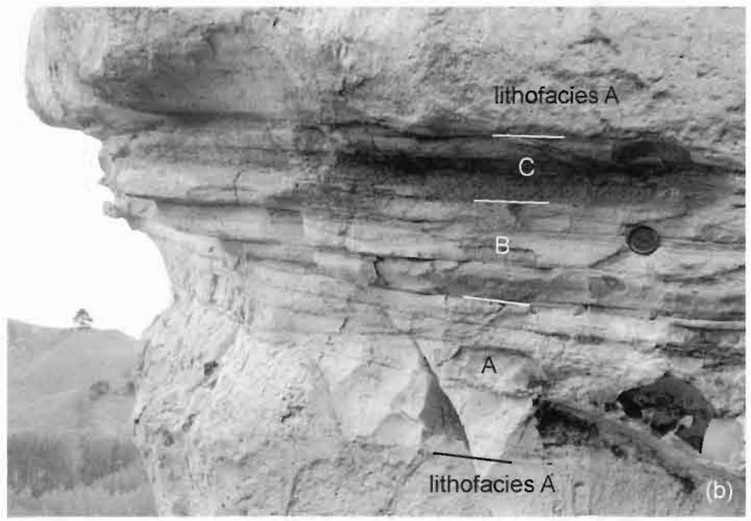

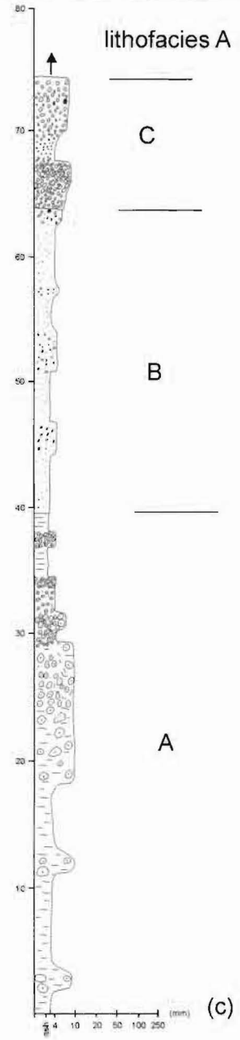

Figure 3.33 (a) View of cliff sections with continuous lithofacies G packages between lithofacies A and B packages. Conspicuous horizontal break in cliff panorama is a plane-parallel package > 200 m in lateral extent and ~ 80 cm thick. (b) Locality Oh170, U16/84021366. Close-up of plane-parallel package characterised by very fine-grained ash beds with accretionary lapilli, fine- to coarse-grained crystal-rich ash beds, and highly concentrated pumice-lapili supported beds. (c) Graphic log showing the variation in lithologies in the close-up photo. Vertical scale is in centimetres and horizontal logarithmic scale is in millimetres. Width of horizontal scale represents estimated grainsizes.

3.4.7 Lithofacies G: Bedded deposit (plane-parallel bedded)

Lithofacies G is confined to the eastern sector of the field area (Figure 3.11) and is characterised by a succession of plane-parallel beds, some with conspicuous accretionary lapilli. Plane-parallel bedded packages of lithofacies G are always sandwiched between packages of massive deposits (lithofacies A), with a sharp undulatory contact on the top and at the base. One particular package of plane-parallel beds is continuous for > 200 m (Figure 3.33a), with a consistent thickness of 80 cm (Figure 3.33b). The predominant feature of this package and other similar packages, is the abundance of accretionary lapilli and crescent-shaped accretionary lapilli fragments. In general, the accretionary lapilli are < 10 mm in diameter with a maximum diameter of 27 mm. They are found in very fine- to fine-grained ash beds and are either scattered throughout the bed or occur as concentration layers with up to 50% accretionary lapilli. In some instances, packages are composed of a series of accretionary lapilli-bearing beds whereby contacts usually separate beds with accretionary lapilli of different sizes (Figure 3.33c). Because of the pervasive silicification and case hardening of the outcrops, it is sometimes difficult to determine whether the juxtaposed accretionary lapilli beds are, in fact, discrete; or whether there is a continuous accumulation of accretionary lapilli and therefore a graded relationship between the beds. Other lithology types included in lithofacies G are thin laminated to cross-laminated coarse crystal-rich ash beds and highly concentrated pumice lapilli (~ 70%) beds (Figure 3.33c).

Lithofacies associations	Lithofacies components	Diagnostic characteristics
Gold (*Gla*)	Lithofacies A, B, and D	> 100 m high cliff outcrops of continuous, structureless lithofacies A deposits
Forest (*Fla*)	Lithofacies A, B, C, and E	Fresh, moderately compacted (not indurated) deposits amenable to granulometry work; vertical contact relationships and lithofacies variation similar to variation observed in OHDG-3 drill core (Appendix 5)
Tahunaatara (*Tla*)	Lithofacies A, B, and F	Interdigitated packages of lithofacies A and F; erosive contact relationships; broad bowl-shaped structures; random channel orientations
Matapan (*Mla*)	Lithofacies A, B, and E	Laterally continuous exposures of quasi-conformable, stacked lithofacies; uniform channel orientations
Stag (*Sla*)	Lithofacies A and G	Alternating packages of structureless lithofacies A and plane-parallel lithofacies G deposits, stacked in a quasi-conformable fashion

Table 3.5 Summary of the Ohakuri lithofacies associations and their characteristics.

3.5 Ohakuri lithofacies associations

Sedimentologists use the term 'lithofacies associations' to group lithofacies that occur together and are genetically and geographically related (Reading, 1986). Because the Ohakuri deposits exhibit widespread lithofacies variations, I have adopted the sedimentological approach and divide the deposits into 5 geographic lithofacies associations: Gold (*Gla*), Forest (*Fla*), Tahunaatara (*Tla*), Matapan (*Mla*), and Stag (*Sla*). The lithofacies associations are all located within 8 km of the inferred Ohakuri caldera rim with the exception of *Gla* which can be observed both proximally and up to 16 km from the inferred caldera rim (Figure 3.34). Each lithofacies association and the relationship between their lithofacies components are described in the following sub-sections, and summarised in Table 3.5.

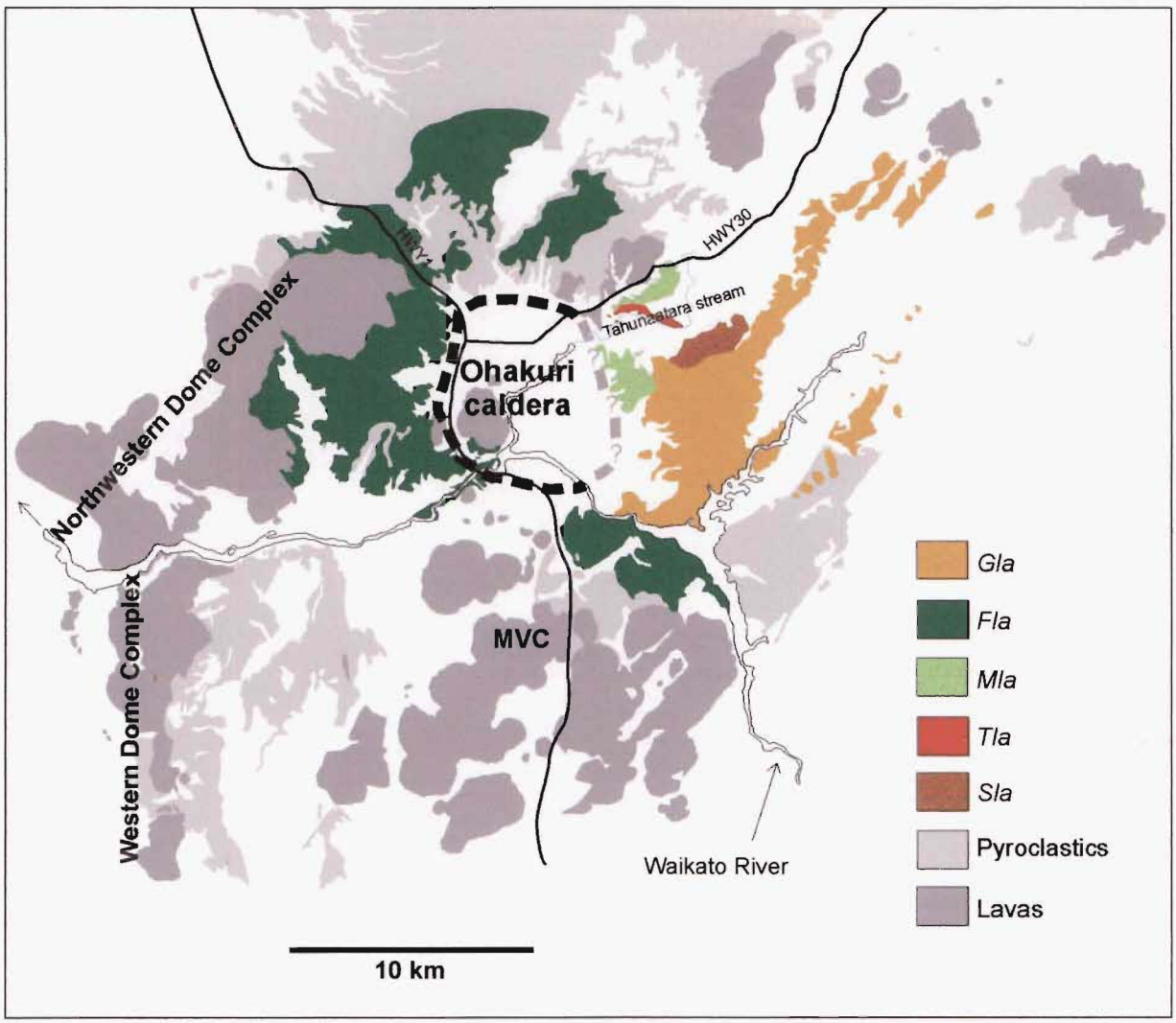

Figure 3.34 Distribution of Ohakuri lithofacies associations. Lavas and pyroclastic deposits are the same as from Figures. 3.5 and 3.11.

3.5.1 Gold lithofacies association (Gla)

The Gold lithofacies association (*Gla*) is named after Alan Gold, who owns a large farm block in the study area. The *Gla* comprises the majority of the eastern and northeastern sectors of the field area (Figure 3.34), and consists of rolling hills dissected by NE-SW trending streams with some steep cliff sections and the highest point on the eastern side of the field area, Ngapoipoiatore trig (590 m ASL). The steep cliff sections provide excellent exposure of the Ohakuri pyroclastic deposits, with access along the sides of the cliffs.

Nowhere within the *Gla* is the base of the Ohakuri pyroclastic deposits exposed. The *Gla* is composed predominantly of structureless lithofacies A deposits with rare, thin packages of reverse graded lithofacies D deposits. Lithofacies A deposits can be greater than 100 metres thick in cliff outcrop sections (Figure 3.14) with subtle vertical variation in pumice concentration and maximum pumice sizes. There is no vertical variation in lithic clast types and, in general, the massive deposits of *Gla* are lithic-poor (< 1%). However, there are rare sections with relatively high lithic concentrations (~ 5%). One of these rare sections is located on the Gold Farm and is ~ 40 m thick and covers an area of 1 km^2 (including localities Oh133, Oh188, and Oh198; see Map 1). Not only is there an increased lithic concentration (~ 5%) but the section is characterised by a high concentration (> 35%) of pink-coloured, crystal-rich pumices up to 440 mm in diameter, and a coarse grained ash- and crystal-rich matrix that is also pink (Figure 3.35). Originally, the pink massive deposits were not considered to be Ohakuri pyroclastic deposits, being mapped by Martin (1961) as the Marshall Ignimbrite. However, careful observation reveals that the highly concentrated pink deposits grade down into buff to light gray coloured, less-concentrated deposits that are unambiguously lithofacies A Ohakuri material. In addition, the pink deposits contain the rare type 3 pumice that is unique to the Ohakuri pyroclastic deposits. The original lateral extent of the pink deposits is unknown due to a lack of outcrop exposure beyond this area.

Rare groups of reverse graded sub-packages (lithofacies D), ranging from tens of centimetres to a couple of metres thick, occur within the massive deposits. Packages of lithofacies D have a conformable, gradational relationship with lithofacies A (Figure 3.20).

3.5.2 Forest lithofacies association (Fla)

The Forest lithofacies association (*Fla*) has the largest areal distribution (predominantly located within Carter Holt Harvey's Kinleith Forest) in the field area, forming an ~ 180° arc around the south, southwest, west, and northwest sides of the Ohakuri caldera (Figure 3.34). *Fla* deposits overlie a variable substrate that includes lavas and fan material from the Northwestern Dome Complex, MVC lavas, mesas of Korotai ignimbrite, eroded hillocks of Pokai ignimbrite, and flat-

Figure 3.35 Locality Oh194, U16/81921101. Massive, highly concentrated, crystal-rich, pink-coloured deposits with large pumice and lithic clasts. The pumice in the bottom photo is 440 mm long.

Locality	Lithofacies	Lithology (sub-lithofacies)	Median (Md_ϕ)	Sorting (σ_ϕ)	F_1	F_2
Oh178a	A	massive	1.23	3.49	63.39	22.80
Oh178b	B	diffusely stratified	3.33	1.95	92.96	31.82
Oh178d	B	diffusely stratified	3.10	1.91	91.57	26.28
Oh178e	B	diffusely stratified	2.98	2.59	84.32	34.66
Oh152b	B	diffusely stratified	1.71	3.18	69.32	21.92
Oh152e	B	diffusely stratified	3.25	2.15	89.89	33.00
Oh155a	B	diffusely stratified	1.88	3.56	69.17	25.98
Oh155b	B	diffusely stratified	2.89	2.36	86.01	22.55
Oh155c	B	diffusely stratified	2.23	3.25	71.11	24.50
Oh155d	B	diffusely stratified	2.98	2.43	86.92	28.96
Oh148f	C	diffusely stratified	0.99	2.14	68.26	7.52
Oh148g	C	diffusely stratified	1.57	2.44	73.72	8.78
Oh148h	C	pumice concentration band	-0.77	1.78	34.78	3.65
Oh148i	C	diffusely stratified	1.76	2.75	71.75	17.87
Oh169f	C	diffusely stratified	2.65	2.40	84.80	25.77
Oh169g	C	diffusely stratified	2.65	2.95	79.49	30.50
Oh184a	C	reverse graded-diffuse	2.03	2.03	84.77	17.63
Oh184b	C	reverse graded-diffuse	2.78	1.97	92.10	24.63
Oh184c	C	pumice concentration band	1.96	2.97	73.89	18.03
Oh204a	C	pumice concentration band	1.21	3.28	65.25	21.57
Oh204b	C	diffusely stratified	3.08	2.44	85.58	31.35
Oh204c	C	pumice concentration band	2.56	3.04	77.17	29.72
Oh204d	C	diffusely stratified	3.29	2.19	91.16	33.27
Oh100a	E	reverse graded-diffuse	1.45	1.61	82.64	5.95
Oh100b	E	pumice concentration band	0.41	2.34	58.13	6.23
Oh100d	E	massive	1.13	1.95	72.77	6.46
Oh100f	E	massive	-1.10	2.13	36.01	3.10
Oh101d	undifferentiated	massive	1.40	2.06	76.27	10.76
Oh114c	undifferentiated	massive	1.05	1.83	65.63	11.71
Oh114d	undifferentiated	crystal-rich, fines-poor layer	0.99	1.98	70.75	7.52
Oh114a	undifferentiated	fines-poor layer	0.50	1.76	55.98	10.62
Oh114b	undifferentiated	reverse graded-diffuse	1.93	1.90	85.77	14.61
Oh155e	undifferentiated	massive	0.58	2.73	59.66	6.38
Oh155f	undifferentiated	massive	3.23	2.24	90.12	28.67

Table 3.6 Grainsize data for the Ohakuri *Fla* deposits including Inman (1952) parameters for median diameter and sorting, and wt% finer than 1 mm (F_1) and 1/16 mm (F_2).

topped, gently inclined Mamaku ignimbrite (see Section 3.2.4). The thickness of *Fla* deposits ranges from ~ 10 m at the edge of the Mamaku plateau to ~ 100 m where they lap up against the Northwestern Dome Complex. The *Fla* distribution area correlates with the area of Ohakuri deposits that lacks the type 3 pumice (compare Figure 3.34 with Figure 3.5). In addition, *Fla* is characterised by conspicuous andesitic juvenile blebs and a lithic population that is dominated by obsidian fragments.

The *Fla* is the only lithofacies association that is not indurated or silicified. The reason for this may be related to the fact that these deposits are outside or on the margin of the Rotorua-Ohakuri volcanotectonic depression (see Section 2.2.2). Compared with the lithofacies associations within the depression, *Fla* is thinner, overlies higher ground, and has a fresh-rock substrate. All these factors may have prevented cementation associated with groundwater and geothermal processes. As a result, the fresh and moderately compacted nature of the *Fla* makes it amenable to granulometry work. Grainsize samples were collected at 11 exposures

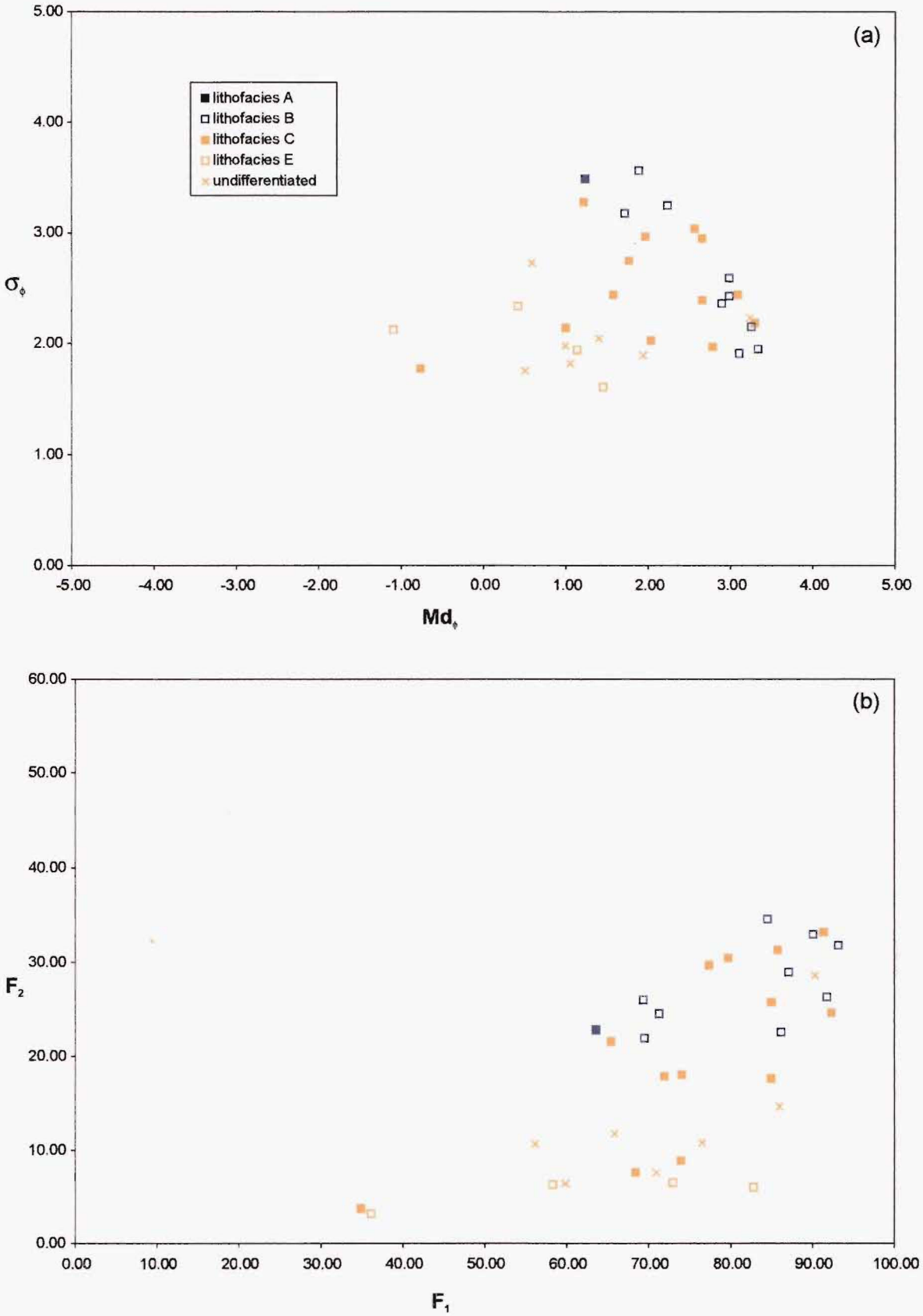

Figure 3.36 Grainsize distribution for the Ohakuri *Fla* deposits. (a) σ_ϕ vs. Md_ϕ (b) F_2 vs. F_1.

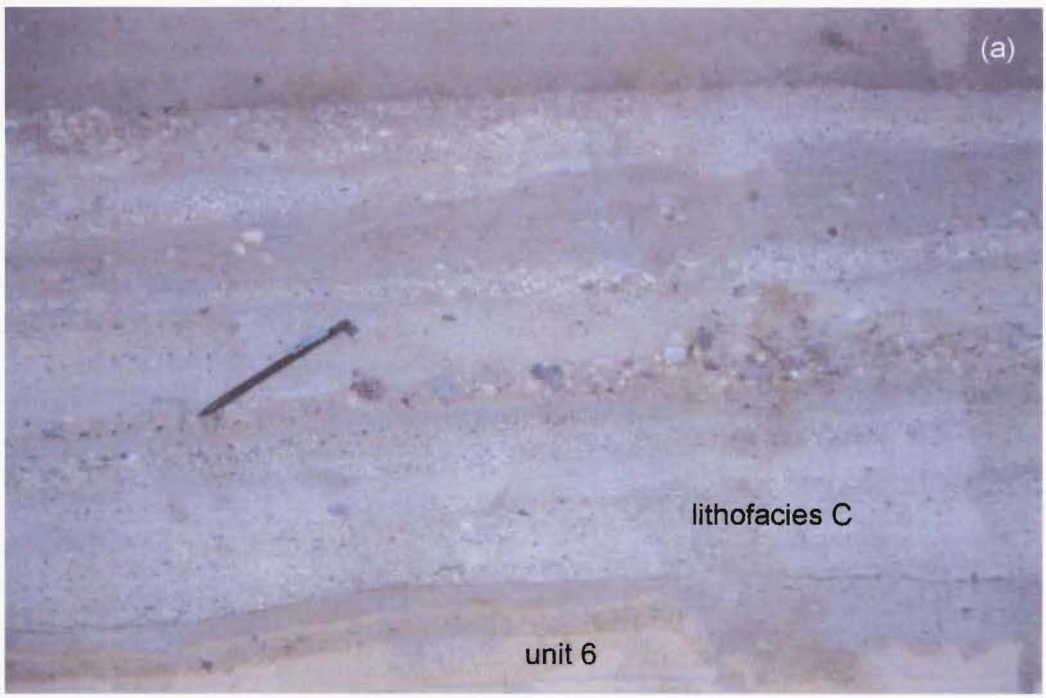

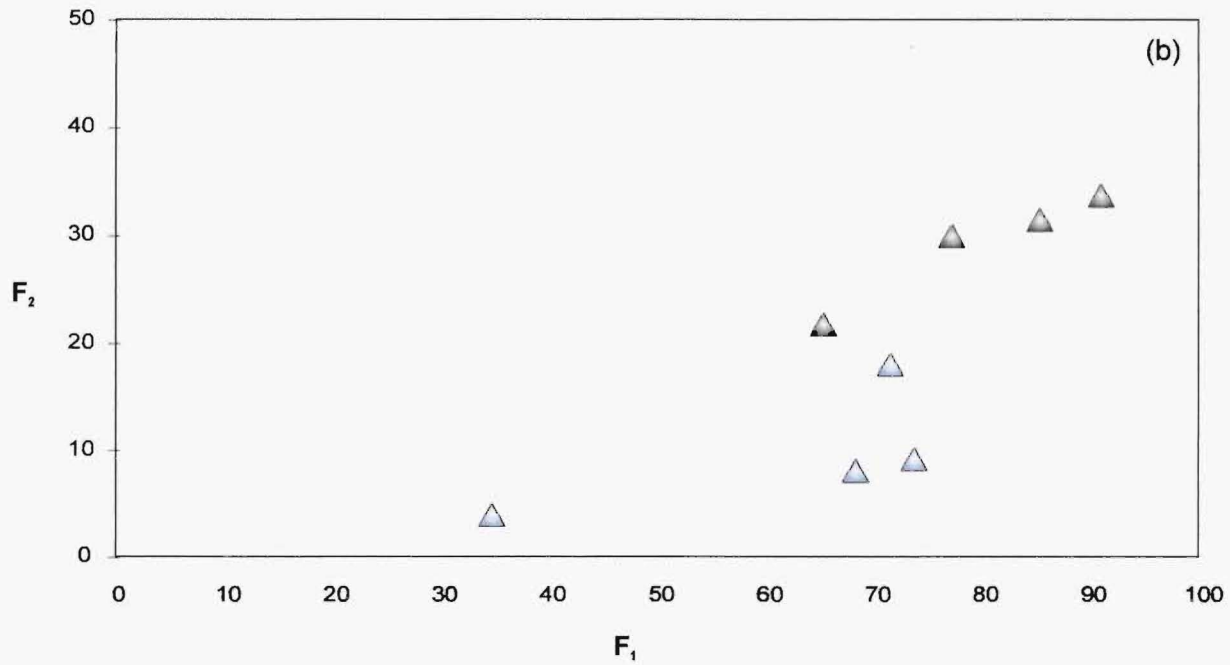

Figure 3.37 (a) Locality Oh148, U16/71301572. Relatively lithic-rich and fines-poor base of Ohakuri lithofacies C overlying unit 6 from the pre-Ohakuri airfall sequence (Section 2.2.2). Pencil is 15 cm long. (b) F_2 vs. F_1 variation diagram for Ohakuri lithofacies C. Blue triangles represent basal deposits and gray triangles represent samples from higher up in the lithofacies C stratigraphy.

from 4 different lithofacies, and 36 sieve analyses were performed (raw data is presented in Appendix 4). A summary of the granulometry results is presented in Table 3.6, and the data has been plotted on sorting (σ_Φ) vs. median diameter (Md_Φ), and wt% finer than 1/16 mm (F_2) vs. wt% finer than 1 mm (F_1) diagrams (Figure 3.36). Note that Inman (1952) parameters are used in this thesis to facilitate comparison with documented deposits from other volcanoes. In Figure 3.36, the grainsize distribution is presented for each lithofacies. Some of the data (undifferentiated) correlates with samples that were taken from outcrops where the lithofacies could not be distinguished because of limited exposure.

The *Fla* lithofacies A and B are characterised by the same lithological properties they exhibit elsewhere, and are often observed vertically grading in and out of one other. Both of these lithofacies are also found in vertical contact with the shallow channel and fill structures of lithofacies E. As depicted in Figure 3.22, the lithofacies E channels exhibit uniform morphologies and orientations. Granulometrically, lithofacies E is relatively fines-poor and better sorted than the other lithofacies (see Figure 3.36). Lithofacies C (giant-dune-bedded deposits) is not observed in contact (vertically or laterally) with the other lithofacies; however, it is regularly found in contact with the underlying Mamaku ignimbrite and pre-Ohakuri airfall units (Figure 2.14). The most laterally continuous exposure of lithofacies C is observed in a series of roadcut benches along State Highway 1. From photos and GPR profiles of the roadcut benches (see Chapter 4), the transport direction associated with the giant-dune forms has been determined and correlates with currents travelling from the southeast to the northwest. The base of lithofacies C is relatively lithic-rich with abundant obsidian lithics (Figure 3.37a). In addition, a F_2 vs. F_1 diagram (Figure 3.37b) shows that the basal deposits contain significantly less material < 1/16 mm than deposits higher up in the lithofacies C stratigraphy. With the exception of the basal deposits, lithofacies C exhibits the same grainsize distribution (Figs. 3.36) as massive lithofacies A and B.

3.5.3 Tahunaatara lithofacies association (Tla)

The Tahunaatara lithofacies association (*Tla*) is located in the northeast part of the field area (Figure 3.34) and draws its name from the stream that meanders through this section. The area is characterised by resistant cliffs of silica case-hardened Ohakuri pyroclastic deposits, ranging in height from 10 to 40 metres and separated or bisected by narrow gullies (~ 20 to 50 m wide). An approximately 1 km long section of cliff outcrops (between U16/78991439 and U16/797146) was documented in detail (Figure 3.38).

The *Tla* is constructed of a complex arrangement of structureless lithofacies A packages and cross bedded lithofacies F packages (Section 3.4.6). Laterally, packages of both lithofacies

Figure 3.38 Approximately 1 km long section of cliff outcrops along the Tahunaatara Stream. The closeup views show the variability of the massive (lithofacies A and/or B) to bedded (lithofacies F) ratios from one cliff outcrop to the next. Oh120 is characterised by an ~ 1:1 ratio of alternating massive and bedded packages. Oh124 has an ~ 1:1 ratio with an uncharacteristically thick accumulation of lithofacies F deposits in the bottom half. Oh127 and Oh260 are comprised entirely of lithofacies A deposits.

vary in thickness such that one cliff outcrop has a completely different ratio of massive to bedded deposits to the next outcrop (Figure 3.38). The inference is that lithofacies A and F are interdigitated in a complex fashion, and are not simply stacked. The degree of overlap of one package relative to another is difficult to determine because of the lack of exposure between cliff outcrops. This interdigitated arrangement highlights a fundamental distinction between lithofacies F and lithofacies E (see Section 3.4.6); lithofacies E as a whole (not individual packages) is laterally continuous over hundreds of metres (i.e. Matapan cliff section, Section 3.5.4), whereas lithofacies F is laterally discontinuous over tens of metres.

Figure 3.39 Locality Oh267, U16/798146. Erosive contact between lithofacies A (top) and lithofacies F (bottom). Lens cap (7.5 cm in diameter) is sitting on the contact.

In most cliff sections (Oh124 being the exception, Figure 3.27 and Figure 3.38), the thicknesses of lithofacies A are greater than for lithofacies F (average ratio is ~ 3 : 1) and their volumes are inferred to be in corresponding proportions. Lithofacies A packages range in thickness from 1 to 30 m, with some cliff outcrops consisting of vertically continuous lithofacies A deposits, with no trace of cross-stratified deposits (Figure 3.38). Individual lithofacies F packages can vary between a few metres to less than 1 m thick. The range of lithofacies F thicknesses can be controlled by the geometry associated with a channel (Figure 3.30) or bowl-shaped structure (Figure 3.29), or lateral pinching into underlying and overlying lithofacies A deposits (e.g. 'pinch point', Figure 3.27). Structureless lithofacies A packages have a sharp lower and upper contact with cross bedded lithofacies F packages, and in some cases the lower contact of lithofacies A is an erosive one (Figure 3.39).

3.5.4 Matapan lithofacies association (Mla)

The Matapan lithofacies association (*Mla*) takes its name from the roughly circular, elevated hill known as Matapan (see Map 1). Several different deposit types are exposed on Matapan including lacustrine sediments, basalt, and Ohakuri deposits. The lacustrine sediments are

observed on the west side of Matapan, and overlie Ohakuri deposits that are poorly exposed and undifferentiated with respect to an Ohakuri lithofacies association. Near the centre of Matapan are the remains of a small basaltic tuff ring (the Matapan basalt of Houghton et al., 1987) that postdate the Ohakuri eruption. Pyroclastic deposits associated with the tuff ring include lithics of the older Ohakuri deposits. On the northeastern and eastern side of the Matapan massif, the Matapan lithofacies association (*Mla)* is well exposed in a precipitous cliff section (*Mla* reference section between U16/80481091 and U16/80301172). The *Mla* deposits are indurated with a reddish-orange oxidised case-hardened crust; however, where the crust is missing, white to pale-yellow deposits can be observed. *Mla* deposits are also exposed to the northeast of the Ohakuri caldera in a NE-SW trending cliff section adjacent to Highway 30 (see Figure 3.34).

Figure 3.40 View of Matapan cliff section from Oh201, U16/81741124. Thin dashed lines represent the inferred contacts between the different lithofacies, which are inclined to the northwest. Thick dashed line in the background marks the inferred boundary of the Ohakuri caldera.

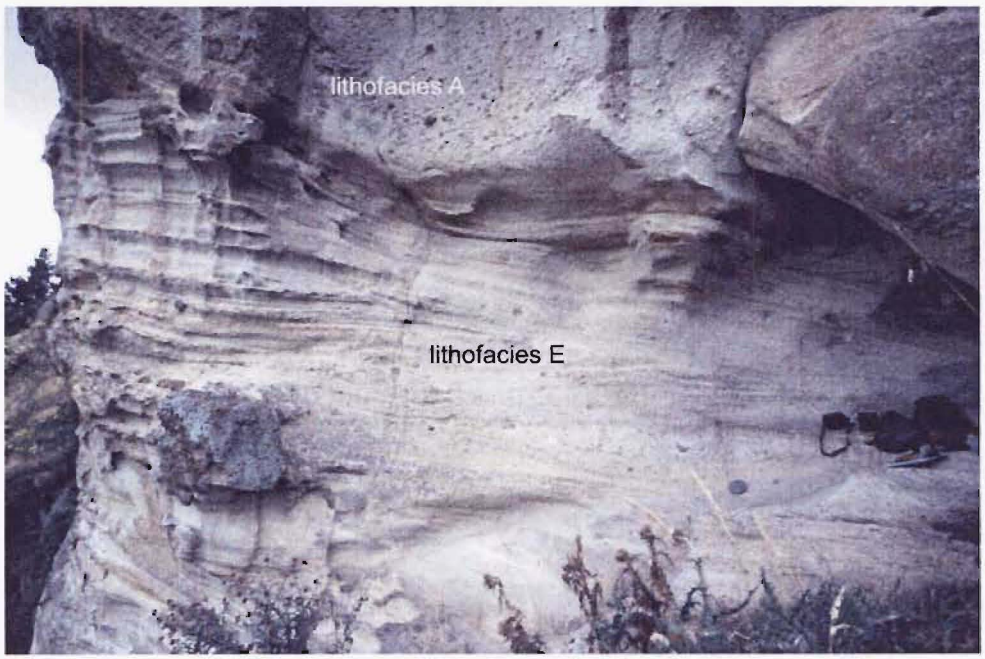

Figure 3.41 Locality Oh130, U16/80301172. Distinct, non-erosive contact between lithofacies E and A.

Mla includes deposits of lithofacies A, B, and E; each of the lithofacies is represented in an approximately 80 m high and 500 m long cliff section (Figure 3.40) above Dunkirk Rd. Unlike the Tahunaatara area, the cliff section is relatively continuous, exposing a convenient cross-sectional view of the lithofacies variation. Relative to *Tla*, the lithofacies architecture is more organised with laterally continuous, lithofacies 'building blocks'. The bottom of the cliff is composed of diffusely stratified lithofacies B and structureless lithofacies A deposits that grade in and out of each other. Towards the middle of the cliff is an approximately 20 m thick section of channel bedded deposits (lithofacies E). The thickness is estimated because the bottom contact of lithofacies E is obscured amongst bush and trees in a section that is not accessible because of its precipitous nature. The top of lithofacies E, however, is accessible and is characterised by a distinct, non-erosive contact with the bottom of a structureless lithofacies A package (Figure 3.41). Lithofacies A grades upwards into lithofacies B. Together, the 3 lithofacies are inclined 5° to 10° to the northwest (see Figure 3.40). *Mla* deposits adjacent to Highway 30 are also inclined (~ 10°); however, they are inclined to the southeast. The origin of their inclination is discussed in Section 3.6.3.

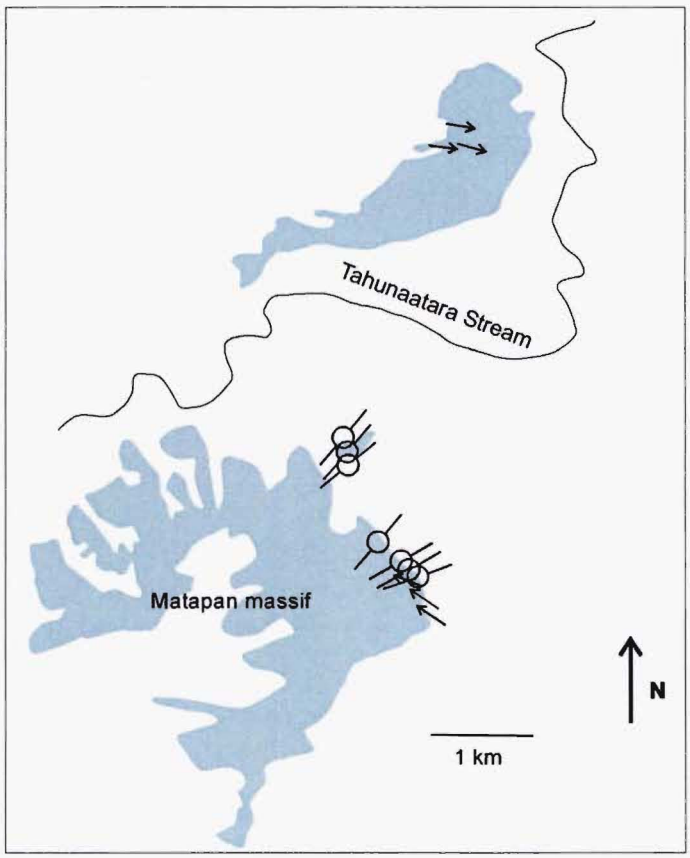

Figure 3.42 Open circles with arms in opposite directions represent channel axes directions, which are almost orthogonal to the inclination direction (arrows) of the lithofacies in the Matapan cliff section.

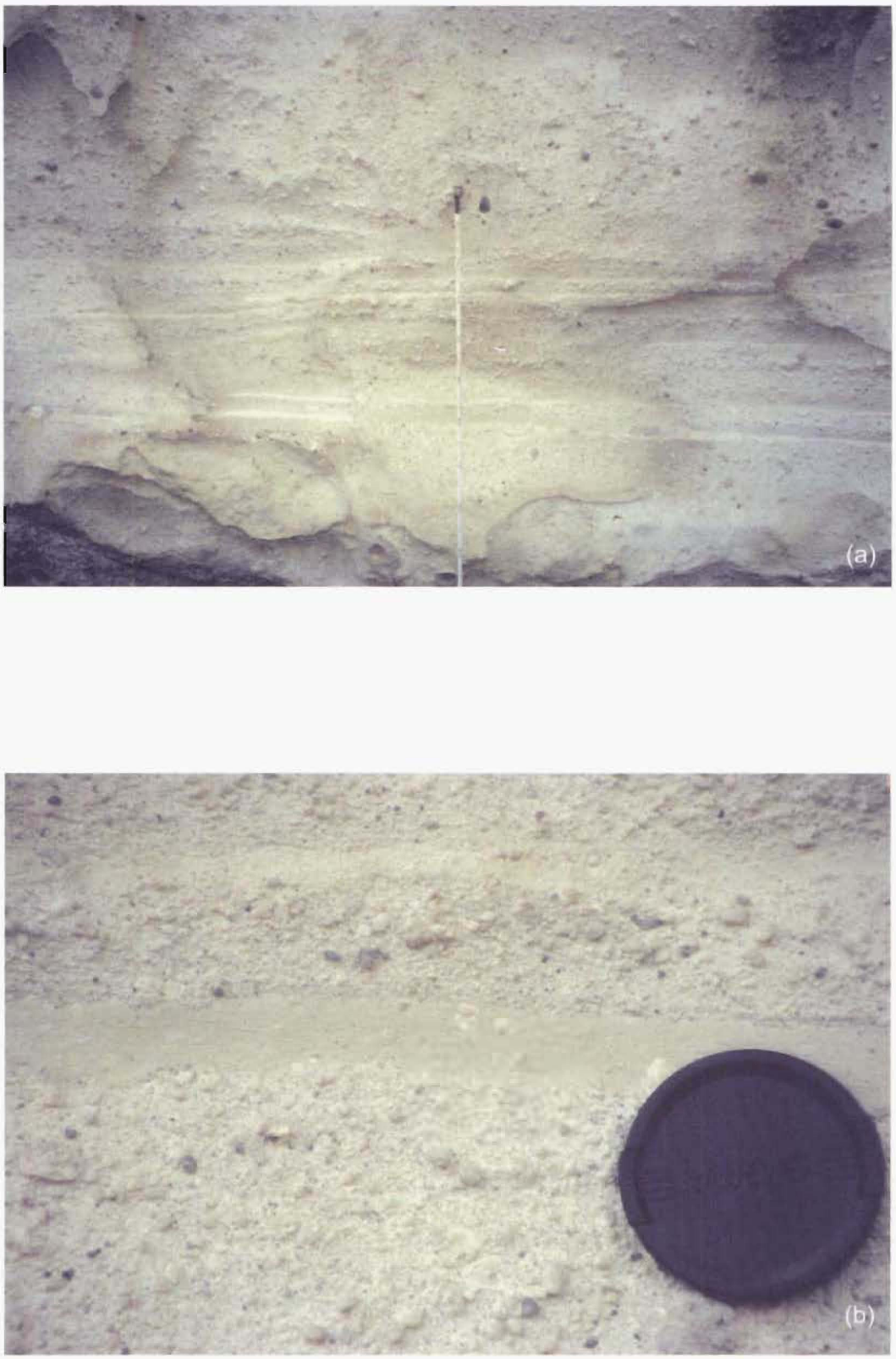

Figure 3.43 Locality Oh129, U16/79781286. (a) Massive, relatively fines-poor beds separated by thin fine-grained ash beds with scattered accretionary lapilli. Thin ash beds pinch out laterally. Tape is just over 1 m long. (b) Close-up view of a thin fine-grained ash bed with some accretionary lapilli. Fine ash is draped over the underlying massive deposit and in some cases has accumulated in the interstices between pumice lapilli. Lens cap is 7.5 cm in diameter.

As mentioned previously in Section 3.4.6, geometrically, the *Mla* lithofacies E is fundamentally different to lithofacies F (seen in the *Tla*). The former is 1) observed at a consistent stratigraphic level across the cliff face, 2) does not wedge laterally into overlying and underlying massive lithofacies, 3) is not observed alternating with massive lithofacies, and 4) uniform channel axes directions can be inferred from channel morphologies in the Matapan cliff section. Figure 3.42 shows that the channel axes are almost orthogonal to the inclination direction mentioned above.

Adjacent to the Matapan massif is a resistant ~ 40 m high knoll of Ohakuri pyroclastic deposits. The knoll is composed of packages of structureless lithofacies A, and stacked and interdigitated channel-fill packages (lithofacies E). In places, there appears to be a gradational relationship between lithofacies E and A. In Figure 3.43, individual beds of massive deposits are separated by fine-grained, ash-rich, accretionary lapilli-bearing beds, and ultimately grade up into massive lithofacies A. The accretionary lapilli-bearing beds (millimetres to a few centimetres thick) thin laterally until they are completely truncated by overlying massive deposits (Figure 3.43).

3.5.5 Stag lithofacies association (Sla)

The Stag lithofacies association (*Sla*) is located on either side of Galatos Road in the eastnortheast sector of the field area (Figure 3.34). Its distribution is restricted to two farm blocks (including a stag-breeding farm) spanning a distance of approximately 3 kilometres. Both farms are characterised by NE-SW trending hill/cliff sections and streams. The Ohakuri pyroclastic deposits crop out in cliff sections as high as 30 metres and, like the *Tla* deposits, are pervasively case-hardened.

The *Sla* can be divided into three lithofacies components; structureless lithofacies A and diffusely stratified lithofacies B deposits, and bedded, plane-parallel lithofacies G deposits. The bedded deposits occur as distinct packages sandwiched between massive deposits. I use the term sandwich because the bedded packages do not grade in or out of massive deposits but occur as a layer with sharp upper and lower boundaries (see Figure 3.33). There are multiple bedded packages (~ 1 m thick) alternating with massive deposits in vertical cliff sections. Some of these bedded packages can be traced laterally for more than 200 metres with no change in thickness.

3.6 Origin of the Ohakuri lithofacies and lithofacies associations

The lithofacies and lithofacies association descriptions, given in Sections 3.4 and 3.5 respectively, provide a framework for understanding the origins of the Ohakuri deposits. However, the origins of the Ohakuri lithofacies cannot be determined from lithological and structural descriptors alone. Deposits, like the Ohakuri, that are characterised by volcanic

fragments (pumice, crystals, glass shards, and rhyolitic lithics) and well developed bedding and sedimentary structures, can be deposited from several different pyroclastic and/or normal sedimentary processes (cf. McPhie, 1987, Cas and Wright, 1987). This is, perhaps, why Grindley (1960; 1965) and Healy et al. (1964) originally proposed a primary pyroclastic and a re-sedimented origin for the range of Ohakuri deposits. Although neither Grindley (1960; 1965) nor Healy et al. (1964) provide specific evidence, it is likely that the sedimentary associations were predicated on 1) their interpretation of a widespread, thick sequence of deposits filling the Taupo-Rotorua Basin (from Grindley, 1960), and 2) the presence of bedded deposits and sedimentary structures (see Langridge, 1990). In this section, both pyroclastic and sedimentary processes are re-evaluated, particularly for the bedded Ohakuri lithologies. The volcaniclastic literature is complicated by the variable use of terminology (i.e. different definitions for 'pyroclastic' and 'epiclastic'), so I will, first, propose a set of terms to be used in this thesis.

There are two schools of thought with respect to pyroclastic vs. epiclastic particles. The Fisher school (e.g. Fisher and Smith, 1991) suggests that the terms pyroclastic and epiclastic refer to the formation of clasts themselves (volcanic fragmentation for pyroclastic, and weathering for epiclastic) and not the transporting agent(s) responsible for their deposition. For example, pyroclastic particles that are remobilised and carried to a new depositional site by wind or river are not epiclastic; they are still pyroclastic because they did not form by weathering. The Cas school (e.g. Cas and Wright, 1987) suggests that it is the transporting agent or process that determines whether a particle is pyroclastic or epiclastic; i.e. pyroclastic particles that are reworked by river or wind can be defined as epiclastic. To avoid confusion with respect to the Ohakuri deposits, I propose a set of terms that does not include 'epiclastic.' I use the term 'pyroclastic' to refer to particles that are formed by volcanic fragmentation and transported by primary pyroclastic processes (i.e. pyroclastic density currents), and the term 'reworked' to describe particles that are originally formed and transported by pyroclastic processes but are, subsequently, re-transported and deposited by sedimentary agents such as wind or water. 'Reworked' incorporates both syn-eruptive and post-eruptive sedimentary processes, as long as the fluid phase associated with transport is not gas (i.e. associated temperatures of the transporting agent are < 100° and not > 100°). For deposits related to secondary processes, such as avalanches of primary ignimbrite from Torres et al. (1996), or secondary hydroeruption deposits from Moyer and Swanson (1987), where transport is driven by gas fluidisation and gravity, I refer to them as 'secondary pyroclastic deposits.'

To determine the origin(s) of the Ohakuri deposits (emphasising pyroclastic vs. reworked), the lithology, structure, context, geometry, and distribution of each Ohakuri lithofacies is evaluated. With respect to the massive lithofacies A and B, the geometry and distribution, in particular, do not correlate well with a normal sedimentary or reworked origin. These deposits are

characterised by thick, landscape forming accumulations (> 200 m thick in the *Gla*), are exposed throughout the Ohakuri areal distribution, and are always found in conformable contact with each other. In addition, *Fla* lithofacies A and B are characterised by poor sorting and a high concentration of fine ash (see Figure 3.36), which are not compatible with water or wind reworking. The lithology, geometry, and context of the massive lithofacies A and B are explained best by deposition from highly concentrated pyroclastic density currents and therefore lithofacies A and B are referred to here as ignimbrite (cf. Sparks, 1976; Wilson, 1986; Druitt, 1998; Freundt et al., 2000). By association, lithofacies D, which is defined by its gradational relationship with lithofacies A (refer to Section 3.5.1), must also be a pyroclastic density current deposit.

For each of the bedded Ohakuri lithofacies, their limited areal distribution (Figure 3.11) suggests that any reworked depositional overprint had to be localised. Resedimentation by wind is therefore unlikely, as aeolian processes tend to be associated with laterally extensive areas (100's to 1000's of km^2; McPhie, 1987 and references therein). Also, aeolian deposits are characterised by thick, high-angle cross-bedded sets and a limited range of grainsizes that are usually well sorted and well rounded (McPhie, 1987 and references therein). In contrast, channel-bedded deposits with a distinct range of lithologies including massive, poorly to moderately sorted beds (lithofacies E and F), plane-parallel bedded deposits (lithofacies G), and giant-dune-bedforms that are fines-rich and exhibit low-angle cross-stratification (lithofacies C) do not correlate well with aeolian sedimentation.

If the bedded Ohakuri lithofacies are associated with a reworked depositional overprint, only local fluvial (including mass flow and tractional currents) and/or lacustrine processes are feasible. At Taupo, fluvial and lacustrine processes were responsible for reworking of the 1.8 ka Taupo ignimbrite (e.g. Smith, 1991a; Smith, 1991b; Manville et al., 1999; Manville, 2001; Riggs et al., 2001; Manville, 2002). Manville (2001) describes several different reworked lithofacies that, together, exhibit a clear transition from the early remobilisation or slumping of hot Taupo ignimbrite (defined in this thesis as a 'secondary pyroclastic deposit'; cf. Torres et al., 1996) to fluvial processes to lacustrine deposition. There are several different fluvial and lacustrine associations including inflow deltas characterised by constructional fans of debris flow deposits and turbidites; and transgressive shoreline facies characterised by low-energy cross-beds and ripples. Lithologically, the secondary pyroclastic deposits (remobilised ignimbrite) share a similar texture, composition, and general appearance with primary Taupo ignimbrite, and are only distinguishable where stratigraphic relationships are resolved, i.e. overlying the regional, co-ignimbrite Taupo ash or where there is an unconformable basal contact with Taupo ignimbrite. The reworked Taupo fluvial and lacustrine lithofacies, described by Manville (2001),

are characteristically fines-poor and well sorted with smoothed, well rounded grains that are organised into pumice gravel beds, crystal-lithic sand beds, and massive silt beds.

In contrast, the bedded Ohakuri lithofacies show no evidence for fluvial to lacustrine transitions. Instead, lithofacies E, F, and G are intimately associated with the massive ignimbrite lithofacies A and B. Within lithofacies association *Fla*, lithofacies E sometimes grades into massive lithofacies A and/or B, suggesting relatively continuous accumulation with no evidence for a hiatus long enough to establish a water-rich sedimentary depositional environment. In the *Tla*, lithofacies F pinches laterally into massive lithofacies A ignimbrite, indicating that the two lithofacies are time equivalents (see Chapter 5), i.e. no evidence for establishment of a fluvial and/or lacustrine environment. And, in the *Sla*, no significant time breaks can be inferred from the alternating lithofacies G and A packages because, together, they are considered to be temporally equivalent to the continuous vertical exposure of lithofacies A deposits within *Gla* (see Section 3.7.2 for *Sla* and *Gla* time equivalent relationship).

Structurally and lithologically, the bedded Ohakuri lithofacies also exhibit clear differences from fluvial and lacustrine deposits. The wavelengths (up to 42 m) of the lithofacies C giant-dune-bedforms are an order of magnitude greater than wavelengths associated with Taupo marginal lacustrine ripples and, lithofacies C deposits are poorly sorted with fine ash concentrations comparable to massive lithofacies A and B ignimbrite (see Figure 3.36). With respect to the other bedded Ohakuri lithofacies, the differences include, 1) massive fine-grained ash beds of lithofacies F and G that contain concentrations of accretionary lapilli, distinguishing them from the basinal lacustrine massive-laminated vitric silt beds of the reworked Taupo deposits (Manville, 2001), 2) Ohakuri pumice exhibit a degree of attrition but are never well-rounded or smoothed, and 3) with the exception of the pumice clast-supported lithology of lithofacies E, F and G, Ohakuri lithofacies have an abundance of matrix fines.

The only Ohakuri deposits that may correlate with the Taupo deposits described by Manville (2001) are some of the thin massive beds of lithofacies E and F and, possibly, some isolated exposures of lithofacies A where there is no context preserved. Without regional stratigraphic control (i.e. the Taupo co-ignimbrite ash (layer 3) deposit) or direct observation (i.e. secondary pyroclastic flows generated from ignimbrite avalanches for more than 2 years following the June 15, 1991 eruption of Mount Pinatubo; Torres et al., 1996), it is possible but not demonstrable that some of the massive Ohakuri deposits originated from slumping of primary ignimbrite.

In summary, the massive and bedded Ohakuri lithofacies do not indicate with a reworked, "normal" sedimentary origin. The componentry, structure, distribution, and particularly the relative timing of emplacement of the different Ohakuri lithofacies associations, are most

consistent with pyroclastic processes, including transport and deposition. Each Ohakuri lithofacies association is characterised by a unique architecture of massive and/or bedded lithofacies that is best explained by variable pyroclastic processes and/or local depositional environments. Possible pyroclastic processes include: airfall and PDC's from primary magmatic eruptions; airfall and base surges from phreatomagmatic eruptions; airfall and base surges associated with secondary hydrovolcanic explosions from the interaction of primary PDC deposits with water; and deposition from processes associated with primary PDC's including co-ignimbrite airfall and surges (McPhie, 1987). In the following sub-sections, the pyroclastic origins of the Ohakuri lithofacies are discussed with respect to Ohakuri lithofacies associations.

3.6.1 Gold lithofacies association (Gla)

Gla lithofacies A

Sparks et al. (1973) recognised 3 characteristic facies or layers associated with an ignimbrite flow unit: layer 1 (ground layer, ground surge deposit), layer 2 (flow unit or body), and layer 3 (fine-ash deposit, ash cloud deposit, or co-ignimbrite ash) (Figure 3.44). Layer 2 is divided into a finer-grained and relatively thin basal layer (2a) and a thick, homogenous and often structureless body (2b). Not all ignimbrite deposits reveal the tripartite layering, and in the case of the massive Ohakuri lithofacies A, only the structureless ignimbrite body (layer 2b) is exposed. Freundt et al. (2000) suggests that thick exposures of layer 2b deposits are common in

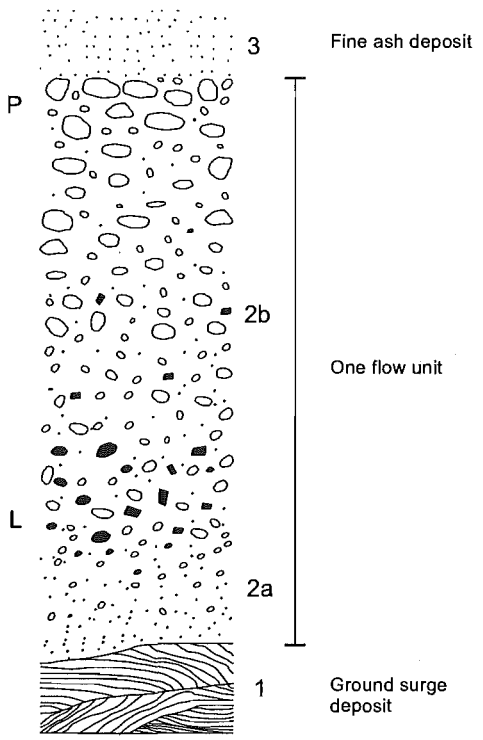

Figure 3.44 Anatomy of an ignimbrite flow unit, from Sparks et al. (1973).

moderate to large volume ignimbrites, making it difficult to discern internal depositional boundaries or discrete flow units. There are two hypotheses for the origin of such thick homogeneous and monotonous exposures of ignimbrite, 1) the layer 2a deposits were never deposited or were not preserved, and mingling of layer 2b deposits between flow units erased any evidence for depositional boundaries, or 2) the transporting pyroclastic density currents were steady in nature and the deposits were continuously aggraded with no depositional breaks: the question of time breaks vs. continuous aggradation is discussed further in Section 3.6.2 and Section 3.7.2.

***Gla* lithofacies D**

With respect to lithofacies A, there are no clues within the deposit itself to suggest whether or not there were short-lived time breaks in the depositional sequence or not; however, there is evidence for a time break where lithofacies A comes into contact with lithofacies D. Figure 3.20 shows a sharp contact between the top of structureless lithofacies A ignimbrite and the first of several reverse graded sub-packages within a package of lithofacies D. Each sub-package resembles an individual, thin ignimbrite unit (deposited from a discrete pyroclastic density current) with a fine-grained, matrix-rich, basal layer 2a and a coarser, reverse graded layer 2b with an upward increase in pumice lapilli concentration. The contact between each sub-package is characterised by a sharp boundary that I correlate with a hiatus in deposition. The gradational transition between sub-package 4 (lithofacies D) in Figure 3.20 and the structureless ignimbrite (lithofacies A) shows no evidence of a hiatus and most likely represents continuous aggradation. In other words, the fine-grained basal layer of sub-package 4 could be interpreted as the layer 2a facies associated with the overlying layer 2b of lithofacies A ignimbrite.

Similar to lithofacies D, thin and stacked ignimbrite packages have been documented at Laacher See, Germany (see Freundt and Schimcke, 1985a; Schumacher and Schmincke, 1990). The 'overbank facies' at Laacher See is characterised by thin packages of poorly sorted ignimbrite, deposited on interfluves and laterally continuous with valley-fill ignimbrite ('valley facies'; Schumacher and Schmincke, 1990). The relationship between the overbank and valley facies is associated with a different origin than the ignimbrite veneer deposit (IVD) and valley ponded ignimbrite (VPI) relationship at Taupo (see Walker et al., 1981; Wilson and Walker, 1982; Wilson, 1985). The overbank facies is a multi-flow deposit that is not derived from the valley facies but originated from pyroclastic density currents that travelled down valleys or over higher topography directly from the volcano source. The valley-confined flows are thought to be thicker with a higher transport capacity, and more capable of carrying coarser-grained material than the flows travelling over higher ground (i.e. the overbank facies is generally finer-grained than the valley facies).

In comparison with the overbank facies, lithofacies D is fundamentally different. Firstly, there is no evidence for paleo-valleys in *Gla* and, therefore, the sandwich-like relationship between lithofacies D and A (Figure 3.20) suggests these two lithofacies were deposited under the same topographic constraints, or lack thereof. Secondly, packages of lithofacies D have a similar maximum pumice size distribution to lithofacies A, and are characterised by a set of sub-packages, each tabular in shape with sharp boundary contacts. The evidence suggests that lithofacies D and its sub-packages represent a hiatus in the more or less continuous and constant supply of material associated with lithofacies A, and probably correlates with changes at the volcano source. Sub-packages of lithofacies D may have formed because of momentary choking of the vent source causing a change in the volume of supply with short time breaks between depositional units. Alternatively, lithofacies D may represent a migration in vent sources and, thus, a perturbation in the supply of pyroclastic material. For example, at Laacher See, Freundt and Schmincke (1985) divide the ignimbrite deposits into separate eruptive units (cycles) that, in some cases, represent several eruptive phases. Each eruptive unit is composed of several flow units, where each flow unit is related to one column collapse; subsequent flow units and column collapses are a vestige of stepwise vent migrations. The time interval between successive column collapses (vent migration) is measured by the presence or absence of ground layers and/or dust layers (co-ignimbrite ash) between flow units. The absence of a ground or dust layer suggests that successive column collapses were too rapid for their formation; the inverse is also true, i.e. where ground or dust layers are present, an increase in the time interval between column collapses is inferred. Although ignimbrite sub-packages (analogous to Laacher See 'flow units') within lithofacies D represent discrete time intervals in the Ohakuri eruption sequence, there is not enough evidence to suggest whether each sub-package is related to one column collapse and vent migration, or partial collapse associated with a momentary choking of an otherwise, sustained eruption from one vent. Regardless of the cause, the lack of ground layers and/or co-ignimbrite ash deposits (dust layer) suggests that any time break between deposition of successive sub-packages was short (seconds to minutes).

3.6.2 Forest lithofacies association (Fla)

Fla lithofacies A

In general, lithofacies A in *Fla* is identical to lithofacies A found elsewhere in the field area. However, a fines-poor variant of lithofacies A is exposed at only 2 outcrops (see Section 3.4.1), including OH110 where it is underlain by a crystal- and lithic-rich ground layer (layer 1 of Sparks et al., 1973). The presence of a ground layer, which overlies a lithofacies B package (Figure 3.13), is taken to indicate a short time break (cf. Druitt and Sparks, 1982; Freundt and Schmincke, 1985b; Freundt and Schmincke, 1986).

The lack of fines associated with the 2 lithofacies A exposures is considered to have a similar derivation as the Taupo fines-depleted ignimbrite (FDI), whereby fines are elutriated due to a high gas throughput and enhanced turbulence associated with the moving pyroclastic density current (Walker et al., 1980). Grainsize analyses comparing Taupo FDI with normal Taupo ignimbrite (NI) show that material finer than 1/16 mm accounts for < 5% of the total weight of the deposit and also reveals a weakly depleted ignimbrite (WDI) that is transitional between the FDI and NI (Walker et al., 1980). Although no grainsize analyses were performed on fines-depleted lithofacies A deposits (these were too weathered to obtain accurate results), it is not fines-depleted to the degree of the Taupo FDI (i.e. lithofacies D is not clast supported) and probably correlates better with the WDI.

At Taupo, a high gas throughput and enhanced turbulent flow were created by a high flow velocity, surface roughness, and ingestion of gases from a forest substrate; however, turbulent flow can also be triggered by travel down a steep slope, or associated with proximity to the vent source (Walker et al., 1980). With respect to lithofacies A (WDI), the case for turbulence is bolstered by the presence of such large lithics (up to 220 mm) at the base of the deposit; however, the cause of turbulence is uncertain. At the two available outcrops there is no evidence for surface roughness or a forest substrate, and the pyroclastic density currents responsible for the emplacement of lithofacies A (WDI) were travelling up hill. Based on available evidence, turbulence is most likely related to its proximity to source.

***Fla* lithofacies B**

The grain size distribution for lithofacies B and A is roughly identical (Figure 3.36), both are characterised by abundant matrix fines. This suggests that, like lithofacies A ignimbrite, lithofacies B is associated with pyroclastic density currents characterised by high concentrations of material. Internal pumice lapilli banding within lithofacies B differs from the thin stacked flow units of lithofacies D in that there is no vertical grading and no distinct depositional boundaries. In this sense, lithofacies B is more like the Taupo ignimbrite veneer deposit (IVD), which also exhibits internal banding characterised by variations in pumice concentration and size (Walker et al., 1981; Wilson and Walker, 1982; Wilson, 1985). Like the Taupo IVD, lithofacies B is likely to be associated with continuous aggradation, whereby the internal banding represents layer by layer deposition from a succession of waves or pulses (Walker et al., 1981; Wilson and Walker, 1982; Wilson, 1985). Continuous aggradation, as described by Branney and Kokelaar (1992) involves frictional deposition where the concentrated boundary layer (traction carpet) of the flow develops a yield strength relative to the substrate surface and is deposited. Frictional deposition can occur from an unsteady (stepwise aggradation) or steady (gradual aggradation) flow (Figure 3.45). Stepwise aggradation involves significantly short time breaks between the

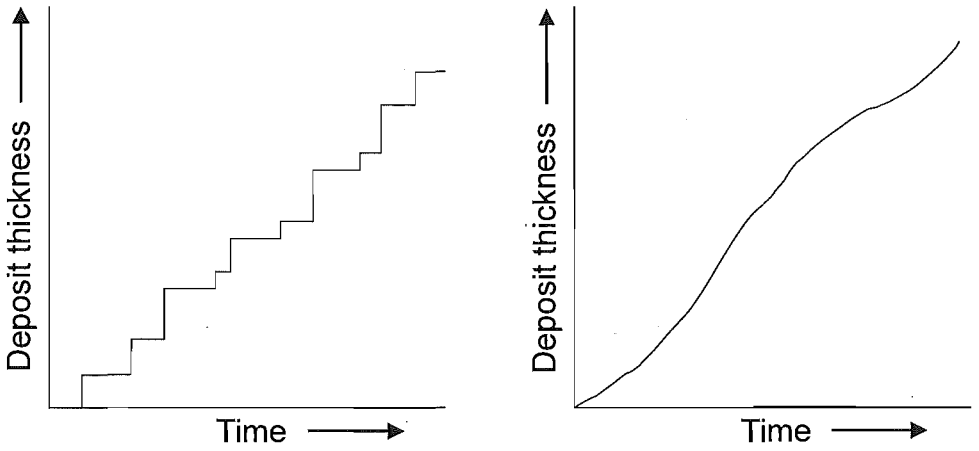

Figure 3.45 Stepwise and gradual aggradation, from Branney and Kokelaar (1992).

deposition of individual batches, and the resulting deposit can exhibit reverse graded layering. With respect to gradual aggradation, deposition occurs uniformly over time and the resulting deposit tends to be massive and structureless. Diffusely stratified deposits are inferred to be the product of a depositional regime that is somewhere in the middle of a stepwise-gradual aggradation continuum. The deposits represent a 'fluctuating input' to the depositional boundary layer (Branney and Kokelaar, 1992) and, in some cases, involve amalgamation of successive batches by shearing (Fisher, 1966; Branney and Kokelaar, 1992; Wilson and Hildreth, 1997; Druitt, 1998). Subtle cross-stratification in some packages of lithofacies B is probably associated with shearing.

Although Lithofacies B and the Taupo IVD are associated with continuous aggradation from multiple pyroclastic density current pulses, they have fundamentally different origins. For exarnple, the Taupo IVD represents deposits that were left behind by the same pyroclastic flow that deposited the much thicker valley-pond ignimbrite (VPI; Walker et al., 1981). The Taupo IVD and VPI are characterised by a laterally graded relationship, with IVD deposits connecting VPI deposits across interfluves (Figure 3.46; Wilson, 1985). Wilson (1985) suggests that the IVD very rarely grades vertically up into the VPI. In contrast, lithofacies A and B are never observed as lateral equivalents; they are always observed grading vertically into one another. This relationship, combined with their proximity to source, may indicate a link to the volcanic source itself, where changes in the eruption could have caused fluctuations in the supply of pyroclasts.

Fla lithofacies C

The origin of lithofacies C is discussed in full detail in Chapter 4, so only a summary will be given here. Lithofacies C has characteristics of both pyroclastic flow and pyroclastic surge deposits. Its most diagnostic feature is the giant-dune forms with wavelengths up to 42 metres.

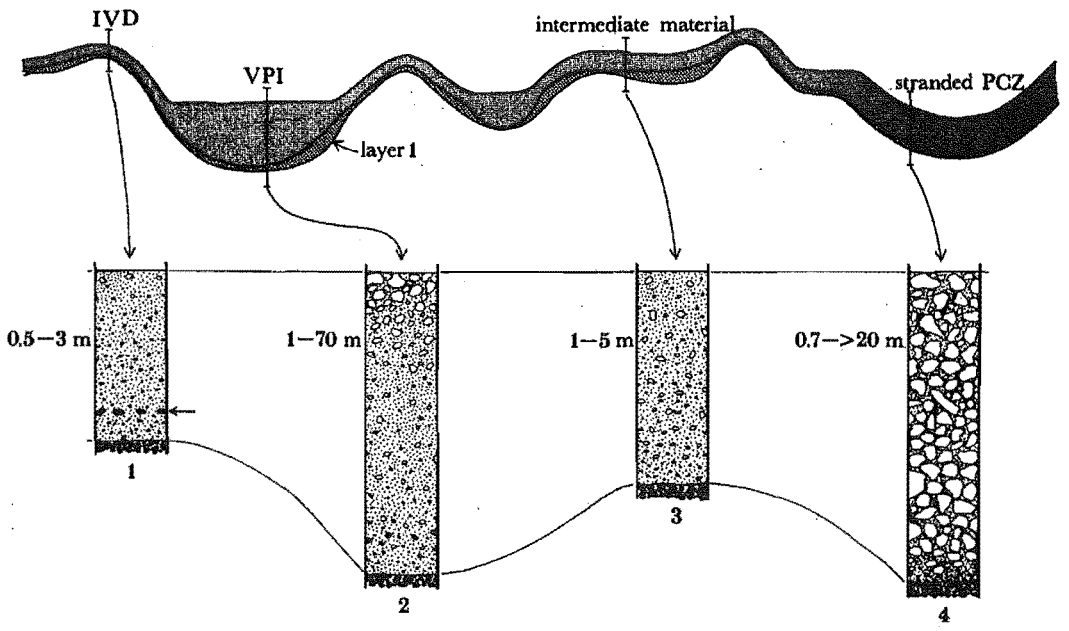

Figure 3.46 Laterally gradational relationship between the Taupo valley-pond ignimbrite (VPI) and the ignimbrite veneer deposit (IVD), from Wilson (1985).

The dunes are recognisable from conspicuous bands associated with variations in pumice-lapilli concentrations, very similar to the bands associated with the diffusely stratified ignimbrite (lithofacies B). Thus, I infer a similar depositional process for lithofacies C where pumice concentration bands, or the dune-bedding in this instance, are associated with layer-by-layer tractional transport and continuous aggradation. Cas and Wright (1987) suggest that the production of dune-bedded deposits from tractional transport implies low particle concentration; however, lithofacies C is anomalous; it is defined by an excessive matrix fines component making its overall grainsize distribution very similar to that of lithofacies A and B ignimbrite (Figure 3.36). With no indication for the presence of liquid water on deposition, I infer that lithofacies C was deposited from highly turbulent, yet heavily loaded pyroclastic density currents.

Fla lithofacies E

Lithofacies E is an unusual pyroclastic deposit that is often found grading into massive ignimbrite (lithofacies A or B), yet it possesses characteristics that are similar to deposits from turbulent PDC's (pyroclastic surges, s.s.). For example, on a σ_ϕ vs. Md_ϕ diagram (Figure 3.47a) lithofacies E (including structureless, diffusely stratified, and reverse graded sub-lithofacies) plots in a similar field to El Chichon massive and dune bedded surge deposits, and is generally

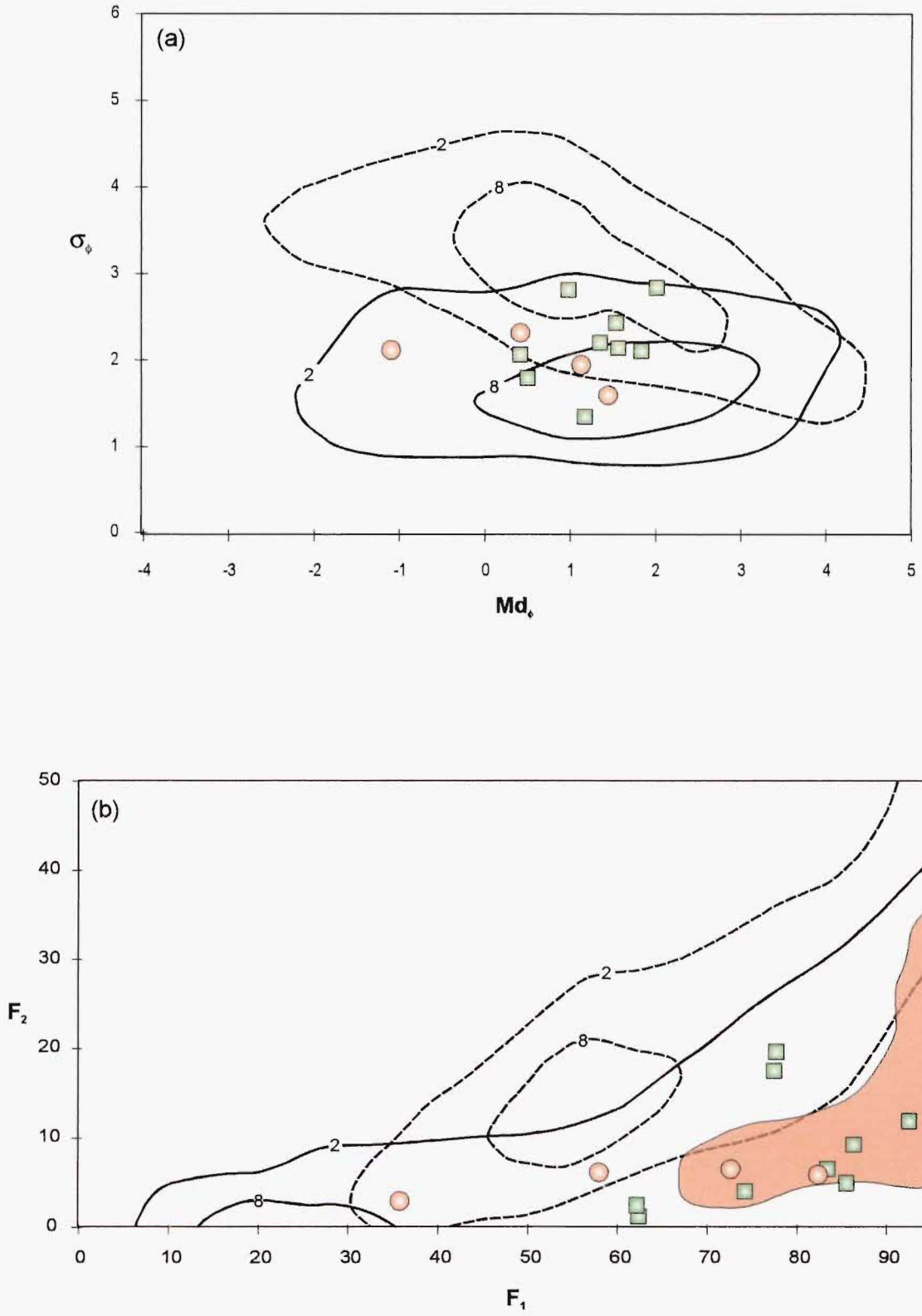

Figure 3.47 Grainsize distribution plots comparing lithofacies E (orange circles) with El Chichon surge deposits (green squares; data fromSigurdsson et al., 1987) and Mount St. Helens massive and bedded lateral blast deposits (orange field; data from Sigurdsson et al., 1987). 2% and 8% contours for pyroclastic flow field (dashed lines) and pyroclastic surge field (solid lines) are from Walker (1984). The fields are based on a number of analyses (N), and the contours represent the percentage of N lying in a circle with a diameter equal to one phi unit, centred at any point. (a) σ_ϕ vs. Md_ϕ. (b) F_2 vs. F_1.

better sorted than Ohakuri ignimbrite lithofacies A and B (cf. Figure 3.36). On a F_2 vs. F_1 plot (Figure 3.47), the lithofacies E deposits correlate better with the pyroclastic surge field and specifically with the El Chichon deposits and some massive and bedded lateral blast deposits from Mount St. Helens. Also, the < 1/16 mm fraction is considerably lower than the Ohakuri ignimbrite lithofacies A and B (cf. Figure 3.36).

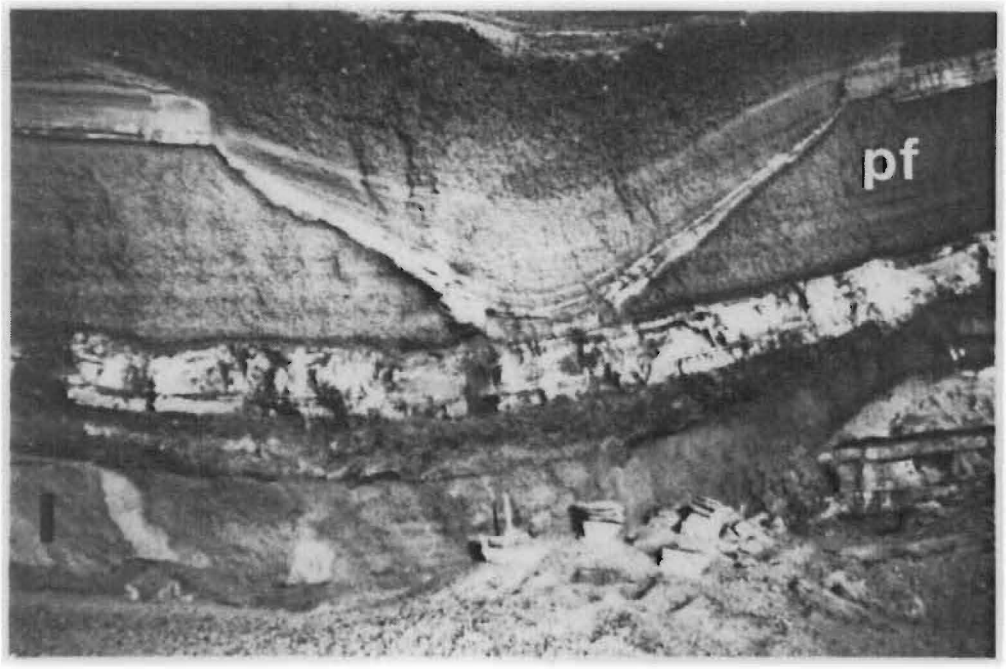

Figure 3.48 Santorini channel structure. Photo from Mellors (1988).

Another characteristic of Lithofacies E that correlates well with pyroclastic surge deposits, is the conspicuous channel and fill structures. Channel and fill structures associated with pyroclastic surge deposits have been documented at several volcanoes including Koko Crater (Fisher, 1977), Laacher See (Fisher and Schmincke, 1984), and Songaksan tuff ring (Sohn and Chough, 1989; Chough and Sohn, 1990). At each of these volcanoes, the channels are understood to be scour structures associated with erosion by pyroclastic surges. However, at Santorini channel structures (see Figure 3.48) filled with pyroclastic surge deposits also have fluvial deposits preserved at the bottom of the channels, which imply that these channels were originally water-cut and, subsequently, exploited and filled by pyroclastic surges (C.J.N. Wilson, pers. comm., 2004). In contrast to the fully-preserved Santorini channel shown in Figure 3.48, only a portion of each lithofacies E channel is preserved due to the erosion associated with overlying channels (Section 3.4.5), which suggests that these channels were formed in quick succession. This, as well as the inferred uniform trend of the channel axes, the geometry of the fill deposits (Figure 3.22) and the absence of fluvial deposits present at the bottom of the channels, are more consistent with scouring by pyroclastic density currents than water. To differentiate between origins, I refer to pyroclastic density current-cut channels and their deposits, herein, as scour and fill structures.

Despite the granulometric and geometric (scour and fill structures) similarities, lithofacies E does not correlate well with pyroclastic surge facies models (e.g. Crowe and Fisher, 1973; Wohletz and Sheridan, 1979; Fisher and Schmincke, 1984; Cas and Wright, 1987; Sohn and Chough, 1989; Chough and Sohn, 1990). For example, lithofacies E deposits may share lithological and structural similarities with proximal massive surge deposits, which are considered to be rapidly sedimented bedload deposits related to an overriding turbulent surge; i.e. the massive deposits at Mount St. Helens (Fisher, 1990; Druitt, 1992), El Chichon (Sigurdsson et al., 1987), and Songaksan tuff ring (Sohn and Chough, 1989; Chough and Sohn, 1990). However, proximal massive deposits are normally associated with both sandwave and plane-parallel beds deposited by the same surge. With respect to lithofacies E, there is no evidence for associated sandwave and plane-parallel facies and therefore it is unlikely that lithofacies E is associated with an overriding surge. Instead, the sometimes-gradational contact with lithofacies A suggests that the lithofacies E deposits are intimately associated with ignimbrite. Lithofacies E may be interpreted as a type of ground surge deposit (cf. Cas and Wright, 1987). In particular, it bears similarities to layer 1(P) of the Taupo ignimbrite (see Wilson and Walker, 1982; Freundt et al. 2000), but differs in 1) the pervasive scour and fill structures, diagnostic of lithofacies E, and 2) the lack of lithic and crystal enriched segregation pods that are found in layer 1(P).

Whether *Fla* lithofacies E is a ground surge deposit or not is a semantics issue. Its proximal location, relative to vent source, suggests that the origin of lithofacies E is likely to be directly related to eruption dynamics as opposed to variations in depositional processes related to the lithofacies A and B ignimbrite. In this sense lithofacies E may represent fluctuations in the collapsing eruption column or oscillatory fountaining (e.g. Fisher et al., 1983; Dobran et al., 1993; Neri and Dobran, 1994; Allen, 2001) that induced unsteadiness and turbulence in the resulting density currents, as evidenced by the succession of scour and fill structures (cf. Chough and Sohn, 1990). Where lithofacies E is observed grading into lithofacies A ignimbrite, the scour and fill structures may be associated with density current lobes (cf. Fisher and Schmincke, 1984) at the advancing front of a large ignimbrite-producing flow fed by more sustained column collapse (fountaining).

3.6.3 Matapan lithofacies association (Mla)

Mla lithofacies E

Scour and fill packages and a contact relationship with massive ignimbrite (lithofacies A or B) suggest that *Mla* lithofacies E has a similar origin to *Fla* lithofacies E. However, there are differences between the two lithofacies E varieties that suggest subtle differences between their origins. As described in Section 3.4.5, *Mla* lithofacies E exhibits a much higher concentration of

pumice lapilli-supported beds and fine-grained ash, accretionary lapilli-bearing beds. The fine accretionary lapilli-bearing ash is normally observed overlying massive reverse graded or structureless PDC beds (Figure 3.43). Figure 3.43b shows that fine ash has accumulated within the interstices between fine lapilli grains at the top of the underlying massive bed, suggesting that the fine ash resembles a co-ignimbrite airfall ash (layer 3 from Sparks et al., 1973). As such, each airfall ash records a time break between discrete pulses of PDC's associated with the massive beds. Figure 3.43a shows that the fine ash layers have a variable thickness due to the erosive capacity of each successive PDC. Some thicker fine ash beds do not immediately overlie massive beds and they are characterised by a higher concentration and much larger accretionary lapilli (up to 20% and 13 mm, respectively). The fact that these larger fine ash beds are not immediately superjacent to a massive bed suggests that they may be ash fallout associated with PDC's that were not deposited in the immediate vicinity, or that they are fallout related to the vent source itself. Their thickness and the higher concentration and greater size of accretionary lapilli suggest the latter; however, either origin confirms a time break in PDC deposition.

The origin of the pumice lapilli-supported beds is difficult to discern. These beds could have been deposited from processes associated with horizontal (surge) or vertical (airfall) particle trajectories, or a combination of both. Airfall deposits are well sorted, parallel bedded, and drape the landscape; where surge deposits are well to poorly sorted, do not evenly drape the landscape, and show evidence for lateral transport (i.e. basal scouring, dune beds, and cross-stratification) (Wilson and Houghton, 2000). In Figure 3.25, some pumice lapilli-supported beds are conspicuously truncated by overlying PDC deposits; while other beds appear to thin or wedge against the channel margin, suggesting that there may be a lateral component to their deposition. The pumices themselves are fairly pristine with angular to sub-angular shapes and are very well sorted. From the available evidence, it is likely that a combination of lateral and vertical transport processes is responsible for the deposition of these beds. By association with an obviously energetic transport system that produced numerous scour structures, it is possible that deposits were vertically emplaced originally, and were subsequently transported laterally, 1) at the waning stages of a penecontemporaneous PDC (thus preserving the angular shape of individual pumices), or 2) by swirling winds associated with coeval PDC's (e.g. hybrid fall deposits in the Bishop Tuff from Wilson and Hildreth, 1998).

An interesting side note with respect to the *Mla* lithofacies E, is the origin of the uniform inclination of the deposits in the Matapan cliff section and adjacent to Highway 30 (Section 3.5.4). The inclination is almost orthogonal to PDC transport directions (see Figure 3.42), there is no paleogeographic evidence to support inclined deposition against a large hill, and the directions of inclination correlate well with the regional NE-SW fault trends associated with

rifting. As a result, I infer these to be tilted blocks, where the Matapan tilting is probably associated with the Ngakuru Fault Zone (see Map 1), and the tilted deposits adjacent to HWY30 are associated with a previously unmapped NE-SW trending fault.

3.6.4 Tahunaatara lithofacies association (Tla)

Tla lithofacies F

The *Tla* is characterised by the frequently alternating and interlocking architecture of lithofacies F and lithofacies A (Section 3.5.3). There are several possible scenarios for the origin of *Tla* lithofacies F and its unique relationship with lithofacies A:

1) lithofacies F is a ground surge deposit associated with the massive lithofacies A ignimbrite (layers 1 and 2, respectively, from Sparks et al., 1973)
2) lithofacies F and A represent unrelated PDC processes, i.e. lithofacies F is a surge deposit and lithofacies A is a pyroclastic flow deposit;
3) similar relationship as proposed for lithofacies E and A (*Fla*, Section 3.6.2); i.e. lithofacies F is associated with the advancing front (lobes) of an ignimbrite-producing flow (lithofacies A)
4) lithofacies F is a depositional facies of lithofacies A, i.e. lithofacies F is an ignimbrite veneer deposit (IVD) or overbank facies and lithofacies A is valley-ponded ignimbrite (VPI)
5) lithofacies F is a secondary hydrovolcanic eruption deposit associated with primary PDC's interacting with water

With respect to scenario 1, packages of lithofacies F are laterally discontinuous over 10's of metres (see Section 3.5.3 and Figure 3.27), lithofacies F has a range of lithologies including the presence of massive PDC beds (Section 3.46 and Figure 3.26), and there are no crystal- and lithic-rich layers. Together, these attributes are not compatible with a ground surge origin (cf. Sparks and Walker, 1973). In addition, if lithofacies F is a ground surge deposit, one would expect to see evidence for similar ground surge deposits in other sectors of the Ohakuri pyroclastic distribution, but such evidence is absent. With respect to a base surge origin (scenario 2), lithofacies F is not characterised by lateral facies variation and the array of channel axes directions (see Section 3.5.3) is not consistent with radial transport from a single source area. Variably trending channel axes in one cliff exposure (Oh124, see Section 3.5.3) indicate that successive currents depositing lithofacies F were travelling in directions that were oblique to one another. For this reason, lithofacies F is unlikely to have the same origin as lithofacies E (scenario 3) which is characterised by channel axes that exhibit a consistent direction. Also, the sometimes-gradational relationship between lithofacies E and lithofacies A suggests that lithofacies E may be associated with the advancing front of an ignimbrite-producing flow (see

Section 3.6.2). Lithofacies F, on the other hand, does not exhibit the same gradational relationship with lithofacies A. With respect to scenario 4, there is no evidence for pre-existing valleys or deep channels; therefore, the geometric relationships shown by the IVD and VPI, such as in the Taupo ignimbrite, are not present.

The high frequency of alternations between lithofacies F and A, the lateral wedging out of lithofacies F packages against lithofacies A deposits, and the variability of channel axis directions is best explained by scenario 5. In this scenario, each lithofacies A package represents a discrete ignimbrite-forming event from the volcanic source vent followed by a localised hydroeruption and emplacement of a secondary pyroclastic package (lithofacies F). As such, each hydroeruption and the emplacement of its products reflect an interaction between a wet depositional environment and primary PDC deposits, and a time break in the eruption sequence from the volcanic source vent. This time break is concealed where two separate lithofacies A packages, above and below a lithofacies F package, come together where the lithofacies F package pinches into them (see Figure 3.27). The implication is that some of the cliff outcrops consisting solely of lithofacies A deposits, may be comprised of more than one, temporally distinct package (see Section 3.7.2 and Chapter 5 for a further discussion of time breaks).

The random orientation of channel axis directions in the *Tla* (Sections 3.4.6 and 3.5.3) provides supporting evidence for scenario 5. The randomness suggests that the channel and fill structures are not all associated with scouring from primary PDC's (i.e. lithofacies E), but that these structures may actually represent portions of secondary hydroeruption craters in cross-section (i.e. the bowl-shaped structure in Figure 3.28 and Figure 3.29). In Chapter 5, the *Tla* bowl-shaped structures are compared to funnel structures associated with documented secondary hydroeruptions. Also in Chapter 5, the lithofacies F deposits are compared with secondary hydroeruption deposits elsewhere, and the *Tla* is discussed with respect to the types of depositional environments responsible for triggering hydroeruptions.

3.6.5 Stag lithofacies association (Sla)

Sla lithofacies G

Like the *Tla*, the *Sla* exhibits similar alternations between bedded deposits (lithofacies G) and massive ignimbrite (lithofacies A); however, the bedded deposits are plane-parallel with individual packages traceable for > 200 metres. The combination of fine ash beds with high concentrations of accretionary lapilli and the pumice-lapilli supported beds (Figure 3.33) suggests that lithofacies G has an airfall origin or at least an origin with a dominant component of vertical trajectory; cross-larninations in the coarse crystal-rich ash beds suggest a minor

lateral component. If these deposits are associated with regional airfall (i.e. from an Ohakuri vent source), one would expect to see them exposed in the ~ 140 metre thick *Gla* cliff outcrops that are < 1 km away (refer to lithofacies association map, Figure 3.34). There is no evidence for significant fault displacement between *Sla* and *Gla* (see Section 3.7.2), therefore I suggest that lithofacies G has a more localised origin associated with secondary hydroeruptions. As with *Tla* hydroeruption deposits (lithofacies F), *Sla* lithofacies G is discussed in further detail in Chapter 5.

3.7 Discussion

3.7.1 Phreatomagmatism

Water is inferred to have not only played an important role in the variable depositional environment associated with the Ohakuri pyroclastic deposits (i.e. secondary hydroeruptions) but evidence also exists for water at the vent source(s). The Ohakuri pyroclastic deposits exhibit several characteristics that, together, suggest a phreatomagmatic origin. These characteristics are comparable to other documented phreatomagmatic silicic eruptions (cf. Self, 1983; McPhie, 1986; Wilson, 2001).

1) Accretionary lapilli in the Ohakuri pyroclastic deposits are observed as clasts within ignimbrite or as concentrations in fine-ash beds. Regardless of where they were formed, i.e. within PDC's, ash clouds, or eruption plumes (see Schumacher and Schmincke, 1995 for review), the origin of the accretionary lapilli, with the exception of those associated with secondary hydroeruptions, is best explained by scavenging of fine ash by water that condensed from steam produced in a phreatomagmatic eruption. Rain from passing storms can contribute to the formation of accretionary lapilli but the deposits are usually localised and reflect a storm pattern (Self and Sparks, 1978; McPhie, 1986). With respect to the Ohakuri pyroclastic deposits, the presence of accretionary lapilli in PDC deposits throughout their distribution does not correlate with a clear storm pattern. Further, accretionary lapilli within co-ignimbrite ash layers (*Mla*, Section 3.6.3) suggest that the presence of steam in PDC's must have been generated at the vent source (cf. McPhie, 1986).

2) A two-part fragmentation process is responsible for finer grain sizes associated with phreatomagmatic eruptions (Self and Sparks, 1978). Figure 3.36b shows that the Ohakuri PDC deposits favour the finer-grained end of the Walker (1983) 'normal ignimbrite' field on F_2 vs. F_1 plot, and are comparable to PDC deposits from the Oruanui eruption (C.J.N. Wilson, pers. comm., 2004).

3) Episodicity in eruptions can be characteristic of phreatomagmatic volcanism (e.g. White and Houghton, 2000; Wilson, 2001). In particular, Wilson (2001) correlates longer scale eruptive events/time breaks with major bedding units in the Oruanui pyroclastics. Likewise, discrete packages in the Ohakuri lithofacies associations show conclusive evidence for time breaks (see discussion below, Section 3.7.2) in the eruption sequence (i.e. alternating primary PDC deposition and deposition from secondary hydroeruptions in *Tla*, Section 3.6.4).

4) The entire exposed volume of Ohakuri PDC deposits is non-welded, including > 100 metre thick exposures in the *Gla*. The low grade of the ignimbrite is most likely related to water-cooling of magma at the vent source (Walker, 1983; McPhie, 1986). Cooling can also be generated by air ingestion in the eruption column; however, the presence of accretionary lapilli, the high concentration of fine ash, as well as relatively low crystal enrichment (cf. Wilson, 1985; Wilson and Walker, 1985), and the absence of plinian interbeds (cf. Hildreth, 1983; Fierstein and Hildreth, 1992), favour a phreatomagmatic origin. Water-cooling is also consistent with the inferred presence of a paleo-lake in the vicinity of the Ohakuri vent source(s) as described in Chapter 2.

5) Turbulent, highly concentrated PDC's (see origin for lithofacies C, Section 3.6.2 and Chapter 4) may be associated with phreatomagmatic volcanism.

Phreatomagmatism associated with the Ohakuri eruption is presumed to be similar to the Oruanui eruption as described by Wilson (2001). In particular, both eruptions are characterised by episodicity and a magma:water ratio that produced low grade ignimbrite with excessive matrix fines. In addition, the pyroclastic products of both eruptions show no signs of contemporaneous deposition of liquid water suggesting that the magma:water ratio was fairly consistent throughout the eruption (cf. fluctuations of magma:water interaction and syneruptive erosion associated with Hatepe and Rotongaio deposits (Walker, 1981), and Cana Creek Tuff (McPhie, 1986)). A noticeable difference in the two eruptions is the generation of pyroclastic airfall deposits, or the lack of airfall deposits in the case of the Ohakuri eruption. The Oruanui eruption generated a greater volume of pyroclastic fall deposits than PDC deposits (430 km^3 vs. 320 km^3, respectively; Wilson, 2001) and its dispersal index of 225,000,000 km^2 (C.J.N. Wilson, unpublished data in Houghton et al., 2000) makes it one of the most widespread phreatomagmatic eruptions ever recorded (Wilson, 2001). The Ohakuri eruption, on the other hand, is characterised by a remarkable dearth of exposed airfall deposits. Part of the reason for this is probably related to the burial of a large volume of Ohakuri pyroclastic deposits and the fact that Ohakuri proximal deposits have not been correlated with airfall deposits in the distal tephra record. However, proximal airfall (units 1, 2, and 3; Section 2.2.2) underlying Ohakuri

PDC deposits in the *Fla* are relatively insignificant with respect to documented thicknesses of phreatoplinian fall (e.g. Self and Sparks, 1978; Walker, 1981; Hayakawa, 1983; Hayakawa, 1990; Smith and Houghton, 1995; Wilson, 2001) and suggest that the Ohakuri eruption may have been associated with different dynamics. Evidence for fountaining, as opposed to plinian column collapse, is presented in Chapter 4 with respect to the origin of the giant-dune-bedded lithofacies C.

3.7.2 Time breaks

Episodicity in the Ohakuri eruption sequence is defined by time breaks that are inferred to have occurred on three different time scales; a long time scale (days to years), a moderate time scale (minutes to hours), and a short time scale (seconds to minutes). The long time scale is associated with episodicity of the precursor events leading up to the main Ohakuri pyroclastic eruption (refer to Section 2.2.2 for full details), where the deposition of 4 fall units originating from a body of water within what became the Ohakuri caldera, the Mamaku ignimbrite from Rotorua caldera, and the first PDC's associated with the Ohakuri pyroclastic deposits were separated by time breaks that varied from days to years. Moderate-scale time breaks are associated with alternations between primary PDC packages and packages of secondary hydroeruption deposits in the *Tla* and *Sla*. The short-term time scale is associated with time breaks between deposits from successive but distinct pulses of PDC's, i.e. reverse graded sub-packages of lithofacies D and scour and fill structures of lithofacies E.

The presence of each secondary hydroeruption package in the *Tla* and *Sla* is evidence for a hiatus in the Ohakuri eruption sequence. The deposits themselves and their alternating relationship with primary PDC deposits provide few clues into the length of each hiatus; however, comparing areas that exhibit alternating packages with areas that do not, can narrow down the elapsed time frame. For example, the alternations observed in the *Sla* are not present in ~ 140 metres of vertical exposure in the nearby (< 1 km) *Gla*, which is inferred from its stratigraphic relationships to have been deposited over much the same time period. Although cliff exposures of both the *Sla* and *Gla* are associated with two different strands of the Ngakuru Fault (see Map 1), differential displacement between the two strands is considered to be negligible as Villamor and Berryman (2001) suggest the total offset measured on the Ngakuru Fault is approximately 40 metres. Consequently, *Sla* and *Gla* are considered to be at a similar stratigraphic level, suggesting that time breaks evident in the *Sla* must be hidden in the massive ignimbrite (lithofacies A) of the *Gla*. As previously suggested in Section 3.6.4, there is evidence for similar time breaks in the *Tla*, where two distinct lithofacies A packages come together at the lateral pinch point of a lithofacies F package (Figure 3.27). At *Gla*, the lack of visible depositional boundaries is compounded by the fact that there is very little variation in grainsize (with the exception of the increased concentration and large clast sizes of the pink ignimbrite,

Gla, Section 3.5.1) and no variation in composition of clasts. Concealed depositional boundaries, like those in the *Gla* and *Tla*, have been documented in massive ignimbrite of the Bishop Tuff (Wilson and Hildreth, 2003). By comparing ignimbrite packages where no partings or boundaries can be discerned with the same packages in locations where they are separated by airfall, Wilson and Hildreth (2003) estimate time breaks of hours to tens of hours from airfall accumulation rates. A similar time break-scale may be assumed for Ohakuri massive *Gla* and *Tla* ignimbrite; however, the duration of a particular hiatus is constrained by secondary hydroeruptions occurring elsewhere, not the accumulation of airfall (cf. Wilson and Hildreth, 2003). Secondary hydroeruptions are discussed further in Chapter 5.

An important implication associated with concealed depositional boundaries in thick accumulations of ignimbrite is the depositional process responsible for the thick accumulation. At Long Valley caldera, Wilson and Hildreth (2003) provide quantitative evidence for time breaks in thick accumulations of the Bishop Tuff where there is no evidence for depositional boundaries. Thus, they conclude that thick accumulations of ignimbrite with no visible flow unit boundaries do not necessarily imply grain by grain, continuous aggradation (cf. Fisher, 1966; Branney and Kokelaar, 1992; Branney and Kokelaar, 1997). The lack of flow unit boundaries in the Bishop Tuff and the Ohakuri pyroclastic deposits by no means disqualify the progressive aggradation model but suggest that the model cannot be used universally for thick ignimbrite accumulations. It is possible that each structureless ignimbrite package (lithofacies A) in *Gla* or in any of the other lithofacies associations was deposited by progressive, grain by grain aggradation, or in punctuated fashion, or by processes transitional to en masse deposition (Sparks, 1976).

Other evidence for moderate time breaks in the Ohakuri eruption sequence includes the presence of co-ignimbrite ash (dust layers) overlying packages of the massive sub-lithofacies in *Mla* lithofacies E (Figure 3.43). In ignimbrite eruptions, the buoyant co-ignimbrite dust cloud (also referred to as a phoenix column, e.g. Dobran et. al, 1993) cannot always be distinguished from the buoyant eruption column. As a result, the time frame associated with dust layer accumulation may be similar to that of primary airfall, i.e. hours to tens of hours (refer to list of published accumulation periods and rates in Wilson and Hildreth, 1997).

With respect to the short time scale, the sharp contacts between reverse-graded sub-packages in lithofacies D and the scour structures in lithofacies E record very short depositional breaks. Both lithofacies D and E are associated with unsteady (nonsustained) PDC's that may be perceived as separate deposits from discrete flows, or as stepwise aggradation (see Branney and Kokelaar, 1992). Regardless of the depositional model, sharp contacts within lithofacies D and E represent time breaks that may only be seconds in duration.

3.7.3 Eruption history and formation of the Ohakuri caldera

The Ohakuri eruption sequence can be divided into 4 phases. The stratigraphic evidence is clear for the first 3 phases, and is presented in Section 2.2.2. However, for reasons given in the 'Introduction' of this chapter (Section 3.1), the stratigraphy for phase 4 (the Ohakuri pyroclastic deposits) is less well defined. To reconstruct the timing of phase 4 events, I combine lithological, geochemical, and geomorphological evidence.

The eruption of the Ohakuri pyroclastic deposits can be divided into two main events. The first event commenced with the eruption and emplacement of *Fla* deposits that directly overlie phase 1, 2 and 3 deposits (see Figure 2.14 and Figure 2.15). The surface exposure of the *Fla* forms an arc around the Ohakuri caldera from the southeast, clockwise to the north; however, this may not represent the total distribution of pyroclastic deposits associated with the first eruptive event. Evidence for the paleogeography prior to the Ohakuri eruptions (see Figure 2.4 and Figure 2.6) supports the presence of a large basin to the northeast and east of the Ohakuri caldera, which may have been a depocentre for eruptives from the first event (i.e. *Fla* correlatives). If *Fla* correlatives were deposited to the northeast and east, they would have been subsequently buried by deposits from later eruptive events, including the lithofacies associations *Gla*, *Mla*, *Sla*, and *Tla*. Drill core data from OHDG-3 (see Map 1 for hole location, and Appendix 5 for core log) neither confirms nor denies the presence of *Fla* correlatives at depth. The alternating packages of structureless, diffusely stratified and bedded deposits in drill core may be attributed to first event (*Fla*) or second event (*Gla*, *Mla*, *Sla*, and *Tla*) eruptives.

With respect to the eruption dynamics associated with the *Fla* PDC deposits, thick, massive ignimbrite is most likely related to stable collapse of an eruption plume; however, the mechanism for the generation of the scour and fill and dune-bedded ignimbrite is more complex. As suggested in Section 3.6.2, these deposits come from turbulent and unsteady PDC's that may have been associated with the advancing front of the massive ignimbrite-forming PDC's, or alternatively, they may be related to oscillatory fountaining or partial collapse from more sustained eruption columns (cf. units B and C of the Kos Plateau Tuff; Allen, 2001). Repeated sequences of massive and bedded deposits (i.e. lithofacies A, and C or E, respectively) may be associated with eruptions migrating between multiple vent sources (cf. T1 eruption cycles at Laacher See; Freundt and Schmincke, 1985). Eruption dynamics, particularly associated with turbulent, unsteady PDC's, are discussed in greater detail in Chapter 4.

Following the first Ohakuri pyroclastic event and a probable hiatus (length of time break is uncertain), the second event commenced. PDC's were directed to the east and northeast, depositing pyroclastic material in variable depositional environments that are distinguished, today, by the presence or absence of secondary hydroeruption deposits (i.e. lithofacies

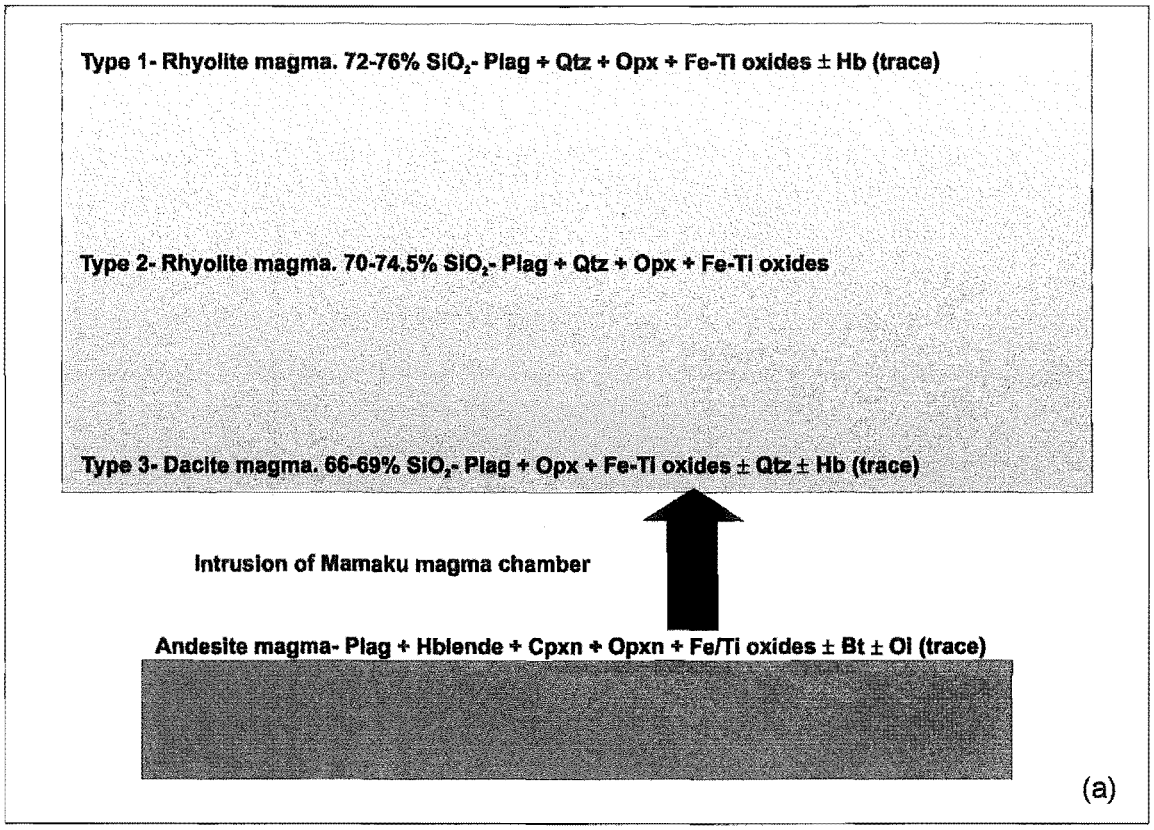

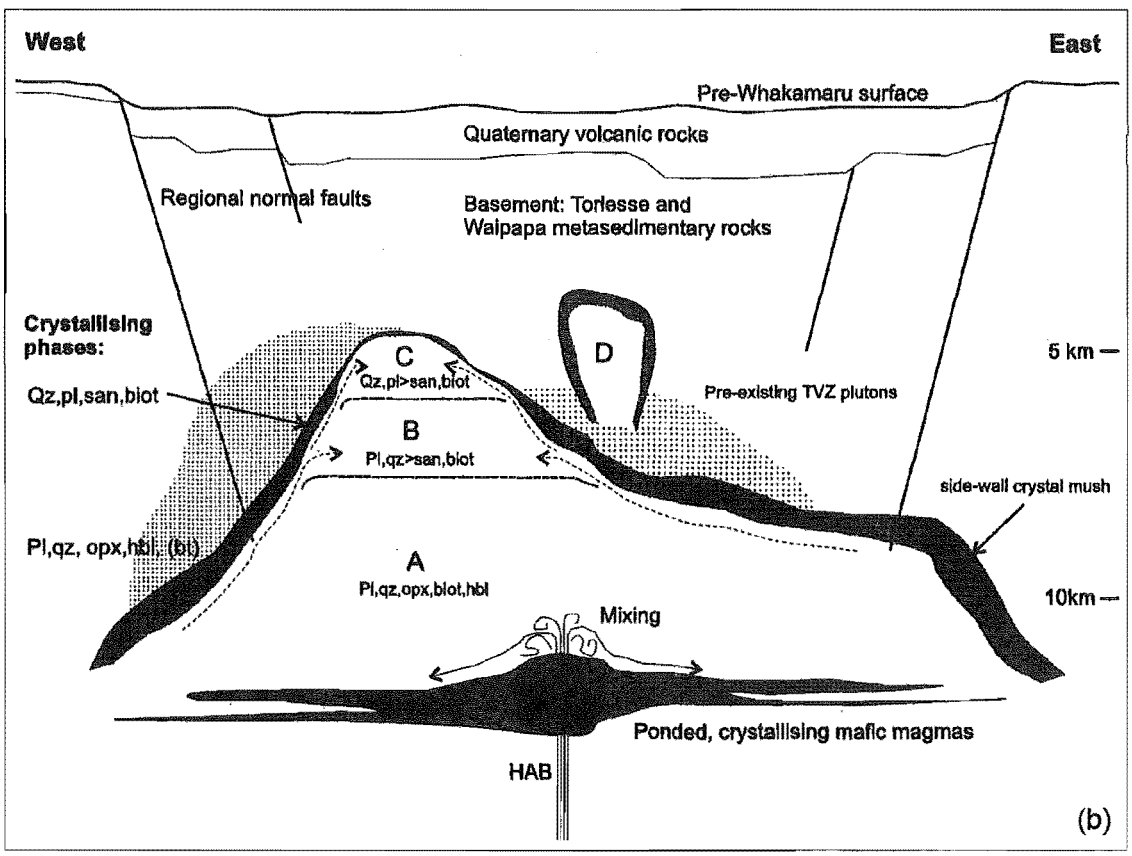

Figure 3.49 Schematic models of vertically zoned magma chambers. (a) Mamaku magma chamber, from Milner et al. (2003). (b) Whakamaru magma chamber, from Brown et al. (1998).

associations *Tla* and *Sla*). As such, wet vs. dry depositional environments as well as variation in eruption styles (i.e. oscillatory vs. sustained fountaining) are considered by me to be responsible for the lithofacies variation between the *Gla*, *Mla*, *Sla*, and *Tla*. The deposits of these lithofacies associations provide evidence for episodicity in the eruption sequence. Episodicity seems to be commonly associated with phreatomagmatism (Section 3.7.1; White and Houghton, 2000), but, as with the Oruanui eruption (Wilson, 2001), the cause(s) for individual hiatuses in the Ohakuri eruption is/are uncertain. As previously suggested, multiple vents may have been active during the Ohakuri eruption; however, any evidence for multiple vents and, therefore, evidence for episodicity related to vent migration has been lost through burial. The intensity (mass flux) of the episodic eruptions is perceived to be uniform, as there is very little variation in pumice and lithic sizes and concentrations in more than 200 metres of vertical exposure (in the *Gla*). The exception is the pink coloured ignimbrite (Section 3.5.1) with a marked increase in pumice and lithic sizes and concentrations. These attributes suggest a local, temporary increase in mass flux, and a relatively hotter emplacement temperature.

Two questions remain with respect to the Ohakuri eruption history: at which point in the Ohakuri eruption sequence did the caldera collapse and why were the PDC's in the second event of phase 4 directed to the east and northeast? To answer these questions, the Ohakuri pumice chemistry needs to be compared with the paleogeographic evolution associated with the Ohakuri eruption sequence. The first event deposits (*Fla*) and the second event deposits (*Gla*, *Mla*, *Sla*, and *Tla*) are chemically distinguishable by the absence and presence, respectively, of the less evolved, type 3 Ohakuri pumice (see Section 3.3.1 and compare Figure 3.5 and Figure 3.34). The chronostratigraphic relationship between the first and second event deposits may be explained by a model for a pre-eruption, vertically-zoned magma chamber where the Ohakuri type 1 and 2 magmas fractionated from a parent type 3 magma (cf. vertically zoned magma chambers associated with the Mamaku ignimbrite eruption from Rotorua caldera, and the Whakamaru ignimbrite eruption; Figure 3.49). The Ohakuri major and trace element variation is similar to that in Mamaku and Whakamaru ignimbrites (with the exception of the 'Whakamaru D' pumice) (see Figure 3.8 and Figure 3.9, respectively), that Milner et al. (2003) and Brown et al. (1998), respectively, used to support their zoned magma chamber models. The Ohakuri pyroclastic deposits are characterised by a mixture of pumice types throughout their stratigraphy, suggesting that magma withdrawal from a hypothetical Ohakuri zoned magma chamber would have to be associated with the simultaneous tapping of different levels of the magma chamber by multiple vent sources (cf. Milner et al., 2003).

The problem with this model is that the paleogeographic evolution associated with the Ohakuri eruption does not support the observed distribution of the different lithofacies associations and multilevel withdrawal of magma from a single zoned magma chamber beneath the Ohakuri

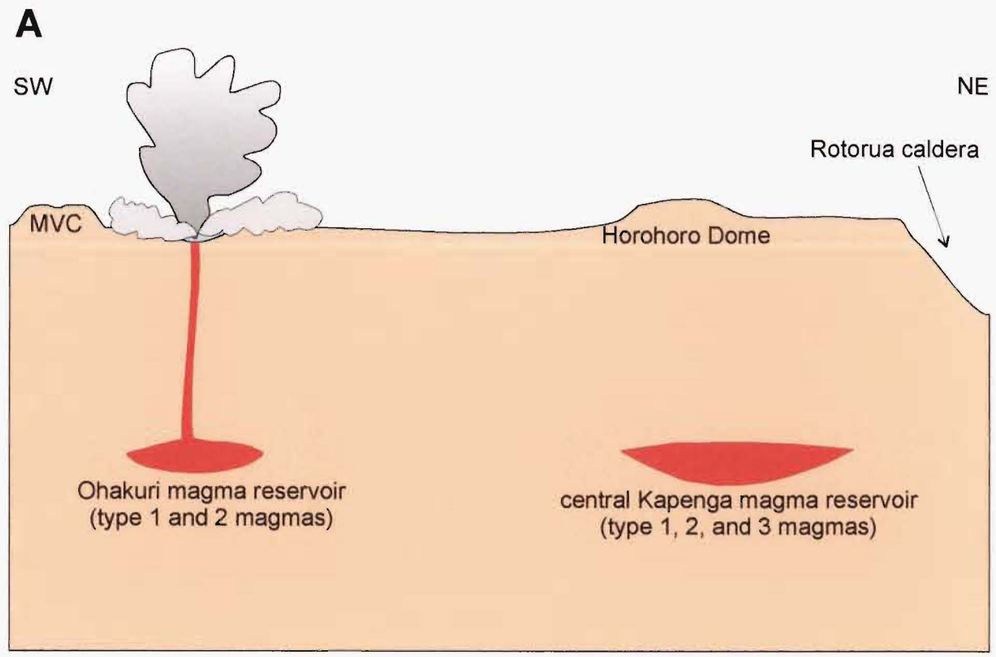

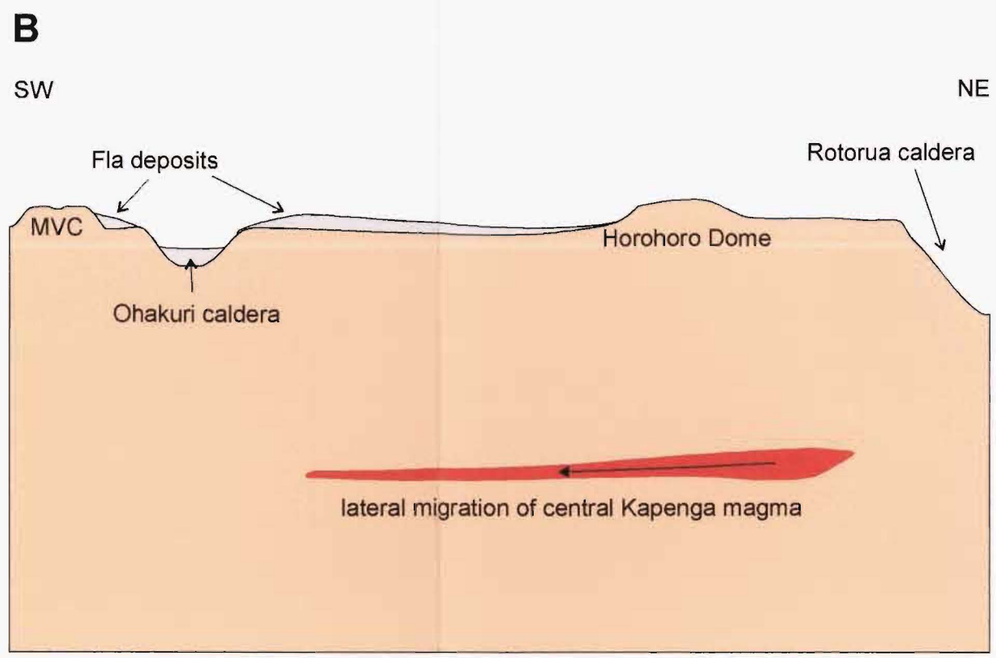

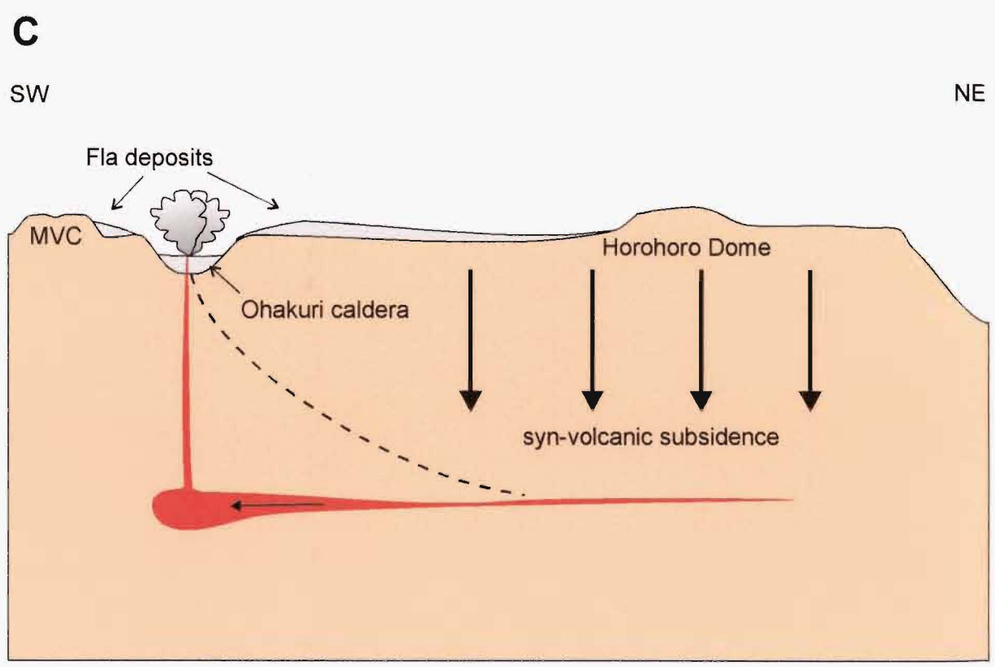

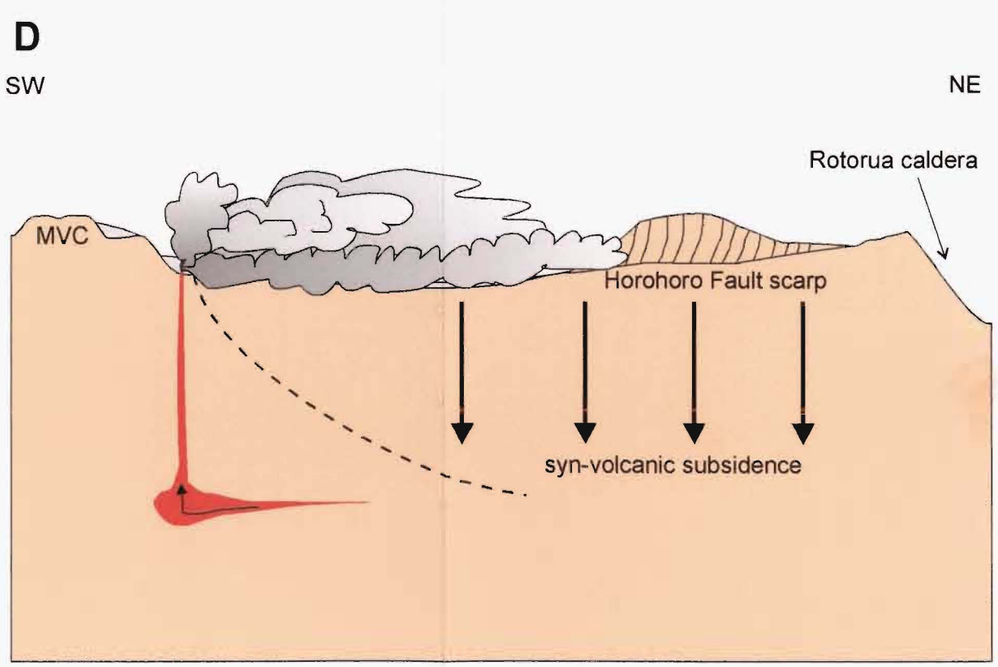

Figure 3.50 Ohakuri eruption sequence. (A) Eruption of the Ohakuri magma reservoir (the first event) which lead to the emplacement of the *Fla* deposits and the formation of the Ohakuri caldera. (B) Lateral migration of magma from beneath central Kapenga to beneath the Ohakuri caldera. (C) Eruption of the central Kapenga magma (the second event) from vent(s) within the Ohakuri caldera and the syn-volcanic collapse of the area above the former central Kapenga magma reservoir and the NE-SW trending conduit system. (D) Asymmetrical emplacement of the *Gla*, *Mla*, *Sla*, and *Tla* deposits within the subsided depression to the north and northeast.

caldera area. In Chapter 2, evidence is put forward for the passive (non-eruptive) subsidence of the central Kapenga area and the growth of a superfault (expressed today as the ~ 400 m high Horohoro Fault scarp) during the Ohakuri eruption. The passive (non-eruptive) subsidence may be explained by lateral withdrawal of magma from central Kapenga to the Ohakuri caldera. The following is a description of the entire Ohakuri eruption sequence (summarised in Figure 3.50) and my preferred model for the associated magma bodies.

The magma beneath the Ohakuri caldera erupted in the first event of explosive volcanism and was emplaced as the *Fla* PDC deposits. It is likely that the caldera began to collapse at some time during, or immediately following this event. The evidence for the onset of the collapse is based on the lack of second event deposits (the *Gla*, *Mla*, *Sla*, and *Tla*) south, west, and north of the caldera (refer to Figure 3.34), and the inferred displacement of the *Fla* deposits. The first eruptive event created space beneath the caldera floor and, at the same time, triggered the withdrawal of magma from beneath central Kapenga that was then erupted in the second event. Synvolcanic subsidence and the formation of a NE-SW graben, related to the lateral withdrawal of magma (Figure 3.50), encouraged the asymmetric distribution of PDC's to the northeast and east. It is uncertain as to how far to the southwest the laterally migrating magma travelled beneath the Ohakuri caldera because there is no evidence preserved at the surface that depicts the southwestern extent of the NE-SW graben structure.

Although simplified, this model is consistent with the fact that the inferred size of the Ohakuri caldera (~ 9 x 7 km) is somewhat underfit for a voluminous eruption of ~ 100 km^3 magma from one large, zoned magma chamber. As previously discussed in Chapter 2, the shape and lateral extent of the magma bodies associated with the Ohakuri caldera and the central Kapenga subsidence structure are uncertain. To further constrain this model, much more geochemical research is necessary including single crystal analyses (e.g. volatile determinations and/or U-Pb or U-Th zircon dating) to establish not only the chemical properties of the associated magma but the physical properties of the magma bodies and ages of the crystal populations in the different magma types of the Ohakuri and contemporaneous Mamaku eruptions.

4 The giant-dune-bedded lithofacies C, as revealed by ground penetrating radar (GPR)

4.1 Introduction

In Chapter 3, where lithofacies C has been described, it was suggested that the giant-dune deposits exhibit characteristics of both pyroclastic flow and surge deposits. In this chapter, the giant-dune deposits are characterised using ground penetrating radar (GPR) and grain-size techniques, and their origin is investigated with particular emphasis placed on flow and eruption dynamics.

To review, the giant-dune-bedded lithofacies C is exposed in the north and northwest sectors of the field area (Section 3.4.3, Chapter 3), forming a wedge-shaped veneer on top of the Mamaku ignimbrite slope that descends from the Mamaku Plateau (Section 2.2.2, Chapter 2). Lithofacies C extends only 8 km from the inferred north-northwestern margin of the Ohakuri caldera, as it thins rapidly as it rises on to the Mamaku Plateau. The scale and continuity of the giant-dune-bedforms of lithofacies C are observed best in a ~ 3 km stretch of benched roadcuts along Highway 1 (Figure 4.1), where the deposit is up to 20 m thick. The roadcuts were established during realignment construction of Highway 1 in 1995 (see Figure 4.2); however, the dune deposits were not studied at the time (only some photographs were taken by C.J.N. Wilson) and have since been obscured by vegetation growth. To unveil the giant-dune beds and document them, particularly in the sub-surface, a ground penetrating radar (GPR) study was performed.

4.2 GPR and volcanic deposits

GPR is a portable geophysical technique used to assist investigations where shallow, unexposed rocks are too difficult to study using conventional geological techniques (e.g. Davis and Annan, 1989; Russell and Stasiuk, 1997; Cagnoli and Russell, 2000). The GPR consists primarily of a pulse generator/transmitting antenna unit, and a receiving antenna/laptop computer unit. The transmitting and receiving units are moved together along a transect, keeping a constant separation from each other. The pulse generator creates an electromagnetic current with a known frequency that is transmitted into the shallow subsurface along the transect. The propagating current is scattered or reflected by changes in dielectric properties of the subsurface material; dielectric discontinuities in the subsurface are controlled primarily by water content, chemical composition and texture of rocks (Davis and Annan, 1989; Cagnoli and Russell, 2000). The reflected waves are picked up by the receiving antenna and logged into the laptop. On the laptop, data are automatically recorded at each antenna location

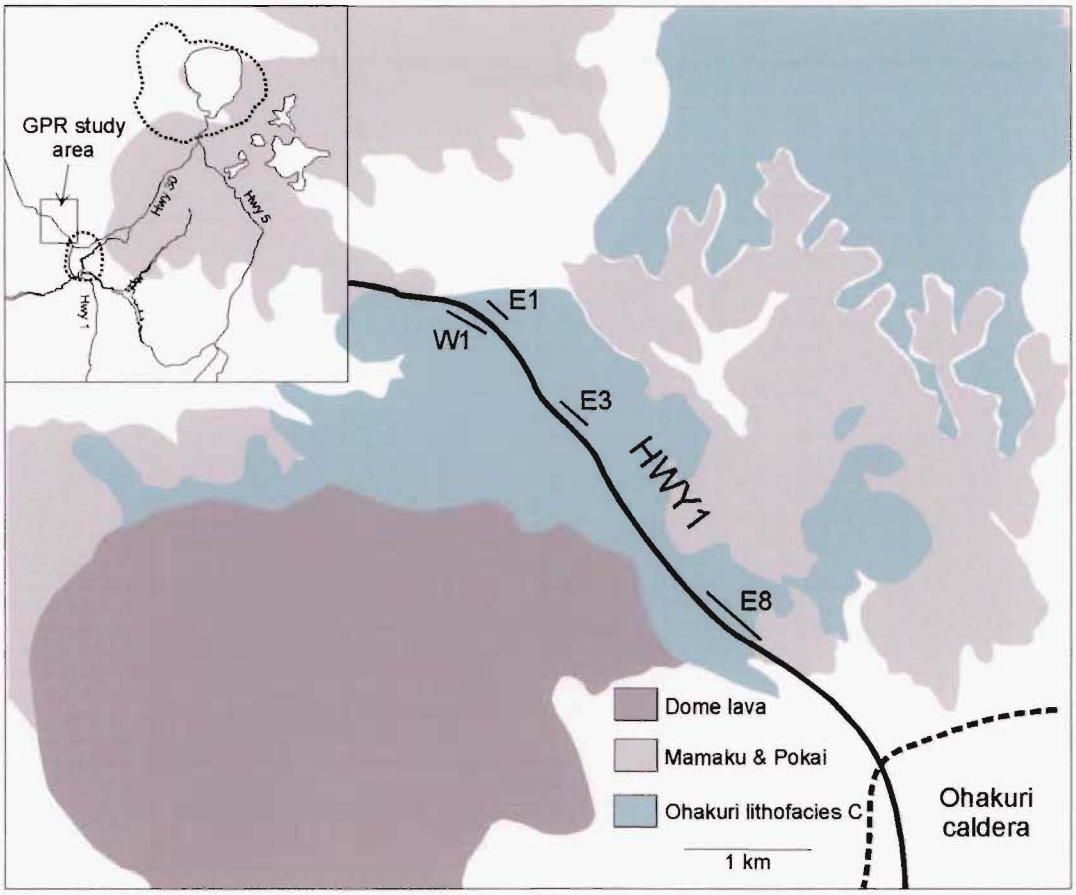

Figure 4.1 Location map of the GPR study area including the profile locations for W1, E1, E3, and E8.

and is equal to a single trace. The sequential compilation of a finite number of traces is presented as a GPR profile.

GPR has been used successfully in a wide range of environments and fields of study, including: glaciology, geology, environmental studies, civil engineering, archaeology and, more recently, volcanology (e.g. Russell and Stasiuk, 1997; Cagnoli and Russell, 2000; Rust and Russell, 2000; Cagnoli and Ulrych, 2001a; Cagnoli and Ulrych, 2001c; Cagnoli and Ulrych, 2001b). Russell and Stasiuk (1997) surveyed lavas, block and ash flows, and pumiceous pyroclastics from Mount Meager (British Columbia, Canada) to assess the utility of GPR on a variety of volcanic deposits and specifically the variation in dielectric properties. Their results suggest that GPR is particularly effective on pumiceous pyroclastic material, which has a low dielectric constant due to high porosity and resistivity (Russell and Stasiuk, 1997). In addition, pumiceous deposits are generally characterised by a wide grain-size distribution and relatively thin layers, optimising the potential for elucidating finer-scale internal structures (Russell and Stasiuk, 1997).

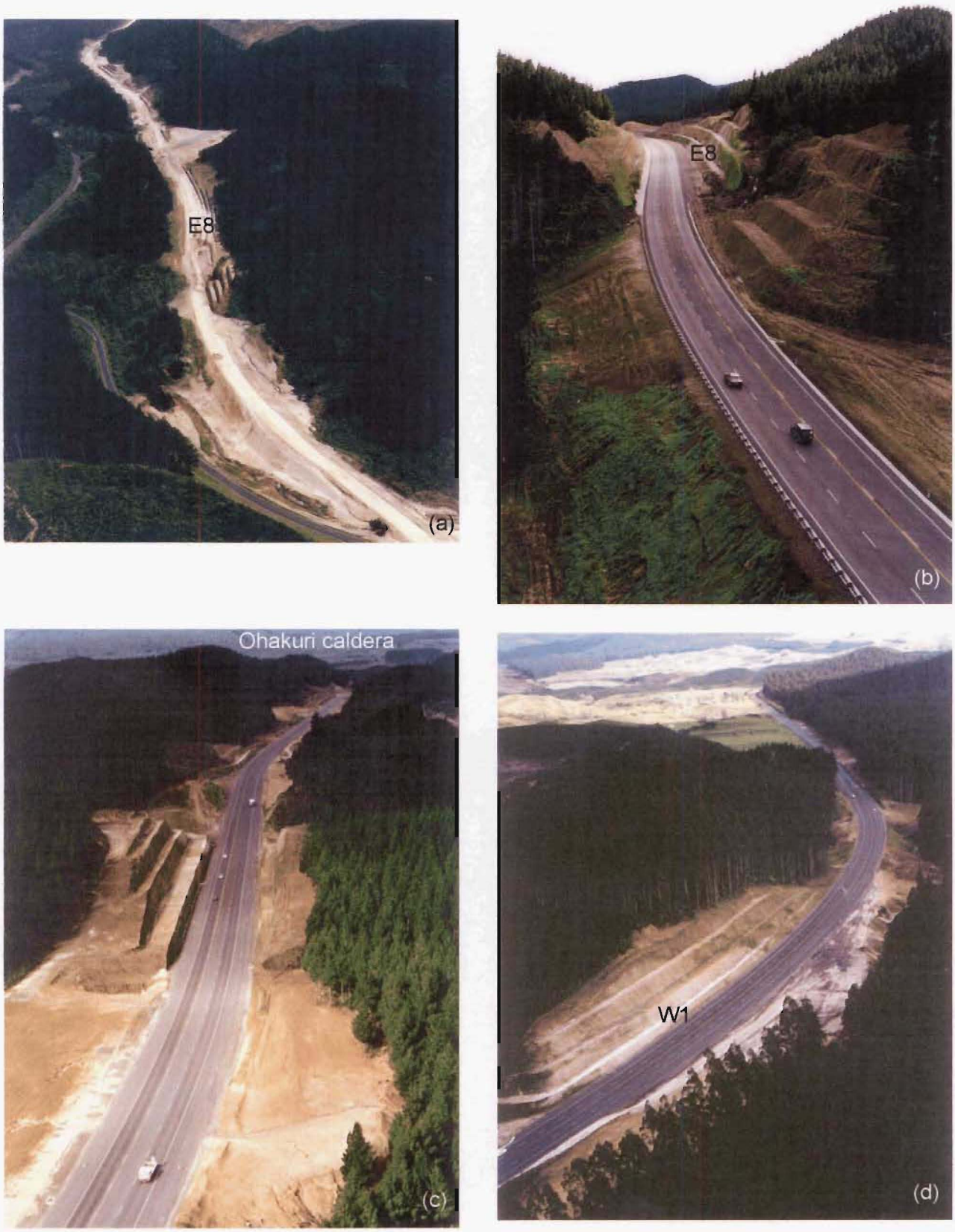

Figure 4.2 Oblique aerial views of the GPR study area and the HWY1 roadcuts. (a) View of the realignment construction, looking north from the bottom of the study area. (b) View looking north from the bottom of the study area. (c) View looking south with the Ohakuri caldera in the distance. (d) View of the WI profile, looking north.

Despite the utility of GPR in volcanic terrain, it has only recently been used to help interpret physical volcanological processes. GPR results from the Ubehebe hydrovolcanic field in Death Valley, California (see Cagnoli and Russell, 2000; Cagnoli and Ulrych, 2001a, b, c) were the impetus for the Ohakuri giant-dune bed study. At Ubehebe, Cagnoli and Ulrych (2001a, b, c) used GPR to help interpret the transport and deposition of base surge deposits in a volcanological context.

4.3 GPR and lithofacies C

4.3.1 GPR data acquisition

GPR profile measurements were taken along four lines (E1, W1, E3 and E8; Figure 4.1). Each of the four lines was on top of a different roadcut bench. The profile measurements were made using a commercially available SIR-20 (GSSI) system and a GSSI 400 MHz frequency antenna that was shielded to minimise above-ground interference from the vertical walls of the road cutting. The vertical resolution of this antenna is better than 5 cm, and depth penetration within the deposit is > 5 m. Controlled by a digital survey wheel, the antenna was pulled across the ground surface at a walking pace (Figure 4.3) and measurements (scans) were taken at 1 cm intervals (acquisition rate of 100 scans per metre). Each trace, which is equal to a finite antenna location, was digitised into 512 samples with 16 bits per sample.

Figure 4.3 GPR antenna is being pulled along the top of the roadcut. The antenna is connected to a laptop in the back of the car via a cable. The car is driven along at the same pace as the person pulling the antenna.

It is possible to collect data using air-launched antennae (e.g. over very rough terrain); however, a ground-coupled antenna was used in this study to increase the signal penetration. With the ground-coupled antenna, the smoothest surfaces had to be chosen to avoid the sudden introduction of air gaps beneath the antenna elements. Air gaps can modify the signal propagation into the ground and have a significant impact on the data quality.

4.3.2 GPR data processing

Post-processing of the GPR data was required to reduce the levels of high and low frequency noise from above-ground objects, and from within the GPR control system, the antenna, and the control cables. All GPR profiles were processed using RADAN-NT software. The initial data processing included frequency spectrum analysis, which involved graphical representation of the frequency spectra along each profile line. From the frequency spectra, optimum low and high pass filters were chosen to exclude the noise components of the data. A low pass filter rejects all frequencies above a specified value, which for this data set was typically 750 MHz. The high pass filter that was chosen eliminated low frequency noise below 95 MHz. In addition, a background noise-removal filter was also used to reduce the effect of system noise in the form of horizontal lines, often caused by interference within the antenna or cable.

Other processing steps included trace stacking and gain adjustments to boost the reflection amplitude of deeper, weaker reflections. A process called 'migration' was also used to remove the effects of reflector curvature and dip, and bring all reflections into their true subsurface positions. The final profile data are displayed as a gray scale variable intensity plot, with shades of gray corresponding to the amplitude of the GPR signal reflection.

4.3.3 GPR data presentation and results

GPR profiles for W1 and E8 provide the most data with respect to the giant-dunes, and are presented in Appendix 6. For ground-truthing purposes, a comparison between two sections of the W1 profile and a photograph of the W1 roadcut (taken in 1995, after grass spraying but before significant growth of vegetation) is shown in Figure 4.4. The close resemblance between the GPR profile and the photograph, combined with the high resolution imagery of the profile, suggests that the continuous, flat roadcut benches and the high porosity of the unwelded pyroclastic material are optimal GPR conditions. The vivid reflections in the profiles reveal a sharp contrast in the dialectric properties between the coarser pumice concentration bands and finer ash layers. The result is a clear image of the giant-dune-bedforms.

In Appendix 6, an interpretation has been drawn beneath the W1 and E8 profiles to highlight the giant-dune structures. Fortuitously, these two profiles are located at opposite ends of the ~ 3 km long study area, providing important information with respect to changes in the depositing

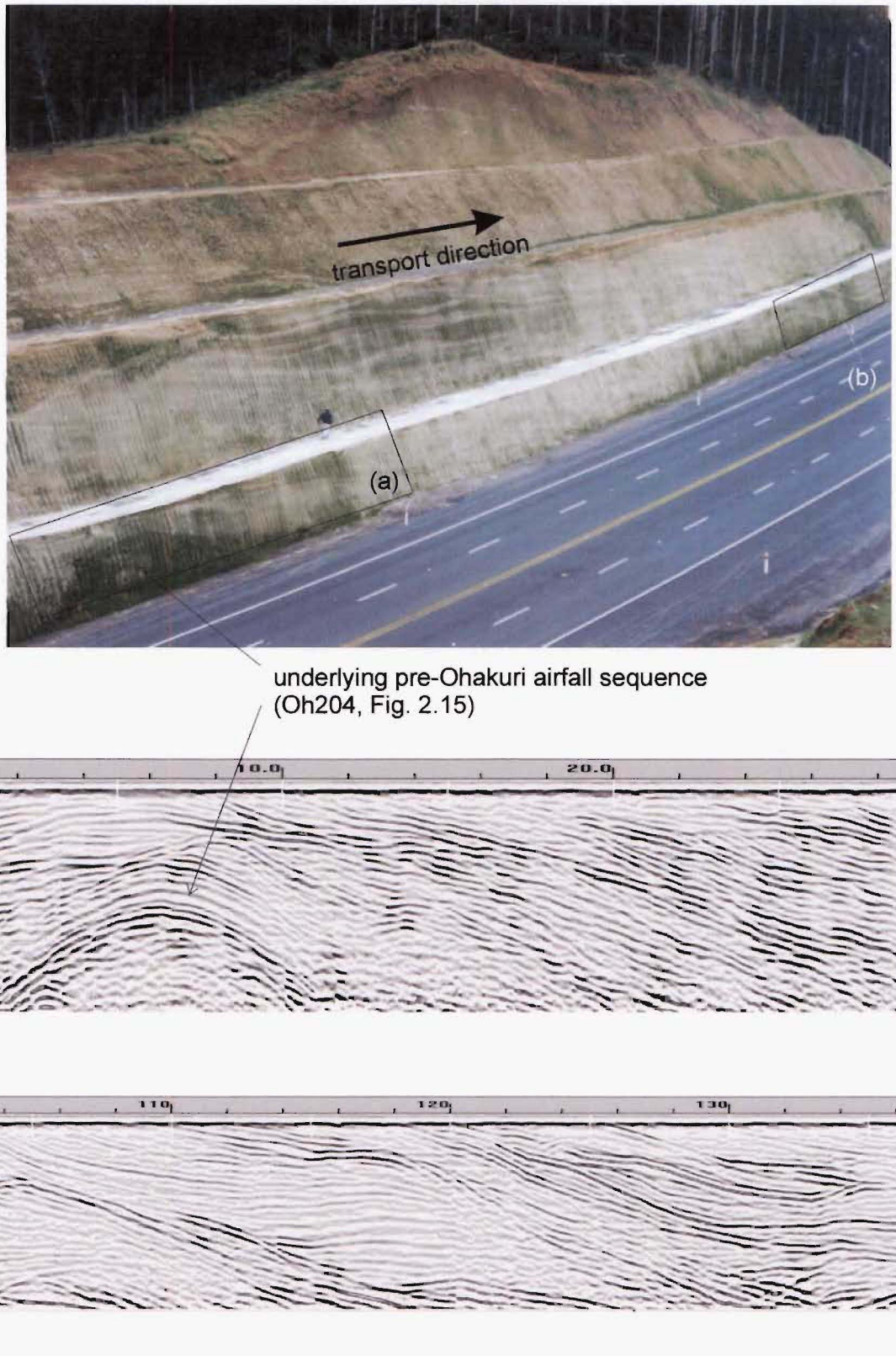

Figure 4.4 Comparison between a photograph of the W1 roadcut bench (courtesy of C.J.N. Wilson) and 2 sections from the W1 GPR profile.

parent PDC's. Comparing W1 and E8 with dune profiles from the Ubehebe hydrovolcanic field (Figure 4.5), the Ohakuri giant-dunes are > 20x larger than those at Ubehebe. Dunes in the E8 profile exhibit wavelengths up to 42 m and waveheights > 5 m, where dunes in the W1 profile are approximately half the size (20 m in wavelength). The dunes are characterised by progressive-type foreset bedding with low angles of deposition on the lee sides and low angle truncations on the stoss sides. Profile W1 also shows evidence for smaller scale regressive-type dunes as depicted in the area enclosed by the box in the W1 profile (Appendix 6). The boxed area is characterised by abundant truncations of stacked dune formations that exhibit both regressive-type backset bedding and progressive-type foreset bedding.

Other features that are apparent in the profiles are conspicuous hyperbolae. Hyperbolae may represent reflections of large lithic blocks, or in some cases vertical drainage pipes (see E8 profile).

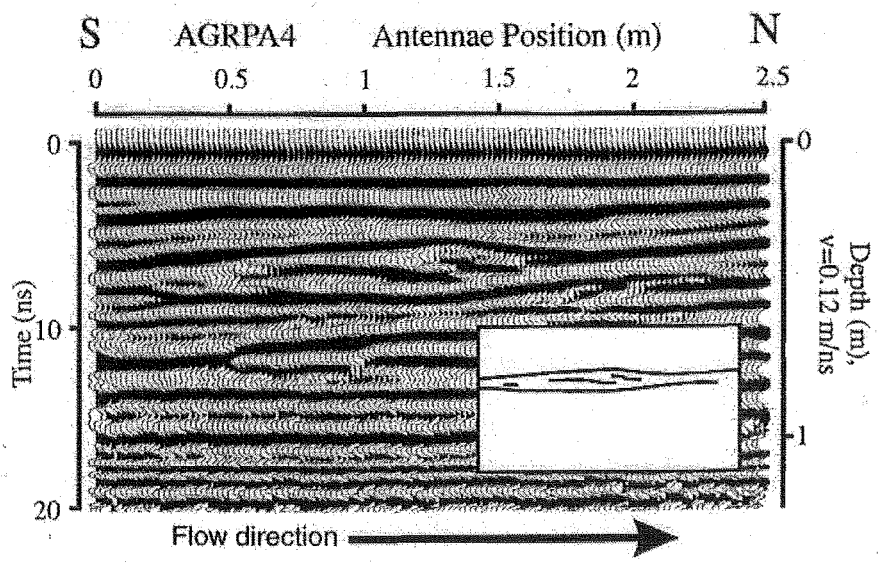

Figure 4.5 GPR profile showing the crest of a climbing dune form, emphasised in the inset, from the Ubehebe hydrovolcanic field. Image is taken from Cagnoli and Ulrych (2001b).

4.3.4 Volcanological interpretation

Flow dynamics

The giant-dune-bedforms and their large wavelengths are indicative of highly turbulent flow. The diffuse stratification (pumice banding) that characterises the anatomy of each giant-dune represents multiple pulses of continuously aggrading density currents. Giant-dunes in profiles E8 and W1 clearly show that the transport direction for the turbulent, parental currents was from the southeast to the northwest, consistent with an explosive eruption from a vent within what I establish in this thesis as the Ohakuri caldera. The close proximity of the giant-dunes to the Ohakuri caldera and the conspicuous downstream decrease in dune wavelength suggests that

the transporting PDC's were decelerating away from the vent source where the turbulence was initiated. A downstream/downflow decrease in wavelength and the low dip angles of foreset and backset laminae invite comparison of the Ohakuri dunes with documented dunes associated with pyroclastic density currents at Taal (Waters and Fisher, 1971), Laacher See (Schmincke et al., 1973), Ubehebe (Crowe and Fisher, 1973), El Chichon (Sigurdsson et al., 1987), and Mount St. Helens (Druitt, 1992).

Example	λ (m)	max λ (m)	λ/max λ	d (km)	max d (km)	d/max d
El Chichon	40.0	40.0	1.00	4.0	5.7	0.70
	30.0	40.0	0.75	4.4	5.7	0.77
	16.0	40.0	0.40	5.2	5.7	0.91
	1.0	40.0	0.03	5.7	5.7	1.00
Mount St. Helens	20.0	20.0	1.00	8.2	16.1	0.51
	10.0	20.0	0.50	10.6	16.1	0.66
	6.0	20.0	0.30	11.8	16.1	0.73
	2.0	20.0	0.10	13.5	16.1	0.84
	0.5	20.0	0.03	16.1	16.1	1.00
Taal	19.0	19.0	1.00	0.0	2.0	0.00
	11.5	19.0	0.61	0.8	2.0	0.38
	9.0	19.0	0.47	1.0	2.0	0.50
	5.5	19.0	0.29	1.5	2.0	0.75
	4.0	19.0	0.21	2.0	2.0	1.00
Ubehebe	2.1	2.1	1.00	0.0	1.2	0.00
	0.3	2.1	0.14	1.2	1.2	1.00
Ohakuri	42.0	42.0	1.00	2.0	5.0	0.40
	20.0	42.0	0.48	5.0	5.0	1.00

Table 4.1 Wavelength, maximum wavelength, distance, and maximum distance data for documented dune bedforms from El Chichon (Sigurdsson et al., 1987), Mount St. Helens (Druitt, 1992), Taal (Waters and Fisher, 1971), Ubehebe (Crowe and Fisher, 1973), and Ohakuri lithofacies C.

Dune wavelengths can provide information with respect to the velocity and deceleration of turbulent PDC's with increasing distance from source. For example, by comparing the dune bedforms from Taal and Ubehebe (at similar distances from source), Crowe and Fisher (1973) suggest that the larger wavelengths at Taal correlate with higher flow velocities. It is, therefore, probable that El Chichon wavelengths of ~ 40 m (Sigurdsson et al., 1987), twice the length of the largest Taal wavelengths and further from vent (see Table 4.1), correlate with higher flow velocities than those at Taal. A corollary to the proportionality between dune wavelength and current velocity, is that the decrease in dune wavelength away from vent (rate of wavelength decay, $\Delta\lambda$) is proportional to the deceleration rate (Δv) of the current (Schmincke et al., 1973),

$$\Delta\boldsymbol{\lambda} \;\alpha\; \Delta\mathbf{v}$$

where $\boldsymbol{\lambda}$ is wavelength and $\mathbf{v}$ is velocity.

For El Chichon, Sigurdsson et al. (1987) take the maximum and minimum wavelength values (40 m and 1 m) and their respective distances from vent (4.0 km and 5.7 km) to calculate a $\Delta\lambda$ of 23 m/km, which is at least one order of magnitude greater than the $\Delta\lambda$ values for Ubehebe and Taal (0.4 to 1.0 m/km). Sigurdsson et al. (1987), therefore, infer that currents with higher initial velocities exhibit a higher $\Delta\lambda$; however, if the El Chichon wavelength and distance from

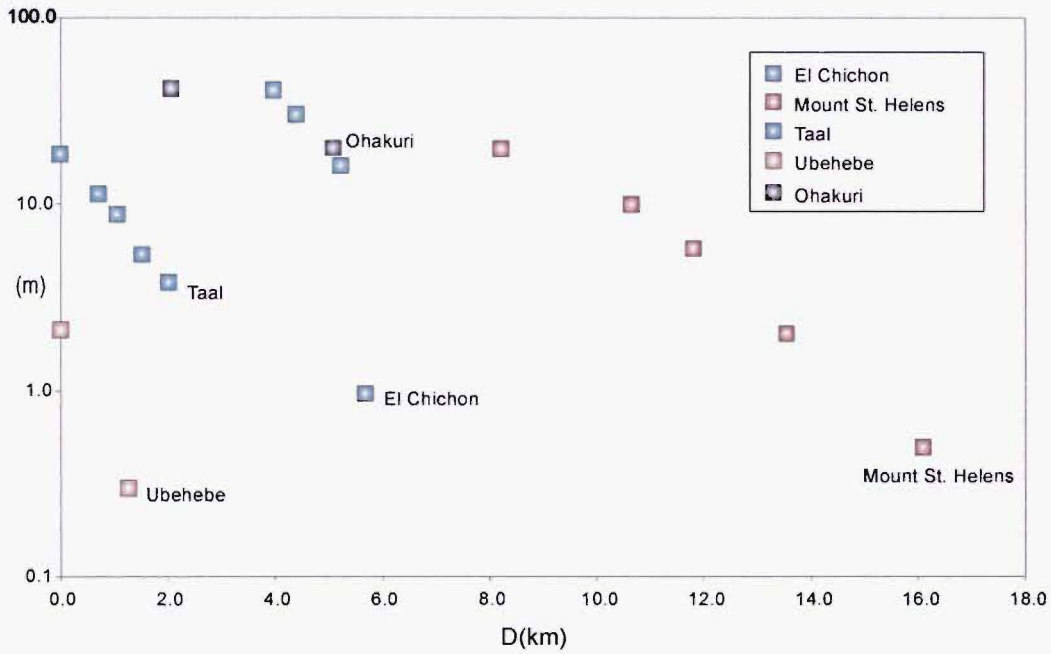

Figure 4.6 Wavelength (λ) vs. distance (d) variation diagram for dune bedforms from El Chichon, Mount St. Helens, Taal, Ubehebe, and Ohakuri lithofacies C. Data are from Table 4.1.

vent data from Table 4.1 are plotted on a variation diagram (Figure 4.6), it is clear that the minimum wavelength value used to calculate the 23 m/km rate of decay is grossly inconsistent with the other data points. In addition, Figure 4.6 does not provide a good basis for comparison between the different data sets (i.e. El Chichon vs. Ubehebe or Taal) because there is too much of a discrepancy between the size of their respective wavelengths and the distance from vent where the wavelengths were measured. To provide a more consistent basis for comparison, I have normalised the data by calculating wavelength/maximum wavelength and distance/maximum distance values (see Table 4.1) and plotted them on a new variation diagram (Figure 4.7). In Figure 4.7, the slope of the El Chichon best fit line reflects a $\Delta\lambda$, or Δv, that is only slightly higher than Ubehebe and Taal. The inference is that a high initial velocity does not necessarily correlate with such a high Δv (cf. Sigurdsson et al., 1987) and, in fact, the slope of the best fit line through the Ohakuri lithofacies C data points suggests that the opposite can be true (i.e. a Δv value for a higher velocity current can be smaller than that for a slower-moving current).

For comparative purposes, the Ohakuri lithofacies C and El Chichon dune deposits are well matched. The dune bedforms are of a similar size (viz. similar current velocities), and the

exposures where wavelengths have been measured are a similar distance from vent (see Table 4.1 and Figure 4.6), yet the slope of their respective best fit lines (see normalised plot, Figure 4.7) suggests that the rate of wavelength decay ($\Delta\lambda$) and, therefore, the deceleration rate (Δv) is

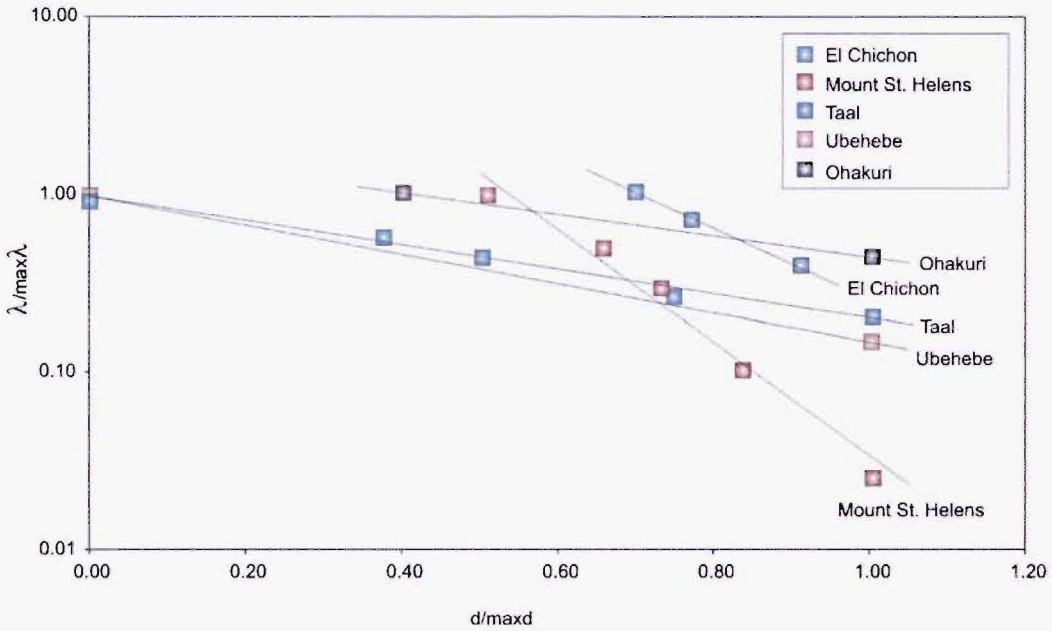

Figure 4.7 Variation diagram for normalised wavelength and distance values for El Chichon, Mount St. Helens, Taal, Ubehebe, and Ohakuri lithofacies C.

lower for the Ohakuri lithofacies C. This contrast in Δv values is amplified even more if the role of slope-related velocity changes is adjusted for in both examples. El Chichon currents were erupted from an elevated source (1100 m above sea level (ASL) '1982 crater'; see Macias et al., 1997) and the dunes studied by Sigurdsson et al. (1987) were deposited on relatively flat topography below the crater (~ 400 m ASL). Applying the law of conservation of energy,

$$\mathbf{KE_1 + PE_1 = KE_2 + PE_2,}$$

where KE is kinetic energy and PE is potential energy, and then substituting this equation for

$$\mathbf{1/2mv^2_1 + mgh_1 = 1/2mv^2_2 + mgh_2,}$$

where **m** is mass, **g** is acceleration of gravity, **h** is height, and **v** is velocity, the contributions to the velocity of the El Chichon currents at 400 m ASL can be determined with respect to the elevation change of ~ 700 m from the 1982 crater. Note, the contribution of the initial velocity, largely related to column collapse (see Macias et al., 1997 and references therein), is not factored into the equation,

$$\mathbf{0 + mgh_1 = 1/2mv^2_2 + 0}$$

where $\mathbf{mgh_1}$ is the potential energy at 1100 m ASL, and $\mathbf{1/2mv^2_2}$ is the kinetic energy at 400 m ASL. If this equation is manipulated to solve for the velocity of the currents at 400 m ASL,

$$v_2 = (2gh_1)^{1/2}$$

then it becomes clear that the elevation change ($\mathbf{h_1}$) and the acceleration of gravity ($\mathbf{g}$) are the primary contributors. In contrast, Ohakuri lithofacies C currents were erupted from within a topographic low and were deposited on a gentle uphill slope. Despite the fact that the uphill climb and the acceleration of gravity were acting against the Ohakuri currents, the change in velocity between 2 and 5 km reflects a slower deceleration rate than that of the El Chichon currents. This is most apparent at ~ 5 km from vent, which is approximately the distance where the El Chichon and Ohakuri wavelengths are the same (see Figure 4.6) and therefore the velocities are inferred to be the same, but the deceleration rates are significantly different. The implication is that the Ohakuri lithofacies C dunes are related to PDC's with fundamentally different physical properties.

Grainsize characteristics for the two different deposits can provide insight into the physical characteristics of the transporting current, particularly its mass. In Figure 4.8, dune bed deposits from several different volcanoes are plotted on a sorting (σ_Φ) vs. median diameter (Md_Φ), and a wt% finer than 1/16 mm (F_2) vs. wt% finer than 1 mm (F_1) diagram. On both diagrams, El Chichon deposits plot well within the 'pyroclastic surge' field, whereas Ohakuri lithofacies C correlates better with pyroclastic flow deposits. With respect to turbulent PDC deposits, Ohakuri lithofacies C is anomalous and only the Tsumaya dune deposits (Figure 4.9a) from the 22 ka Aira caldera eruption (Aramaki, 1984; Fukushima and Kobayashi, 2000; Fukushima and Kobayashi, 2003) and the proximal 1.8 ka Taupo ignimbrite veneer dune deposits (Figure 4.9b) (Wilson, 1981; Wilson, 1985) have a similar grainsize distribution (Figure 4.8). In particular, the high < 1/16 mm fraction (> 30%) for these dune deposits (see Figure 4.10 for Tsumaya fine ash content) suggests their parental PDC's were carrying a much higher fine ash component just prior to deposition. As suggested in Section 3.5.3, Ohakuri lithofacies C (with the exception of the basal deposits) has a similar or higher fine ash content as the massive lithofacies A and B ignimbrite. The implication is that, like currents associated with ignimbrite, lithofacies C was deposited from heavily loaded currents with a high mass per unit volume. In contrast, the lack of fine ash in the El Chichon dune beds is attributed to winnowing processes within dilute, density stratified currents (Sigurdsson et al., 1987).

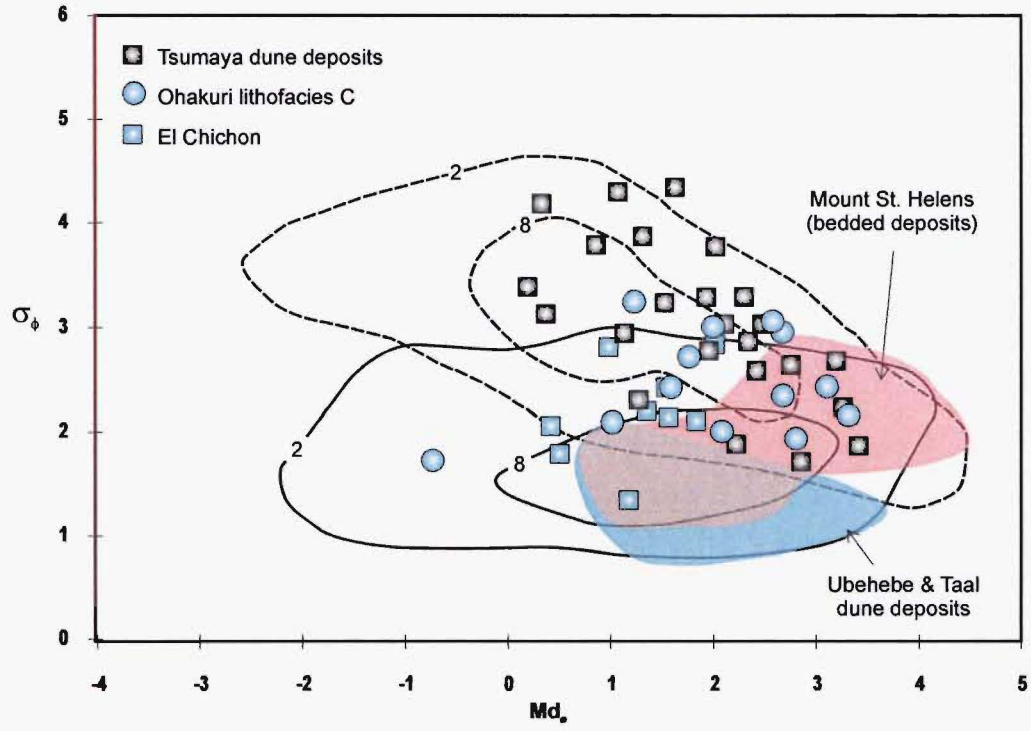

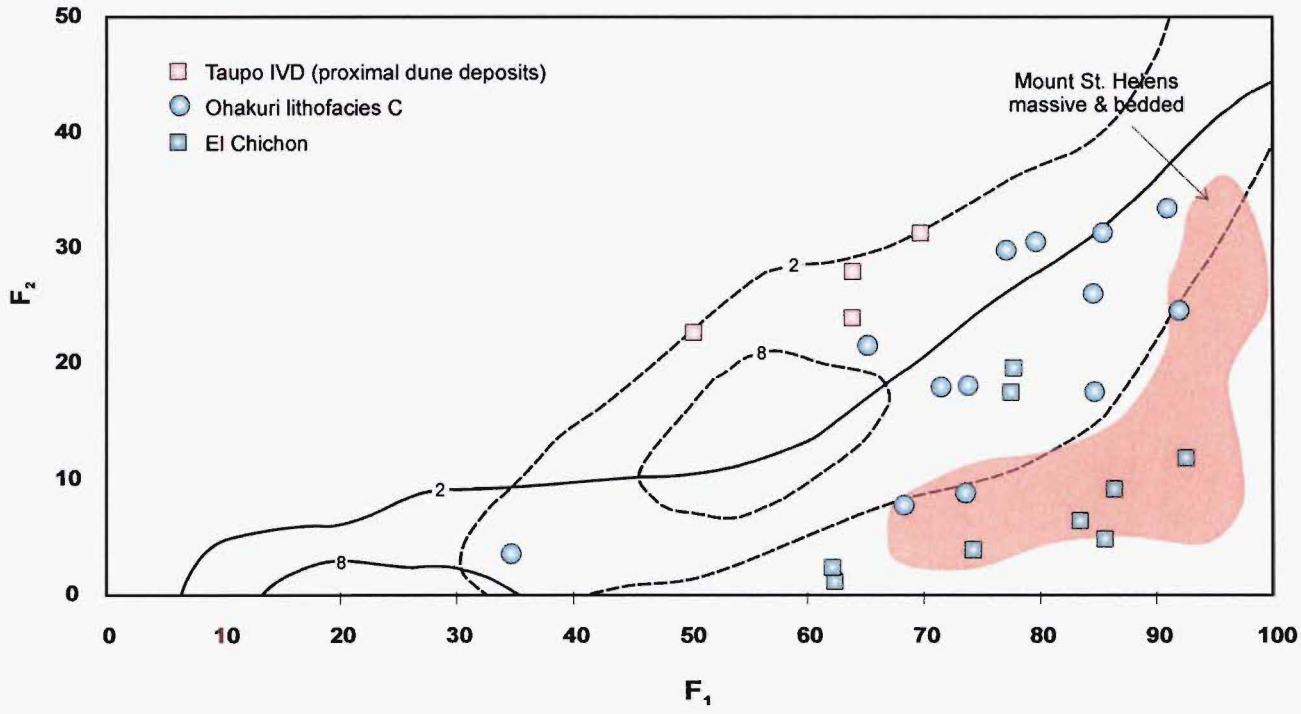

Figure 4.8 Grainsize distribution (σ_ϕ vs. Md_ϕ, and F_2 vs. F_1) of dune deposits from El Chichon (data from Sigurdsson et al., 1987), Mount St. Helens (data from Sigurdsson et al., 1987), Ubehebe and Taal (Fisher and Schmincke, 1984), Tsumaya (Fukushima and Kobayashi, 2000), Taupo (Wilson, 1981), and Ohakuri lithofacies C. Refer to Figure 3.47 for explanation of contoured fields.

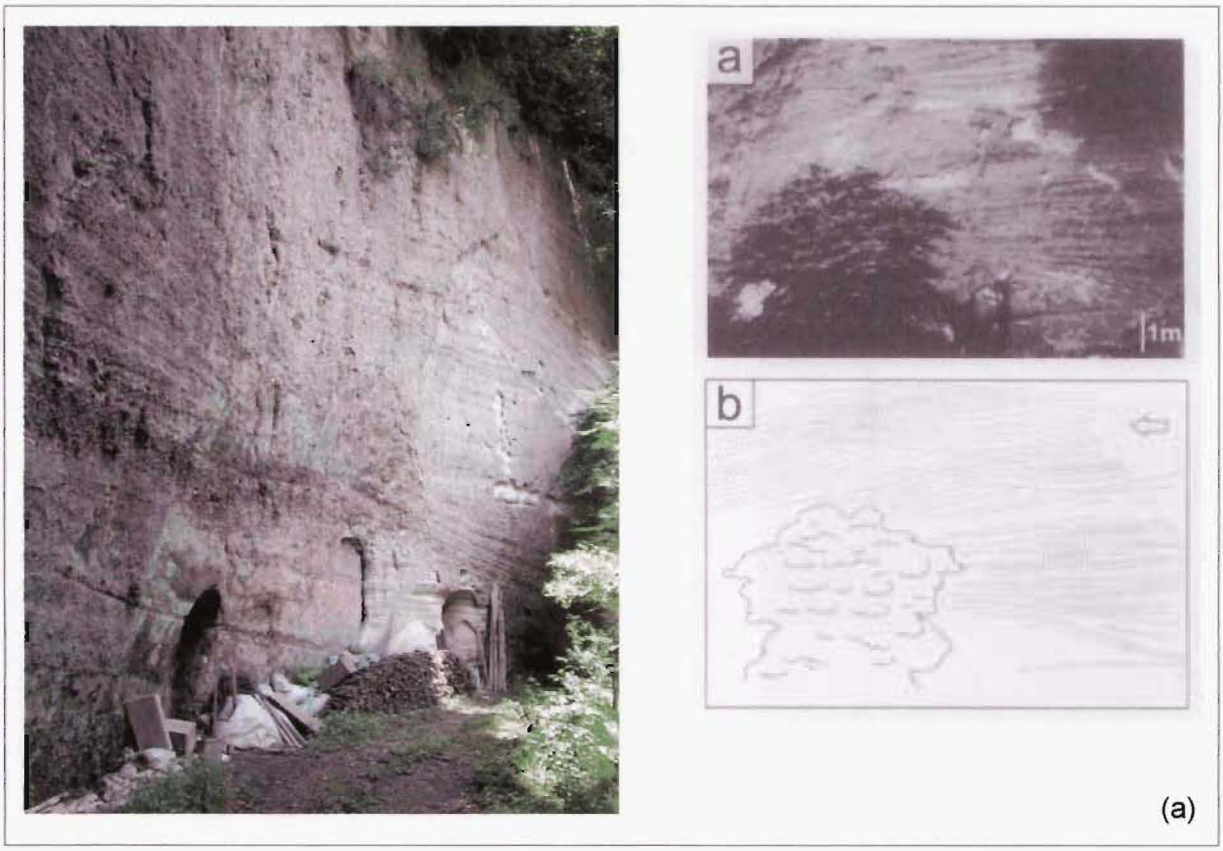

Figure 4.9 Dune bedforms in the (a) Tsumaya ignimbrite (black and white photo and sketch is from Fukushima and Kobayashi, 2000) and (b) proximal Taupo (IVD); photo is from Wilson (1981).

I propose that the contrast in mass between the Ohakuri lithofacies C currents and the El Chichon currents is most likely to be the primary variable associated with the difference in their respective deceleration rates (Δv). Applying a simple equation for momentum,

$$p = mv$$

and assuming a constant velocity (i.e. the same velocity for Ohakuri lithofacies C and El Chichon currents), the Ohakuri lithofacies C currents must have had more momentum due to their higher mass per unit volume. Although the El Chichon currents had a topographic advantage, their dilute nature meant less momentum and a higher deceleration rate (cf. Valentine, 1988).

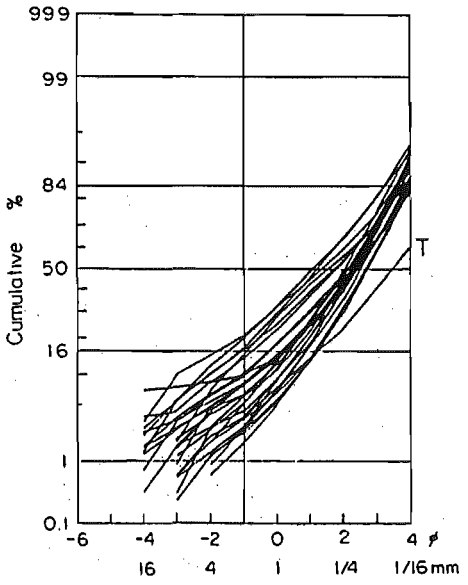

Figure 4.10 Grainsize distribution curves for the 22 ka Ito ignimbrite and the Tsumaya ignimbrite (T) from Aramaki (1984). The Tsumaya ignimbrite (T) has a < 1/16 mm content of close to 40 wt%.

Secondary turbulence

There is also evidence for secondary turbulence induced by variable topography. Regressive and progressive dune bedforms that are considerably smaller than the giant-dunes are observed within the area enclosed by the box in the W1 profile (Appendix 6). These smaller dunes appear to be related to infilling of a trough between two giant-dunes. It is probable that within the trough, regressive dunes, as well as progressive dunes with steep stoss sides, formed from the collision between density currents and the stoss side of the downstream, giant-dune. Rapid deceleration of successive pulses caused a 'traffic jam' effect until the trough was completely filled. These smaller, secondary dune features are interesting with respect to the topographic effects on turbulent pyroclastic density currents and need to be studied further; however, they are not mentioned in the following section because, compared with the giant-dunes, they provide less information with respect to eruption dynamics.

Eruption dynamics

It has been suggested above that dune deposits from highly concentrated, turbulent PDC's are rare and, as far as I am aware, they have only been documented at Aira and Taupo calderas. Highly concentrated, turbulent PDC's have not been modelled with respect to eruption dynamics, nor have they been predicted from theoretical pyroclastic eruption models (Carey et al., 1988; Valentine et al., 1991; Dobran et al., 1993; Neri and Dobran, 1994). This makes it difficult to relate Ohakuri lithofacies C to a definitive eruption model; however, there is some latitude for speculation based on the diagnostic characteristics of lithofacies C (i.e. grainsize distribution, dune bedforms, and proximity to source) and eruption models proposed for more dilute, turbulent PDC's (e.g. Fisher et al., 1983; Allen, 2001).

At Laacher See, Fisher et al. (1983) suggest that turbulence and near vent dune formation are associated with phreatomagmatic volcanism and fluctuations in the eruption column, whereby the dunes are fed from a continuous but pulsating pattern of marginal collapses of the eruption column. Similar eruption dynamics and a phreatomagmatic origin are postulated for wavy stratification described in unit B of the Kos Plateau Tuff (KPT; see Allen, 2001). With respect to Ohakuri lithofacies C, it has already been suggested in Section 3.7.1 that the higher than 'average' (cf. Walker, 1983) very fine grainsized material (< 1/16 mm) is indicative of phreatomagmatism. In addition, multiple pulses of currents associated with the construction of the Ohakuri lithofacies C giant-dunes are best explained, like the Laacher See dunes and KPT unit B deposits, by unsteadiness in the eruption column, whether this be fountaining (continuous column rise and collapse) or partial collapse off the margin of a Plinian eruption column. The fact that lithofacies C is not associated with plinian airfall deposits (see Section 3.7.1, Chapter 3) suggests that fountaining is the most likely source of the unsteady PDC's. Even if there was a prevailing westerly wind during the eruption (i.e. blowing away from lithofacies C which is proximally located within 2 to 5 km of source), evidence for plinian fall within or nearby lithofacies C would be expected.

In their computer simulations, Neri and Dobran (1994) observed stationary and oscillatory fountaining. The causes of oscillatory fountaining are complex and can involve a number of variables including mass flux, vent diameter, column temperatures and particle size (Neri and Dobran, 1994). In addition, Valentine et al. (1991) observed that even when the mass flux is steady, fountain unsteadiness can occur from 1) recirculation of pyroclastic flow material back into the base of the column, 2) ash that is swept back into the column from convecting phoenix clouds, and 3) waves reflected back into the base of the column from pyroclastic flows colliding with topographic obstacles. Like the causes, the effects of oscillatory fountaining are complex, producing a wide range of deposit types. Neri and Dobran (1994) observed pyroclastic flows and surges associated with pulsatory or waves of currents with periods of 15 to 50 s. In

addition, they found that oscillatory fountaining can produce interbedded flow and fall deposits. Airfall beds found in association with dunes are not uncommon (e.g. Walker, 1984); however, with respect to Ohakuri lithofacies C they have not been observed. This suggests that if the fountaining was oscillatory, then periods associated with individual pulses, as well as the elapsed time between pulses, were not long enough for airfall to accumulate.

More evidence for shorter rather than longer pulsation periods are the short runout distances of the Ohakuri lithofacies C currents. The distribution of Ohakuri lithofacies C extends to ~ 8 km from source where the deposits thin on top of the Mamaku Plateau. This, combined with a decrease in dune wavelength away from source suggests that the Ohakuri lithofacies C is associated with fountaining characterised by low mass flux and a finite supply of material to the parental PDC's. Interestingly, the exposure of the KPT unit B and the Tsumaya PDC dune deposits also reveal a limited runout distance and relatively rapid dissipation of energy for their parental currents; however, they are inferred to have been fed by the partial collapse of a Plinian column (Allen and Cas, 1998; Allen, 2001; Fukushima and Kobayashi, 2003). For the KPT unit B and the Tsumaya currents, the runout distance and the ability to surmount obstacles with high topographic relief were much less than for currents produced later in the same eruption sequence (i.e. the KPT unit E currents (Allen, 2001) and the Ito currents (Aramaki, 1984), respectively). KPT unit B currents were unable to surmount obstacles higher than 140 m ASL, where KPT unit E currents climbed over topography higher than 300 m ASL (Allen, 2001). The Tsumaya currents were completely confined within the pre-Aira basin, whereas the Ito currents were capable of surmounting the surrounding 400 metre high basin ridges (Aramaki, 1984).

4.3.5 Conclusion

The eruption dynamics associated with the origin of Ohakuri lithofacies C cannot be further constrained without theoretical modelling and further field investigations. Based on the available information it is likely that Ohakuri lithofacies C currents were fed from an eruption column characterised by some form of fountaining; however, there are no existing models, that I am aware of, that predict pulses of highly concentrated, turbulent, giant-dune-producing currents. The closest analogue to the Ohakuri lithofacies C is the Tsumaya dune deposits and the proximal Taupo veneer deposits. Despite the fact that the Tsumaya dune deposits and the Taupo veneer deposits are associated with Plinian eruption columns (Fukushima and Kobayashi, 2003; and Wilson, 1985, respectively), they are characterised by the same high, very fine ash (< 1/16 mm) content as the Ohakuri lithofacies C. Not only does the relatively high fine-ash content suggest that Ohakuri lithofacies C is probably associated with phreatomagmatic volcanism (see Section 3.7.1), but it also suggests that the currents which deposited lithofacies C were somewhat different from PDC's associated with dune beds at El

Chichon, Taal, and Ubehebe. The Ohakuri lithofacies C currents are inferred to have been denser and, thus, to have exhibited greater momentum and slower deceleration rates (as indicated by changes in dune wavelength) than archetypical dilute (pyroclastic surge, s.s.) currents. Consequently, the giant-dune-bedforms of Ohakuri lithofacies C cannot be modelled solely using assumptions that are applicable to stratified flow dynamics (e.g. Valentine, 1988, pp. 88-90). However, Valentine's (1988) model may be an appropriate starting place to assess dune bed formation from more concentrated currents

5 Ohakuri lithofacies F and G; secondary hydroeruptions and their deposits

5.1 Introduction

Much of what is known about secondary hydroeruptions comes from observations made on the pumice plain at Mount St. Helens. The term 'secondary hydroeruption' was introduced by Moyer and Swanson (1987) to describe explosive cratering on the pumice plain, during and following the emplacement of the May 18, 1980 pyroclastic flows at Mount St. Helens. The term refers to steam explosions induced by the vaporisation of surface water (i.e. oceanic, fluvial, lacustrine, or melted glacial ice) that comes into contact with hot pyroclastic deposits, and therefore, excludes 'phreatic eruptions' which are associated with groundwater (Moyer and Swanson, 1987). Secondary hydroeruptions and their deposits have been documented at a few volcanoes (see review in Moyer and Swanson, 1987) including Mount St. Helens, Crater Lake (Oregon), Katmai, Krakatau, and Taupo; however, in general, vestiges of secondary hydroeruptions are rarely preserved. There are several factors that preclude secondary hydroeruption features and deposits from having better representation in the rock record, including: 1) high rates of erosion and reworking in the environments they are formed (near streams, lakes, oceans); 2) secondary hydroeruption deposits are often exposed at the surface, overlying or occupying the stratigraphic position of layer 3 of Sparks et al. (1973); 3) secondary hydroeruption deposits are limited in their distribution and thickness; and 4) it is possible that secondary hydroeruption deposits have been misinterpreted as primary or water-reworked volcaniclastics.

In this chapter, a review of secondary hydroeruptions is presented and then the Ohakuri lithofacies F and G are compared with documented secondary hydroeruption deposits associated with the 1980 Mount St. Helens eruption, 1.8 ka Taupo eruption (Taupo ignimbrite), 22 ka Aira eruption (Ito ignimbrite) and 5.7 ka Ikeda eruption in southern Kyushu, Japan. In the discussion, the alternating relationship between Ohakuri primary PDC and secondary hydroeruption deposits is emphasised with specific reference to time breaks in the Ohakuri eruption sequence and wet depositional environments.

5.2 Secondary hydroeruptions: background

5.2.1 Depositional environment

Secondary hydroeruptions are associated with several different depositional environments. In littoral environments, where hot pyroclastic density currents entered the sea, secondary hydroeruptions have occurred (Krakatau (see Francis and Self, 1983), and the southern coast

of Kyushu, Japan; T. Kobayashi, pers. comm., 2003). At Katmai, the hot VTTS deposits triggered secondary hydroeruptions where they came into contact with glacial ice or running water (Hildreth, 1983). Secondary hydroeruptions associated with stream environments have also been documented at Taupo (Manville, 2001) and Mount St. Helens (Moyer and Swanson, 1987). At Mount St. Helens, secondary hydroeruptions occurred where the May 18, 1980 pyroclastic flow deposits covered pre-existing drainage, including the North Fork of the Toutle River (Figure 5.1). Today, only a few of the hydroeruption craters are preserved, as most of them have been destroyed by the re-establishment of the Toutle River drainage. Mount St. Helens secondary hydroeruptions also occurred on the shores of Spirit Lake.

Figure 5.1 Oblique aerial view of hydroeruption craters on the pumice plain at Mount St. Helens, from Rowley et al. (1981).

Because of the extensive nature of the depositional environments associated with secondary hydroeruptions (i.e. ocean and lake shorelines, glaciers, and river or stream drainage systems); they rarely occur as isolated events. As a result, craters and deposits from multiple events often overlap. This is described in more detail below.

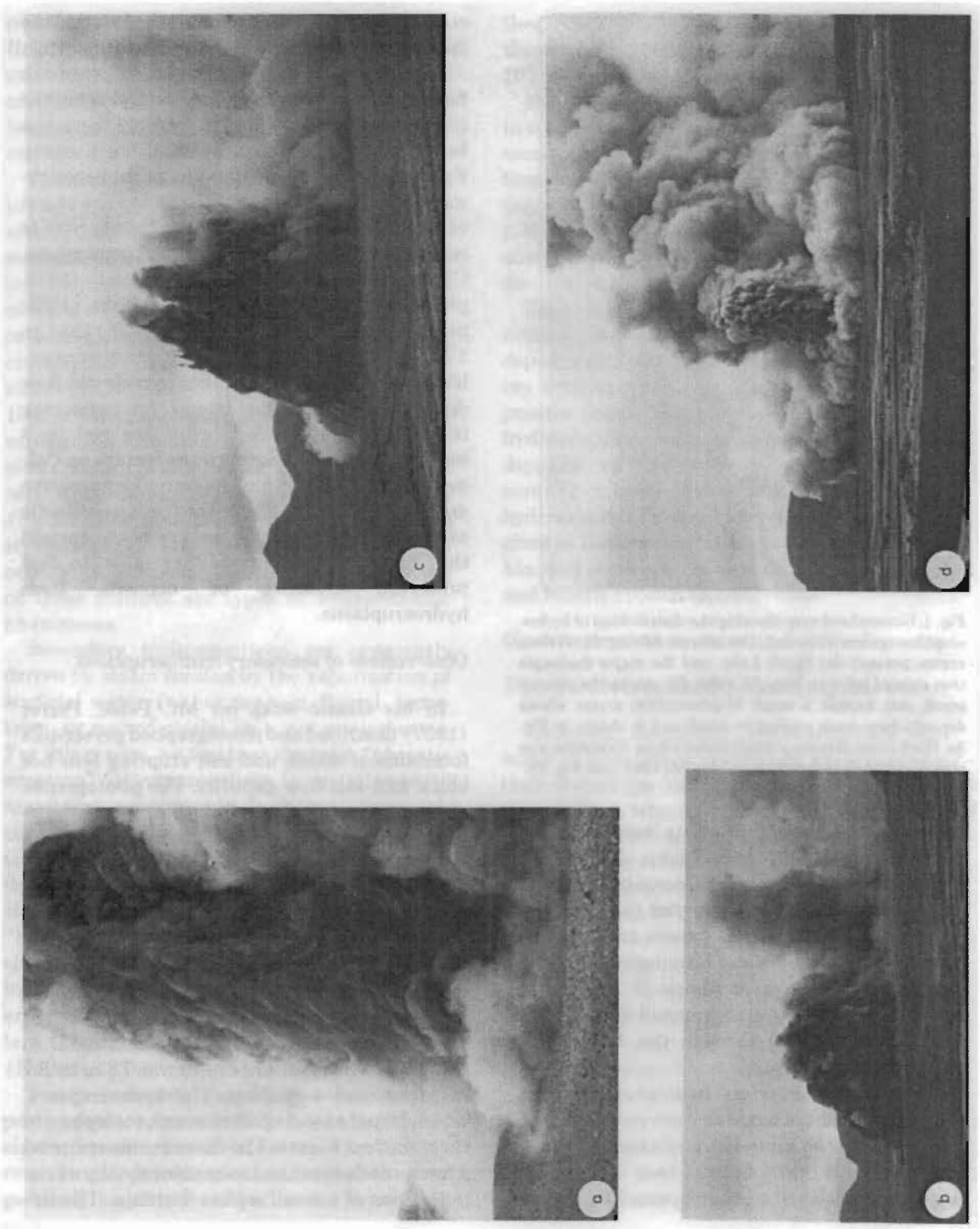

Figure 5.2 Low-energy hydroeruption observed on the Mount St. Helens pumice plain, May 16, 1981 (from Moyer and Swanson, 1987).

5.2.2 Magnitude

The magnitude or intensity of a secondary hydroeruption is a function of several factors including the volume of water buried by the primary PDC deposit, and the temperature, lithostatic pressure, and permeability associated with the primary deposit (Moyer and Swanson, 1987). As such, the magnitude can vary immensely, ranging from fumarolic activity to vigorous eruptions characterised by high tephra fountains and base surges. To facilitate discussion of the pumice plain hydroeruption features and deposits at Mount St. Helens, Moyer and Swanson (1987) developed an arbitrary magnitude scale for the hydroeruption events (i.e. low, moderate, and high energy). In the context of Mount St. Helens, low-energy events ranged from passive fumarolic degassing to low tephra fountains, and moderate- to high-energy eruptions were associated with increasing levels of tephra fountaining that produced energetic base surges. Figure 5.2 depicts a low-energy hydroeruption photographed on the pumice plain at Mt. St. Helens.

5.2.3 Time lag

Periodicity is defined here as the elapsed time between the emplacement of hot primary pyroclastic material over surface water and the secondary hydroeruption event. Periodicity is highly variable, and I suggest that it is likely to be related to the same factors that control the magnitude. The permeability of the primary PDC deposit may be the primary factor with respect to periodicity because it not only influences the temperature and pressure controls on the boiling point of water, but it also regulates the balance between the vapor pressure produced by the boiling water and the confining pressure exerted by the overlying PDC deposit (Moyer and Swanson, 1987). Moyer and Swanson (1987) suggest that this is a delicate balance and the addition or loss of thermal energy in the system can either trigger or suppress a hydroeruption.

Two places where periodicities for secondary hydroeruptions have been determined to some extent are Mount St. Helens and Taupo. At Mount St. Helens, periodicities ranged from zero (hydroeruptions occurred synchronously with the emplacement of primary PDC deposits) to several months (Moyer and Swanson, 1987). The hydroeruption in Figure 5.2 occurred on May 16, 1981, almost one year following the emplacement of primary PDC deposits. At Taupo, Manville (2001) describes secondary hydroeruption deposits that lie, stratigraphically, above and below the Taupo co-ignimbrite ash (a regional chronostratigraphic marker). The secondary hydroeruption deposits above the co-ignimbrite ash are overlain by reworked volcaniclastics that Manville (2001) correlates with fluvial and lacustrine processes related to the formation of the supra-ignimbrite Lake Reporoa. From the chronostratigraphy, Manville (2001) approximates a periodicity ranging from zero to 1 year, which agrees with Elgar's (1990) estimations at Taupo.

Figure 5.3 Aerial view of a circular hydroeruption crater on the pumice plain at Mount St. Helens, from Moyer and Swanson (1987).

Figure 5.4 Oblique aerial view of a hydroeruption crater with scalloped edges at Mount St. Helens, from Moyer and Swanson (1987).

5.3 Secondary hydroeruptions: features

5.3.1 Craters

Craters associated with secondary hydroeruptions are shaped like an inverted cone, with crater rims that form nearly perfect circles (Figure 5.3). At Mount St. Helens, the diameter of the craters ranges from < 2 m to 100 m, and they are 1 m to 20 m deep. Interestingly, the diameter

to depth ratio (2 : 5) is comparable to ratios for the Ubehebe tuff rings (Moyer and Swanson, 1987). Moyer and Swanson (1987) found that the size of an individual hydroeruption crater at Mount St. Helens is proportional to the magnitude of the eruption event. For example, the smallest craters (< 50 m in diameter) are related to low-energy events, craters with diameters ranging from 50 to 75 m correlate with moderate-energy eruptions, and the largest craters (> 75 m in diameter) are produced by high-energy eruptions. The size of some craters, however, may be misleading because they are actually composite craters related to multiple hydroeruptions that occurred in close spatial proximity. Composite craters are often recognisable by their scalloped edges (Figure 5.4).

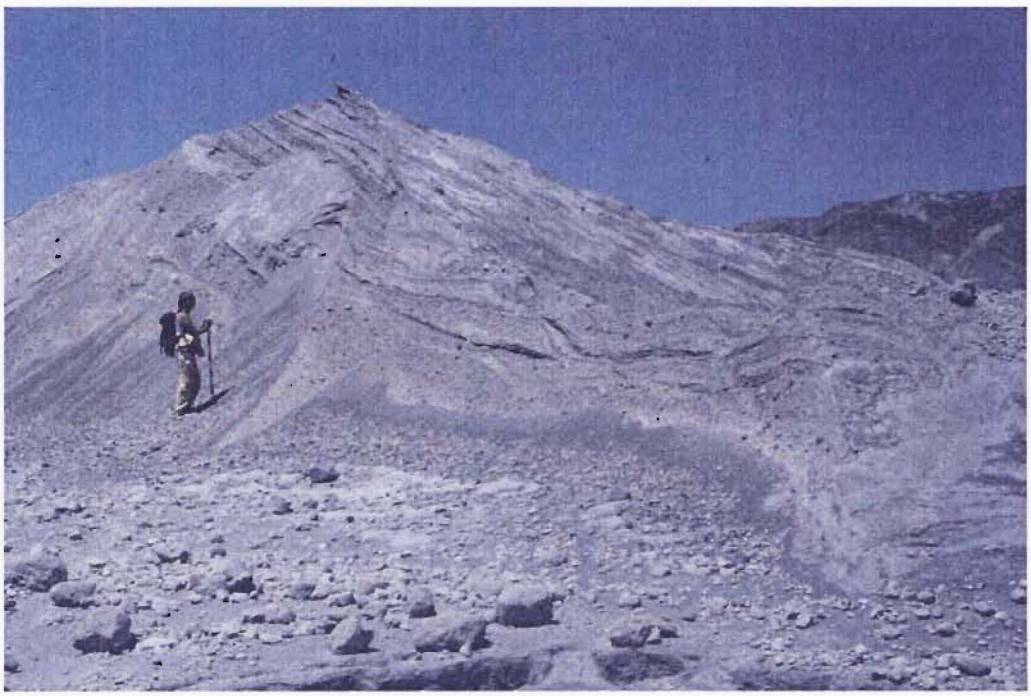

Figure 5.5 Cross-section of inclined hydroeruption deposits at Mount St. Helens. Photo is courtesy of C.J.N. Wilson.

Despite their utility in understanding hydroeruption processes, craters are rarely preserved. Upon visiting Mount St. Helens in August 2001 (~ 21 years after the pumice plain hydroeruptions), only 5 of the ~ 30 originally observed craters remained; most were destroyed by lahars and the re-establishment of drainage paths between the years 1982 and 1985 (Moyer and Swanson, 1987). However, rather fortuitously, erosion has exposed cross-sections of hydroeruption deposits (Figure 5.5) and, in some cases, a two-dimensional slice of the crater itself. Because hydroeruption craters are poorly preserved as geomorphologic features, sometimes these cross-sectional slices are their only vestige. Where a crater has been sliced or eroded near its core, a funnel-shaped structure is exposed.

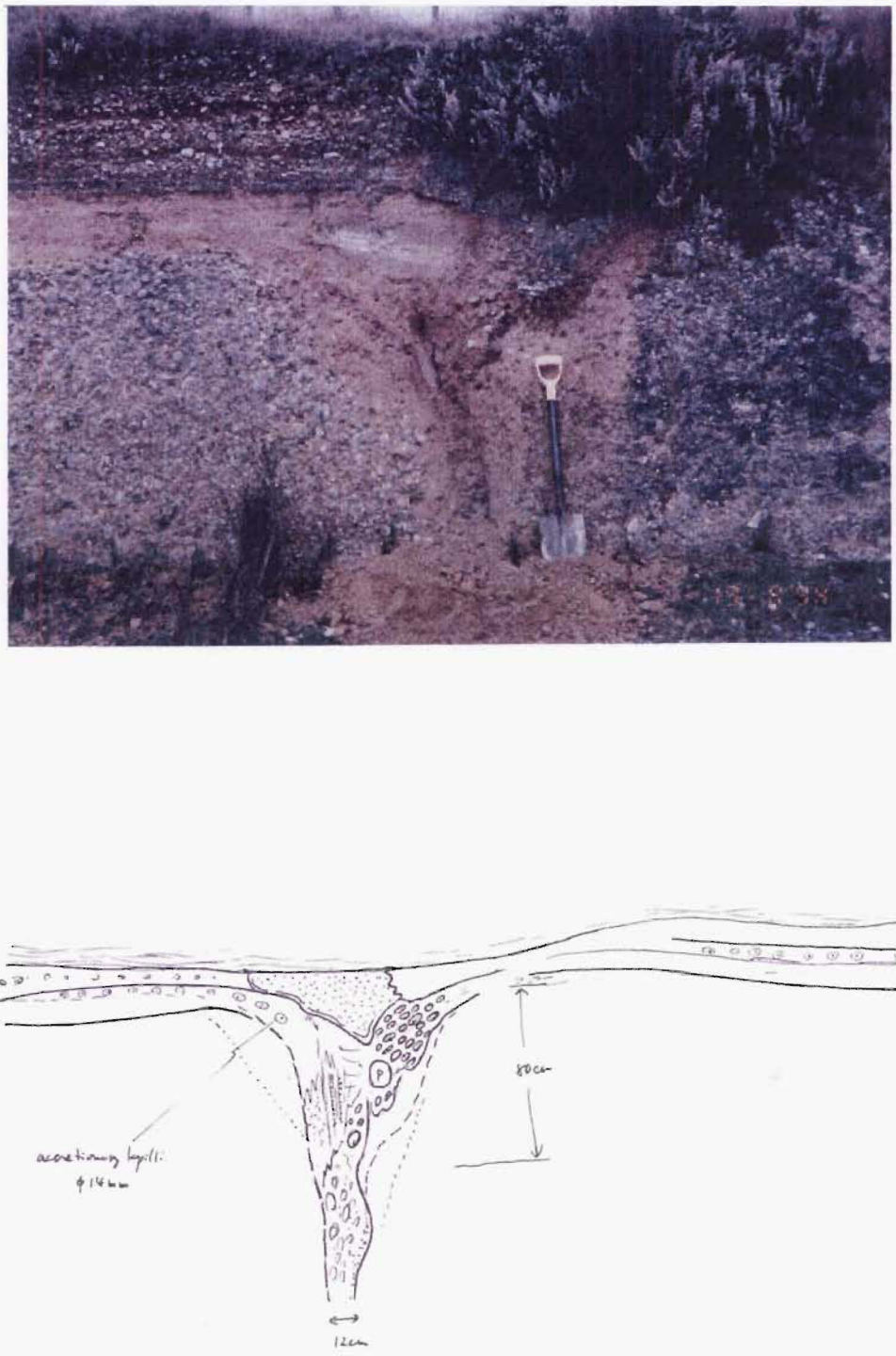

Figure 5.6 Photo and sketch of a small funnel structure in the Taupo ignimbrite, courtesy of T. Kobayashi. The funnel structure is related to passive gas-streaming as opposed to an energetic hydroeruption.

5.3.2 Two-dimensional funnel structures

Funnel structures depicted in Figure 5.6, Figure 5.7 and Figure 5.8 are interpreted as conduits for secondary hydroeruptions that resulted from the vaporisation of surface water that was covered by primary pyroclastic deposits (Kobayashi, pers. comm., 2003). The funnel structure in Figure 5.7 is one of many bowl-shaped structures found in a sea cliff exposure at Takeyama beach on the south coast of Kyushu, Japan, and is inferred by T. Kobayashi (pers. comm., 2003) to be a littoral vent, associated with and penetrating the 5.7 ka Ikeda ignimbrite. Like craters, funnel structures vary in size. The small size (< 2 m wide) and the oxidation at the margins of a series of funnel structures cutting across the Ito ignimbrite (Figure 5.8) suggest that these structures are associated with fumarolic degassing. However, the thick accumulation of plane-parallel to cross-laminated hydroeruption deposits overlying these funnel structures is indicative of a much larger hydroeruption vent nearby (the relationship between types of hydroeruption deposits and eruption magnitude is discussed below). At Taupo, a range of hydroeruption magnitudes can also be inferred by comparing the funnel structure in Figure 5.6 with a preserved crater that is ~ 300 m in diameter (Figure 5.9; Elgar, 1990).

Figure 5.7 Ikeda bowl-shaped funnel structure in cliff section at Takeyama beach on the south coast of Kyushu.

Figure 5.8 Funnel structure in the Ito ignimbrite, photo courtesy of T. Kobayahsi.

Figure 5.9 Aerial view of an ~ 300 m wide hydroeruption crater at Taupo, from Elgar (1990).

With respect to the Ohakuri pyroclastics, there are no hydroeruption craters preserved; only portions of bowl-shaped structures observed in the cliff outcrops of the *Tla* lithofacies (see Sections 3.4.6 and 3.5.3; Figure 3.28 and Figure 3.29). These 2-dimensional bowl-shaped structures are very similar in morphology to the Ikeda funnel structure (cf. Figure 5.7), except there are no conduits exposed. It is likely that the *Tla* exposures represent eroded cross-sectional slices away from the centre of the hydroeruption crater, thus not exposing the conduit. Without knowing exactly how far the eroded cross-section is from the centre of the crater, it is difficult to ascertain the size of the original crater. The estimated size of the *Tla* bowl-shaped structure in Figure 3.28 suggests that this particular crater was > 30 m across.

5.4 Secondary hydroeruptions: deposits

Secondary hydroeruption deposits are highly variable with respect to sedimentary structures and lithologies, and correlate well with typical base surge deposits (cf. Waters and Fisher, 1971; Crowe and Fisher, 1973; Wohletz and Sheridan, 1979; Fisher and Schmincke, 1984; Cas and Wright, 1987; Sohn and Chough, 1989). With respect to the magnitude of a particular hydroeruption event, the structure and lithology of the deposits can provide as much insight as the size of the crater or funnel structure. For example, at Mount St. Helens, Moyer and Swanson (1987) describe low to moderate-energy eruptions (< 75 m diameter craters) that produced massive and planar-stratified deposits, and high-energy eruptions (> 75 m diameter craters) that primarily produced dune bed deposits. The geometry of hydroeruption deposits, such as the thickness and lateral extent, also correlate well with the magnitude of the eruption.

The following is a description of the lateral facies variation of the secondary hydroeruption deposits at Mount St. Helens, Taupo, and Aira. Mount St. Helens' descriptions are from Moyer and Swanson (1987) and field observations made by me in 2001; Taupo descriptions are from Elgar (1990) and supplemented by C.J.N. Wilson (pers. comm., 2003) and T. Kobayashi (pers. comm., 2003); and Aira descriptions are from T. Kobayashi (pers. comm., 2003). There are obvious lithological similarities between these deposits and the Ohakuri lithofacies F and G secondary hydroeruption deposits (previously described in Sections 3.4.6 and 3.4.7, respectively); however there are also differences that are primarily related to the context and geometry of the deposits. To facilitate a comparison of the similarities, I have divided secondary hydroeruption deposits into extra-crater deposits (tephra fountain airfall and base surge deposits emplaced beyond the rim of the crater) and intra-crater/funnel deposits (deposits observed within the crater rim). A discussion of the differences is presented last.

5.4.1 Extra-crater deposits

At Mount St. Helens and Taupo, extra-crater hydroeruption deposits overlie or occupy the stratigraphic position of layer 3 of Sparks et al. (1973), and include massive, plane-parallel, and

dune-bedded lithologies. The relationship between these different lithologies is a function of lateral facies variations (sometimes related to increasing distance from source) and the magnitude of the hydroeruption.

Massive deposits

Massive deposits are observed in close proximity to source at both Mount St. Helens and Taupo. Mount St. Helens massive deposits (Figure 5.10) are relatively fines-poor (i.e. 4.73 wt% < 1/16 mm from representative sample 81-166; Moyer and Swanson, 1987). Moyer and Swanson (1987) interpret the massive deposits at Mount St Helens as fallback from low-energy tephra fountains; the lack of fine ash is related to elutriation in the fountain itself. In contrast to the Mount St. Helens massive deposits, the Taupo massive deposits resemble primary ignimbrite in appearance, and are characterised by a significantly higher fine ash content (i.e. 21.70 wt% < 1/16 mm from representative sample 27; Elgar, 1990). The massive deposits form a wedge-shape in cross-section and the median grainsize decreases with increasing distance from source (Elgar, 1990). As a result, Elgar (1990) interprets these deposits as secondary pyroclastic flow deposits. However, alternatively, the massive secondary hydroeruption deposits could simply represent masses of primary ignimbrite ejecta that, upon landing, flowed a short distance from vent (cf. hot avalanches of primary ignimbrite; Torres et al., 1996). This explanation accounts for the relatively high fine-ash content, as well as the wedge-shaped geometry.

Figure 5.10 Cross-section of massive deposits at the rim of a hydroeruption crater at Mount St. Helens.

Plane-parallel deposits

Plane-parallel hydroeruption deposits are characterised by different lithologies. At Mount St. Helens, plane-parallel packages are comprised of alternating coarse lapilli, fines-poor beds and relatively thin, fines-rich beds (Figure 5.11). Like the massive deposits described above, these deposits are located near the rim of the hydroeruption crater from which they came; however, they are associated with moderate-energy eruptions (Moyer and Swanson, 1987). The fines-rich beds are characterised by ripple laminations and sandwaves with 50 to 100 cm wavelengths and low angle dips on both stoss-side backsets and lee-side foresets. Moyer and Swanson (1987) infer the fines-rich beds to be related to surge processes. In contrast, the fines-poor beds are well-stratified and reverse-graded, and Moyer and Swanson (1987) suggest that they may be associated with surges or, alternatively, lateral flow generated by inclined tephra fountains. The latter origin is based on observations from an inclined tephra fountain associated with the May 16, 1981 hydroeruption in Figure 5.2.

At Taupo, Elgar (1990) describes two different occurrences of plane-parallel beds associated with a 300 m-diameter crater (Figure 5.9). As at Mount St. Helens, plane-parallel sequences can be characterised by alternations between fines-poor and fines-rich beds. One particular plane-parallel package (unit A; Elgar, 1990) of alternating fine ash and coarse pumice lapilli beds is characterised by a wedge-shaped geometry, decreasing in thickness from ~ 60 cm near the crater rim to < 10 cm, 500 m from the rim. Plane-parallel beds in unit A are transitional with sandwave deposits (50 cm wavelengths, low angle stoss- lee-side dips), and are inferred by Elgar (1990) to have a lateral transport origin.

Other Taupo plane-parallel sequences exhibit pumice lapilli beds interbedded with fine ash layers, as well as packages with thick accumulations of fine ash only. The fine ash interbeds, and the thicker accumulations, are characterised by accretionary lapilli, which Elgar (1990) interprets to be of airfall origin. In comparison with the wedge-shaped geometry of the plane-parallel surge beds, these plane-parallel packages often show a uniform thickness within 400 m of the crater rim (e.g. the ~ 50 cm thick unit I; Elgar, 1990). Similar airfall packages, with alternating fines-poor and fines-rich beds, conspicuous accretionary lapilli, and uniform thicknesses are observed at Aira, overlying the Ito ignimbrite (cf. Figure 5.12; T. Kobayashi, pers. comm. 2003).

Dune deposits

Dune bed lithologies are also characteristic of secondary hydroeruption deposits. As mentioned above, sandwaves observed at Mount St. Helens and Taupo are often associated with plane-parallel deposits. However, at Mount St. Helens, a proximal dune bed facies also exists, and is only associated with high-energy hydroeruptions (Moyer and Swanson, 1987). These dunes

Figure 5.11 Plane-parallel beds of alternating coarse lapilli, fines-poor layers and relatively thin, fines-rich layers that are ripple laminated. Photo taken on the pumice plain of Mount St. Helens.

Figure 5.12 Plane parallel hydroeruption deposits overlying the Ito ignimbrite. There is a very high concentration of accretionary lapilli within the bed that the pen is resting on. Photo courtesy of T. Kobayashi.

are characterised by 2 to 3 m wavelengths, high amplitudes (25 to 30 cm) and steep stoss-sides (Figure 5.13a), and in some cases are interpreted as antidunes (Rowley et al., 1981). The largest of these dunes are derived from the 'pumice pond', which is an elongate pit (700 m by 300 m in diameter) formed by the coalescence of numerous craters. Dunes associated with the 'pumice pond' have a radial distribution, which on the ground surface, can be recognised by a conspicuous hummocky terrain (Figure 5.13b; Moyer and Swanson, 1987).

Ohakuri extra-crater deposits

The Ohakuri extra-crater secondary hydroeruption deposits include massive, plane-parallel and sandwave facies (see Figure 3.26, Figure 3.32 and Figure 3.33) that are comparable to the Mount St. Helens and Taupo hydroeruption deposits described above. Massive, plane-parallel, and sandwave deposits (lithofacies F) are exposed in the *Tla*, but only plane-parallel deposits (lithofacies G) have been observed in the *Sla*.

Massive deposits

In the *Tla*, massive lithofacies F deposits are very similar, lithologically, to primary lithofacies A ignimbrite (cf. Taupo massive secondary hydroeruption deposit-primary ignimbrite relationship; Elgar, 1990), and can only be distinguished by their distinct geometry, which is defined by much thinner packages and a limited lateral distribution (a few to 10's of metres). Where the massive lithofacies F deposits are observed in proximity to a hydroeruption vent source, they are characterised by a lateral graded relationship with intra-crater deposits (see Figure 3.28 and Figure 3.29). This relationship is discussed in more detail below (Section 5.4.2) with respect to the origin of these massive deposits.

Plane-parallel deposits

Extra-crater plane-parallel deposits are exposed in the *Sla* and the *Tla*. In the *Sla*, packages of lithofacies G are composed of plane-parallel, very fine ash-rich, accretionary lapilli-bearing beds and well-sorted, fines-poor pumice lapilli beds (see Figure 3.33). Packages of lithofacies G are laterally extensive and form a quasi-conformable stratigraphic relationship with packages of lithofacies A ignimbrite (Section 3.5.5). One particular lithofacies G package, described in Sections 3.4.7 and 3.5.5, is exposed in multiple outcrops over a distance of > 200 m, exhibiting a uniform thickness (~ 80 cm) for its entire extent. Together, the geometry and lithology of the lithofacies G packages are very similar to the uniformly thick and extensive plane parallel packages at Taupo and Aira, and are most likely of airfall origin.

In the *Tla*, the lithofacies F plane-parallel deposits are both similar to and distinct from *Sla* lithofacies G. Stacked, fines-rich accretionary lapilli-bearing ash beds resemble those observed

Figure 5.13 (a) photo of a high-amplitude dune derived from high magnitude hydroeruption from the pumice pond at Mount St. Helens (from Moyer and Swanson, 1987). (b) Mount St. Helens' hydroeuption dunes and hummocky surface terrain, photo courtesy of C.J.N. Wilson.

in *Sla* lithofacies G. However, fines-rich ash beds are sometimes interbedded with massive and reverse graded pumice lapilli beds (see Figure 3.26), similar to those described, above, from Mount St. Helens. Also, the reverse graded pumice lapilli beds are sometimes associated with sandwave deposits (see Figure 3.32; cf. plane-parallel and sandwave association at Mount St. Helens and Taupo). Geometrically, *Tla* and *Sla* plane-parallel packages are fundamentally different. In contrast to the laterally extensive *Sla* lithofacies G packages, the plane-parallel lithofacies F packages form laterally discontinuous exposures (a few metres at most) as a result of the interdigitated arrangement of lithofacies F and lithofacies A packages in the *Tla* (see Section 3.5.3). It is difficult to ascertain the origin of these deposits (i.e. vertical vs. horizontal transport regimes) from the limited exposure of plane-parallel lithofacies F packages. The exception is where pumice lapilli beds are observed in close association with sandwave deposits; there is a clear lateral transport component.

Sandwave deposits

Sandwave deposits are rarely observed in the *Tla* (see Section 3.4.6); but where they are found, their size and morphology (300 mm half wavelengths and low angle stoss- and lee-side dips) are very similar to the Mount St. Helens and Taupo sandwave deposits described above. Larger dunes and antidunes, like those associated with the 'pumice pond' at Mount St. Helens, have not been observed in the *Tla.*

5.4.2 Intra-crater deposits

Material found inside craters and funnel structures is remarkably varied and can include: 1) fumarolic material; 2) eruptives from tephra fountaining that have fallen back into the crater; 3) eruptives from surges associated with the crater-producing eruption; 4) eruptives from nearby hydroeruptions that have been laterally or vertically deposited in the crater; or 5) primary pyroclastic deposits from the magmatic vent source. The last two types of infill are particularly apparent in the Ohakuri *Tla.* Note that no intra-crater deposits have been observed in the *Sla.*

Funnel structures (< 2 m wide) are related to streaming gas (degassing from hot pyroclastic material below) and are primarily filled with very fine ash. At Taupo and Aira, the intra-crater (funnel) fine ash is massive and often contains abundant accretionary lapilli (Figure 5.6). In the sketch diagram of the Taupo example (Figure 5.6), the intra-funnel accretionary lapilli appear to be mantling the funnel margins and are laterally consistent with accretionary lapilli concentration layers outside the funnel.

In contrast to relatively passive gas-streaming, more energetic hydroeruptions are associated with tephra fountains, and are more efficient at excavating the vent area (e.g. moderate- to high-

energy hydroeruptions at Mount St. Helens). As a result, the inverted cone-shaped vacancy left by these eruptions can be filled by a variety of deposits. Intra-crater deposits that are generated from the hydroeruption itself, include massive coarse-grained fall back deposits (e.g. Elgar, 1990) and massive- to cross-bedded surge deposits. Cross-bedding associated with the funnel structure in Figure 5.7, located at Takeyama beach in southern Kyushu is characterised by a sequence of bed truncations. The bed truncations are similar to those observed from typical trough bedded associations (e.g. where laterally transported deposits have filled excavated channels or troughs), except that the deposits in the Takeyama beach example were emplaced on their way out as opposed to their way in (T. Kobayashi, pers. comm., 2003). The planar-stratified beds that overlie the cross-bedded hydroeruption deposits within the funnel structure are associated with primary airfall (Ikedako ash) from the Ikeda caldera (T. Kobayashi, pers. comm., 2003). Primary airfall beds are also observed adjacent to, or stratigraphically beneath, the funnel structure (Figure 5.7) suggesting that the secondary hydroeruption occurred coevally with the Ikedako eruption event.

In comparison to the Ohakuri, the Ikeda funnel structure is roughly the same size and has a similar morphology (with the exception of the conspicuous conduit in the Ikeda example) as the Ohakuri *Tla* bowl-shaped structure in Figure 3.28 and Figure 3.29. Truncated beds at the margins of the *Tla* structure grade laterally into extra-crater massive beds near the rim of the structure (mentioned previously in Section 5.4.1). This intra- and extra-fill geometric relationship is consistent with these deposits being laid down from surges generated from the hydroeruption responsible for excavating the crater (bowl-shaped structure). Immediately above the cross-bedded surge deposits (across the top of the bowl-shaped structure), it is not clear whether the more planar deposits are products of the same hydroeruption or whether they are infill from another nearby hydroeruption or primary PDC deposits from a magmatic vent source. The complexities associated with the range of possible origins for some of the *Tla* deposits are discussed below.

5.4.3 Context and geometry of the Ohakuri secondary hydroeruption deposits

A diagnostic difference between the association of Ohakuri secondary hydroeruption deposits and secondary hydroeruption deposits at Mount St. Helens, Taupo, and Aira, is the fact that the *Sla* and *Tla* are characterised by alternating packages of primary PDC deposits and secondary hydroeruption deposits (Section 3.6.4 and 3.6.5, respectively). The episodic nature of the Ohakuri eruption sequence meant that following the emplacement of a secondary hydroeruption package, the package was soon eroded and/or buried by a primary PDC deposit.

With respect to the *Tla*, the complex interdigitated relationship is characterised by laterally discontinuous secondary hydroeruption packages (Section 3.5.3; Figure 3.27). As a result,

often, the geometry associated with the laterally discontinuous secondary hydroeruption packages is not sufficient to ascertain the hydroeruption source direction and the mode of emplacement, particularly where lithological information is also insufficient. The potential causes for a discontinuous hydroeruption package include truncations associated with explosive cratering from another hydroeruption and scouring by a primary PDC.

The complex geometry of *Tla* secondary hydroeruption packages suggests that hydroeruptions in the Tahunaatara area occurred in relative proximity to one another, both laterally in space and time, and vertically in space. There are a few possible origins for deposits associated with closely spaced hydroeruptions. Some *Tla* hydroeruption deposits may be associated with multiple hydroeruption events, i.e. they were originally primary pyroclastic deposits that were subsequently erupted and re-emplaced by a hydroeruption, then re-erupted again from another hydroeruption, and so forth. Because the processes associated from one hydroeruption to the next are so similar, particularly eruptions of the same magnitude, it is difficult to ascertain how many times the material in a particular deposit has been re-erupted based on its lithology or associated sedimentary structures. In addition, the secondary hydroeruption deposits are characterised by a similar range of lithologies to some primary PDC deposits, i.e. lithofacies E (see Sections 3.4.5 and 3.4.6), compounding the difficulty in recognising the origin of some deposits. This is particularly evident where limited exposure and geometry provide little context for a deposit (i.e. proximity to an obvious hydroeruption crater or bowl-shaped structure). For example, the bed truncations and the morphology of the channel structure in Figure 3.30 appear to be similar to primary pyroclastic scour and fill structures observed in the *Mla* and *Fla*. It is clear that for some of the *Tla* deposits, more lithological, contextual, and geometrical data is needed to accurately constrain their origin(s). The reality is that this may not be possible in an environment characterised by such intense hydroeruption activity and such limited modern exposure.

In the *Sla*, the quasi-conformable stratigraphic succession of alternating primary PDC and secondary hydroeruption airfall packages and the lack of evidence for nearby hydroeruptions (i.e. exposed funnel structures and/or massive, planar, and sandwave surge deposits) suggest that the lithofacies G airfall packages were deposited further from source than the *Tla* deposits. With respect to the hydroeruption source and its direction, the uniform thickness of lithofacies G packages (see Section 5.4.1) provides insufficient information. However, placed in context, the relatively close proximity of the *Sla* and *Tla* to one another (see Figure 3.34) suggests that *Sla* lithofacies G and *Tla* lithofacies F could be facies associated with the same hydroeruptions. More field evidence is needed to support this hypothesis, such as an increase in the thickness of lithofacies G packages toward the *Tla* and/or exposures with lithofacies G airfall and lithofacies F surge deposits found together.

5.5 Discussion

Compared with the Mount St. Helens and Taupo examples, hydroeruption features and deposits associated with the Ohakuri *Tla* and *Sla* are not well enough exposed to provide the full story (i.e. the range of magnitudes of the hydroeruptions, the source location for the *Sla* hydroeruption deposits, and whether the *Tla* and *Sla* deposits are lateral facies equivalents) of their existence. In particular, the absence of craters or fully-preserved funnel structures makes it difficult to estimate the relative magnitudes of the *Tla* hydroeruptions; only educated guesses can be made based on similarities drawn between the Ohakuri hydroeruption deposits and deposits documented elsewhere (see Section 3.4.1). For example, it is likely that Ohakuri hydroeruptions were not low energy, passive gas-streaming events, but, based on a comparison of deposit types (see Section 5.4), were probably within the range of moderate- to high-energy hydroeruptions at Mount St. Helens.

Although it may be difficult to accurately characterise the Ohakuri hydroeruptions, the evidence for their existence is important to the overall Ohakuri eruption story. The context associated with the alternations between Ohakuri secondary hydroeruption deposits and primary PDC deposits provides a record of time breaks in the Ohakuri eruption sequence (Section 3.7.2) and insight into the evolving depositional environment.

5.5.1 Time breaks and time lag

As previously explained above, secondary hydroeruptions are characterised by a time lag which is defined as the elapsed time between the emplacement of hot primary pyroclastic material over surface water, or a water-saturated substrate, and the secondary hydroeruption event. At Mount St. Helens, time lags for the hydroeruptions were recorded from observations of the events themselves; and at Taupo, estimations have been made based on chronostratigraphy (see Section 5.2.3). Both Mount St. Helens and Taupo are characterised by time lags ranging from zero to one year.

With respect to the Ohakuri *Sla* and *Tla*, estimations for time lags are based on the alternating relationship between secondary hydroeruption deposits and primary PDC deposits. As suggested in Section 3.7.2, the presence of a secondary hydroeruption package in the *Tla* and *Sla* is evidence for a hiatus or time break in the Ohakuri eruption sequence. As such, time breaks associated with *Sla* lithofacies G must be hidden in the continuous lithofacies A cliff outcrops of the *Gla*, which are considered to be at a similar stratigraphic level. Likewise, in the *Tla*, a similar hidden depositional boundary can be inferred between two lithofacies A packages at the pinch point of a lithofacies F package (see Figure 3.27). Time breaks associated with concealed depositional boundaries between ignimbrite packages in the Bishop Tuff have been recently documented by Wilson and Hildreth (2003). By correlating these ignimbrite packages

with the same packages in locations where they are separated by airfall, and then estimating the accumulation rate of the airfall, Wilson and Hildreth (2003) were able to estimate time breaks of hours to tens of hours. If a similar time frame is assumed in the Ohakuri example, the time between the emplacement of a primary PDC and a hydroeruption (time lag) associated with the *Sla* and *Tla* cannot be more than a few days. In other words, in any particular location, a hydroeruption occurred almost immediately following the emplacement of a primary PDC deposit, or it never occurred because the potential for a hydroeruption diminished with the burial and increased overburden associated with a subsequent primary PDC deposit.

5.5.2 Depositional environment

In modern volcanic settings, a depositional environment can be determined easily from direct observation or from photographic interpretation before and after a volcanic event. At Mount St. Helens, secondary hydroeruptions occurred where the May 18, 1980 pyroclastic flow deposits covered the shores of Spirit Lake and pre-existing streams and rivers (Moyer and Swanson, 1987). With respect to the location of buried drainage courses, they could be depicted by aligning hydroeruption craters and comparing this alignment with observations prior to the volcanic eruption (e.g. the recognition of the buried drainage associated with the Toutle River; Rowley et al., 1981). In ancient volcanic settings, such as the Ohakuri caldera and its environs, determining the depositional environment from a before and after direct account or photographic interpretation, is obviously not possible. However, hypotheses for depositional environments can be developed by characterising lithofacies associations and their deposits, and comparing these with modern analogues. It is clear that the secondary hydroeruption deposits of the *Tla* and *Sla* are associated with a wet depositional environment. A dark organic paleosol beneath unit 1 of the Rotorua-Ohakuri eruption sequence and the presence of charcoal between unit 1 and 2 (see Section 2.2.2) suggests that the Ohakuri pyroclastic deposits were erupted and emplaced during an interglacial period and therefore secondary hydroeruptions were not related to snow cover (cf. Katmai secondary hydroeruptions; Hildreth, 1983). With the Ohakuri, the question is whether a wet environment was related to ponded water (lakes) or streams, or simply water-saturated deposits?

There is paleogeographic evidence for a lake that spanned the approximate area north of and across the inferred Ohakuri caldera (see Figure 2.4). Phreatomagmatic volcanism, associated with the first 3 phases of the Ohakuri eruption sequence and the first event of phase 4 (Sections 2.2.2 and 3.7.3, respectively), is inferred to be related to this lake. Following the first phase 4 event and the emplacement of the *Fla* deposits, it is probable that the lake was buried. Incision into the newly deposited, unconsolidated *Fla* pyroclastics probably commenced immediately, with drainage coming off the Mamaku Plateau and high-ground to the north. Evidence for the location of the Ohakuri hydroeruptions is exposed in the cliff sections of the *Tla*, coincident with

the present-day course of the Tahunaatara Stream (see Figure 3.34). Considering the modern Mount St. Helens analogue, where drainage (during and after hydroeruption activity) re-established its pre-1980 course and subsequently incised through aligned hydroeruption craters (Moyer and Swanson, 1987), it is possible that the present-day course of the Tahunaatara stream is a relic of the drainage established before and during the emplacement of the *Tla* deposits. This hypothesis, combined with the interdigitated *Tla* architecture, suggests that water was consistently draining through this area, saturating the deposits and triggering successive hydroeruptions following each magmatic episode.

5.6 Conclusion

From comparisons with more recent analogues (e.g. Mount St. Helens and Taupo), secondary hydroeruption features and deposits can be recognised in the Ohakuri *Tla* and *Sla* lithofacies associations. Specifically, the *Tla* lithofacies F and *Sla* lithofacies G exhibit characteristics consistent with deposition from surges and fallout associated with hydroeruption tephra fountains. The magnitude of the Ohakuri hydroeruptions cannot be accurately determined from the available outcrop exposure; however, relative magnitudes are estimated to be within the range of moderate- to high-energy Mount St. Helens hydroeruptions.

The alternating relationship between Ohakuri primary PDC and secondary hydroeruption deposits is unique for a couple reasons. Firstly, it is evidence for an episodic magmatic eruption sequence, whereby the length of time associated with each hiatus (hours to a few days at most) can be approximated by comparing areas where lithofacies G and F are present with areas, at a similar stratigraphic level, where they are not present. Secondly, the rapid burial of secondary hydroeruption packages by primary PDC deposits has preserved a record of the hydroeruption phenomena. Secondary hydroeruption deposits are rarely observed in the rock record because their preservation potential is hindered by several factors. These include 1) their association with wet environments (e.g. streams and lake and ocean shorelines) where they are prone to post-eruptive erosion and resedimentation, 2) they tend to have a limited distribution and thickness, and 3) they are often the last deposits to be emplaced, occupying or overlying the stratigraphic position of layer 3 of Sparks et al. (1973).

The Ohakuri lithofacies F and G are the oldest documented occurrences of secondary hydroeruption deposits as far as I am aware; however, there are likely to be secondary hydroeruption deposits as old or older that have been misinterpreted. Secondary hydroeruption deposits share very similar lithological and structural characteristics to primary pyroclastic and some reworked deposits, and therefore need to be carefully assessed. For example, *Tla* lithofacies F deposits were probably interpreted, originally, as volcaniclastic sediments (e.g. Grindley, 1959) and have since been interpreted by Langridge (1990) as primary, near-source

surge-like deposits. Without the establishment of lithofacies associations, it may be difficult to place unusual lithofacies (such as lithofacies F and G) within the context of surrounding deposits from the same eruption sequence.

6 Conclusions

In this thesis, new research is presented that establishes the evolution of the Rotorua-Ohakuri volcanotectonic depression, which owes much of its present surface morphology to an intense period of caldera volcanism ~ 240 ka. Stratigraphic evidence, presented in Chapter 2, reveals essentially synchronous eruptions (probably only days to weeks apart) from vents ~ 25 km apart, including the caldera-forming eruptions of the Mamaku (> 145 km^3 magma; Milner et al, 2003) and Ohakuri pyroclastic deposits (> 100 km^3 magma) from the Rotorua and Ohakuri calderas, respectively. Caldera volcanism and tectonics share a close cause and effect relationship in the rifted setting of the central TVZ, and therefore, I suggest that the most feasible way to link these two caldera-forming events is by way of a regional tectonic event or tectonic readjustment. An intimate volcano-tectonic relationship is also evident from paleogeographic evidence that supports the contemporaneous NE-SW lateral migration of magma (sub-parallel to the regional structural trend) and non-eruptive subsidence associated with the Ohakuri eruption.

These conclusions, i.e. temporally-linked eruptions from geographically distinct sources, the existence of the Ohakuri caldera, and the lateral migration of magma and non-eruptive subsidence of the central Kapenga area, are dependent on the fact that the Ohakuri pyroclastic deposits are not simply a lateral variation of the Mamaku ignimbrite. Geochemically, the Ohakuri and Mamaku type 1 and 2 pumices plot in similar fields, however, the Ohakuri is characterised by a distinct dacitic type 3 pumice. In addition, juvenile mafic blebs from the Ohakuri and Mamaku have distinctly different compositions. Petrographically, the Ohakuri pumice types are distinguishable from one another by their crystal content and plagioclase:quartz ratios, whereas the Mamaku pumice types are relatively uniform with respect to crystal content and plagioclase:quartz ratios. The most obvious difference between the Ohakuri and Mamaku pyroclastic deposits is the range of Ohakuri lithofacies.

The Ohakuri deposits and their origin (both volcanic source, and modes of emplacement) have been considered both sedimentary and primary pyroclastic by different previous workers. By dividing them into 7 different lithofacies and 5 different lithofacies associations, based on structural, lithological, geometrical, and contextual variation, I have established that most of the Ohakuri deposits are primary pyroclastic deposits and some are secondary pyroclastic (i.e. hydroeruption) deposits. The Forest lithofacies association (*Fla*) is exposed in the southern, western, and northern sectors of the field area. The other lithofacies associations (*Gla*, *Mla*, *Sla*, and *Tla*) are distributed to the east and northeast of the Ohakuri caldera. By comparing the distribution of the lithofacies associations with the distribution of the three Ohakuri pumice

types, the Ohakuri eruption sequence (see Fig. 3.50) is divided into two different events. In the first event, type 1 and 2 magmas from beneath the Ohakuri caldera were erupted and the *Fla* deposits were emplaced. As a result, the Ohakuri caldera collapsed and lateral migration of magma from beneath the central Kapenga area was induced. In the second event, the central Kapenga type 1, 2, and 3 magmas were erupted from the Ohakuri caldera and the *Gla*, *Mla*, *Sla*, and *Tla* deposits were emplaced within the subsiding basin to the northeast. The lithological, structural, and geometrical variation between *Gla*, *Mla*, *Sla*, and *Tla* provides evidence for diverse depositional environments. Primary pyroclastic density currents (PDC's) that came into contact with surface water (most likely streams) or water-saturated deposits triggered secondary hydroeruptions that produced *Tla* lithofacies F and *Sla* lithofacies G deposits. Secondary hydroeruption deposits are hardly represented in the rock record. Part of the reason for this is that they are often deposited in the late stages of an eruption sequence and therefore susceptible to erosion. However, it is also possible that some secondary hydroeruption deposits have been misinterpreted as primary bedded pyroclastic or reworked (re-sedimented) deposits. Because the Ohakuri secondary hydroeruption deposits of the *Sla* and *Tla* were quickly buried by primary ignimbrite, they provide a useful marker for time breaks in the Ohakuri eruption sequence. Alternating packages of ignimbrite and secondary hydroeruption deposits in the *Sla* and *Tla* suggest that there must be obscured depositional boundaries within the thick (> 200 m) accumulations of structureless ignimbrite in the *Gla*.

Episodicity in the Ohakuri eruption sequence may have been associated with phreatomagmatism. Phreatomagmatic volcanism associated with the Ohakuri is supported by paleogeographic evidence for a paleo-Lake Ohakuri covering the area of what became the caldera, the presence of accretionary lapilli and the high concentration of fine ash in the Ohakuri PDC deposits, the non-welded nature of the Ohakuri deposits, and the evidence for turbulent, highly concentrated PDC's (i.e. the giant-dune-bedded lithofacies C). The Ohakuri lithofacies C is considered to be related to fluctuations in the eruption column (oscillatory fountaining) associated with phreatomagmatic volcanism (cf. Fisher et al., 1983; Allen, 2001). However, the lithofacies C giant-dune-beds are anomalous for their high concentration of very fine ash (< 1/16 mm). Only the dune-bedded Tsumaya deposits from Aira caldera and the proximal Taupo veneer deposits have a similar high concentration of very fine ash. Such high concentrations of fine ash distinguish these deposits from typical pyroclastic surge (s.s.) dune-bed deposits. In comparison, the Ohakuri lithofacies C currents are inferred to have been denser and exhibited greater momentum and slower deceleration rates than more dilute (pyroclastic surge, s.s.) currents. As a result, they offer an interesting problem to the existing models for stratified flow dynamics.

There are several inferences, questions, and scope for future research that comes out of the work presented in this thesis. As far as I am aware, the rapid succession of eruptions, including two caldera collapse events, has not been documented anywhere else in the world. However, if reviewed in detail, statistical averages for the frequency of caldera collapse events, particularly those associated with extensional tectonic settings, may be obscuring the clustering of such events. By discovering more of these clustered caldera collapse events it is likely that the complex relationship between caldera volcanism and tectonics in extensional settings will become clearer. In particular, the apparent problem with differentiating slip rates on regional faults from instantaneous superfault events necessitates more research. Also, the tectonic controls on the shape, size, and location of silicic magma reservoirs may be further elucidated. For example, preliminary geochemical work suggests that the Ohakuri, central Kapenga, and Rotorua magmas share many similarities as well as differences. Currently, it is not known whether these magmas were associated with one laterally-zoned and extensive reservoir that stretched from Rotorua to Ohakuri, or whether the magmas were held in geographically distinct chambers. Further geochemical research, particularly single crystal analyses including volatile determinations and U-Pb or U-TH zircon dating, may provide important information with respect to the chemical and physical properties of the magma reservoir(s) and ages of the crystal populations in the different magmas.

Finally, the prospect of future temporally-linked, geographically distinct caldera collapse events is an ominous volcanic hazards problem. This is why understanding the subsurface magmatic systems, including the connectivity of geographically-spaced magma bodies, may be vital when it comes to predicting the areal extent of caldera hazards. The notion that the central TVZ may be one large composite caldera may not be just a semantic issue after all.

References

Allen, S.R., 2001. Reconstruction of a major caldera-forming eruption from pyroclastic deposit characteristics: Kos Plateau Tuff, eastern Aegean Sea. Journal of Volcanology and Geothermal Research, 105: 141-162.

Allen, S.R. and Cas, R.A.F., 1998. Rhyolitic fallout and pyroclastic density current deposits from a phreatoplinian eruption in the eastern Aegean Sea, Greece. Journal of Volcanology and Geothermal Research, 86: 219-251.

Aramaki, S., 1984. Formation of the Aira caldera, Southern Kyushu, ~ 22,000 years ago. Journal of Geophysical Research, 89: 8485-8501.

Bailey, R.A. and Carr, R.G., 1994. Physical geology and eruptive history of the Matahina Ignimbrite, Taupo Volcanic Zone, North Island, New Zealand. New Zealand Journal of Geology and Geophysics, 37: 319-344.

Bailey, R.A., Dalrymple, G.B. and Lanphere, M.A., 1976. Volcanism, structure, and geochronology of Long Valley caldera, Mono County, California. Journal of Geophysical Research, 81: 725-744.

Beresford, S.W. and Cole, J.W., 2000. Kaingaroa Ignimbrite, Taupo Volcanic Zone, New Zealand: evidence for asymmetric caldera subsidence of the Reporoa Caldera. New Zealand Journal of Geology and Geophysics, 43: 471-481.

Bibby, H.M., Caldwell, T.G., Davey, F.J. and Webb, T.H., 1995. Geophysical evidence on the structure of the Taupo Volcanic Zone and its hydrothermal circulation. Journal of Volcanology and Geothermal Research, 68: 29-58.

Branney, M.J., 1991. Eruption and depositional facies of the Whorneyside Tuff Formation, English Lake District: An exceptionally large-magnitude phreatoplinian eruption. Geological Society of America Bulletin, 103: 886-897.

Branney, M.J. and Kokelaar, B.P., 1994. Volcanotectonic faulting, soft-state deformation, and rheomorphism of tuffs during development of a piecemeal caldera, English Lake District. Geological Society of America Bulletin, 106: 507-530.

Branney, M.J. and Kokelaar, P., 1992. A reappraisal of ignimbrite emplacement: progressive aggradation and changes from particulate to non-particulate flow during emplacement of high-grade ignimbrite. Bulletin of Volcanology, 54: 504-520.

Branney, M.J. and Kokelaar, P., 1997. Giant bed from a sustained catastrophic density current flowing over topography: Acatlan ignimbrite, Mexico. Geology, 25: 115-118.

Briggs, N.D., 1973. Investigations of New Zealand pyroclastic-flow deposits. Ph.D Thesis, Victoria University, Wellington, 438 pp.

Brown, S.J.A., 1994. Geology and geochemistry of the Whakamaru Group ignimbrites, and associated rhyolite domes, Taupo Volcanic Zone, New Zealand. Ph.D Thesis, University of Canterbury, Christchurch, 286 pp.

Brown, S.J.A., Wilson, C.J.N., Cole, J.W. and Wooden, J., 1998. The Whakamaru group ignimbrites, Taupo Volcanic Zone, New Zealand: evidence for reverse tapping of a zoned silicic magmatic system. Journal of Volcanology and Geothermal Research, 84: 1-37.

Cagnoli, B. and Russell, J.K., 2000. Imaging the subsurface stratigraphy in the Ubehebe hydrovolcanic field (Death Valley, California) using ground penetrating radar. Journal of Volcanology and Geothermal Research, 96: 45-56.

Cagnoli, B. and Ulrych, T.J., 2001a. Downflow amplitude decrease of ground penetrating radar reflections in base surge deposits. Journal of Volcanology and Geothermal Research, 105: 25-34.

Cagnoli, B. and Ulrych, T.J., 2001b. Ground penetrating radar images of unexposed climbing dune-forms in the Ubehebe hydrovolcanic field (Death Valley, California). Journal of Volcanology and Geothermal Research, 109: 279-298.

Cagnoli, B. and Ulrych, T.J., 2001c. Singular value decomposition and wavy reflections in ground-penetrating radar images of base surge deposits. Journal of Applied Geophysics, 48: 175-182.

CANZ, 1996. Undersea New Zealand (New Zealand Region Physiography), 2nd, Miscellaneous Series No. 74, 1:4 000 000. N.Z. Oceanographic Institute.

Carey, S.N., Sigurdsson, H. and Sparks, R.S.J., 1988. Experimental studies of particle-laden plumes. Journal of Geophysical Research, 93: 15314-15328.

Cas, R.A.F. and Wright, J.V., 1987. Volcanic Successions: modern and ancient. Chapman & Hall, London, 528 pp.

Charlier, B.L.A., Peate, D.W., Wilson, C.J.N., Lowenstern, J.B., Storey, M. and Brown, S.J.A., 2003. Crystallisation ages in coeval silicic magma bodies: 238U-230Th disequilibrium evidence from the Rotoiti and Earthquake Flat eruption deposits, Taupo Volcanic Zone, New Zealand. Earth and Planetary Science Letters, 206: 441-457.

Charlier, B.L.A., Wilson, C.J.N., Lowenstern, J.B., Blake, S., van Calsteren, P.W. and Davidson, J.P., sub judice. Magma generation at a large, hyperactive silicic volcano (Taupo, New Zealand) revealed by U/Th and U/Pb systematics in zircons.

Chough, S.K. and Sohn, Y.K., 1990. Depositional mechanics and sequences of base surges, Songaksan tuff ring, Cheju Island, Korea. Sedimentology, 37: 1115-1135.

Cole, J.W., 1990. Structural control and origin of volcanism in the Taupo volcanic zone, New Zealand. Bulletin of Volcanology, 52: 445-459.

Cole, J.W., Darby, D.J. and Stern, T.A., 1995. Taupo Volcanic Zone and Central Volcanic Region: backarc structures of North Island, New Zealand. In: B. Taylor (Editor), Backarc Basins: Tectonics and Magmatism. Plenum Press, New York, pp. 1-28.

Cole, J.W., Spinks, K. and Milner, D.M., in press. Calderas and Caldera Structures: A Review. Earth Science Review.

Crowe, B.M. and Fisher, R.V., 1973. Sedimentary structures in base-surge deposits with special reference to cross-bedding, Ubehebe Craters, Death Valley, California. Geological Society of America Bulletin, 84: 663-682.

Darby, D.J., Hodgkinson, K.M. and Blick, G.H., 2000. Geodetic measurement of deformation in the Taupo Volcanic Zone, New Zealand: the north Taupo network revisited. New Zealand Journal of Geology and Geophysics, 43: 157-170.

Davis, J.L. and Annan, A.P., 1989. Ground penetrating radar for high-resolution mapping of soil and rock stratigraphy. Geophysical Prospect, 37: 531-551.

Dobran, F., Neri, A. and Macedonio, G., 1993. Numerical simulation of collapsing volcanic columns. Journal of Geophysical Research, 98: 4231-4259.

Druitt, T.H., 1992. Emplacement of the 18 May 1980 lateral blast deposit ENE of Mount St Helens, Washington. Bulletin of Volcanology, 54: 554-572.

Druitt, T.H., 1998. Pyroclastic density currents. In: J.S. Gilbert and R.S.J. Sparks (Editors), The physics of explosive volcanic eruptions. Geological Society of London Special Publication, pp. 145-182.

Druitt, T.H. and Sparks, R.S.J., 1982. A proximal ignimbrite breccia facies on Santorini, Greece. Journal of Volcanology and Geothermal Research, 13: 147-171.

Dunham, P.B., 1981. Quaternary geology of the Guthrie region, Taupo Volcanic Zone, New Zealand. MSc. Thesis, University of Waikato, Hamilton.

Eichelberger, J.C. and Izbekov, P.E., 2000. Eruption of andesite triggered by dyke injection: contrasting cases at Karymsky volcano, Kamchatka and Mt Katmai, Alaska. Philosophical Transactions of the Royal Society of London, A358: 1465-1485.

Elgar, N.E., 1990. The Volcanology and Stratigraphy of Secondary Hydroeruption Deposits in Taupo Ignimbrite. BSc (Hons.) Thesis, Victoria University, Wellington, 60 pp.

Fierstein, J. and Hildreth, W., 1992. The plinian eruptions of 1912 at Novarupta, Katmai National Park, Alaska. Bulletin of Volcanology, 54: 646-684.

Fisher, R.V., 1966. Mechanism of deposition from pyroclastic flows. American Journal of Science, 264: 350-363.

Fisher, R.V., 1977. Erosion by volcanic base-surge density currents: U-shaped channels. Geological Society of America Bulletin, 88: 1287-1297.

Fisher, R.V., 1990. Transport and deposition of a pyroclastic surge across an area of high relief: The May 1980 eruption of Mount St. Helens, Washington. Geological Society of America Bulletin, 102: 1038-1054.

Fisher, R.V., Schmincke, H.-U. and Bogaard, P.V., 1983. Origin and emplacement of a pyroclastic flow and surge unit at Laacher See, Germany. Journal of Volcanology and Geothermal Research, 17: 375-392.

Fisher, R.V. and Schmincke, H.-U., 1984. Pyroclastic Rocks. Springer-Verlag, Berlin, 472 pp.

Fisher, R.V. and Smith, G.A., 1991. Volcanism, tectonics, and sedimentation. In: R.V. Fisher and G.A. Smith (Editors), Sedimentation in Volcanic Settings. SEPM Special Publication, pp. 1-5.

Francis, P.W. and Self, S., 1983. The eruption of Krakatau. Scientific American, 249(5): 172-187.

Freundt, A. and Schmincke, H.-U., 1985a. Hierarchy of facies of pyroclastic flow deposits generated by Laacher See-type eruptions. Geology, 13: 278-281.

Freundt, A. and Schmincke, H., 1985b. Lithic-enriched segregation bodies in pyroclastic flow deposits of Laacher See Volcano (East Eifel, Germany). Journal of Volcanology and Geothermal Research, 25: 193-224.

Freundt, A. and Schmincke, H.-U., 1986. Emplacement of small-volume pyroclastic flows at Laacher See (East-Eifel, Germany). Bulletin of Volcanology, 48: 39-59.

Freundt, A., Wilson, C.J.N. and Carey, S.N., 2000. Ignimbrites and block-and-ash deposits. In: H. Sigurdsson, B.F. Houghton, S. McNutt, H. Rymer and J. Stix (Editors), Encyclopedia of Volcanoes. Academic Press, San Diego, pp. 581-599.

Fukushima, D. and Kobayashi, T., 2000. Mechanism of generation and emplacement of the Tarumizu pyroclastic flow associated with Osumi plinian eruption from Aira caldera, Japan. Bulletin of Volcanological Society of Japan, 45: 225-240.

Fukushima, D. and Kobayashi, T., 2003. Formation of the Aira pyroclastic eruption, Aira caldera, Japan, IUGG, Sapporo, Japan, pp. 531.

Gamble, J.A., Wright, I.C. and Baker, J.A., 1993. Seafloor geology and petrology in the oceanic to continental transition zone of the Kermadec-Havre-Taupo Volcanic Zone arc system, New Zealand. New Zealand Journal of Geology and Geophysics, 36: 417-435.

Grindley, G.W., 1959. Sheet N85 Waiotapu. "Geological Map of New Zealand 1:63,360". Department of Scientific and Industrial Research, Wellington, New Zealand.

Grindley, G.W., 1960. Sheet 8 Taupo. "Geological Map of New Zealand, 1:250,000". Department of Scientific and Industrial Research, Wellington, New Zealand.

Grindley, G.W., 1965. The Geology, Structure, and Exploitation of the Wairakei Geothermal Field, Taupo, New Zealand. New Zealand Geological Survey, n.s. 75.

Hayakawa, Y., 1983. The Hachinohe Ash: an example of an accretionary lapilli-fall deposit from Towada volcano, Japan. Bulletin of the Volcanological Society of Japan, 28: 25-40.

Hayakawa, Y., 1990. Mode of eruption and deposition of the Hachinohe phreatoplinian ash from the Towada volcano, Japan. Geographical Reports of Tokyo Metropolitan Museum, 25: 167-182.

Healy, J., 1962. Structure and Volcanism in the Taupo Volcanic Zone, New Zealand, Crust of the Pacific Basin, Geophysical Monograph 6. American Geophysical Union, Washington, D.C., pp. 151-157.

Healy, J., Schofield, J.C. and Thompson, B.N., 1964. Sheet 5 Rotorua. "Geological Map of New Zealand 1:250,000". Department of Scientific and Industrial Research, Wellington, New Zealand.

Heiken, G. and Wohletz, K.H., 1987. Tephra deposits associated with silicic domes and lava flows. Geological Society of America Special Paper, 212: 55-76.

Henneberger, R.C., 1983. Petrology and evolution of the Ohakuri hydrothermal system, Taupo Volcanic Zone, New Zealand. MSc. Thesis, University of Auckland, Auckland, 141 pp.

Hildreth, W., 1979. The Bishop Tuff: evidence for the origin of compositional zonation in silicic magma chambers. Geological Society of America Special Paper, 180: 43-75.

Hildreth, W., 1983. The compositionally zoned eruption of 1912 in the Valley of Ten Thousand Smokes, Katmai National Park, Alaska. Journal of Volcanology and Geothermal Research, 18: 1-56.

Hildreth, W. and Mahood, G., 1986. Ring-fracture eruption of the Bishop Tuff. Geological Society of America Bulletin, 97: 396-403.

Houghton, B.F., Lloyd, E.F., Wilson, C.J.N. and Lanphere, M.A., 1991. K-Ar ages from the Western Dome Belt and associated rhyolitic lavas in the Maroa-Taupo area, Taupo Volcanic Zone, New Zealand. New Zealand Journal of Geology and Geophysics, 34: 99-101.

Houghton, B.F., Wilson, C.J.N., Fierstein, J. and Hildreth, W., 2004. Complex proximal deposition during the Plinian eruptions of 1912 at Novarupta, Alaska. Bulletin of Volcanology, 66: 95-133.

Houghton, B.F., Wilson, C.J.N., McWilliams, M.O., Lanphere, M.A., Weaver, S.D., Briggs, R.M. and Pringle, M.S., 1995. Chronology and dynamics of a large silicic magmatic system: Central Taupo Volcanic Zone, New Zealand. Geology, 23(1): 13-16.

Houghton, B.F., Wilson, C.J.N., Smith, R.T. and Gilbert, J.S., 2000. Phreatoplinian eruptions. In: H. Sigurdsson, B.F. Houghton, S. McNutt, H. Rymer and J. Stix (Editors), Encyclopedia of Volcanoes. Academic Press, San Diego, pp. 513-525.

Inman, D.L., 1952. Measures for describing the size distribution of sediments. Journal of Sedimentary Petrology, 22: 125-145.

Jellinek, A.M. and DePaolo, D.J., 2003. A model for the origin of large silicic magma chambers: precursors of caldera-forming eruptions. Bulletin of Volcanology, 65: 363-381.

Karhunen, R.A., 1993. The Pokai and Chimp Ignimbrites of NW Taupo Volcanic Zone. Ph.D Thesis, University of Canterbury, Christchurch, 356 pp.

Keall, J.M., 1988. Volcanology and ignimbrite stratigraphy along the Paeroa Fault, Taupo Volcanic Zone. M.Sc Thesis, Victoria University, Wellington, 118 pp.

Kobayashi, T., Ishihara, K. and Hirabayashi, J., 1988. A Guide Book For Sakurajima Volcano. In: S. Aramaki, K. Kamo and M. Kamada (Editors), Kagoshima International Conference On Volcanoes. Kagoshima Prefectural Government, Kagoshima, Japan, pp. 1-88.

Kobayashi, T., Ishihara, K., Suzuki-Kamata, K. and Fukushima, D., 2003. Sakurajima volcano and pyroclastic deposits in southern Kyushu, IUGG Field Trip A4, June 25-29, 2003, guidebook, pp. 1-27.

Kohn, B.P. and Topping, W.W., 1978. Time-space relationships between late Quaternary rhyolitic and andesitic volcanism in the southern Taupo Volcanic Zone, New Zealand. Geological Society of America Bulletin, 89: 1265-1271.

Langridge, R.M., 1990. The geology of the Upper Atiamuri region, Taupo Volcanic Zone, with special reference to the existence of the Kapenga caldera volcano. MSc. Thesis, University of Waikato, Hamilton, 168 pp.

Le Maitre, R.W., Bateman, P., Dudek, A., Keller, J., Lemeyre, J., Le Bas, M.J., Sabine, P.A., Schmid, R., Sorensen, H., Streckeisen, A., Wooley, A.R. and Zanettin, B., 1989. A classification of igneous rocks and glossary of terms. Recommendations of the IUGS Subcommission on the Systematics of Igneous Rocks. Blackwell Sci. Publ., Oxford, 193 pp.

Leonard, G.S., 2003. The evolution of Maroa Volcanic Centre. Ph.D Thesis, University of Canterbury, Christchurch, 322 pp.

Leonard, G.S., Wilson, C.J.N., Cole, J.W. and Gravley, D.M., 2003. Rapid post-collapse infilling of calderas: evidence from Taupo Volcanic Zone, New Zealand, Geological Society of New Zealand Conference, Dunedin, New Zealand, pp. 88.

Lipman, P.W., 1997. Subsidence of ash-flow calderas: relation to caldera size and magma-chamber geometry. Bulletin of Volcanology, 59: 198-218.

Lipman, P.W., 2000a. Calderas. In: H. Sigurdsson, B.F. Houghton, S. McNutt, H. Rymer and J. Stix (Editors), Encyclopedia of Volcanoes. Academic Press, San Francisco, pp. 643-662.

Lipman, P.W., 2003. Geometrically complex calderas and underlying magma chambers in the western USA, IUGG, Sapporo, Japan, pp. 526.

Lipman, P.W., Dungan, M.A., Brown, L.L. and Deino, A., 1996. Recurrent eruption and subsidence at the Platoro caldera complex, southeastern San Juan volcanic field, Colorado: new tales from old tuffs. Geological Society of America Bulletin, 108: 1039-1055.

Macias, J.L., Sheridan, M.F. and Espinola, J.M., 1997. Reappraisal of the 1982 eruptions of El Chichon Volcano Chiapas, Mexico: new data from proximal deposits. Bulletin of Volcanology, 58: 459-471.

Manville, V., 2001. Sedimentology and history of Lake Reporoa: an ephemeral supra-ignimbrite lake, Taupo Volcanic Zone, New Zealand. In: J.D.L. White and N.R. Riggs (Editors), Volcaniclastic Sedimentation in Lacustrine Settings. Blackwell Science, pp. 109-140.

Manville, V., 2002. Sedimentary and geomorphic responses to ignimbrite emplacement: readjustment of the Waikato River after the A.D. 181 Taupo eruption, New Zealand. The Journal of Geology, 110: 519-541.

Manville, V., 2003. Volcanogenic floods in the Taupo Volcanic Zone, New Zealand, Geological Society of New Zealand Conference, Dunedin, New Zealand, pp. 96.

Manville, V., White, J.D.L., Houghton, B.F. and Wilson, C.J.N., 1999. Paleohydrology and sedimentology of a post-1.8 ka breakout flood from intracaldera Lake Taupo, North Island, New Zealand. Geological Society of America Bulletin, 111(10): 1435-1447.

Manville, V. and Wilson, C.J.N., 2003. Interactions between volcanism, rifting and subsidence: implications of intracaldera palaeoshorelines at Taupo volcano, New Zealand. Journal of the Geological Society, London, 160: 3-6.

Martin, R.C., 1961. Stratigraphy and structural outline of the Taupo Volcanic Zone. New Zealand Journal of Geology and Geophysics, 4: 449-478.

Marx, R.S., White, J.D.L. and Manville, V., 2003. The evolution of Lake Rotorua, Geological Society of New Zealand Conference, Dunedin, New Zealand, pp. 99.

McPhie, J., 1984. Eruption styles and setting of late Palaeozoic silicic volcanic centres, New England Orogen, Northeastern New South Wales. Ph.D Thesis, University of New England, Armidale, 316 pp.

McPhie, J., 1986. Primary and redeposited facies from a large-magnitude, rhyolitic, phreatomagmatic eruption: Cana Creek Tuff, Late Carboniferous, Australia. Journal of Volcanology and Geothermal Research, 28: 319-350.

McPhie, J., 1987. The Hianana Volcanics: Remnants of a Late Permian tuff ring and lava flow, Coombadjha Volcanic Complex, northeastern New South Wales. Australian Journal of Earth Sciences, 34: 417-433.

McWilliams, M.O., 2001. Global correlation of the 223 ka Pringle Falls Event. International Geology Review, 43: 191-195.

Mellors, R.A., 1988. Studies of volcanism on Santorini, Greece and Mount St. Helens, U.S.A. Ph.D Thesis, University of Cambridge, Cambridge, 248 pp.

Milner, D.M., 2001. The structure and eruptive history of Rotorua Caldera, Taupo Volcanic Zone, New Zealand. Ph.D Thesis, University of Canterbury, Christchurch, 434 pp.

Milner, D.M., Cole, J.W. and Wood, C.P., 2002. Asymmetric, multiple-block collapse at Rotorua Caldera, Taupo Volcanic Zone, New Zealand. Bulletin of Volcanology, 64: 134-149.

Milner, D.M., Cole, J.W. and Wood, C.P., 2003. Mamaku Ignimbrite: a caldera-forming ignimbrite erupted from a compositionally zoned magma chamber in Taupo Volcanic Zone, New Zealand. Journal of Volcanology and Geothermal Research, 122: 243-264.

Moyer, T.C. and Swanson, D.A., 1987. Secondary hydroeruptions in pyroclastic-flow deposits: examples from Mount St Helens. Journal of Volcanology and Geothermal Research, 32: 299-319.

Nairn, I.A., Kobayashi, T. and Nakagawa, M., 1998. The ~ 10 ka multiple vent pyroclastic eruption sequence at Tongariro Volcanic Centre, Taupo Volcanic Zone, New Zealand: Part 1. Eruptive processes during regional extension. Journal of Volcanology and Geothermal Research, 86: 19-44.

Nairn, I.A. and Kohn, B.P., 1973. Relation of the Earthquake Flat Breccia to the Rotoiti Breccia, Central North Island, New Zealand. New Zealand Journal of Geology and Geophysics, 16: 269-279.

Nairn, I.A., Wood, C.P. and Bailey, R.A., 1994. The Reporoa Caldera, Taupo Volcanic Zone: source of the Kaingaroa Ignimbrites. Bulletin of Volcanology, 56: 529-537.

Nakagawa, M., Kitagawa, J. and Furukawa, R., 2003. Sequential caldera-forming eruptions from multiple magma chambers of Shikotsu caldera, Hokkaido, Japan. IUGG, Sapporo, Japan, Abstract: 525.

Nakagawa, M., Nairn, I.A. and Kobayashi, T., 1998. The ~ 10 ka multiple vent pyroclastic eruption sequence at Tongariro Volcanic Centre, Taupo Volcanic Zone, New Zealand: Part 2. Petrological insights into magma storage and transport during regional extension. Journal of Volcanology and Geothermal Research, 86: 45-65.

Naruo, H. and Kobayashi, T., 2002. Two large-scale earthquakes triggered by a 6.5 ka BP eruption from Kikai caldera, Southern Kyushu, Japan. The Quaternary Research, 41(4): 287-299.

Neri, A. and Dobran, F., 1994. Influence of eruption parameters on the thermofluid dynamics of collapsing volcanic columns. Journal of Geophysical Research, 99: 11833-11857.

Newhall, C.G. and Dzurisin, D., 1988. Historical unrest at large calderas of the world, 1855. United States Geological Survey Bulletin.

Reading, H.G. (Editor), 1986. Sedimentary Environments and Facies. Blackwell Scientific Publications, Oxford, 615 pp.

Riggs, N.R. and Busby-Spera, C.J., 1991. Facies analysis of an ancient, dismembered, large caldera complex and implications for intra-arc subsidence: Middle Jurassic strata of Cobre Ridge, southern Arizona, USA. In: R.A.F. Cas and C.J. Busby-Spera (Editors), Volcaniclastic Sedimentation. Sedimentary Geology, pp. 39-78.

Riggs, N.R., Ort, M.H., White, J.D.L., Wilson, C.J.N., Houghton, B.F. and Clarkson, R., 2001. Post-1.8-ka marginal sedimentation in Lake Taupo, New Zealand: effects of wave energy and sediment supply in a rapidly rising lake. In: J.D.L. White and N.R. Riggs (Editors), Volcaniclastic Sedimentation in Lacustrine Settings. Blackwell Science, pp. 151-177.

Rogan, A.M., 1982. A geophysical study of the Taupo Volcanic Zone, New Zealand. Journal of Geophysical Research, 87: 4073-4088.

Rowland, J.V. and Sibson, R.H., 2001. Extensional fault kinematics within the Taupo Volcanic Zone, New Zealand: soft-linked segmentation of a continental rift system. New Zealand Journal of Geology and Geophysics, 44: 271-283.

Rowley, P.D., Kuntz, M.A. and MacLeod, N.S., 1981. Pyroclastic-flow deposits. In: P.W. Lipman and D.R. Mulineaux (Editors), The 1980 Eruptions of Mount St. Helens, Washington. U.S. Geol. Surv., pp. 489-512.

Russell, J.K. and Stasiuk, M.K., 1997. Characterization of volcanic deposits with ground-penetrating radar. Bulletin of Volcanology, 58: 515-527.

Rust, A. and Russell, J., 2000. Detection of welding in pyroclastic flows with ground penetrating radar: insights from field and forward modelling data. Journal of Volcanology and Geothermal Research, 95: 23-34.

Schmincke, H.U., Fisher, R.V. and Waters, A.C., 1973. Antidune and chute and pool structures in the base surge deposits of the Laacher See area, Germany. Sedimentology, 20: 553-574.

Schumacher, R. and Schmincke, H.-U., 1990. The lateral facies of ignimbrites at Laacher See volcano. Bulletin of Volcanology, 52: 271-285.

Schumacher, R. and Schmincke, H.-U., 1995. Models for the origin of accretionary lapilli. Bulletin of Volcanology, 56: 626-639.

Self, S., 1983. Large-scale phreatomagmatic silicic volcanism: a case study from New Zealand. Journal of Volcanology and Geothermal Research, 17: 433-469.

Self, S. and Sparks, R.S.J., 1978. Characteristics of widespread pyroclastic deposits formed by the interaction of silicic magma and water. Bulletin of Volcanology, 41-43: 196-212.

Sigurdsson, H., Carey, S.N. and Fisher, R.V., 1987. The 1982 eruptions of El Chichon volcano, Mexico (3): Physical properties of pyroclastic surges. Bulletin of Volcanology, 49: 467-488.

Smith, R.C.M., 1991a. Landscape response to a major ignimbrite eruption, Taupo Volcanic Centre, New Zealand. In: R.V. Fisher and G.A. Smith (Editors), Sedimentation in Volcanic Settings. SEPM Special Publication, pp. 123-137.

Smith, R.C.M., 1991b. Post-eruption sedimentation on the margin of a caldera lake, Taupo Volcanic Centre, New Zealand. In: R.A.F. Cas and C.J. Busby-Spera (Editors), Volcaniclastic Sedimentation. Sedimentary Geology, pp. 89-138.

Smith, R.T. and Houghton, B.F., 1995. Vent migration and changing eruptive style during the 1800a Taupo eruption: new evidence from the Hatepe and Rotongaio phreatoplinian ashes. Bulletin of Volcanology, 57: 432-439.

Sohn, Y.K. and Chough, S.K., 1989. Depositional processes of the Suwolbong tuff ring, Cheju Island (Korea). Sedimentology, 36: 837-855.

Sparks, R.S.J., 1976. Grain size variations in ignimbrites and implications for the transport of pyroclastic flows. Sedimentology, 23: 147-188.

Sparks, R.S.J., Self, S. and Walker, G.P.L., 1973. Products of ignimbrite eruptions. Geology, Boulder, 1: 115-118.

Sparks, R.S.J. and Walker, G.P.L., 1973. The ground surge deposit : a third type of pyroclastic rock. Nature Physical Science, 241: 62-64.

Spray, J.G., 1997. Superfaults. Geology, Boulder, 25: 579-582.

Stagpoole, V.M. and Bibby, H.M., 1999. Residual gravity anomaly map of the Taupo Volcanic Zone, New Zealand, 1:250 000, version 1.0. Institute of Geological and Nuclear Sciences geophysical map 13, Lower Hutt.

Stern, T.A. and Davey, F.J., 1987. A seismic investigation of the crustal and upper mantle structure within the Central Volcanic Region of New Zealand. New Zealand Journal of Geology and Geophysics, 30: 217-231.

Tanaka, H., Turner, G.M., Houghton, B.F., Tachibana, T., Kono, M. and McWilliams, M.O., 1996. Palaeomagnetism and chronology of the central Taupo Volcanic Zone, New Zealand. Geophysical Journal International, 124: 919-934.

Torres, R.C., Self, S., Martinez, M.M.L., 1996. Secondary pyroclastic flows from the June 15, 1991, ignimbrite of Mount Pinatubo. In: C.G. Newhall and R.S. Punongbayan (Editors), Fire and Mud: eruptions and lahars of Mount Pinatubo, Philippines. University of Washington Press, Seattle.

Valentine, G.A., 1988. Field and theoretical aspects of explosive volcanic transport processes. Ph.D Thesis, University of California, Santa Barbara, Santa Barbara, 216 pp.

Valentine, G.A., Wohletz, K.H. and Kieffer, S.W., 1991. Sources of unsteady column dynamics in pyroclastic flow eruptions. Journal of Geophysical Research, 96: 21887-21892.

Villamor, P. and Berryman, K.R., 2001. A late Quaternary extension rate in the Taupo Volcanic Zone, New Zealand, derived from fault slip data. New Zealand Journal of Geology and Geophysics, 44: 243-269.

Walker, G.P.L., 1973. Explosive volcanic eruptions - a new classification scheme. Geologische Rundschau, 62: 431-446.

Walker, G.P.L., 1981. Characteristics of two phreatoplinian ashes, and their water-flushed origin. Journal of Volcanology and Geothermal Research, 9: 395-407.

Walker, G.P.L., 1983. Ignimbrite types and ignimbrite problems. Journal of Volcanology and Geothermal Research, 17: 65-88.

Walker, G.P.L., 1984. Characteristics of dune-bedded pyroclastic surge bedsets. Journal of Volcanology and Geothermal Research, 20: 281-296.

Walker, G.P.L., Wilson, C.J.N. and Froggatt, P.C., 1980. Fines-depleted ignimbrite in New Zealand- The product of a turbulent pyroclastic flow. Geology, 8: 245-249.

Walker, G.P.L., Wilson, C.J.N. and Froggatt, P.C., 1981. An ignimbrite veneer deposit: the trail-marker of a pyroclastic flow. Journal of Volcanology and Geothermal Research, 9: 409-421.

Waters, A.C. and Fisher, R.V., 1971. Base surges and their deposits: Capelinhos and Taal volcanoes. Journal of Geophysical Research, 76: 5596-5614.

Waythomas, C.F., Walder, J.S., McGimsey, R.G. and Neal, C.A., 1996. A catastrophic flood caused by drainage of a caldera lake at Aniakchak Volcano, Alaska and implications for volcanic- hazards assessment. Geological Society of America Bulletin, 108: 861-871.

White, J.D.L. and Houghton, B., 2000. Surtseyan and related phreatomagmatic eruptions. In: H. Sigurdsson, B.F. Houghton, S. McNutt, H. Rymer and J. Stix (Editors), Encyclopedia of Volcanoes. Academic Press, San Diego, pp. 495-511.

Wilson, C.J.N., 1981. Studies on the origins and emplacement of pyroclastic flows. Ph.D Thesis, Imperial College, London, 402 pp.

Wilson, C.J.N., 1985. The Taupo eruption, New Zealand II. The Taupo ignimbrite. Philosophical Transactions of the Royal Society of London, A314: 229-310.

Wilson, C.J.N., 1986. Pyroclastic flows and ignimbrites. Science Progress, Oxford, 70: 171-207.

Wilson, C.J.N., 1993. Stratigraphy, chronology, styles and dynamics of late Quaternary eruptions from Taupo volcano, New Zealand. Philosophical Transactions of the Royal Society of London, 343: 205-306.

Wilson, C.J.N., 2001. The 26.5 ka Oruanui eruption, New Zealand: an introduction and overview. Journal of Volcanology and Geothermal Research, 112: 133-174.

Wilson, C.J.N. and Hildreth, W., 1997. The Bishop Tuff: New insights from Eruptive Stratigraphy. The Journal of Geology, 105: 407-439.

Wilson, C.J.N. and Hildreth, W., 1998. Hybrid fall deposits in the Bishop Tuff, California: a novel pyroclastic depositional mechanism. Geology, Boulder, 26: 7-10.

Wilson, C.J.N. and Hildreth, W., 2003. Assembling an ignimbrite: Mechanical and thermal building blocks in the Bishop Tuff, California. Journal of Geology, 111: 653-670.

Wilson, C.J.N. and Houghton, B.F., 2000. Pyroclast transport and deposition. In: H. Sigurdsson, B.F. Houghton, S. McNutt, H. Rymer and J. Stix (Editors), Encyclopedia of Volcanoes. Academic Press, San Diego, California, pp. 545-554.

Wilson, C.J.N., Houghton, B.F. and Lloyd, E.F., 1986. Volcanic history and evolution of the Maroa-Taupo area, central North Island. In: I.E.M. Smith (Editor), Late Cenozoic Volcanism in New Zealand. Royal Society of New Zealand, Bulletin, Wellington, New Zealand, pp. 194-223.

Wilson, C.J.N., Houghton, B.J., McWilliams, M.O., Lanphere, M.A., Weaver, S.D. and Briggs, R.M., 1995. Volcanic and structural evolution of Taupo Volcanic Zone, New Zealand: a review. Journal of Volcanology and Geothermal Research, 68: 1-28.

Wilson, C.J.N., Rogan, A.M., Smith, I.E.M., Northey, D.J., Nairn, I.A. and Houghton, B.F., 1984. Calderas volcanoes of the Taupo Volcanic Zone, New Zealand. Journal of Geophysical Research, 89: 8463-8484.

Wilson, C.J.N. and Walker, G.P.L., 1982. Ignimbrite depositional facies: the anatomy of a pyroclastic flow. Journal of the Geological Society, London, 139: 581-592.

Wilson, C.J.N. and Walker, G.P.L., 1985. The Taupo eruption, New Zealand I. General aspects. Philosophical Transactions of the Royal Society of London, A314: 199-228.

Wohletz, K.H. and Sheridan, M.F., 1979. A model of pyroclastic surge. Geological Society of America Special Paper 180: 177-194.

Wright, I.C., 1992. Shallow structure and active tectonism of an offshore continental back-arc spreading system: the Taupo Volcanic Zone, New Zealand. Marine Geology, 103: 287-309.

Appendix 1 Localities and grid references

Localities and grid references for outcrop exposures in the study area. The type of deposit, lithofacies association (if Ohakuri), pumice, lithic, whole rock, and granulometry samples are provided for each locality.

Locality	Grid Ref.	Deposit	L.A.	Pumice	Lithic	Whole Rock	Granulometry
OH100	U17/773063	Ohakuri pyroclastics	Fla				x
OH101	U17/780046	Ohakuri pyroclastics	Fla	D160	OH101		x
OH102	U17/781051	reworked Ohakuri		D142			
OH103	U17/743089	Whangapoa beds ?					
OH104	U17/745099	Whangapoa beds ?					
OH105	U17/736081	Ohakuri pyroclastics	Fla	D152			
OH106	U17/815027	Ohakuri pyroclastics	Fla	D143-D146		D161	
OH107	U17/772044	Atiamuri ignimbrite					
OH108	U17/769034	Atiamuri ignimbrite					
OH109	T17/692087	Ohakuri pyroclastics	Fla	M408	M408		
OH110	T17/691087	Ohakuri pyroclastics	Fla	M409	M409, OH110b		
OH111	U17/866023	Kaingaroa ignimbrite					
OH112	U17/880062	Kaingaroa ignimbrite				D147	
OH113	U16/923256	Mamaku ignimbrite		D147	D-148	D-149	
OH114	T17/686075	Ohakuri pyroclastics	Fla	M412			x
OH115	T17/687075	Korotai ignimbrite					
OH116	T17/688078	Korotai ignimbrite		M414			
OH117	T17/689084	Ohakuri pyroclastics	Fla	D16,D17,D19,D20		D-18	
OH118	T17/689084	Ohakuri pyroclastics, pre-Ohakuri airfall	Fla	D212			
OH119	U16/78971413	Ohakuri pyroclastics	Tla			D150	
OH120	U16/78991439	Ohakuri pyroclastics	Tla				
OH121	U16/78981440	Ohakuri pyroclastics	Tla				
OH122	U16/79221454	Ohakuri pyroclastics	Tla				
OH123	U16/79231456	Ohakuri pyroclastics	Tla				
OH124a	U16/79331455	Ohakuri pyroclastics	Tla	D151			
OH124b	U16/79331458	Ohakuri pyroclastics	Tla				
OH124c	U16/79341460	Ohakuri pyroclastics	Tla				
OH125	U16/79281464	Ohakuri pyroclastics	Tla				
OH126	U16/79471458	Ohakuri pyroclastics	Tla				
OH127	U16/79631465	Ohakuri pyroclastics	Tla				
OH128	U17/77800639	Ohakuri pyroclastics	Fla				
OH129a	U16/79781286	Ohakuri pyroclastics	Mla				
OH129b	U16/79781286	Ohakuri pyroclastics	Mla				
OH129c	U16/79781286	Ohakuri pyroclastics	Mla	D126-D130	D70	D164	
OH130a	U16/80301172	Ohakuri pyroclastics	Mla	D90, D91, D153,D154	D92,D107		

Locality	Grid Ref.	Deposit	L.A.	Pumice	Lithic	Whole Rock	Granulometry
OH130b	U16/80301172	Ohakuri pyroclastics	Mla				
OH130c	U16/80301172	Ohakuri pyroclastics	Mla				
OH131	U16/81591164	Ohakuri pyroclastics	Gla	D155, D80		D156,D79	
OH132	U16/81571154	Ohakuri pyroclastics	Gla			D81	
OH133	U16/81331113	Ohakuri pyroclastics	Gla	D157, D82	D83		
OH134	U16/80481091	Ohakuri pyroclastics	Gla	D131-D134			
OH135	U16/80501098	Ohakuri pyroclastics	Gla	D77	D78		
OH136	U16/80501098	Ohakuri pyroclastics	Gla	D71-D75	D76		
OH137	U16/85111299	Ohakuri pyroclastics	Gla	D58-D60, D62-D69	D158, D66	D61	
OH138	U16/85041298	Ohakuri pyroclastics	Gla		D159	D159	
OH139	U16/84931300	Ohakuri pyroclastics	Gla				
OH140	U17/84210007	Huka Formation?					
OH141	U16/97761860	Mamaku ignimbrite				D162	
OH142	U16/97661870	Mamaku ignimbrite					
OH143	U16/97421809	Ngakuru Formation					
OH144	U16/90722007	Ohakuri pyroclastics	Gla			D163	
OH145	U16/91122089	Ohakuri pyroclastics	Gla				
OH146	U16/743096	post Rotoehu tephras					
OH147	U16/71391557	Mamaku ignimbrite, pre-Ohakuri airfall, Pokai ignimbrite		D165,166		D167	
OH148	U16/71301572	Ohakuri pyroclastics, Mamaku ignimbrite, pre-Ohakuri airfall	Fla	D101, D102, D140, D141	D180, M449		x
OH149	U16/74051699	Pokai ignimbrite					
OH150	U16/73481710	Pokai ignimbrite					
OH151	U16/73521719	Pokai ignimbrite					
OH152	U16/72821910	Ohakuri pyroclastics	Fla	D207			x
OH153	U16/72351879	Waimakiriri ?					
OH154	U16/72241782,	Ohakuri pyroclastics	Fla	D179			
OH155	U16/72261736	Ohakuri pyroclastics	Fla	D178,206			x
OH156	U16/72371621	Mamaku ignimbrite				OH156	
OH157	U16/72061567	Mamaku ignimbrite				OH157	
OH158	U16/73741710	Ohakuri pyroclastics	Fla				
OH159	U16/80971588	Ohakuri pyroclastics	Mla			D170	

Locality	Grid Ref.	Deposit	L.A.	Pumice	Lithic	Whole Rock	Granulometry
OH160	U16/80951582	Ohakuri pyroclastics	Mla	D37		D35, D36	
OH161	U16/80791579	Ohakuri pyroclastics	Mla				
OH162	U16/80711574	Ohakuri pyroclastics	Mla	D40		D39	
OH163	U16/80661573	Ohakuri pyroclastics	Mla	D41			
OH164	U16/80661571	Ohakuri pyroclastics	Mla				
OH165	U16/80411160	Ohakuri pyroclastics	Mla				
OH166	U16/80471137	Ohakuri pyroclastics	Mla				
OH167	U16/80471131	Ohakuri pyroclastics	Mla				
OH168	U16/80621119	Ohakuri pyroclastics	Mla	D93	D94		
OH169	U16/739181	Ohakuri pyroclastics, Mamaku ignimbrite, pre-Ohakuri airfall	Fla	D173,174,211		D175	x
OH170	U16/84021366	Ohakuri pyroclastics	Sla	D51			
OH171	U16/84001363	Ohakuri pyroclastics	Sla			D52	
OH172	U16/83951344	Ohakuri pyroclastics	Sla				
OH173	U16/83651313	Ohakuri pyroclastics	Sla			D171, D54-D57	
OH174	U16/83221296	Ohakuri pyroclastics	Sla			D46-D49	
OH175	U16/72061572	Ohakuri pyroclastics, Mamaku ignimbrite, pre-Ohakuri airfall	Fla	D173,175		D174, 176	
OH176	U16/71871673	Ohakuri pyroclastics	Fla	D177			
OH177	T17/68510820	Ohakuri pyroclastics	Fla	D203,204,205			
OH178	T17/69210751	Ohakuri pyroclastics	Fla	D202			x
OH179	T17/	Korotai ignimbrite					
OH180	T17/	Korotai ignimbrite					
OH181	T17/	Korotai ignimbrite					
OH182	T17/	Korotai ignimbrite					
OH183	T17/	Korotai ignimbrite					
OH184	U16/71162202	Ohakuri pyroclastics	Fla	D120-D122			x
OH185	U16/81981280	Ohakuri pyroclastics	Sla			D181,182,183	
OH186	U16/82021270	Ohakuri pyroclastics	Sla		D187	D184,185,186	
OH187	U16/82021270	Ohakuri pyroclastics	Sla		D188		
OH188	U16/82271116	Ohakuri pyroclastics	Gla	D189,190		D191	
OH189	U16/82071102	Ohakuri pyroclastics	Gla	D192		D193	
OH190	U16/81991099	Ohakuri pyroclastics	Gla				
OH191	U16/81991095	Ohakuri pyroclastics	Gla				

Locality	Grid Ref.	Deposit	L.A.	Pumice	Lithic	Whole Rock	Granulometry
OH192	U16/82111086	Ohakuri pyroclastics	Gla				
OH193	U16/81951102	Ohakuri pyroclastics	Gla				
OH194	U16/81921101	Ohakuri pyroclastics	Gla				
OH195	U16/81481101	Ohakuri pyroclastics	Gla	D194			
OH196	U16/81481101	Ohakuri pyroclastics	Gla		D195,196		
OH197	U16/81531104	Ohakuri pyroclastics	Gla				
OH198	U16/81711113	Ohakuri pyroclastics	Gla	D197,198,199			
OH199	U16/81711116	Ohakuri pyroclastics	Gla			D200	
OH200	U16/81731118	Ohakuri pyroclastics	Gla				
OH201	U16/81741124	Ohakuri pyroclastics	Gla				
OH202	U16/81661148	Ohakuri pyroclastics	Gla				
OH203	U17/0910998	Onuku pyroclastics					
OH204	T16/69391819	Ohakuri pyroclastics, Mamaku ignimbrite, pre-Ohakuri airfall, Pokai ignimbrite	Fla	D95-D100, D137-D139			x
OH205	U16/90691196	Ohakuri pyroclastics	Gla			D201	
OH206	U16/91621233	Ohakuri pyroclastics	Gla				
OH207	U16/79631889	Ohakuri pyroclastics?		D208			
OH208	T16/682268	Pokai ignimbrite		D209			
OH209	U16/740340	Mamaku ignimbrite		D210			
OH210	U16/776239	pre-Mamaku tephras					
OH211	U16/76041888	Mamaku ignimbrite		D213			
OH212	U16/76111913	Mamaku ignimbrite		D214			
OH213	U16/70230934	Ohakuri pyroclastics	Fla	D215			
OH214	U16/81491082	Ohakuri pyroclastics	Gla		D216		
OH215	T16/695243	Mamaku ignimbrite, Pokai ignimbrite					
OH216	T16/649193	pre-Pokai tephras		OH216	OH216		
OH217	T16/65091753	Ohakuri pyroclastics, Mamaku ignimbrite, pre-Ohakuri airfall, Pokai ignimbrite	Fla				
OH218	T16/65671271	Ohakuri pyroclastics	Fla				
OH219	T16/679117	Ohakuri pyroclastics	Fla				

Locality	Grid Ref.	Deposit	L.A.	Pumice	Lithic	Whole Rock	Granulometry
OH220	U16/70431602	Ohakuri pyroclastics	Fla				
OH221	U16/70771608	Mamaku ignimbrite					
OH222	T16/69221797	Ohakuri pyroclastics	Fla	OH222	OH222		
OH223	U17/734078	Dome pumice breccia					
OH224	U16/78552051	Mamaku ignimbrite, Pokai ignimbrite					
OH225	U16/77122015	Mamaku ignimbrite, Pokai ignimbrite					
OH226	U16/77581756	Mamaku ignimbrite, Pokai ignimbrite					
OH227	U16/73452275	Ohakuri pyroclastics	Fla				
OH228	U16/774063	Ohakuri pyroclastics	Fla				
OH229	U16/774126	reworked pyroclastics					
OH230	U16/775126	reworked pyroclastics					
OH231	U16/782127	Matapan basalt					
OH232	U16/783126	reworked pyroclastics					
OH233	U16/784127	reworked pyroclastics					
OH234	U16/785126	reworked pyroclastics					
OH235	U16/867153	Ohakuri pyroclastics	Gla	D4, D5			
OH236	U16/8691575	Ohakuri pyroclastics	Gla			D6-D9	
OH237	U16/855130	Ngakuru Formation		D10			
OH238	U16/87191601	Ohakuri pyroclastics	Gla			D42	
OH239	U16/87161605	Ohakuri pyroclastics	Gla	D43		D44	
OH240	U16/87221597	Ohakuri pyroclastics	Gla	D45			
OH241	U16/87231596	Ohakuri pyroclastics	Gla				
OH242	U16/83601316	Ohakuri pyroclastics	Sla			D50	
OH243	U16/83971351	Ohakuri pyroclastics	Sla			D53	
OH244	U16/83951348	Ohakuri pyroclastics	Sla				
OH245	U16/817125	Ohakuri pyroclastics	Sla				
OH246	U16/818124	Ohakuri pyroclastics	Sla				

Locality	Grid Ref.	Deposit	L.A.	Pumice	Lithic	Whole Rock	Granulometry
OH247	U16/8182124	Ohakuri pyroclastics	Sla				
OH248	U16/8185124	Ohakuri pyroclastics	Sla				
OH249	U16/82051265	Ohakuri pyroclastics	Sla				
OH250	U16/821131	Ohakuri pyroclastics	Sla				
OH251	U16/8195132	Ohakuri pyroclastics	Sla				
OH252	U16/8061105	Ohakuri pyroclastics	Gla		D84		
OH253	U16/808113	Ohakuri pyroclastics	Gla	D85	D86		
OH254	U16/806117	Ohakuri pyroclastics	Gla	D87			
OH255	U16/80651165	Ohakuri pyroclastics	Gla	D89		D88	
OH256	U16/7981455	Ohakuri pyroclastics	Tla	D3, D3a		D2	
OH257	U16/800146	Ohakuri pyroclastics	Tla	D1			
OH258	U16/802151	Ohakuri pyroclastics	Mla	D11	D15	D12-D14	
OH259	U16/797146	Ohakuri pyroclastics	Tla				
OH260	U16/797146	Ohakuri pyroclastics	Tla		D21	D22	
OH261	U16/79651465	Ohakuri pyroclastics	Tla				
OH262	U16/79651465	Ohakuri pyroclastics	Tla			D23	
OH263	U16/7965147	Ohakuri pyroclastics	Tla				
OH264	U16/797148	Ohakuri pyroclastics	Tla				
OH265	U16/7961465	Ohakuri pyroclastics	Tla		D24		
OH266	U16/7961465	Ohakuri pyroclastics	Tla	D26, D27		D25, D28	
OH267	U16/798146	Ohakuri pyroclastics	Tla		D29-D32, D108		
OH268	U16/7985147	Ohakuri pyroclastics	Tla				
OH269	U16/7981455	Ohakuri pyroclastics	Tla		D33		
OH270	U16/805151	Ohakuri pyroclastics	Tla				
OH271	U16/806151	Ohakuri pyroclastics	Tla				
OH272	U16/803149	Ohakuri pyroclastics	Tla				
OH273	U16/80931581	Ohakuri pyroclastics	Mla		D34		
OH274	U16/80781574	Ohakuri pyroclastics	Mla			D38	
OH275	U16/774127	Ohakuri pyroclastics		D103, D105		D104, D106	
OH276	T16/697114	Ohakuri pyroclastics	Fla	D124, D125			
OH277	U16/713216	Ohakuri pyroclastics	Fla	D109, D123			
OH278	U16/726207	Ohakuri pyroclastics	Fla	D110			
OH279	U16/727206	Ohakuri pyroclastics	Fla	D111, D113-D119			
OH280	U16/759182	Ohakuri pyroclastics	Fla	D112			
OH281	U16/780114	Matapan basalt				D136	
OH282	U16/782117	Matapan basalt				D135	

Appendix 2 XRF analyses

X-ray Fluorescence (XRF) analyses were performed on single pumice clasts from the Ohakuri pyroclastic deposits and the Mamaku ignimbrite, at the University of Canterbury. Samples were cleaned and then crushed and milled into a fine powder. Glass fusion beads and compressed powder pellets were prepared for major and trace element analyses, respectively.

The analyses were carried out by the author and Stephen Brown, in a Phillips PW-2400 XRF spectrometer. The spectrometer was calibrated using standard reference materials sourced from ANRT(GIT/IWG), CCRMP, GSJ, NIST, SABS, and USGS.

The data have been recalculated to 100% volatile free (i.e. LOI values are not included in the 100% totals). The deposit and pumice type is provided for each analysis. See Appendix 1 for the sample localities.

Sample	D1	D3	D3a	D4	D5	D10	D16	D17	D19	D20	D26	D27	D40
Deposit	Ohakuri	Ohakuri	Ohakuri	Ohakuri	Ohakuri	Ohakuri	Ohakuri	Ohakuri	Ohakuri	Ohakuri	Ohakuri	Ohakuri	Ohakuri
Pum. Type	type 1	type 3	type 2	type 2	type 1	type 2	type 1	type 2	type 1	type 2	type 2	type 3	type 1
SiO2	77.64	68.02	75.61	70.66	76.10	68.33	76.61	72.58	76.34	72.55	73.04	69.41	77.27
TiO2	0.15	0.56	0.25	0.44	0.17	0.39	0.17	0.31	0.12	0.31	0.31	0.48	0.15
Al2O3	12.50	16.53	13.42	15.27	13.63	19.18	13.18	15.47	14.05	15.40	14.04	15.94	12.43
Fe2O3T	1.06	4.12	2.24	3.30	1.72	3.20	1.55	2.48	1.40	2.55	2.24	2.82	1.44
MnO	0.04	0.13	0.07	0.14	0.05	0.13	0.06	0.09	0.05	0.09	0.06	0.08	0.05
MgO	0.11	0.80	0.24	0.65	0.14	0.39	0.12	0.31	0.07	0.34	0.72	0.64	0.11
CaO	1.03	2.89	1.26	2.23	0.83	1.79	0.83	1.55	0.62	1.51	1.69	2.62	0.84
Na2O	4.01	4.66	3.39	3.77	3.23	4.34	3.74	4.19	3.40	4.26	5.15	5.23	3.73
K2O	3.44	2.26	3.49	3.46	4.07	2.26	3.73	3.01	3.93	2.96	2.67	2.68	3.96
P2O5	0.02	0.02	0.02	0.06	0.06	0.01	0.01	0.01	0.01	0.02	0.07	0.10	0.02
(LOI)	4.76	2.54	4.51	3.32	3.84	4.08	2.96	3.08	3.78	3.20	4.46	2.79	3.41
Total	100.00	100.00	100.00	100.00	100.00	100.00	100.00	100.00	100.00	100.00	100.00	100.00	100.00
V	8	21	10	23	9	13	6	11	6	10	12	19	8
Cr	3	3	3	3	3	3	3	3	3	3	3	3	3
Ni	3	3	4	3	3	3	5	3	4	3	4	3	3
Zn	21	77	54	78	45	76	45	58	44	60	57	75	42
Zr	141	408	216	321	167	326	160	266	138	267	247	341	146
Nb	8	10	9	10	9	13	9	11	10	11	8	9	8
Ba	814	639	751	683	729	692	785	741	822	744	861	605	704
La	21	9	22	11	22	17	22	17	26	18	19	19	23
Ce	78	49	65	57	64	86	70	80	78	81	66	61	61
Nd	25	15	25	14	31	11	17	<10	28	21	37	34	41
Ga	13	18	14	17	15	21	14	16	15	16	15	17	13
Pb	10	12	17	14	20	21	18	22	25	22	8	7	18
Rb	117	78	118	97	123	75	120	95	138	95	111	124	130
Sr	73	258	96	179	58	153	55	126	33	122	123	221	57
Th	15	8	12	9	10	13	11	11	15	12	9	7	12
Y	37	25	35	27	33	27	35	32	39	32	35	31	36

Sample	D41	D43	D45	D58	D59	D60	D63	D64	D65	D68	D69	D71	D72
Deposit	Ohakuri	Ohakuri	Ohakuri	Ohakuri	Ohakuri	Ohakuri	Ohakuri	Ohakuri	Ohakuri	Ohakuri	Ohakuri	Ohakuri	Ohakuri
Pum. Type	type 1	type 2	type 1	type 1	type 3	type 2	type 1	type 1	type 1	type 1	type 2	type 2	type 1
SiO2	77.31	74.40	76.79	77.12	69.17	74.47	77.22	76.93	76.67	77.05	72.08	75.95	77.58
TiO2	0.10	0.27	0.14	0.16	0.50	0.26	0.16	0.17	0.15	0.15	0.31	0.19	0.15
Al2O3	12.19	13.55	12.87	12.61	16.02	13.87	13.01	13.11	12.58	12.60	15.70	13.05	12.51
Fe2O3T	1.19	2.27	1.46	1.50	3.68	2.20	1.56	1.58	1.46	1.43	2.57	1.74	1.42
MnO	0.06	0.08	0.05	0.05	0.12	0.08	0.05	0.06	0.05	0.05	0.09	0.05	0.05
MgO	0.08	0.30	0.11	0.12	0.67	0.30	0.11	0.14	0.16	0.11	0.35	0.12	0.11
CaO	0.78	1.39	0.79	0.81	2.61	1.43	0.85	0.84	0.86	0.80	1.51	1.16	0.83
Na2O	2.92	3.44	3.14	3.45	4.35	3.31	2.81	2.52	3.36	3.18	4.11	4.13	3.41
K2O	5.35	4.25	4.60	4.16	2.80	4.01	4.19	4.64	4.69	4.60	3.23	3.59	3.92
P2O5	0.01	0.04	0.02	0.02	0.08	0.07	0.02	0.01	0.03	0.02	0.04	0.03	0.01
(LOI)	4.11	3.35	3.01	3.80	3.06	3.76	4.10	3.95	3.77	4.03	4.07	3.00	3.61
Total	100.00	100.00	100.00	100.00	100.00	100.00	100.00	100.00	100.00	100.00	100.00	100.00	100.00
V	7	9	8	6	17	10	8	9	7	8	9	7	6
Cr	3	3	3	3	3	3	3	3	3	3	3	3	3
Ni	6	5	5	6	3	3	5	3	3	4	4	3	3
Zn	40	56	56	44	75	54	42	46	43	43	66	47	41
Zr	118	234	148	147	381	221	151	146	146	143	253	197	144
Nb	8	9	9	8	11	9	9	9	8	8	11	8	8
Ba	734	712	789	792	634	697	746	752	767	767	674	762	776
La	31	21	22	24	14	17	20	24	26	24	17	18	22
Ce	77	65	73	59	62	60	76	61	64	60	60	65	69
Nd	42	29	32	34	16	33	20	21	24	25	45	15	42
Ga	13	14	14	13	16	14	13	14	13	13	16	13	13
Pb	19	16	20	20	12	17	19	20	20	18	21	20	20
Rb	145	119	138	126	84	114	127	138	132	142	98	124	132
Sr	51	109	55	53	231	110	57	57	57	54	125	90	54
Th	11	8	12	11	6	8	11	12	12	13	12	11	10
Y	41	36	36	36	26	33	35	34	38	36	31	30	36

Sample	D73	D75	D77	D80	D82	D85	D87	D89	D90	D91	D95	D96	D97
Deposit	Ohakuri	Ohakuri	Ohakuri	Ohakuri	Ohakuri	Ohakuri	Ohakuri	Ohakuri	Ohakuri	Ohakuri	Ohakuri	Ohakuri	Ohakuri
Pum. Type	type 1	type 2	type 1	type 1	type 2	type 1	type 3	type 2	type 1	type 1	type 2	type 2	type 2
SiO2	77.36	74.53	77.44	76.09	73.57	77.96	69.80	72.36	77.65	77.57	73.31	74.66	74.83
TiO2	0.15	0.27	0.14	0.19	0.29	0.11	0.48	0.30	0.15	0.15	0.34	0.28	0.26
Al2O3	12.56	13.84	12.52	14.02	14.32	12.35	15.35	15.43	12.45	12.53	13.92	13.39	13.44
Fe2O3T	1.38	2.10	1.43	1.77	2.34	1.22	3.55	2.53	1.37	1.32	2.64	2.26	2.17
MnO	0.08	0.07	0.06	0.06	0.08	0.05	0.12	0.09	0.05	0.05	0.09	0.08	0.08
MgO	0.10	0.28	0.10	0.15	0.34	0.07	0.69	0.33	0.10	0.10	0.40	0.30	0.29
CaO	0.84	1.54	0.81	0.87	1.55	0.62	2.75	1.57	0.82	0.87	1.76	1.42	1.45
Na2O	3.64	3.60	3.55	2.77	4.39	3.50	4.83	4.47	3.30	3.20	4.18	4.08	3.84
K2O	3.86	3.75	3.93	4.08	3.08	4.09	2.30	2.91	4.07	4.18	3.28	3.48	3.60
P2O5	0.02	0.03	0.02	0.01	0.04	0.02	0.12	0.02	0.02	0.02	0.06	0.04	0.04
(LOI)	4.00	3.51	3.26	4.34	2.04	3.88	2.17	3.43	4.31	4.29	3.24	3.25	3.13
Total	100.00	100.00	100.00	100.00	100.00	100.00	100.00	100.00	100.00	100.00	100.00	100.00	100.00
V	6	11	7	8	9	5	19	12	8	8	12	10	10
Cr	3	3	3	3	3	3	3	3	3	3	3	3	3
Ni	7	4	5	6	3	3	3	3	3	4	3	3	3
Zn	43	52	43	45	59	39	66	61	43	40	57	53	52
Zr	139	225	148	179	243	119	358	272	140	138	246	236	220
Nb	8	9	9	10	9	9	10	11	9	9	10	9	9
Ba	789	723	781	760	739	791	617	742	776	779	711	734	731
La	24	20	27	23	28	25	14	21	22	26	18	22	24
Ce	70	62	67	55	79	67	52	70	68	66	59	57	57
Nd	42	31	24	26	38	37	30	22	41	24	25	37	39
Ga	12	15	13	15	16	13	16	16	13	13	15	14	14
Pb	19	16	20	21	15	23	13	18	20	17	15	16	19
Rb	128	126	132	118	100	145	75	96	122	121	105	111	114
Sr	55	121	54	58	125	34	236	130	53	58	138	110	111
Th	12	11	10	11	10	13	5	12	13	13	11	11	10
Y	37	34	36	33	35	40	29	33	37	36	34	35	35

Sample	D98	D103	D109	D110	D111	D112	D113	D115	D116	D117	D118	D119	D124
Deposit	Ohakuri	Ohakuri	Ohakuri	Ohakuri	Ohakuri	Ohakuri	Ohakuri	Ohakuri	Ohakuri	Ohakuri	Ohakuri	Ohakuri	Ohakuri
Pum. Type	type 1	type 2	type 2	type 1	type 2	type 1	type 1	type 2	type 2	type 2	type 2	type 2	type 2
SiO2	77.38	70.68	71.02	73.66	72.25	76.88	76.45	70.94	71.89	70.82	67.75	71.94	74.63
TiO2	0.13	0.37	0.35	0.19	0.32	0.12	0.15	0.34	0.32	0.35	0.41	0.31	0.26
Al2O3	12.41	16.97	16.25	16.47	15.49	13.48	13.22	17.01	15.83	16.95	19.89	16.14	13.55
Fe2O3T	1.38	2.51	2.87	1.89	2.84	1.36	1.55	2.80	2.87	2.97	3.35	2.62	2.19
MnO	0.05	0.08	0.12	0.06	0.09	0.05	0.06	0.09	0.09	0.09	0.10	0.08	0.07
MgO	0.11	0.40	0.42	0.15	0.36	0.06	0.13	0.37	0.36	0.40	0.45	0.33	0.30
CaO	0.81	1.83	1.74	0.85	1.57	0.58	0.84	1.60	1.56	1.63	1.85	1.57	1.36
Na2O	3.59	4.56	4.59	3.65	4.15	3.37	3.83	4.15	4.23	4.07	4.04	4.15	4.15
K2O	4.10	2.56	2.61	3.07	2.89	4.08	3.76	2.67	2.82	2.69	2.15	2.83	3.46
P2O5	0.02	0.02	0.02	0.01	0.03	0.01	0.01	0.02	0.02	0.02	0.02	0.02	0.04
(LOI)	3.09	3.07	2.99	4.70	3.79	3.52	3.53	3.75	3.47	3.48	4.16	3.55	2.90
Total	100.00	100.00	100.00	100.00	100.00	100.00	100.00	100.00	100.00	100.00	100.00	100.00	100.00
V	8	13	17	11	15	13	12	18	15	19	15	17	17
Cr	3	3	3	3	3	3	3	3	3	3	3	3	3
Ni	3	4	5	4	3	3	3	3	3	3	3	3	3
Zn	42	59	68	61	62	44	47	65	64	68	75	61	53
Zr	139	292	307	193	273	134	156	299	279	292	333	271	223
Nb	8	12	12	12	11	9	9	12	11	12	14	12	10
Ba	786	810	758	979	752	797	783	784	737	731	999	758	729
La	23	19	35	29	25	32	31	33	32	25	26	28	38
Ce	64	50	97	65	69	79	75	84	69	71	66	68	75
Nd	34	27	35	23	39	43	41	34	21	34	30	35	43
Ga	13	18	18	18	17	15	14	18	17	18	22	17	15
Pb	21	22	21	26	18	20	20	19	19	20	23	19	18
Rb	136	85	88	99	91	136	117	83	90	84	68	87	116
Sr	52	157	149	64	128	33	58	135	129	137	161	131	102
Th	12	11	14	16	10	15	13	13	12	12	15	13	12
Y	38	28	34	34	36	39	38	36	35	33	32	35	37

Sample	D126	D130	D131	D132	D134	D137	D138	D139	D141	D143	D152a	D152b	D153a
Deposit	Ohakuri	Ohakuri	Ohakuri	Ohakuri	Ohakuri	Ohakuri	Ohakuri	Ohakuri	Ohakuri	Ohakuri	Ohakuri	Ohakuri	Ohakuri
Pum. Type	type 2	type 1	type 1	type 1	type 2	type 2	type 1	type 1	type 1	type 1	type 1	type 1	type 2
SiO2	75.09	77.08	77.42	76.93	74.20	75.11	77.38	77.21	77.26	75.41	76.48	76.83	74.59
TiO2	0.22	0.15	0.14	0.18	0.28	0.26	0.14	0.15	0.15	0.14	0.18	0.14	0.29
Al2O3	13.24	12.55	12.51	12.78	14.03	13.22	12.58	12.49	12.44	15.18	13.25	13.21	13.57
Fe2O3T	2.09	1.43	1.47	1.68	2.36	2.24	1.48	1.50	1.48	1.52	1.67	1.51	2.39
MnO	0.07	0.05	0.05	0.05	0.07	0.07	0.05	0.05	0.05	0.05	0.07	0.05	0.08
MgO	0.28	0.13	0.11	0.12	0.30	0.29	0.13	0.13	0.13	0.10	0.15	0.12	0.38
CaO	1.30	0.86	0.79	0.89	1.47	1.31	0.85	0.84	0.80	0.65	0.94	0.84	1.51
Na2O	3.89	3.54	3.54	3.47	3.90	3.97	3.20	3.64	3.87	3.44	3.65	3.52	3.64
K2O	3.74	4.19	3.94	3.88	3.37	3.49	4.16	3.97	3.80	3.50	3.60	3.76	3.48
P2O5	0.07	0.02	0.02	0.02	0.03	0.04	0.02	0.02	0.02	0.01	0.01	0.01	0.06
(LOI)	4.04	3.65	2.87	3.46	3.19	3.05	3.27	2.84	2.30	4.14	3.02	3.53	3.90
Total	100.00	100.00	100.00	100.00	100.00	100.00	100.00	100.00	100.00	100.00	100.00	100.00	100.00
V	16	16	14	16	17	16	13	13	15	7	9	7	13
Cr	3	3	3	3	3	3	3	3	3	3	3	3	3
Ni	4	3	4	3	3	6	6	3	3	5	3	3	3
Zn	52	46	47	50	60	55	43	44	43	81	62	48	59
Zr	202	140	150	170	252	235	142	155	152	147	163	152	223
Nb	9	9	9	9	10	10	9	9	9	10	8	8	9
Ba	699	751	761	756	709	729	798	791	785	834	779	784	722
La	37	34	36	40	35	30	37	37	38	29	25	33	33
Ce	71	72	70	79	74	68	70	63	71	81	73	71	70
Nd	32	36	38	44	30	33	29	38	34	36	25	24	45
Ga	14	13	14	13	15	14	13	14	13	16	14	14	15
Pb	17	21	21	20	16	16	19	20	19	21	22	21	16
Rb	116	124	127	126	104	111	135	131	127	130	117	119	110
Sr	94	58	54	61	119	101	58	57	55	36	65	57	114
Th	10	12	12	13	12	10	10	13	11	14	13	13	11
Y	37	38	39	38	34	37	38	38	38	36	36	36	36

Sample	D153b	D153c	D154a	D154b	D155	D157	D160a	D160b	D173	D177a	D177b	D177c	D178a
Deposit	Ohakuri	Ohakuri	Ohakuri	Ohakuri	Ohakuri	Ohakuri	Ohakuri	Ohakuri	Ohakuri	Ohakuri	Ohakuri	Ohakuri	Ohakuri
Pum. Type	type 3	type 3	type 2	type 1	type 1	type 3	type 2	type 2	type 1	type 2	type 1	bleb	type 2
SiO2	70.08	67.02	74.22	77.46	76.99	68.40	70.92	73.28	77.15	68.55	73.54	60.11	73.91
TiO2	0.47	0.56	0.30	0.15	0.14	0.51	0.34	0.28	0.14	0.39	0.21	1.07	0.28
Al2O3	15.48	17.09	13.75	12.53	13.11	16.27	16.80	14.65	12.68	19.01	16.28	20.14	14.01
Fe2O3T	3.37	3.85	2.33	1.38	1.48	3.77	2.86	2.35	1.33	3.14	1.98	6.77	2.35
MnO	0.11	0.12	0.08	0.06	0.05	0.13	0.09	0.08	0.05	0.11	0.08	0.16	0.08
MgO	0.68	0.78	0.38	0.13	0.11	0.72	0.40	0.30	0.11	0.41	0.17	1.75	0.33
CaO	2.66	3.40	1.68	0.86	0.83	2.75	1.72	1.53	0.87	1.79	0.97	4.19	1.50
Na2O	4.34	4.95	3.52	3.21	2.85	5.08	3.58	4.16	3.55	4.26	3.75	4.45	4.03
K2O	2.70	2.18	3.67	4.19	4.43	2.26	3.27	3.35	4.11	2.33	3.00	1.34	3.49
P2O5	0.11	0.04	0.06	0.03	0.01	0.10	0.02	0.02	0.01	0.01	0.02	0.02	0.02
(LOI)	2.52	2.41	3.40	3.95	3.75	1.77	4.19	3.82	2.41	4.42	4.03	3.06	3.30
Total	100.00	100.00	100.00	100.00	100.00	100.00	100.00	100.00	100.00	100.00	100.00	100.00	100.00
V	24	21	16	11	10	17	11	12	7	12	8	77	12
Cr	3	3	3	3	3	3	3	3	3	3	3	3	3
Ni	4	3	3	3	3	3	3	3	3	3	3	3	3
Zn	71	70	57	46	45	68	73	58	44	69	78	95	55
Zr	307	376	217	140	147	381	278	233	149	313	203	301	222
Nb	9	9	8	8	9	10	11	9	8	13	11	13	9
Ba	654	628	693	777	749	647	893	742	805	901	1125	603	716
La	20	23	31	37	31	18	19	26	34	27	26	17	28
Ce	69	56	64	68	70	68	81	71	81	85	87	48	69
Nd	32	38	30	32	24	30	16	16	26	31	30	37	20
Ga	16	18	15	13	14	18	17	14	13	21	16	21	14
Pb	13	10	15	19	20	12	18	18	22	23	24	13	16
Rb	86	71	107	120	136	73	90	100	129	78	101	39	108
Sr	213	295	126	57	53	240	142	124	59	152	71	350	122
Th	7	8	11	13	14	8	15	10	11	14	16	10	10
Y	31	26	34	37	37	32	31	33	39	35	38	37	36

Sample	D178b	D189	D190	D192	D194	D198	D202a	D204	D205	D206a	D206b	D206c	D207a
Deposit	Ohakuri	Ohakuri	Ohakuri	Ohakuri	Ohakuri	Ohakuri	Ohakuri	Ohakuri	Ohakuri	Ohakuri	Ohakuri	Ohakuri	Ohakuri
Pum. Type	type 2	type 2	type 2	type 3	type 1	type 2	type 1	type 1	type 2	type 2	type 1	bleb	type 2
SiO2	74.40	73.71	75.81	68.14	76.85	75.24	77.44	76.46	75.94	70.81	75.40	58.25	74.16
TiO2	0.25	0.29	0.22	0.49	0.14	0.22	0.14	0.17	0.16	0.34	0.13	1.11	0.27
Al2O3	13.78	14.00	13.08	16.51	12.79	13.28	12.48	12.77	13.04	16.95	14.87	17.77	13.95
Fe2O3T	2.12	2.47	1.87	3.63	1.45	1.92	1.43	1.60	1.91	2.82	1.52	8.10	2.25
MnO	0.07	0.08	0.06	0.15	0.05	0.07	0.06	0.06	0.07	0.09	0.06	0.15	0.09
MgO	0.28	0.35	0.23	0.80	0.12	0.24	0.11	0.14	0.10	0.37	0.08	3.32	0.30
CaO	1.44	1.57	1.14	2.75	0.82	1.25	0.83	1.04	1.13	1.63	0.64	6.25	1.44
Na2O	4.20	4.16	3.71	4.56	3.57	4.25	3.52	3.95	3.93	4.23	3.61	3.76	4.25
K2O	3.43	3.31	3.86	2.93	4.19	3.48	3.97	3.77	3.70	2.72	3.66	1.23	3.28
P2O5	0.02	0.05	0.03	0.05	0.02	0.03	0.01	0.02	0.02	0.02	0.02	0.06	0.02
(LOI)	3.25	2.90	2.83	3.85	3.68	2.39	2.49	2.72	2.72	3.56	3.59	1.80	2.94
Total	100.00	100.00	100.00	100.00	100.00	100.00	100.00	100.00	100.00	100.00	100.00	100.00	100.00
V	9	13	7	15	6	12	8	12	8	12	7	190	12
Cr	3	3	3	3	3	3	3	3	3	3	3	9	3
Ni	3	3	4	3	3	3	3	3	3	3	3	9	3
Zn	53	63	50	74	43	51	43	44	55	65	51	92	55
Zr	219	238	184	322	147	202	147	178	210	290	144	192	230
Nb	9	9	8	10	9	9	8	8	8	11	9	8	9
Ba	714	722	720	647	748	725	772	786	761	765	813	384	746
La	23	26	27	16	30	27	31	29	29	26	44	11	23
Ce	77	68	67	54	75	71	65	64	66	84	82	36	74
Nd	27	22	25	21	17	25	42	20	24	12	56	36	33
Ga	14	14	14	17	14	14	13	13	14	18	16	19	15
Pb	16	16	20	14	20	17	19	20	23	18	22	6	18
Rb	106	104	122	86	124	113	128	131	127	87	124	29	103
Sr	116	131	89	258	54	99	54	76	91	136	39	422	115
Th	12	10	11	9	11	11	15	14	12	12	17	4	10
Y	36	34	35	26	37	35	38	31	33	34	52	35	35

Sample	D207b	D208a	D208b	D208c	D212	M409a	M412a	M412b	Oh1/1	Oh1/4	Oh2/c	Oh6/2	Oh1/3
Deposit	Ohakuri	Ohakuri	Ohakuri	Ohakuri	Ohakuri	Ohakuri	Ohakuri	Ohakuri	Ohakuri	Ohakuri	Ohakuri	Ohakuri	Ohakuri
Pum. Type	type 2	type 1	type 1	type 1	type 2	type 2	type 2	type 2	type 1	type 1	type 1	type 1	type 1
SiO2	72.84	76.70	76.54	76.43	73.81	71.94	73.94	73.44	77.42	77.34	77.13		
TiO2	0.30	0.12	0.12	0.12	0.26	0.32	0.28	0.28	0.11	0.15	0.14		
Al2O3	15.15	12.96	13.35	13.56	14.27	15.76	14.23	14.68	12.52	12.31	12.55		
Fe2O3T	2.47	1.51	1.47	1.45	2.23	2.65	2.28	2.34	1.24	1.46	1.39		
MnO	0.10	0.05	0.05	0.05	0.07	0.09	0.08	0.08	0.04	0.05	0.05		
MgO	0.33	0.08	0.07	0.08	0.30	0.36	0.31	0.32	0.11	0.19	0.14		
CaO	1.58	0.87	0.82	0.80	1.49	1.68	1.51	1.60	0.59	0.78	0.84		
Na2O	4.19	3.93	3.75	3.64	3.99	4.28	4.23	4.19	3.60	3.78	3.94		
K2O	3.02	3.76	3.80	3.84	3.56	2.89	3.12	3.06	4.33	3.91	3.79		
P2O5	0.01	0.02	0.02	0.02	0.02	0.02	0.02	0.02	0.02	0.02	0.02		
(LOI)	2.83	2.19	2.39	2.24	2.42	3.41	2.75	2.54					
Total	100.00	100.00	100.00	100.00	100.00	100.00	100.00	100.00	100.00	100.00	100.00		
V	9	8	6	6	9	12	12	13	6	8	9	9	9
Cr	3	3	3	3	3	3	3	3	3	3	3	3	3
Ni	3	3	3	3	3	3	3	3	3	3	3	3	3
Zn	57	47	48	48	53	60	59	58	43	45	41	43	41
Zr	246	155	149	148	218	265	222	243	124	154	147	152	152
Nb	10	8	9	9	9	10	9	9	10	9	10	11	11
Ba	770	811	864	860	715	779	761	774	806	803	784	743	802
La	26	26	27	29	24	21	28	29	33	31	32	28	32
Ce	74	73	70	73	73	79	77	80	73	67	66	65	70
Nd	39	27	14	26	33	18	21	20					
Ga	16	14	14	14	15	18	15	15	14	11	14	14	13
Pb	18	19	20	18	18	21	17	18	18	21	21	19	18
Rb	96	131	130	130	112	92	101	99	150	123	126	122	127
Sr	130	63	59	57	120	138	122	131	32	52	55	55	56
Th	11	14	14	15	10	13	10	9	14	11	12	12	11
Y	35	32	33	32	33	32	33	33	45	39	39	39	40

Sample	Oh2/a	Oh3/P	Oh1/25	Oh2/b	Oh6/4	Oh2/d	Oh1/6	Oh6/5	Oh6/1	Oh6/3	Oh6/6	Oh4/2	Oh4/6
Deposit	Ohakuri	Ohakuri	Ohakuri	Ohakuri	Ohakuri	Ohakuri	Ohakuri	Ohakuri	Ohakuri	Ohakuri	Ohakuri	Ohakuri	Ohakuri
Pum. Type	type 1	type 1	type 1	type 1	type 1	type 1	type 1	type 1	type 1	type 1	type 1	type 1	type 1
SiO2		76.84		77.01			77.01		76.75	76.89	76.71	76.70	76.20
TiO2		0.15		0.14			0.16		0.16	0.16	0.16	0.17	0.18
Al2O3		12.86		12.53			12.68		12.43	12.27	12.40	12.50	12.73
Fe2O3T		1.48		1.44			1.45		1.55	1.49	1.56	1.59	1.67
MnO		0.04		0.07			0.04		0.07	0.07	0.08	0.05	0.08
MgO		0.15		0.20			0.18		0.21	0.21	0.24	0.24	0.24
CaO		0.84		0.82			0.84		0.96	1.00	1.11	0.91	1.07
Na2O		3.71		3.93			3.73		4.02	4.06	3.97	4.04	4.27
K2O		3.91		3.82			3.90		3.80	3.78	3.73	3.76	3.52
P2O5		0.02		0.03			0.02		0.04	0.07	0.05	0.04	0.04
(LOI)													
Total		100.00		100.00			100.00		100.00	100.00	100.00	100.00	100.00
V	10	7	7	7	9	6	9	10	9	10	10	13	12
Cr	3	3	3	3	3	3	3	3	3	3	3	3	3
Ni	3	3	4	3	3	3	3	3	3	3	3	3	3
Zn	45	48	45	42	44	43	45	42	44	45	45	43	47
Zr	147	153	155	146	148	148	154	161	148	153	147	154	161
Nb	11	12	10	9	11	10	11	11	11	11	11	10	9
Ba	789	826	825	785	741	782	792	742	749	746	784	743	739
La	33	31	30	33	29	31	30	29	30	27	27	30	26
Ce	66	64	63	75	69	68	71	68	66	66	58	62	58
Nd													
Ga	12	11	12	15	13	14	11	12	12	14	16	15	15
Pb	21	20	18	20	18	20	22	16	20	19	20	20	23
Rb	129	124	128	125	120	127	128	119	119	118	119	132	127
Sr	56	56	57	57	57	58	59	59	60	61	62	63	72
Th	12	15	14	12	12	14	11	12	15	10	13	10	12
Y	39	38	40	39	37	39	38	37	38	37	43	39	36

Sample	Oh3/L	Oh7/a	Oh4/8	Oh7/b	Oh5/b	Oh5/a	Oh4/5	Oh4/1	Oh4/3	Oh4/4	Oh4/7	D166	D165a
Deposit	Ohakuri	Ohakuri	Ohakuri	Ohakuri	Ohakuri	Ohakuri	Ohakuri	Ohakuri	Ohakuri	Ohakuri	Ohakuri	Pokai	Mamaku
Pum. Type	type 2	type 2	type 2	type 2	type 2	type 2	type 2	type 3	type 3	type 3	type 3		
SiO2	76.48	74.36	73.95	73.77		72.81	72.95	67.67		66.03	65.57	76.68	73.50
TiO2	0.20	0.27	0.27	0.29		0.31	0.31	0.55		0.62	0.61	0.12	0.29
Al2O3	12.55	13.50	13.60	13.83		14.08	14.03	16.01		16.77	16.92	12.93	14.59
Fe2O3T	1.56	2.23	2.26	2.27		2.70	2.48	4.01		4.34	4.61	1.57	2.39
MnO	0.06	0.08	0.08	0.08		0.11	0.07	0.14		0.16	0.15	0.05	0.10
MgO	0.21	0.39	0.40	0.43		0.69	0.53	1.02		0.97	1.03	0.09	0.32
CaO	1.20	1.45	1.55	1.61		1.81	1.87	3.16		3.55	3.54	0.84	1.48
Na2O	4.22	4.02	4.23	4.12		4.07	4.55	5.27		5.16	5.41	3.55	4.00
K2O	3.50	3.65	3.55	3.52		3.33	3.12	2.01		2.23	1.98	4.16	3.29
P2O5	0.03	0.05	0.12	0.07		0.09	0.08	0.15		0.17	0.17	0.01	0.05
(LOI)													
Total	100.00	100.00	100.00	100.00		100.00	100.00	100.00		100.00	100.00	100.00	100.00
V	13	14	12	16	21	21	14	20	29	30	20	7	11
Cr	3	3	3	3	3	3	4	5	5	4	3	3	3
Ni	3	3	3	3	3	3	3	3	3	3	3	3	3
Zn	28	49	48	49	57	55	51	63	64	62	70	47	65
Zr	176	217	226	220	246	244	228	374	378	372	431	157	235
Nb	8	9	9	10	10	11	10	9	10	10	10	8	10
Ba	881	718	688	693	683	717	662	645	567	610	597	807	781
La	28	30	25	29	28	27	24	23	24	35	20	31	27
Ce	46	65	62	66	62	62	57	48	54	50	49	74	71
Nd												15	34
Ga	14	13	19	17	16	19	16	17	20	21	15	14	17
Pb	15	18	14	21	16	15	18	14	15	15	20	20	26
Rb	129	115	108	111	113	112	105	65	66	65	66	137	102
Sr	107	113	119	127	141	143	146	263	294	315	325	62	120
Th	14	12	9	12	9	9	8	6	6	7	4	14	12
Y	27	40	35	39	37	37	34	29	32	27	27	33	42

Sample	D165b	D174	D175a	D175b	D175c	D211a	D211b	D213a	D213b	D214a	D214b	D214c
Deposit	Mamaku	Mamaku	Mamaku	Mamaku	Mamaku	Mamaku	Mamaku	Mamaku	Mamaku	Mamaku	Mamaku	Mamaku
Pum. Type												
SiO2	76.60	74.55	71.16	73.94	74.24	77.24	77.28	76.19	76.08	72.17	75.08	74.62
TiO2	0.15	0.27	0.43	0.28	0.26	0.15	0.15	0.15	0.15	0.31	0.18	0.20
Al2O3	13.09	13.78	15.09	13.90	13.95	12.57	12.52	13.80	13.68	15.80	14.60	15.11
Fe2O3T	1.55	2.18	3.19	2.38	2.27	1.44	1.44	1.59	1.57	2.65	1.79	1.94
MnO	0.06	0.07	0.10	0.08	0.08	0.05	0.06	0.06	0.07	0.08	0.05	0.08
MgO	0.12	0.28	0.50	0.32	0.31	0.12	0.11	0.13	0.12	0.33	0.13	0.17
CaO	0.89	1.46	2.05	1.38	1.32	0.86	0.85	0.80	0.85	1.52	0.91	0.91
Na2O	3.85	3.96	4.76	4.31	4.19	3.71	3.69	3.65	3.98	4.20	3.86	3.73
K2O	3.66	3.42	2.70	3.40	3.36	3.86	3.89	3.62	3.48	2.91	3.39	3.23
P2O5	0.02	0.02	0.02	0.02	0.02	0.01	0.01	0.01	0.01	0.02	0.01	0.02
(LOI)												
Total	100.00	100.00	100.00	100.00	100.00	100.00	100.00	100.00	100.00	100.00	100.00	100.00
V	6	10	24	14	12	9	10	8	7	12	9	9
Cr	3	3	3	3	3	3	3	3	3	3	3	3
Ni	3	3	3	3	3	3	3	3	3	3	3	3
Zn	49	52	104	66	66	45	45	50	49	63	54	59
Zr	159	222	337	240	227	147	145	162	164	262	171	193
Nb	9	9	10	9	9	8	8	10	9	10	10	11
Ba	794	742	731	726	705	786	796	855	824	734	808	813
La	32	29	21	27	24	31	29	34	37	28	30	30
Ce	79	69	70	66	61	71	80	80	92	70	79	82
Nd	31	16	24	29	42	33	40	25	27	32	40	46
Ga	14	15	17	15	16	14	15	15	15	17	15	16
Pb	20	17	76	35	48	22	21	21	21	21	20	26
Rb	120	112	95	105	104	128	130	118	119	93	112	108
Sr	61	118	181	122	115	58	56	54	59	131	68	66
Th	13	13	12	12	13	13	14	14	14	14	15	18
Y	44	34	27	34	35	38	38	42	37	40	42	42

Appendix 3 Sr isotope analyses

Sr isotope analytical work was conducted by Dr. B.L.A. Charlier in the Arthur Homes Isotope Geology Laboratory, University of Durham, UK. See Leonard (2003) for analytical protocol.

The results are compiled in the following table. Ohakuri samples are from this thesis, Mamaku (Milner, 2001), Pokai (Karhunen, 1993), MVC dome lavas and pyroclastics (Leonard, 2003), and Western Dome Complex lavas (Brown, 1994).

Sample	Sr	Actual sample wt.	ng Sr	87Sr/86Sr	1se
D154b	57	9.11	519	0.705329	0.000009
D153a	114	5.75	656	0.705291	0.000012
D59	231	21.88	5054	0.705287	0.000014
D139	57	13.46	767	0.705296	0.000008
D95	138	8.27	1141	0.705239	0.000007
MKP35	62	10.13	628	0.705279	0.000004
MKP38	125	12.1	1513	0.705286	0.000004
MKP29	150	9.22	1383	0.705287	0.000008
D213a	54	10.4	562	0.705301	0.000005
D175b	122	11.5	1403	0.705277	0.000007
D175a	181	13.06	2364	0.705215	0.000003
R2/1	68	9.26	630	0.70584	0.000006
R5/1	87	6.1	531	0.705823	0.000007
R10/1	84	6.5	546	0.705815	0.000005
M110	80	7.22	578	0.705304	0.000007
M236	80	8.6	688	0.705555	0.000007
M344	72	7.71	555	0.705259	0.000012
M470	96	9.95	955	0.705806	0.000004
MoP1	126	5.76	726	0.705306	0.000007
MP87	69	17.89	1234	0.705284	0.000011
M5055	144	17.06	2457	0.705589	0.000007
M5060	134	10.32	1383	0.705618	0.000005
M5054	94	8.56	805	0.705607	0.000006
MP86	96	10.52	1010	0.705274	0.000004

Appendix 4 Granulometry analyses

Samples analysed for their grainsize distribution were extracted from unconsolidated Forest lithofacies association (*Fla*). The size of each sample taken field was approximately 5% of the weight of the heaviest clast in the sample.

In the laboratory, samples were dried at 105 °C and weighed before they were sieved at 0.5 phi intervals. Material less than 1/16 mm (63 µm) were analysed in a Coulter Counter (lasersizer). Sieve and lasersize data are presented in the following table as cumulative weight percentages. See Appendix 1 for samples localities.

Sample	oh100a	oh100b	oh100d	oh100f	oh101d	oh114a	oh114b	oh114c	oh114d	oh148a	oh148f	oh148g	oh148h
8.0 mm		7.13	0.75	4.80		18.30		16.59	2.88	1.83	2.57	6.95	1.89
5.6 mm	0.15	11.10	2.04	17.84	0.58	23.28	0.57	18.49	2.98	3.26	5.02	10.47	5.35
4 mm	1.43	15.02	5.55	32.49	1.37	28.02	1.42	20.45	4.82	5.25	8.06	13.17	13.88
2.8 mm	3.72	19.38	9.74	43.78	4.50	32.23	2.88	22.32	8.65	7.54	12.10	15.73	28.85
2 mm	7.52	23.38	15.49	51.98	11.13	36.01	4.89	24.17	14.17	10.41	17.61	18.69	44.65
1.4 mm	11.87	33.48	21.16	58.98	17.50	40.12	8.97	28.85	21.04	14.38	24.80	22.28	57.03
1 mm	17.36	41.87	27.23	63.99	23.73	44.02	14.23	34.37	29.25	20.29	31.74	26.28	65.22
710 µm	27.67	51.97	36.90	70.28	32.82	50.24	23.68	42.18	39.95	32.22	41.48	32.82	72.63
500 µm	39.35	60.20	47.36	76.22	42.06	56.37	33.22	49.63	50.23	43.77	50.44	39.78	77.96
355 µm	51.99	68.31	58.46	82.06	52.19	62.54	42.76	57.02	60.08	53.58	59.73	48.37	82.90
250 µm	63.44	75.20	68.27	86.80	61.93	68.08	51.38	63.65	68.80	61.71	68.46	58.00	87.29
180 µm	72.83	80.52	76.77	90.06	70.10	72.48	58.96	69.53	75.51	67.37	75.05	67.49	90.12
125 µm	82.29	86.34	84.98	93.03	78.24	78.08	68.55	76.30	82.67	73.26	82.06	77.49	92.82
90 µm	89.10	90.26	90.03	95.16	84.15	83.73	77.25	81.97	87.90	77.97	87.63	85.06	94.81
63 µm	94.05	93.77	93.54	96.90	89.24	89.38	85.39	88.29	92.48	82.57	92.48	91.22	96.35
45 µm	96.75	96.25	95.68	98.16	92.04	92.42	90.50	92.05	95.20	87.85	96.05	94.84	97.54
31 µm	98.25	97.74	97.21	98.85	94.18	94.50	93.42	94.39	96.69	91.00	97.66	96.60	98.19
22.4 µm	99.05	98.70	98.29	99.31	95.90	96.19	95.57	96.22	97.79	93.77	98.59	97.67	98.70
16 µm	99.42	99.20	98.89	99.56	97.05	97.31	96.89	97.39	98.48	95.74	99.06	98.26	99.05
11.2 µm	99.61	99.47	99.28	99.71	97.94	98.15	97.81	98.22	98.97	97.20	99.34	98.70	99.33
10 µm	99.65	99.53	99.37	99.74	98.17	98.36	98.03	98.43	99.09	97.55	99.40	98.82	99.40
8 µm	99.72	99.62	99.51	99.79	98.55	98.70	98.39	98.75	99.27	98.11	99.50	99.03	99.52
5.6 µm	99.80	99.74	99.66	99.86	98.99	99.08	98.82	99.12	99.47	98.71	99.64	99.29	99.66
4 µm	99.85	99.80	99.74	99.89	99.29	99.33	99.10	99.35	99.60	99.09	99.73	99.48	99.76
2.8 µm	99.88	99.85	99.81	99.92	99.53	99.54	99.35	99.54	99.70	99.38	99.80	99.65	99.84
2.0 µm	99.90	99.89	99.86	99.94	99.70	99.69	99.55	99.69	99.79	99.60	99.85	99.78	99.90
1.4 µm	99.94	99.93	99.91	99.97	99.84	99.83	99.74	99.83	99.88	99.77	99.93	99.88	99.95
1.0 µm	99.97	99.98	99.95	99.99	99.93	99.93	99.88	99.93	99.94	99.89	99.98	99.95	99.98

Sample	oh148i	oh152b	oh152e	oh155a	oh155b	oh155c	oh155d	oh155e	oh155f	oh169d	oh169f	oh169g	oh178a
8.0 mm	2.67	3.96	0.76	11.09	2.59	7.03	0.51	8.05	0.75		1.54		5.27
5.6 mm	4.42	7.52	1.83	13.59	3.26	9.71	1.47	13.05	0.75	0.17	2.37	0.65	10.55
4 mm	7.52	12.33	2.76	16.73	4.68	13.57	3.39	18.76	1.58	0.94	3.34	3.69	17.06
2.8 mm	12.56	16.72	4.06	19.95	6.34	17.54	5.47	24.46	3.41	3.59	5.25	8.15	23.35
2 mm	18.29	20.70	5.98	23.82	8.45	20.95	7.45	29.68	5.15	9.05	7.53	12.99	29.02
1.4 mm	23.06	26.05	7.69	27.31	10.77	24.98	10.00	34.99	7.14	19.92	11.40	16.76	32.73
1 mm	28.05	30.68	10.11	30.83	13.99	28.89	13.08	40.34	9.88	37.69	15.20	20.51	36.61
710 µm	34.63	36.82	13.95	36.38	19.45	34.15	17.49	48.37	14.42	59.88	21.14	26.23	42.32
500 µm	40.64	42.41	18.18	41.59	25.03	38.93	21.90	56.13	18.21	76.48	27.41	31.72	47.66
355 µm	47.08	47.98	22.82	46.64	30.94	43.47	27.06	63.51	21.34	84.64	34.16	37.53	52.96
250 µm	53.70	53.48	28.20	51.20	36.73	48.11	32.83	69.86	23.73	88.44	41.29	43.40	57.76
180 µm	60.18	57.94	34.54	55.25	43.20	52.39	39.18	74.83	31.42	91.20	47.41	48.27	62.06
125 µm	68.55	64.70	44.70	61.41	51.93	59.45	50.29	80.64	43.84	93.22	56.71	55.19	67.22
90 µm	75.42	71.32	55.21	68.01	61.02	67.15	60.47	87.17	57.73	94.99	66.00	62.26	72.21
63 µm	82.13	78.08	67.00	74.02	77.45	75.50	71.04	93.62	71.33	96.16	74.23	69.50	77.20
45 µm	85.48	82.14	75.53	79.49	80.39	81.13	76.82	94.77	77.20	97.74	80.19	75.83	81.27
31 µm	88.29	85.62	82.63	83.86	84.39	85.85	82.09	96.04	82.26	98.32	84.75	81.01	84.56
22.4 µm	90.94	89.01	88.56	88.05	88.70	90.14	87.02	97.25	87.09	98.77	88.75	85.94	87.95
16 µm	93.01	91.66	92.34	91.26	91.95	93.12	90.58	98.08	90.47	99.09	91.63	89.66	90.79
11.2 µm	94.79	93.92	94.91	93.86	94.42	95.28	93.30	98.68	92.93	99.35	93.90	92.64	93.35
10 µm	95.29	94.54	95.51	94.54	95.04	95.81	93.99	98.83	93.57	99.42	94.50	93.42	94.06
8 µm	96.17	95.61	96.45	95.68	96.05	96.66	95.15	99.06	94.66	99.54	95.53	94.72	95.29
5.6 µm	97.26	96.91	97.48	97.02	97.23	97.63	96.52	99.33	96.04	99.68	96.79	96.28	96.79
4 µm	98.03	97.80	98.13	97.89	98.00	98.26	97.44	99.51	97.07	99.77	97.67	97.32	97.79
2.8 µm	98.70	98.54	98.65	98.59	98.64	98.78	98.23	99.65	98.00	99.85	98.43	98.18	98.59
2.0 µm	99.20	99.09	99.06	99.10	99.12	99.18	98.85	99.77	98.74	99.91	99.01	98.83	99.15
1.4 µm	99.60	99.53	99.44	99.52	99.53	99.53	99.39	99.87	99.36	99.96	99.49	99.39	99.58
1.0 µm	99.86	99.82	99.73	99.80	99.81	99.79	99.75	99.95	99.77	99.99	99.80	99.75	99.84

Sample	oh178b	oh178d	oh178e	oh184a	oh184b	oh184c	oh204a	oh204b	oh204c	oh204d
8.0 mm		0.06	0.07			7.31	4.69	0.48	0.79	0.32
5.6 mm	0.22	0.36	0.80	0.21	0.07	11.39	9.19	1.26	4.20	0.78
4 mm	0.64	1.04	2.27	1.37	0.11	14.90	15.25	2.50	7.65	1.31
2.8 mm	1.54	1.71	5.03	2.84	0.82	17.47	19.90	4.47	11.11	2.28
2 mm	2.73	3.09	9.29	5.66	1.98	19.98	25.43	7.09	14.89	3.89
1.4 mm	4.62	5.42	12.12	9.93	4.48	22.86	30.20	10.75	18.99	6.11
1 mm	7.04	8.43	15.68	15.23	7.90	26.11	34.75	14.42	22.83	8.84
710 µm	11.21	13.34	21.31	23.66	14.06	31.66	41.43	20.13	28.79	13.49
500 µm	15.79	18.17	26.88	32.09	20.71	37.49	47.71	25.52	34.52	18.47
355 µm	20.97	23.55	32.41	40.71	28.24	43.79	53.76	31.03	39.97	24.19
250 µm	26.86	29.58	37.84	49.60	36.70	50.52	58.84	36.42	44.97	29.98
180 µm	32.74	36.20	43.14	56.51	44.12	56.99	62.64	41.17	49.53	35.79
125 µm	42.39	47.44	50.16	65.77	54.71	65.69	67.65	48.60	55.57	44.07
90 µm	54.16	60.68	57.18	74.29	65.04	73.89	72.97	57.51	62.33	54.53
63 µm	68.18	73.72	65.34	82.37	75.37	81.97	78.43	68.65	70.28	66.73
45 µm	77.61	82.42	73.55	88.25	83.03	88.00	83.18	76.84	76.63	75.33
31 µm	85.31	89.05	80.43	91.68	87.96	91.49	86.52	83.40	81.64	82.24
22.4 µm	91.28	93.79	87.12	94.34	91.85	94.17	89.75	88.88	86.48	88.08
16 µm	94.62	96.39	91.90	96.07	94.35	95.91	92.29	92.47	90.20	91.90
11.2 µm	96.60	97.74	95.09	97.34	96.14	97.16	94.47	94.98	93.23	94.57
10 µm	97.03	98.00	95.79	97.65	96.58	97.47	95.07	95.58	94.02	95.22
8 µm	97.66	98.41	96.80	98.16	97.28	97.97	96.08	96.53	95.32	96.24
5.6 µm	98.32	98.86	97.81	98.73	98.09	98.55	97.31	97.57	96.82	97.38
4 µm	98.72	99.13	98.36	99.08	98.61	98.92	98.12	98.22	97.77	98.09
2.8 µm	99.04	99.32	98.78	99.37	99.04	99.24	98.79	98.74	98.52	98.66
2.0 µm	99.29	99.47	99.11	99.58	99.36	99.49	99.26	99.13	99.06	99.10
1.4 µm	99.54	99.68	99.44	99.76	99.64	99.71	99.63	99.50	99.50	99.48
1.0 µm	99.74	99.89	99.71	99.89	99.84	99.88	99.86	99.77	99.79	99.77

Appendix 5 OHDG-3 drillhole graphic log

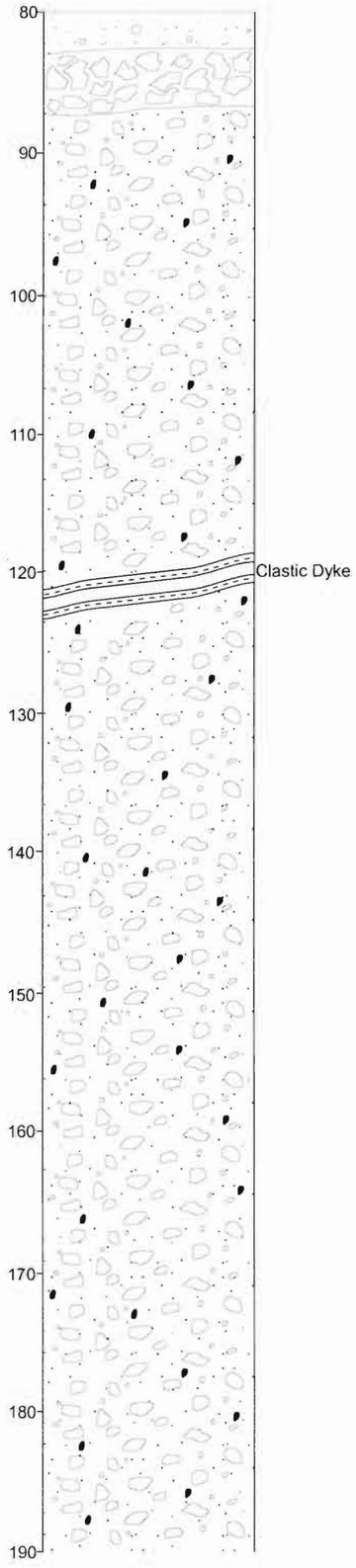

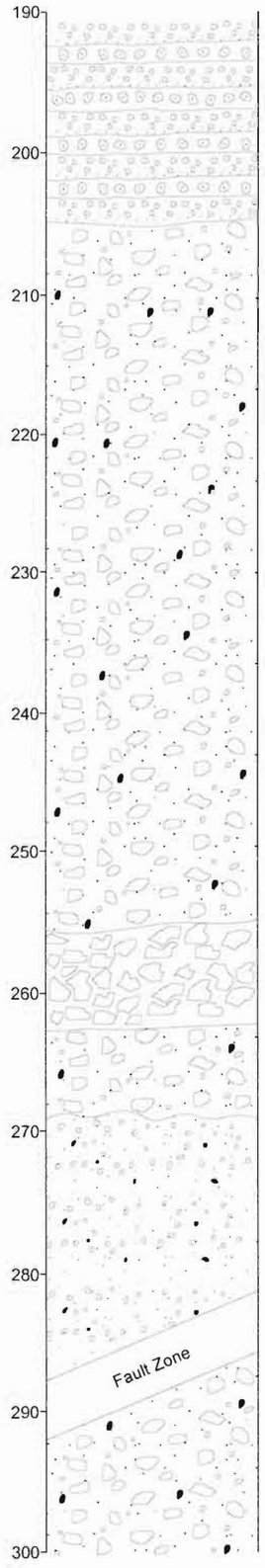

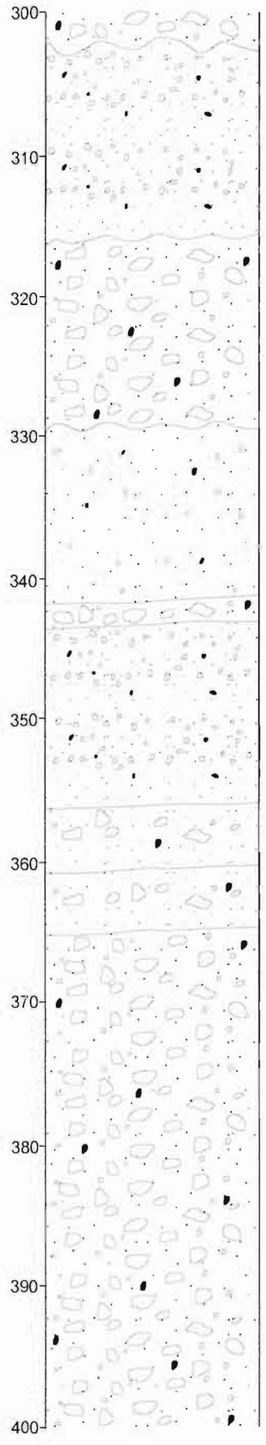

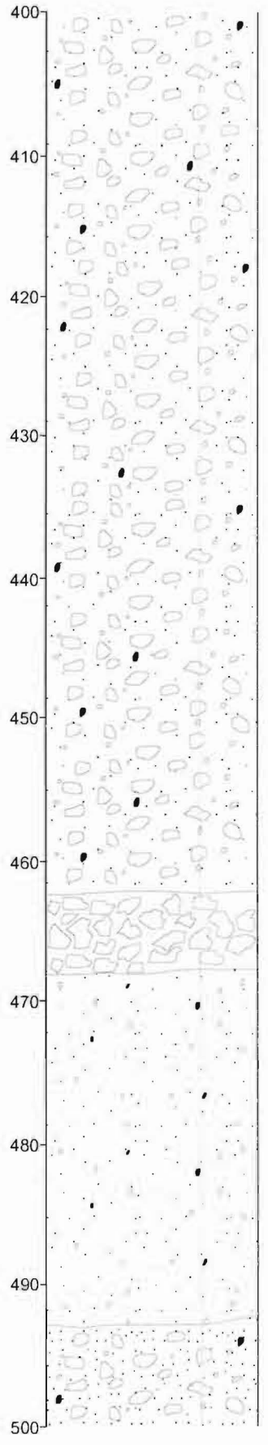

Legend	
	Massive
	Hydrothermal Breccia
	Massive - Lapilli Poor
	Diffusively Stratified
	Bedded
	Reverse Graded

Appendix 6 GPR profiles

The ground penetrating radar (GPR) was provided and operated by Matt Watson of ScanTec. The data was processed by Matt Watson and interpreted by the author. See Chapter 4 for acquisition and processing protocols.

The E8 and W1 profiles are included in the back pocket of the thesis.